2010

# Developing new optical imaging techniques for single particle and molecule tracking in live cells

Wei Sun
*Iowa State University*

## Recommended Citation

Sun, Wei, "Developing new optical imaging techniques for single particle and molecule tracking in live cells" (2010). *Graduate Theses and Dissertations*. 11783.
https://lib.dr.iastate.edu/etd/11783

# Developing new optical imaging techniques for single particle and molecule tracking in live cells

by

**Wei Sun**

A dissertation submitted to the graduate faculty

in partial fulfillment of the requirements for the degree of

DOCTOR OF PHILOSOPHY

Major: Analytical Chemistry

Program of Study Committee:
Ning Fang, Major Professor
Robert S. Houk
Klaus Schmidt-Rohr
Xueyu Song
Robert L. Jernigan

Iowa State University

Ames, Iowa

2010

## TABLE OF CONTENTS

# ABSTRACT

Differential interference contrast (DIC) microscopy is a far-field as well as wide-field optical imaging technique. Since it is non-invasive and requires no sample staining, DIC microscopy is suitable for tracking the motion of target molecules in live cells without interfering their functions. In addition, high numerical aperture objectives and condensers can be used in DIC microscopy. The depth of focus of DIC is shallow, which gives DIC much better optical sectioning ability than those of phase contrast and dark field microscopies. In this work, DIC was utilized to study dynamic biological processes including endocytosis and intracellular transport in live cells.

The suitability of DIC microscopy for single particle tracking in live cells was first demonstrated by using DIC to monitor the entire endocytosis process of one mesoporous silica nanoparticle (MSN) into a live mammalian cell. By taking advantage of the optical sectioning ability of DIC, we recorded the depth profile of the MSN during the endocytosis process. The shape change around the nanoparticle due to the formation of a vesicle was also captured.

DIC microscopy was further modified that the sample can be illuminated and imaged at two wavelengths simultaneously. By using the new technique, noble metal nanoparticles with different shapes and sizes were selectively imaged. Among all the examined metal nanoparticles, gold nanoparticles in rod shapes were found to be especially useful. Due to their anisotropic optical properties, gold nanorods showed as diffraction-limited spots with disproportionate bright and dark parts that are strongly dependent on their orientation in the 3D space. Gold nanorods were developed as orientation nanoprobes and were successfully used to report the self-rotation of gliding microtubules on kinesin coated substrates. Gold nanorods were further used to study the rotational motions of cargoes during the endocytosis and intracellular transport processes in live mammalian cells. New rotational information was obtained: (1) during endocytosis, cargoes lost their rotation freedom at the late stage of internalization; (2) cargoes performed train-like motion when they were transported along the microtubule network by motor proteins inside live cells; (3) During the pause stage of fast axonal transport, cargoes were still bound to the microtubule tracks by motor proteins.

Total internal reflection fluorescence microscopy (TIRFM) is another non-invasive and far-field optical imaging technique. Because of its near-field illumination mechanism, TIRFM has better axial resolution than epi-fluorescence microscopy and confocal microscopy. In this work, an auto-calibrated, prism type, angle-scanning TIRFM instrument was built. The incident angle can range from subcritical angles to nearly 90°, with an angle interval less than 0.2°. The angle precision of the new instrument was demonstrated through the finding of the surface plasmon resonance (SPR) angle of metal film coated glass slide. The new instrument improved significantly the precision in determining the axial position. As a result, the best obtained axial resolution was ~ 8 nm, which is better than current existing instruments similar in function.

The instrument was further modified to function as a pseudo TIRF microscope. The illumination depth can be controlled by changing the incident angle of the excitation laser beam or adjusting the horizontal position of the illumination laser spot on the prism top surface. With the new technique, i.e., variable-illumination-depth pseudo TIRF microscopy, the whole cell body from bottom to top was scanned.

# CHAPTER 1. GENERAL INTRODUCTION

## Dissertation Organization

This dissertation begins with a general introduction (chapter 1), followed by 8 chapters presented as eight scientific manuscripts including cited literature, tables and figures.

Chapter 2 shows an experimental example demonstrating the optical sectioning ability of DIC microscopy and its suitability for 3D tracking in live cells. In this chapter, the tracked mesoporous silica nanoparticle (MSN) was fluorescent labeled to help identify the MSN from other cellular nano-objects.

Chapter 3 describes a new method to distinguish and identify nanoparticles from other cellular nano-objects. The new method is based on the localized surface plasmon resonance (LSPR) effect of noble metal nanoparticles, and it requires no fluorescent labeling.

Chapter 4 describes the application of using gold nanorods as rotational probes. The new method was demonstrated useful by studying the self-rotation of microtubules on kinesin coated substrates.

Chapter 5 provides one more example of using gold nanorods as rotaitional probes in live cells. The translational motion and the rotational motion of cargoes during the endocytosis process were recorded and analyzed. By using the new technique, the exact scission point of the vesicle’s cut off from the cell membrane was extracted precisely.

Chapter 6 further studies the rotational motions of cargoes during intracellular transport. To confirm that the moving track for gold nanorod inside live cells was microtubule, a normal DIC microscopy was modified to function as DIC and epi-fluorescence microscopy simultaneously. The whole process of intracellular transport of gold nanorod including docking, transport and unbinding was recorded and analyzed.

Chapter 7 studies the axonal transport in neuron cells. Both the pause and move stages of active axonal transport were captured. The results showed that the cargoes were still bound to the microtubules during the pause stage. The move or pause of cargoes was mainly determined by the net force placed on the cargoes by different directional motor proteins.

Chapter 8 describes an auto-calibrated scanning angle prism-type total internal reflection fluorescence microscopy (TIRFM). The new TIRFM instrument can provide axial resolution better than 10 nm.

Chapter 9 shows the further modification and application of the newly developed TIRFM instrument. The TIRFM was modified to function as variable-illumination-depth pseudo TIRFM. And the illumination depth can be controlled through changing the incident angle or adjusting the horizontal position of the laser spot on the prism surface. By using the modified instrument, the whole cell body from the bottom to the top can be scanned.

Chapter 10 summarizes the whole dissertation work and provides some prospective for future research.

## Introduction

In my home country China, there is an old saying: “what you heard is questionable; what you saw is trustable.” It points out the importance of our eyes: the images collected by eyes are the concrete evidence that convinces us, and thus “seeing is believing.” However, human eyes are not omnipotent; they have their own limited detection scope. For instances, only the “visible” light with wavelength ranging from 400 nm to 700 nm can be detected directly by naked eyes; unaided human eyes cannot resolve details of a human face at a distance of 1 km. We have to rely on special tools to help extend the detection scope of naked eyes: from simplest a magnifier made of a single convex lens to much more complex microscopes; from early photographic films to more sensitive, modern detectors such as charge coupled devices (CCD)[1], photomultiplier tubes (PMT)[2] and avalanche photodiodes (APD)[3]. The great achievement in imaging instrumentation greatly benefits the progress in analytical and bioanalytical fields and expands our knowledge over the past several decades[4, 5].

Among all the microscopy techniques (optical, electron and scanning probe, etc.), optical microscopy emerged first and has been pursued by humans in the past several centuries. The credit for the first complex optical microscope (more than 1 optical component) is generally given to Zacharias Jansen (1580-1638) around the year 1595 with the help from his farther. Since then, early microscopes underwent rapid development and attracted people’ high attention.

However, the further application was hampered by two optical aberrations: (1) spherical aberration--peripheral rays and axial rays have different focal points; (2) chromatic dispersion—light beams with different wavelengths are refracted to different extents. The optical aberrations resulted in the blurring of the images in early optical microscopy. The aberrations were not successfully solved until new types of high numerical aperture objectives were invented by Ernst Abbe and Carl Zeiss in the late 19th century. Simultaneously, the gradually improved theory predicted the resolution limit (d as in formula 1) of optical microscopy, which is still being used today:

$$d = \frac{1.22\lambda}{N.A.(obj.)+NA(cond.)} \qquad (1)$$

where λ is the wavelength of light; N.A.(obj.) and N.A.(cond.) are the numerical apertures of the objective and condenser, respectively. Numerical aperture is defined as the refractive index of the imaging medium (n) multiplied by the sine of the aperture angle (α): N.A.= n • sin (α). It is straightforward that to improve the resolution, the numerical apertures of the objective and the condenser have to be maximized.

The basic and simplest type of optical microscopy is **bright field microscopy** (figure 1), which depends on the opacity of the specimen. However, in practice, there are transparent samples that have insufficient natural pigmentation or are too small. Because they lack opacity, the samples don’t absorb light much and are thus barely visible in bright field microscopy. To overcome this obstacle, different contrast-enhancing techniques with different illumination schemes have been invented.

### Dark field microscopy

In 1903, dark field microscopy (DF) was invented by Richard Adolf Zsigmondy, an Austrian chemist and Nobel Prize winner in 1923. A schematic configuration of DF microscopy is shown in figure 1. In DF microscope, the numerical aperture of the condenser is always larger than that of the objective. There is an annular stop in the condenser which blocks the central part of the illumination light beam coming from the base of the microscope. When there is no sample on the microscope stage, the entire field of view appears dark thus the name dark field microscopy. When a sample is placed on the stage, the oblique illumination light cone strikes the sample and creates scattered rays that are captured by the objective front lens. In the DF image, the structures of the specimen appear bright against the dark background and become more detectable. It is similar to the effect by which we can see the stars shinning in the sky much easier at night than in the day.

DF microscopy allows low contrast samples in bright field microscopy to be examined. For example, metallic nanoparticles that are larger than 20 nm can be detected readily in DF[6]. However, DF microscopy also has its own drawbacks. For example, to increase the signal, the sample needs to be illuminated by a strong light source, which can cause potential photo-damage to the sample. In addition, it was noticed that when eukaryotic cells were observed, the scattered light around the cell nucleus could be too strong to block the structural details of neighboring fine cellular features[7].

### Phase contrast microscopy

In 1934, Frits Zernike, a Dutch physicist, described a new microscopy method to observe thin and unstained biological samples like live cells[8]. The new method is named phase contrast microscopy (figure 1), which utilizes very small refractive index differences existing among the surrounding aqueous solutions, the cell cytoplasm and the cell nucleus. The refractive index differences shift the phase of the wave front to varying degrees when the light passes through different parts of the cell. Compared to dark field microscope, phase contrast microscope has a similar annular stop in the condenser, and it has an additional phase ring in the objective pupil. The phase ring attenuates the light directly coming from the phase stop of the condenser and adds a constant phase shift to this light. The light rays coming from different parts of the cell have varying phase shifts and most of them do not pass through the phase ring. Two types of beams are superimposed in the intermediate image plane, where they amplify or attenuate each other through interference. As a result, the phase differences inside the sample are converted into light intensity differences which are visible to the eye. The new method earned the inventor the Nobel Prize in 1953 and is still a major imaging tool utilized in many cell biology labs today.

Compared to DF, phase contrast microscope does not need a strong light source. But it has one different accompanying problem--light haloes surrounding the structure borders. In case of thick specimens, it is more annoying since the haloes can be superimposed many times over, and the optical sectioning ability of phase contrast microscopy is reduced.

### Differential interference contrast microscopy (DIC)

DIC microscopy, also known as Nomarski Interference Contrast or Nomarski microscopy, is an optical microscopy technique developed by Georges Nomarski in 1955. Compared to dark field and phase contrast microscopies, DIC adopts a much more sophisticated scheme. It has two additional polarizers and two Nomarski prisms inserted in the light path of a bright field microscope (figure 2). In an upright DIC microscope, the first polarizer and the Nomarski prism lie below the condenser. The first Nomarski prism splits the incoming polarized illumination light passing through the first polarizer into two orthogonal polarized beams with lateral displacement a little smaller than the resolution limit of the objective. Then the condenser directs the two beams to the sample placed on the microscope stage. Two intermediate images of a sample are formed by the two independent orthogonal vibration beams. The second Nomarski prism on top of the objective removes the lateral displacement caused by the first Nomarski prism and shifts the two intermediate images. Then the two images project their orthogonal vibration light components to the vibration direction of the second polarizer to interfere with each other to generate the amplitude contrast. The image contrast is contributed by the optical path difference, which is introduced by the specimen resulting from the refractive index gradients inside the specimen.

DIC microscopy can detect fine structures such as unstained microtubules (25 nm in diameter)[9-11], metallic nanospheres as small as 10 nm[12]. The sample images obtained in DIC have a unique feature: the specimen image always has a bright and a dark side and it appears to be three dimensional. The effect is much like when a subject is illuminated and shadowed by a point light source. Compared to phase contrast and dark field microscopy, DIC has no halo effect and produces less light scattering. More importantly, since objectives and condensers with high numerical apertures can be used in DIC, the depth of focus is shallow, which enables DIC to perform optical sectioning with minimal interference from obscuring structures above and below the focal plane[13].

## Electron microscopy (EM)

As predicted in formula 1, there is a limit to the resolution obtained in an optical microscope operated with visible light: a little better than 250 nm when N.A. is 1.4 and λ is 550 nm. The resolution of an optical microscope can be further improved when ultraviolet (UV) light is used[14]. For example, a 250 nm microscope allows for an increase in resolving power of a factor of around 2 compared to a 500 nm microscope. However, more expensive optical components are required when operating the microscope with UV light because few materials are suitable for producing focusing lenses at very short wavelengths[15]. Commonly used refractive materials made of glass become opaque at short wavelengths due to their strong absorption of UV light, while others (such as quartz) may exhibit birefringence which is not welcome in DIC.

To further push the resolution, a totally new type of microscopy technique was invented: electron microscopy (EM). In 1931, Ernst Ruska invented the EM for which he won the Noble Prize in 1986. The basic principle of EM is based on the wave-particle duality of the electron. The wavelength of the electron beam can be defined as formula 2.

$$\lambda = \frac{h}{mv} \qquad (2)$$

Where λ is the wavelength; *h* is Planck's constant; *m* is the mass of the electron; *v* is the velocity of the electron. When electrons are accelerated in a vacuum, their wavelength can be extremely short--only one hundredth that of the visible light. Because of the much shorter illumination beam wavelength, EM is a technique that possesses much better resolution than an optical microscopy. Then electron microscope can be used to examine specimens in details on a much smaller scale than an optical microscope. A standard EM is usually performed at very low pressures. The purpose is to reduce the collision frequency of electrons with gas atoms to negligible levels, and thus increase the mean free path of electrons. Low pressure also helps avoid generating an arc between the electron source and the ground when there is a large voltage difference between them.

The EM usually consists of an electron gun, anode, electrostatic or magnetic lenses, apertures, specimen stage and image recording system (figure 3). The electron source produces electrons that are accelerated by an anode and are focused by electrostatic or magnetic lenses. The apertures help filter out scattered electrons. Then the monochromatic electrons interact with the specimen. These interactions can be recorded in an image form by detectors such as a fluorescent screen coated with phosphor material or CCD camera.

**Scanning electron microscope (SEM)**[16] and **transmission electron microscope (TEM)**[17] are the two common types of EM, both of which can provide significantly higher resolution than optical microscopes. SEM images the sample surface by raster scanning it with a beam of high-energy electrons a few nanometers in diameter to produce signals that contain information about the sample's surface topography. Specimens that can be imaged in SEM must be electrically conductive. Nonconductive specimens are therefore usually coated with an electrically-conducting material (usually gold) by vacuum evaporation to make the surface conductive. At each point on the specimen surface the incident electron beam exchanges energy with the sample and generates signals in different forms, such as emission of low-energy secondary electrons by inelastic scattering or emission of electromagnetic radiation. Specialized detectors record the varying intensity of these signals in the location where the signals are generated and convert them into the final images.

In TEM, the electrons have higher speed since they need to pass through the sample. Thus the anode’s voltage and corresponding velocity of electrons in TEM is higher than that in SEM, and TEM generally possesses better resolution than SEM. To help the electrons travel through the sample, the thickness of TEM specimens are required to be only a few tens of nanometers which is comparable to the mean free path of the electrons[17, 18]. Thick specimens need to be sectioned to thin slices that are transparent or semitransparent to electrons. A diamond or disposable glass knife can be used to produce ultrathin slices about 60-90 nm thick.

**Scanning tunneling microscopy (STM)** was another type of EM invented by Gerd Binnig and Heinrich Rohrer in 1981 and the new technique won the inventors the Nobel Prize in 1986.[19, 20] The principle of STM is based on the concept of quantum tunneling. In classic physical world, electrons can’t penetrate through the barrier between a conducting tip and the to-be-examined surface as long as they don’t physically contact. However, in the quantum world, electrons have wavelike properties. The probability of an electron being on the other side of the barrier is small but larger than zero. Given enough electrons, some electrons will tunnel through the barrier. In STM (figure 3), the tunneling current between the conducting tip and the to-be-examined surface is created by bringing the tip very close (a few nanometers) to the surface and applying a bias voltage between them. The resulting tunneling current depends greatly on the applied voltage and the distance between the tip and the specimen surface. The tip is a very sharp needle usually made of metal and is connected to a 3 dimensional positioning device made of piezoelectric materials discovered by Pierre Curie in 1880. When working in the constant current mode, the tip scans the sample surface following its topography with angstrom precision, and the tunneling current carried by the outermost atom of the tip is sent to the feedback electronic loop. If the tunneling current exceeds the pre-set value, the tip is moved away from the sample surface, and vice versa. The topography of the sample surface is acquired and reconstructed in image forms. STM offers down to atomic level resolution in three-dimensions of object and is still the strongest microscope to date.

Non-conductive samples can’t be examined directly in STM because STM depends on the flow of the tunneling current and thus requires a conductive substrate. Non-conductive sample can be coated with a conductive layer such as gold like that performed in SEM and TEM. But this coating procedure may mask fine features of the sample. When the best resolution is desired, STM operates in a high vacuum environment since oxygen or water molecules may oxidize and contaminate the surfaces of the sample and the sharp scanning tip.

### Scanning probe microscopy (SPM)

After the invention of STM, several other different kinds of high resolution SPM techniques were following invented, one of which is **atomic force microscopy (AFM)** or scanning force microscopy (SFM)[21-23].

AFM was first invented by Quate and Gerber in 1986. The AFM consists of a cantilever with a sharp tip as the scanning probe at the cantilever’s end (figure 3). The sharpness of the tip greatly affects the final resolution and is then controlled to be on the order of nanometers or even smaller. As in STM, the motion of the tip over the sample surface in the X, Y and Z directions is generated by piezoelectric ceramics. When the tip is brought into proximity of a sample surface, Van der Waals force between the tip and the surface occurs. The force can be either the short range repulsive force (in contact-mode) or the longer range attractive force (in non-contact mode). Under the force, the cantilever deflects and performs motion that is governed by Hook‘s law. The deflection can be precisely measured by a laser and a position sensitive detector which consists of two closely spaced photodiodes. Laser light is reflected from the top of the cantilever into the array of photodiodes. Deflection of the cantilever results in one photodiode collecting more light than the other photodiode, producing an output signal collected by a differential amplifier. The signal is sent to a feedback electronic circuit to control the position of the Z piezoelectric ceramic to maintain a constant force between the tip and sample surface. By recording the Z-directional motion of the tip as it scans across the sample surface in X and Y directions, a three dimensional image of the surface can be constructed. Like all the other scanning probe microscopes, the scanning speed of an AFM sets a limitation for its application. Traditionally, an AFM requires several minutes for a typical scan.

High resolution AFM has been demonstrated to possess comparable resolution to TEM, and even to STM[24, 25]. One advantage of AFM over EM is that the sample doesn’t require a metal coating which would irreversibly change or damage the sample. Besides, AFM not only can function well in ultra-high vacuum environment, it can also work properly in an ambient air or even a liquid environment[26]. This makes it possible to study living biological samples such as live cells in their physiological conditions by using AFM.

**Near-field scanning optical microscopy (NSOM)** is another type of SPM for nanostructure investigation that breaks the optical diffraction limit[27-29]. The interaction between the light and a specimen generates both near-field and far-field light components. The far-field light propagates through the space in a diffraction limited manner and is the main light component utilized in a conventional far-field optical microscope. The near-field light component carries more high-frequency spatial information of the specimen but decays exponentially from the sample surface. The decay distance is less than one wavelength of the light and is hard to be captured by far-field optics. To utilize and detect the near-field light component to obtain spatial resolution much smaller than the light diffraction limit, NSOM has been invented[28, 30].

The pioneering work describing NSOM imaging technique at visible wavelength was first published by two groups of scientists: one group at IBM Corporation's Zurich laboratory[30] and the other one at Cornell University[31]. In a practical NSOM, the probe is placed close to the specimen surface with distance smaller than the light wavelength (figure 4). The probe is usually made of an elongated, metal-coated optical fiber with a nanometer-scale aperture fabricated at its end. The aperture can be used as a localized light source or signal collector only allowing the near-field light to pass through. When being used as light source, near-field light travels through the probe aperture, and the signal can be collected by a common microscope objective; when being used as a signal collector, the sample is illuminated from a large far-field light source, and the probe collects and directs the near-field signal to an ultra-sensitive detector such as PMT. Similarly, the probe can function as both the light source and signal collector simultaneously. Like in the other SPM techniques, the NSOM images are obtained by scanning the probe over the specimen surface in close proximity using a 3D piezoelectric stage. In an aperture NSOM, the resolution of the image is limited by the size of the aperture instead of by the wavelength of the illumination light.

Since the amount of light that can pass through a small aperture limits the strength of the illumination light or signal, the aperture size and the corresponding resolution can’t be infinitely small. People recently tried to develop aperture-less NSOM[32, 33]. The metallic tip used in the aperture-less NSOM is very sharp and does not have a hole in it. Illuminating sharpened metallic tips can lead to oscillating surface charges which produce significant near-field enhancement. The near-field enhancement converts the evanescent waves into propagating waves which can be detected by far-field optics.[32,33]

**Fluorescence microscopy**

Different from AFM, NSOM can also be classified as an optical microscopy and it permits the user to collect signals using a different contrast enhancing method—fluorescence. The phenomenon of fluorescence was first described and named by British scientist George G. Stokes in 1852. He observed that the mineral fluorspar emitted red light when it was illuminated by UV light. The molecules responsible for fluorescence emission inside fluorspar and later discovered auto-fluorescent materials are termed fluorophore. Nowadays, a variety of fluorophores are used extensively in live cell investigations to stain sub-cellular components. Those fluorophores were first extracted from natural products. Later, many efforts have been devoted in synthesizing and developing new fluorescent probes such as more stable fluorophores derived from Fuorescein isothiocyanate (FITC)[34], quantum dots (Qdots)[35, 36] and derivatives of green fluorescent protein (GFP)[37]. GFP was first discovered from the jellyfish *Aequorea victoria* in 1994, and it could be fused with other proteins in many cell types to form fluorescent fusion proteins[38]. This discovery helped researchers to specifically label sub-cellular components and led to the considerable progress in single cell studies[39, 40]. Fluorescent probes are of critical importance in the modern life sciences.

Along with the rapid development of fluorescent probes, extremely sensitive detectors such as back illuminated electron multiplying CCD which allows the detection of single molecules were invented. More stable fluorescent probes and more sensitive detectors make fluorescence microscopy an essential tool in biology and biomedical sciences[41]. Since there are various fluorophores that absorb light and emit fluorescence at different wavelengths, components of interest in the specimen can be labeled simultaneously and specifically with different fluorophores. Thus fluorescence microscopy is more chemically selective compared to the aforementioned imaging techniques.

The basic function of a fluorescence microscope is to irradiate the specimen with excitation light of a short wavelength, and then to separate the emitted long wavelength fluorescence from the excitation light. The final images are composed of fluorescent target of interest and a dark background with high contrast between them. Since the emitted fluorescence is much weaker than the excitation light, the brightness of the background affects the image quality greatly and needs to be controlled at a level as low as possible. In a conventional fluorescence microscope such as wide-field **epi-fluorescence microscope** (figure 5), all parts of the specimen in the excitation light path are excited simultaneously. Then the secondary fluorescence emitted from the out-of-focus parts of the specimen interferes with the primary fluorescence from the specimen in the region of interest and decreases the final resolution level. This situation is especially problematic for thick specimens.

### Confocal micriscopy

To reduce the interference from the out-of-focus fluorescence, confocal microscopy was invented[42]. The invention is usually attributed to Marvin Minsky, who produced a working confocal microscope in 1955. In a laser scanning confocal microscope (figure 5), the laser beam passes through the first pinhole and is focused by the microscope objective into a small focal volume within the specimen. The emitted fluorescence from the target of interest as well as the reflected excitation laser light is collected by the same objective and is separated by a beam splitter--dichroic mirror. The dichroic mirror separates the light mixture by reflecting the short wavelength excitation light while transmitting the long wavelength fluorescent light. In front of the detector (usually PMT), the second pinhole is placed to reject the out-of-focus light.

By using point illumination and pinholes to eliminate the out-of-focus light, confocal microscopy increases the resolution not only in the lateral direction but also in the axial direction[43, 44]. The better resolution in sample depth direction thus enables the optical sectioning of thick samples and allows the reconstruction of sample’s three-dimensional structures[42, 45]. The classification of confocal microscope designs is based on the method to scan the specimens: to scan either the specimen stage[46] or the illumination beam[43]. It should be noticed that the increased resolution of confocal microscope is at the cost of decreased signal intensity since much of the light from sample fluorescence is rejected at the pinhole. As a result, long exposure time or highly sensitive detector is required.

### Two-photon microscopy

In confocal microscopy, although the fluorescence from the out-of-focus specimen area is eliminated, the specimen above and below the focal plane is still excited. Thus causes unnecessary photo-bleaching or photo-toxicity. To overcome this fundamental drawback, an imaging technique named two-photon microscopy has grown fast[47-49]. The concept of two-photon excitation was first described by Maria Goeppert-Mayer (1906-1972) in 1931, and was first observed in 1962 by Isaac Abella[50]. Generally when a single photon doesn’t have enough energy to excite one fluorophore molecule to a higher energy state, it can’t be absorbed and causes no fluorescence. However, when the photon density is intense and each photon carries approximately half the energy necessary to excite the molecule, it is possible for one fluorophore to absorb two photons; and this two-photon absorption results in the emission of fluorescence with a shorter wavelength than the absorbed light.

Since the virtual absorption of a photon of non-resonant energy lasts very short time, a second photon must reach the same fluorophore molecule within the short period and together the two photons contribute their energy to excite the fluorophore to an excited state. Not surprisingly, the event of near-simultaneous absorption of two photons has a very low probability at low light intensities. Ultrafast pulsed lasers with high energy to provide high flux of excitation photons are required and is the main drawback of two-photon microscopy because ultrafast pulsed lasers are still very expensive compared to the continuous wave lasers used in normal confocal microscopy. Much more two-photon fluorescence is generated within the focal volume of the objective where the laser beam is tightly focused and the light intensity is the highest (figure 5). There is very low chance to excite the fluorophores located in out-of-focus areas. This specific localization of excitation results in a high degree of rejection of out-of-focus fluorescence and the background level is greatly reduced. Two-photon microscopy also provides excellent optical sectioning ability[51]. More importantly, it causes low photo-bleaching or damage to the objects outside the focal volume[52].

A key advantage of two-photon microscopy over confocal microscopy is that there is no need to employ additional pinholes to reject the out-of-focus fluorescence. In addition, because near infrared laser which has long penetration depth and low elastic light scattering is usually used in two-photon microscopy, it allows imaging of thick biological specimen up to about one millimeter without image deterioration[49, 53]. Since the invention of two-photon microscopy, similar technique named multi-photon microscopy also appears[54].

### Total internal reflection fluorescence microscopy (TIRFM)

The invention of various imaging techniques such as aforementioned confocal or two-photon microscopy is driven by the purpose of improving the spatial resolution in certain directions. The underlying mechanisms can be either to restrict the excitation or the detection of fluorophores within a small region in the specimen. TIRFM is a type of wide-field optical microscopy technique providing high axial resolution based on the mechanism to restrict the excitation region.

In TIRFM, when an incident light beam travelling from a medium of high refractive index ($n_1$) into a medium of low refractive index ($n_2$) at an incident angle greater than the critical angle ($\theta_c$) which is defined as $\theta_c=\sin^{-1}(n_2/n_1)$, the light beam is totally reflected from the interface back into the high refractive index medium, rather than refracting according to Snell's Law. Meanwhile, a very thin layer of electromagnetic field extending into the low refractive index medium with depth of several hundred nanometers is generated. The field is called the **evanescent field (EF)** and its intensity exponentially decays from the interface. The illumination depth in TIRFM can be adjusted by changing the incident excitation angle. In practice, the most commonly utilized interface in the application of TIRFM is the contact area between a specimen and a glass substrate. Since only a limited specimen region immediately adjacent to the interface is selectively illuminated, the specimen outside the EF can’t produce fluorescence and has negligible interference to the image background. The signal-to-noise ratio is dramatically improved and the spatial resolution is consequently improved. There are two basic approaches to configure a TIRFM instrument**:** the objective type and the prism type[55]. In objective type (figure 6), the direction of incident excitation light into interface and the collection of fluorescence signal are carried out by the same microscope objective with numerical aperture larger than 1.45. In prism type, the excitation light is directed into the prism in a different light path from that used by objective type. The objective is only used to collect emitted fluorescence. The Prism type TIRFM is usually cheaper than objective type, and there is more space to play with the incident angle in prism type TIRFM.

Since the development of TIRFM by Daniel Axelrod in 1980s[56], TIRFM has become an indispensable tool to study cellular organization and dynamic processes that occur near the cell culture and glass substrate interface[57, 58]. It has also been used extensively to study molecular dynamics, including diffusion and absorption, at liquid/solid interfaces[59]. All of these applications rely on TIRFM’s ability to selectively excite fluorophores very close to the interface while minimizing background fluorescence from out-of-focus planes and the explosion of new fluorescent proteins, organic dyes, and quantum dots (Qdots).

### Stimulated Emission Depletion microscopy (STED)

For those above described fluorescence microscopy techniques, the spatial resolution in lateral direction is still mainly restricted by the light diffraction to be around 250 nm. There is always a desire to have one far-field optical microscopy which can break the optical diffraction limit. **Structured illumination microscopy (SIM)** is such one technique. However, SIM can only improve the resolution by a factor of 2 at most[60, 61]. In 1990s, Stefan Hell invented STED to provide sub-diffraction limit resolution[62]. The instrumental configuration of STED is similar to that of a standard confocal laser scanning microscopy. And like all the other far-field optical microscopes, STED allows for non-invasive imaging of the sample. When a fluorophore is excited by light with wavelength at its absorption peak, the fluorophore enters a high energy state. If the excited fluorophore is irradiated with red-shifted 'de-excitation' light at its emission wavelength, the molecule immediately returns to the ground state and emits photons of the same wavelength. The fluorophore is therefore “switched off”. This process is called stimulated emission (figure 7) which is the core principle of STED.

In a STED microscope, two synchronized laser pulses are applied (figure 7). The first excitation laser is focused onto the sample, producing an ordinary diffraction limited spot. And the fluorophores within the spot are excited by the excitation laser. The sample is immediately irradiated by the second “de-excitation” laser which has a “donut” shape intensity profile after going through a phase modulator. Then the fluorophores located in the ring part are switched off through stimulated emission while the fluorophores in the center of the illumination spot can still emit fluorescence[63]. By modulating the intensity of the de-excitation laser, the size of “donut” spot center which corresponds to the achievable resolution can get smaller and smaller.

Basically, the better lateral resolution obtained in STED is achieved by controlling the excited specimen area smaller than the light diffraction limit. With STED, resolution of around 20-50nm[64, 65] in lateral direction can be accomplished and structures which are smaller than the light diffraction limit can be resolved. However, STED requires raster scanning over the sample surface before getting the final full image. Thus the temporal resolution is limited.

**Stochastic optical reconstruction microscopy (storm)**

STORM (developed by Xiaowei Zhuang[66, 67]) and photo- activated localization microscopy (PALM, developed by Eric Betzig[68]) are two sub-diffraction limited far-field optical microscopy techniques. They are similar to each other in theory. Both of them utilize centroid fitting of point spread function (PSF) which is the image of a point source, such as a fluorophore, on a CCD detector. Although the size of PSF is limited by the light diffraction to be around 250 nm, the center of PSF thus the location of the fluorophore can be located with precision much smaller than the light diffraction limit by simply fitting PSF with a Gaussian function. The precision of this analysis mainly depends on the number of photons collected as well as the CCD pixel size.

To perform STORM or PALM, the to-be-imaged target needs to be labeled with a special type of fluorophore that can be photo-activated. Two lasers are applied: an excitation laser with wavelength overlapping with the absorption peak of the fluorophore and an activation laser with a shorter wavelength. The specimen is irradiated by the excitation laser first until all the excited fluorophores go into a stable dark state by forming complex with the chemical having a thiol group. The complex can be reversed back into the excitable state after being illuminated by the shorter wavelength activation laser. Then the fluorophores can be excited again and emit fluorescence photons[69]. The centers of their PSFs are fitted out and mapped with high precision. Because the photo-activation is stochastic, only a few well-separated fluorophores are switched on after one cycle of activation and excitation. Thus many cycles are required to provide all the fluorophores a chance to be turned on. This process is repeated many times until the final image is built up (figure 8).

The resolution of STORM can be 20-30nm in lateral direction and 50-60nm in axial direction[67]. The major problem with STORM and PALM is that it takes up to hours to collect enough data before getting the final full images. As a result, they may not be suitable for dynamic biological process study.

## Imaging Probes

Besides the varying functions of different imaging techniques, there is one more concern we need to keep in mind: how to choose the proper probes that produce stable and detectable signals. Different microscopy techniques detect samples based on different types of signals which can be absorption, scattering or fluorescence.

Fluorescence microscopy is most often used with multi-wavelength fluorescent probes that selectively label cellular structures or materials of interest. Although fluorescent molecules and quantum dots have been used extensively in biological research, they suffer from photo-stability associated problems. Fluorescence dyes can be photo-bleached quickly within seconds that limits their application in long time tracking. Quantum dots have blinking effects that may preclude them from being used in dynamic process tracking[77].

Non-fluorescence microscopy detects the absorption or scattering of the non-fluorescent nanoparticles. In contrast to fluorescent probes, most non-fluorescent nanoparticles display better photo-stability, thus allowing the particles to be observed for long time without being bleached. Moreover, individual nanoparticles such as gold and silver nanoparticles can be localized with high spatial and temporal resolution[78]. In fact, the precision in localization of an isolated particle or a single fluorophore is only limited by the total number of photons that can be collected per unit time. Non-fluorescent nanoparticles are advantageous in this aspect, because they have large optical cross-sections that enable super-localization in short integration times. They are especially useful in live cell optical imaging.

## Live cell imaging

As discussed above, there is not a single imaging technique that is omnipotent enough to examine all types of samples or meet all research requirements. There only exists a better or more proper technique for a specific scientific question. Then how to choose the most proper imaging techniques is of critical importance.

Among all those imaging techniques, EM provides the highest resolution. However, acceptable specimen types are limited and the sample preparation is more complex for EM. For example, thick samples need to be sectioned to thin slices less than 100 nm for TEM; non-conducting specimens need to be coated with a conductive layer for SEM and STM. More importantly, fixation and complete dehydration of biological specimen is generally required prior to carrying out sectioning or coating. Apparently, it is impossible to use EM to study the dynamic biological processes which only happen inside live cells. Thus the achievement in spatial resolution is at the cost of losing temporal resolution for EM.

AFM and NSOM are two types of SPM techniques that can offer spatial resolution in three dimensions comparable to EM. AFM and NSOM may be non-invasive techniques as long as the scanning probe doesn’t physically contact the target. Since they don’t require those special specimen preparation or low pressure working environment, AFM and NSOM can be utilized to study live biological samples in ambient conditions. However, there also exist limitations for their further application. First, only the sample surface can be imaged by AFM and NSOM; biological events happening inside the sample can’t be observed. In addition, since the image provided by SPM is formed by reconstruction after scanning the entire sample surface pixel by pixel, it takes longer time than wide-field optical microscopy techniques to image the same area. And naturally, the information provided by each pixel within the same image is not from the same time. Then to some degree, AFM and NSOM still lose the temporal resolution compared to wide-field optical microscopy techniques.

The other techniques can be classified into far-field microscopy which can detect the signal both on the surface and inside the sample. Because far-field optical microscopy techniques require no physical contact between the detector and the samples, they are thus non-invasive imaging techniques. **(1)** Among them, STED and STORM (or PALM) are newly developed techniques and have the best lateral resolution at around 20-50 nm. However, STED uses point illumination technique like that in SPM; STORM (or PLAM) takes time up to hours to obtain the final image based on its stochastic illumination mechanism. Both of them are restricted from being applied to track dynamic biological processes. **(2)** Confocal and two-photon microscopy techniques, both of which require point illumination, improve the lateral resolution a little better than epi-fluorescence or TIRFM. They remain to be the main non-invasive tools to image sub-cellular structures especially in thick biological specimens. After increasing the point scanning speed, they could be used to track the dynamic biological processes of living cells in 3D. **(3)** TIRFM is a unique technique that uses far-field detection and near-field illumination in the sample depth direction. The lateral resolution of TIRFM is worse than that of confocal or two-photon microscopy. However, since the effective illumination field depth in TIRFM is usually within 200 nm, TIRFM has a better resolution in axial direction than confocal or two-photon microscopy. **(4)** Bright field, dark field, phase contrast and DIC microscopy techniques can also be classified into wide-field microscopy and non-fluorescence techniques since they image a large specimen area simultaneously instead of scanning the specimen point by point. Among them, BF does not have enough contrast when observing live cells; phase contrast has limited optical sectioning ability due to the halo effect; DF has a lower resolving power because of the strong scattered light. Only DIC microscopy is more suitable for tracking highly dynamic biological process. Although DIC has fair spatial resolution, it can possess very high temporal resolution. Moreover, compared to fluorescence microscopy, DIC can observe the target in its native state since there is no labeling process which may alter the target's native behavior. However, this advantage sometimes can be interpreted as a disadvantage. Because nano-objects smaller than the light diffraction limit appear in similar size and shape in DIC images, it becomes too hard to distinguish the target of interest from other objects and thus the imaging selectivity of DIC drops compared to fluorescence microscopy.

Nowadays, imaging of living cells and tissue is common in many fields of the life and physical sciences[70-72]. Since cells are almost heterogeneous in function and fate, these experiments are usually performed at single cell level[73, 74]. Although tracking the highly dynamic biological processes in live cells is a challenging task, many scientific questions can only be addressed in this way. To understand the mechanisms that keep cell functioning properly, cell's viability is the first priority to ensure that the physiological and biological processes to be investigated are not altered. Thus non-invasive imaging techniques are necessary. Moreover, biological events happening inside live cells can be very quick. For examples, early events in cell signaling can happen within seconds of the stimulus[75]; the scission process of vesicle from membrane during endocytosis lasts no more than one minute[76]. The most suitable imaging tool for dynamic tracking in live cells is a technique that can illuminate and detect in far-field and wide-field way: far-field allows the non-invasive 3D imaging in live cells; wide-field can promise better temporal resolution. DIC and TIRFM are such imaging techniques.

This dissertation mainly focused on the application of DIC and TIRFM in bioanalytical field and the further exploitation and modification of DIC and TIRFM. The work was carried out in four main directions:

**(1) Modify DIC to allow it detect non-fluorescent nanoprobes and distinguish them from other nano-objects in live cells.**

DIC microscopy not only increases the contrast when imaging cells, it is also demonstrated to be a very powerful imaging technique for single particle tracking. With DIC, nano-objects which are smaller than the theoretical resolution limit of optical microscopy can be detected. More importantly, nanoprobes and live cells can be imaged simultaneously for several hours without staining the cells. Thus DIC microscopy enables direct observation of biological systems while minimizing the level of intrusion on the system. However, when tracking the non-fluorescent nanoparticles in live cells, the native cellular nano-objects and the foreigner nanoprobes are both detected. Because both of them could be smaller than the light diffraction limit, they may appear in similar size and shape in DIC images. How to identify and differentiate these nanoparticles remains a technical challenging. In this work, noble metal nanoparticles especially gold nanoparticles with different shapes and sizes were tested and utilized. These noble metal nanoparticles own a unique property--the localized surface plasmon resonance (LSPR) effect. It was found that the apparent refractive indices of noble metal nanoparticles varied according to the illumination light wavelength. Since the DIC image contrast greatly depends on the refractive index difference between target of interest and the surrounding environment, the metal nanoparticles showed different contrast when changing the illumination light wavelength in DIC microscope. Then it became possible to distinguish the noble metal nanoparticles from other cellular organelles whose refractive indices didn’t change much no matter how the wavelength changed.

**(2) Develop new rotational nanoprobes that can provide the orientation information of target.**

In the past several decades, many efforts have been devoted in improving the lateral resolution of optical microscopy which can benefit the translational motion tracking of nano-objects. Nowadays, translational motion as small as few nanometers in complex environment can be tracked readily. For example, people can detect the 8nm step size of motor proteins (kinesin and dynein) in live cells[79]. However, objects also perform rotational motions. Unfortunately, rotational motions in live cells are still largely unknown due to limited imaging techniques. For example, single molecule fluorescence polarization microscopy (FPM) was only reported to study the molecular rotation on membrane or film[80, 81]. In FPM, the vibration direction of emitted fluorescence light is directly related to the orientation of the fluorophore.

When the fluorescence passes through a polarizer to the detector, the intensity fluctuates because the projected fluorescence to the polarizer changes when the fluorophore rotates. But it is still challenging to use FPM to track the rotational motions inside live cells. It is mainly due to the high auto-fluorescence background[82] and high bleaching propensity of single fluorophores in the cellular environment. By using a different method, people successfully observed the rotation pattern of single ATPase molecule by attaching a micrometer sized filament to ATPase[83]. Since the filament was larger than the light diffraction limit, the orientation pattern of the filament could be detected. However, in live cells, micrometer sized probe can alter the native behavior of the nanometer sized target.

In this work, non-fluorescent gold nanorods are used as the rotational probe which can be detected by DIC microscopy. Gold nanorods show two geometrically confined plasmon resonance modes: the longitudinal mode (along the long axis) and the transverse mode (along the short axis)[84, 85]. This results in anisotropic absorption and scattering properties of gold nanorods and thus allows their orientation determined in high precision by using DIC microscopy which utilizes two orthogonally polarized illumination beams. There are two main advantages of using gold nanorod as the rotational probe: (1) it is non-bleaching probe which allows long time observation; (1) its size is small which helps to keep the native behavior of target. The new orientation tracking method was applied to study biological processes including endocytosis and intracellular transport in mammalian cells which are strongly related with virus infection and drug delivery.

**(3) Construct auto-calibrated variable angle TIRFM with high axial resolution.**

For a normal far-field optical microscopy, the axial resolution, which is worse than the lateral resolution, is the bottleneck. Although the resolution in axial direction is enhanced to be around 500nm in confocal or two-photon microscopy, it is not really sufficient. For example, the displacement of virus penetrating through the cell membrane can be smaller than 10nm, which is too small to be precisely resolved by current existing far-field optical microscopy techniques. TIRFM can be a possible far-field microscopy technique to overcome the difficulty based on its near-field illumination nature. The illumination depth in TIRFM depends mainly on the incident angle: the larger the angle is, the smaller the illumination depth is. After collecting the fluorescence intensity of the target at different angles, the absolute z-position of the target can be determined by fitting the fluorescence intensity decay curve with theoretical decay function. The fitting precision is affected by the number of angles scanned. An auto-calibrated variable angle prism type TIRFM was developed in this work. The new instrument can scan the incident angles and run the calibration procedure automatically and reliably. The angle range can be from subcritical angles to nearly 90° with intervals smaller than 0.2°, which results in more number of incident angles available to be scanned. As a result, the best axial resolution less than 10nm can be obtained.

### (4) Construct variable-illumination-depth pseudo TIRFM for whole cell scanning.

Because the evanescent field in TIRFM is no more than a few hundred nanometers, TIRFM is mostly used to study dynamic processes that occur near the basolateral membrane of mammalian cells. However, these dynamic processes often continue beyond the evanescent field. For example, using TIRFM alone is impossible to answer the question about how vesicles formed during endocytosis move away from the membrane towards cell nuclear or other organelles. To help solve these technical problems, the variable angle TIRFM was modified to function as variable-illumination-depth pseudo TIRFM which was designed to work at subcritical angles that are smaller than yet still close to the critical angle. At a subcritical incident angle, the excitation laser beam is refracted to produce a slanted illumination path. It is possible to extend the illumination depth several micrometers into the cell body.

## References

(1) Janesick, J. R.; Elliott, T.; Collins, S.; Blouke, M. M.; Freeman, J. *Optical Engineering* **1987**, *26*, 692-714.

(2) Lubsandorzhiev, B. K. *Nuclear Instruments & Methods in Physics Research Section a-Accelerators Spectrometers Detectors and Associated Equipment* **2006**, *567*, 236-238.

(3) Wu, W. S.; Hawkins, A. R.; Bowers, J. E. In *Optoelectronic Integrated Circuits*; Park, Y. S., Ramaswamy, R. V., Eds.; Spie - Int Soc Optical Engineering: Bellingham, 1997; Vol. 3006, pp 38-47.

(4) Waterman-Storer, C. M. *Molecular Biology of the Cell* **1998**, *9*, 3263-3271.

(5) Oheim, M.; Loerke, D.; Stuhmer, W.; Chow, R. H. *European Biophysics Journal with Biophysics Letters* **1998**, *27*, 83-98.

(6) Lee, K. J.; Nallathamby, P. D.; Browning, L. M.; Osgood, C. J.; Xu, X. H. N. *Acs Nano* **2007**, *1*, 133-143.

(7) Li, H. W.; McCloskey, M.; He, Y.; Yeung, E. S. *Analytical and Bioanalytical Chemistry* **2007**, *387*, 63-69.

(8) Zernike, F. *Science* **1955**, *121*, 345-349.

(9) Allen, R. D.; Weiss, D. G.; Hayden, J. H.; Brown, D. T.; Fujiwake, H.; Simpson, M. *Journal of Cell Biology* **1985**, *100*, 1736-1752.

(10) Salmon, E. D. *Trends in Cell Biology* **1995**, *5*, 154-158.

(11) Cassimeris, L.; Pryer, N. K.; Salmon, E. D. *Journal of Cell Biology* **1988**, *107*, 2223-2231.

(12) Sun, W.; Wang, G. F.; Fang, N.; Yeung, E. S. *Analytical Chemistry* **2009**, *81*, 9203-9208.

(13) Tsunoda, M.; Isailovic, D.; Yeung, E. S. *Journal of Microscopy-Oxford* **2008**, *232*, 207-211.

(14) Heimann, P. A.; Urstadt, R. *Applied Optics* **1990**, *29*, 495-501.

(15) Zeskind, B. J.; Jordan, C. D.; Timp, W.; Trapani, L.; Waller, G.; Horodincu, V.; Ehrlich, D. J.; Matsudaira, P. *Nature Methods* **2007**, *4*, 567-569.

(16) Smith, K. C. A.; Oatley, C. W. *British Journal of Applied Physics* **1955**, *6*, 391-399.

(17) Crewe, A. V.; Wall, J.; Welter, L. M. *Journal of Applied Physics* **1968**, *39*, 5861-&.

(18) Newcomb, S. B.; Boothroyd, C. B.; Stobbs, W. M. *Journal of Microscopy-Oxford* **1985**, *140*, 195-207.

(19) Binning, G.; Rohrer, H.; Gerber, C.; Weibel, E. *Physical Review Letters* **1982**, *49*, 57-61.

(20) Binnig, G.; Rohrer, H. *Helvetica Physica Acta* **1982**, *55*, 726-735.

(21) Giessibl, F. J. *Reviews of Modern Physics* **2003**, *75*, 949-983.

(22) Hofer, W. A.; Foster, A. S.; Shluger, A. L. *Reviews of Modern Physics* **2003**, *75*, 1287-1331.

(23) Poggi, M. A.; Gadsby, E. D.; Bottomley, L. A.; King, W. P.; Oroudjev, E.; Hansma, H. *Analytical Chemistry* **2004**, *76*, 3429-3443.

(24) Fukuma, T.; Higgins, M. J.; Jarvis, S. P. *Biophysical Journal* **2007**, *92*, 3603-3609.

(25) Sugimoto, Y.; Pou, P.; Abe, M.; Jelinek, P.; Perez, R.; Morita, S.; Custance, O. *Nature* **2007**, *446*, 64-67.

(26) Chen, L. W.; Cheung, C. L.; Ashby, P. D.; Lieber, C. M. *Nano Letters* **2004**, *4*, 1725-1731.

(27) Ash, E. A.; Nicholls, G. *Nature* **1972**, *237*, 510-&.

(28) Betzig, E.; Trautman, J. K. *Science* **1992**, *257*, 189-195.

(29) Durig, U.; Pohl, D. W.; Rohner, F. *Journal of Applied Physics* **1986**, *59*, 3318-3327.

(30) Pohl, D. W.; Denk, W.; Lanz, M. *Applied Physics Letters* **1984**, *44*, 651-653.

(31) Betzig, E.; Lewis, A.; Harootunian, A.; Isaacson, M.; Kratschmer, E. *Biophysical Journal* **1986**, *49*, 269-279.

(32) Zenhausern, F.; Oboyle, M. P.; Wickramasinghe, H. K. *Applied Physics Letters* **1994**, *65*, 1623-1625.

(33) Yang, T. J.; Lessard, G. A.; Quake, S. R. *Applied Physics Letters* **2000**, *76*, 378-380.

(34) Berlier, J. E.; Rothe, A.; Buller, G.; Bradford, J.; Gray, D. R.; Filanoski, B. J.; Telford, W. G.; Yue, S.; Liu, J. X.; Cheung, C. Y.; Chang, W.; Hirsch, J. D.; Beechem, J. M.; Haugland, R. P. *Journal of Histochemistry & Cytochemistry* **2003**, *51*, 1699-1712.

(35) Jaiswal, J. K.; Goldman, E. R.; Mattoussi, H.; Simon, S. M. *Nature Methods* **2004**, *1*, 73-78.

(36) Walling, M. A.; Novak, J. A.; Shepard, J. R. E. *International Journal of Molecular Sciences* **2009**, *10*, 441-491.

(37) Tsien, R. Y. *Annual Review of Biochemistry* **1998**, *67*, 509-544.

(38) Chalfie, M.; Tu, Y.; Euskirchen, G.; Ward, W. W.; Prasher, D. C. *Science* **1994**, *263*, 802-805.

(39) Feng, G. P.; Mellor, R. H.; Bernstein, M.; Keller-Peck, C.; Nguyen, Q. T.; Wallace, M.; Nerbonne, J. M.; Lichtman, J. W.; Sanes, J. R. *Neuron* **2000**, *28*, 41-51.

(40) Fire, A.; Xu, S. Q.; Montgomery, M. K.; Kostas, S. A.; Driver, S. E.; Mello, C. C. *Nature* **1998**, *391*, 806-811.

(41) Lichtman, J. W.; Conchello, J. A. *Nature Methods* **2005**, *2*, 910-919.

(42) Conchello, J. A.; Lichtman, J. W. *Nature Methods* **2005**, *2*, 920-931.

(43) White, J. G.; Amos, W. B.; Fordham, M. *Journal of Cell Biology* **1987**, *105*, 41-48.

(44) Webb, R. H. *Reports on Progress in Physics* **1996**, *59*, 427-471.

(45) Vandervoort, H. T. M.; Brakenhoff, G. J. *Journal of Microscopy-Oxford* **1990**, *158*, 43-54.

(46) Brakenhoff, G. J.; Blom, P.; Barends, P. *Journal of Microscopy-Oxford* **1979**, *117*, 219-232.

(47) Svoboda, K.; Yasuda, R. *Neuron* **2006**, *50*, 823-839.

(48) Denk, W.; Strickler, J. H.; Webb, W. W. *Science* **1990**, *248*, 73-76.

(49) So, P. T. C.; Dong, C. Y.; Masters, B. R.; Berland, K. M. *Annual Review of Biomedical Engineering* **2000**, *2*, 399-429.

(50) Abella, I. D. *Physical Review Letters* **1962**, *9*, 453-&.

(51) Piston, D. W.; Masters, B. R.; Webb, W. W. *Journal of Microscopy-Oxford* **1995**, *178*, 20-27.

(52) Patterson, G. H.; Piston, D. W. *Biophysical Journal* **2000**, *78*, 2159-2162.

(53) Helmchen, F.; Denk, W. *Nature Methods* **2005**, *2*, 932-940.

(54) Mertz, J. *European Physical Journal D* **1998**, *3*, 53-66.

(55) Schneckenburger, H. *Current Opinion in Biotechnology* **2005**, *16*, 13-18.

(56) Axelrod, D. *Methods in Cell Biology* **1989**, *30*, 245-270.

(57) Axelrod, D. *Traffic* **2001**, *2*, 764-774.

(58) Michalet, X.; Weiss, S.; Jager, M. *Chemical Reviews* **2006**, *106*, 1785-1813.

(59) Xu, X. H. N.; Yeung, E. S. *Science* **1998**, *281*, 1650-1653.

(60) Gustafsson, M. G. L.; Agard, D. A.; Sedat, J. W. In *Three-Dimensional and Multidimensional Microscopy: Image Acquisition Processing Vii*; Conchello, J. A., Cogswell, C. J., Wilson, T., Eds.; Spie-Int Soc Optical Engineering: Bellingham, 2000; Vol. 1, pp 141-150.

(61) Gustafsson, M. G. L. *Journal of Microscopy-Oxford* **2000**, *198*, 82-87.

(62) Hell, S. W.; Wichmann, J. *Optics Letters* **1994**, *19*, 780-782.

(63) Klar, T. A.; Engel, E.; Hell, S. W. *Physical Review E* **2001**, *64*, 9.

(64) Willig, K. I.; Rizzoli, S. O.; Westphal, V.; Jahn, R.; Hell, S. W. *Nature* **2006**, *440*, 935-939.

(65) Eggeling, C.; Ringemann, C.; Medda, R.; Schwarzmann, G.; Sandhoff, K.; Polyakova, S.; Belov, V. N.; Hein, B.; von Middendorff, C.; Schonle, A.; Hell, S. W. *Nature* **2009**, *457*, 1159-U1121.

(66) Rust, M. J.; Bates, M.; Zhuang, X. W. *Nature Methods* **2006**, *3*, 793-795.

(67) Huang, B.; Wang, W. Q.; Bates, M.; Zhuang, X. W. *Science* **2008**, *319*, 810-813.

(68) Betzig, E.; Patterson, G. H.; Sougrat, R.; Lindwasser, O. W.; Olenych, S.; Bonifacino, J. S.; Davidson, M. W.; Lippincott-Schwartz, J.; Hess, H. F. *Science* **2006**, *313*, 1642-1645.

(69) Dempsey, G. T.; Bates, M.; Kowtoniuk, W. E.; Liu, D. R.; Tsien, R. Y.; Zhuang, X. W. *Journal of the American Chemical Society* **2009**, *131*, 18192-+.

(70) Stephens, D. J.; Allan, V. J. *Science* **2003**, *300*, 82-86.

(71) Liou, J.; Fivaz, M.; Inoue, T.; Meyer, T. *Proceedings of the National Academy of Sciences of the United States of America* **2007**, *104*, 9301-9306.

(72) Megason, S. G.; Fraser, S. E. *Cell* **2007**, *130*, 784-795.

(73) Spiller, D. G.; Wood, C. D.; Rand, D. A.; White, M. R. H. *Nature*, *465*, 736-745.

(74) Mullassery, D.; Horton, C. A.; Wood, C. D.; White, M. R. H. In *Essays in Biochemistry: Systems Biology, Vol 45*; Portland Press Ltd: London, 2008; Vol. 45, pp 121-133.

(75) Dolmetsch, R. E.; Lewis, R. S.; Goodnow, C. C.; Healy, J. I. *Nature* **1997**, *386*, 855-858.

(76) Merrifield, C. J.; Perrais, D.; Zenisek, D. *Cell* **2005**, *121*, 593-606.

(77) Nirmal, M.; Dabbousi, B. O.; Bawendi, M. G.; Macklin, J. J.; Trautman, J. K.; Harris, T. D.; Brus, L. E. *Nature* **1996**, *383*, 802-804.

(78) Nan, X. L.; Sims, P. A.; Xie, X. S. *Chemphyschem* **2008**, *9*, 707-712.

(79) Kural, C.; Kim, H.; Syed, S.; Goshima, G.; Gelfand, V. I.; Selvin, P. R. *Science* **2005**, *308*, 1469-1472.

(80) Jameson, D. M.; Ross, J. A. *Chemical Reviews*, *110*, 2685-2708.

(81) Edmiston, P. L.; Lee, J. E.; Cheng, S. S.; Saavedra, S. S. *Journal of the American Chemical Society* **1997**, *119*, 560-570.

(82) Monici, M. *Cell and tissue autofluorescence research and diagnostic applications*; Elsevier Science Bv, 2005.

(83) Sambongi, Y.; Iko, Y.; Tanabe, M.; Omote, H.; Iwamoto-Kihara, A.; Ueda, I.; Yanagida, T.; Wada, Y.; Futai, M. *Science* **1999**, *286*, 1722-1724.

(84) Jana, N. R.; Gearheart, L.; Murphy, C. J. *Journal of Physical Chemistry B* **2001**, *105*, 4065-4067.

(85) Sonnichsen, C.; Alivisatos, A. P. *Nano Letters* **2005**, *5*, 301-304.

## Figure captions

Figure 1.1. Schematic drawing of three types of optical microscopy instruments. (A) Bright field microscopy. The angle α stands for the angle of aperture. (B) Dark field microscopy. (C) Phase contrast microscopy.

Figure 1.2. Principle of DIC microscopy. (A) Illumination light path in DIC microscopy. (B) The imaging light path in DIC.

Figure 1.3. Schematic drawing of EM and AFM instruments. (A) SEM and TEM. SEM collects the secondary electrons scattered from the sample. TEM collects the electrons that pass through the specimen. (B) STM. (C) AFM.

Figure 1.4. Schematic drawing of NSOM. (A) The working principle of aperture NSOM. Laser is directs through optical fiber to the back aperture of the probe. The signal is collected by a far-field objective. (B) Three working modes of NSOM. The probe can be used a light source, signal collector or both simultaneously.

Figure 1.5. Schematic drawing of epi-fluorescence microscopy and confocal microscopy. (A) Working principle of epi-fluorescence microscopy. CCD is used as the detector. Hg lamp is used as the excitation light source. (B) Working principle of confocal microscopy. PMT is used as the signal collector. Laser is used as the excitation light source. There are pinholes used in confocal microscopy. The pinhole placed in the laser is optional. The specimen is illuminated point by point. (B) Light intensity and excitation efficiency in the focal point. Left: wide field epi-fluorescence microscopy. Middle: confocal microscopy. Right: two-photon microscopy.

Figure 1.6. Schematic drawing of TIRFM. (A) Objective type TIRFM. (B) Prism type TIRFM.

Figure 1.7. Mechanism of STED. (A) Principle of stimulated emission. The lifetime before it relaxes to ground state is nano-second. The stimulated emission of one electron in the excited

state is finished within pico-second. (B) Schematic drawing of STED instrument. The instrument is similar to confocal microscopy in structure. (C) Principle of sub-diffraction limit resolution obtained in STED.

Figure 1.8. Mechannism of STORM. (A) Principle of improved resolution in STORM. When three dyes are located within 250 nm, there can be resolved when they are excited simultaneously in a normal fluorescence microscopy. In STOM, the three dyes are controlled to be excited one by one. The location of each dye can be determined through centroid fitting. (B) Schematic drawing of STORM instrument. The instrument is similar to TIRFM microscopy in structure.

**Figures**

Figure 1.1

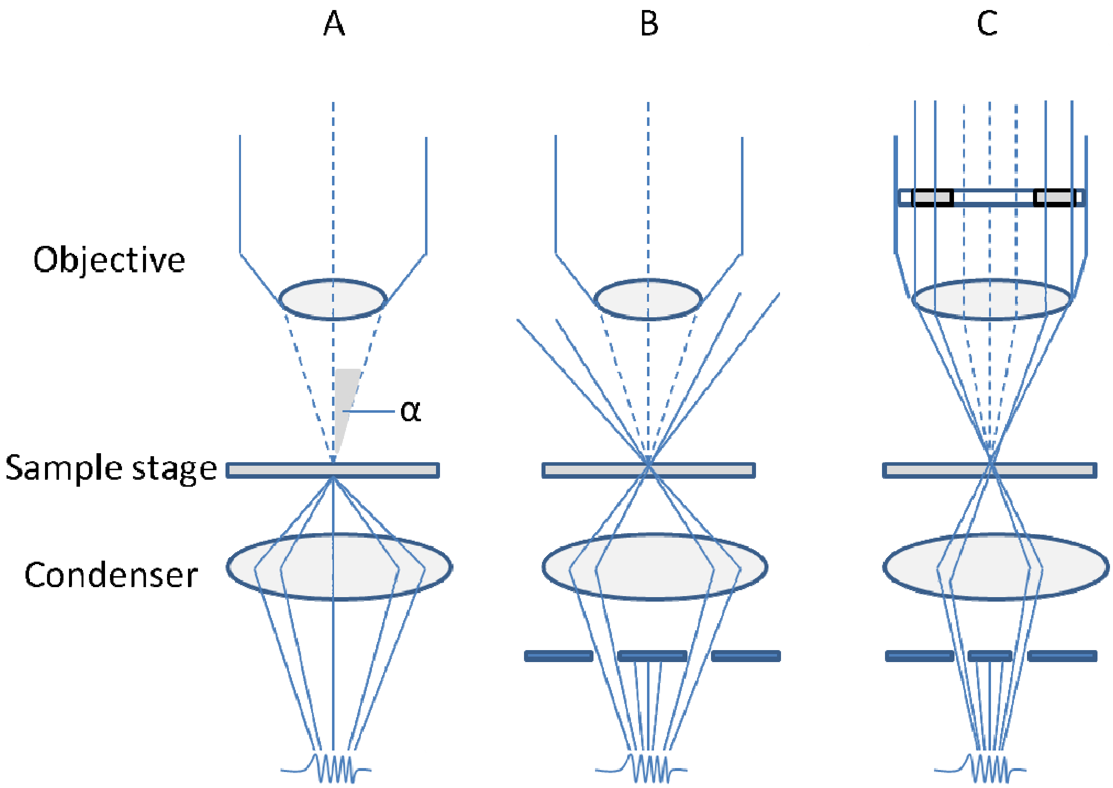

Figure 1.2

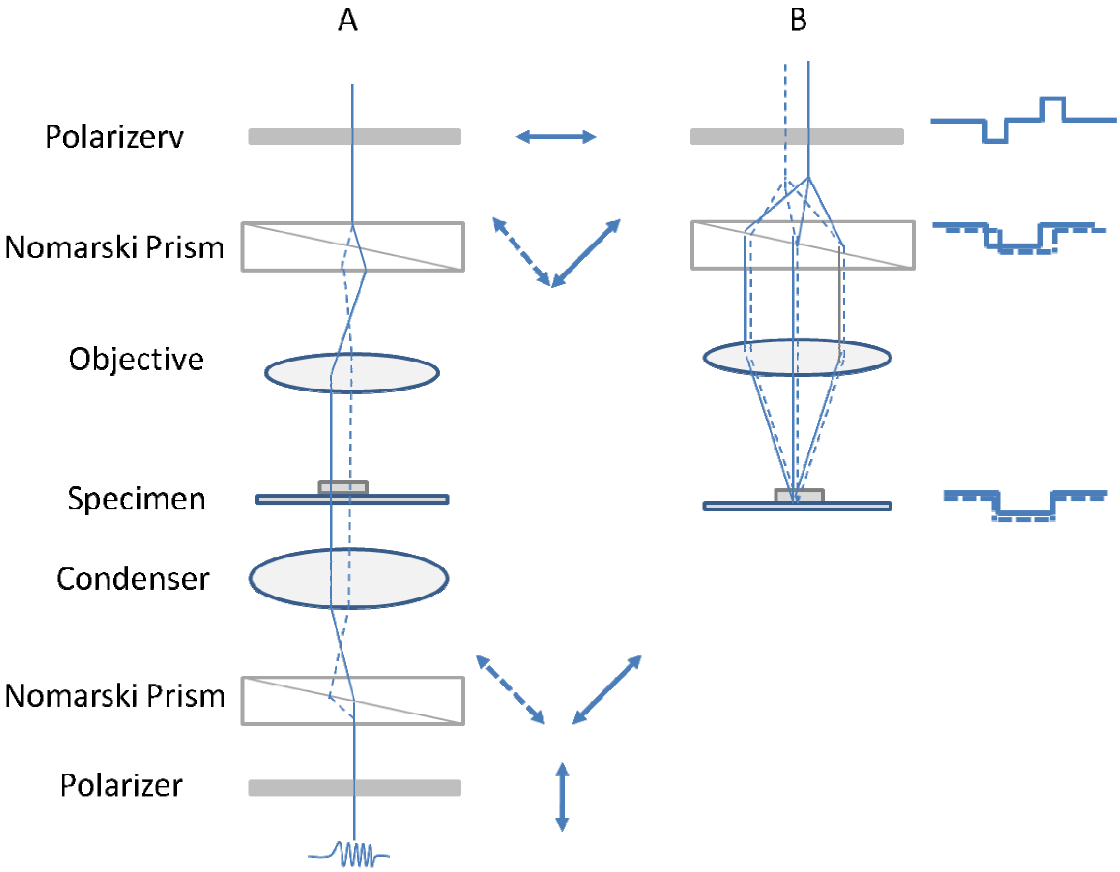
A
B
Polarizerv
Nomarski Prism
Objective
Specimen
Condenser
Nomarski Prism
Polarizer

Figure 1.3

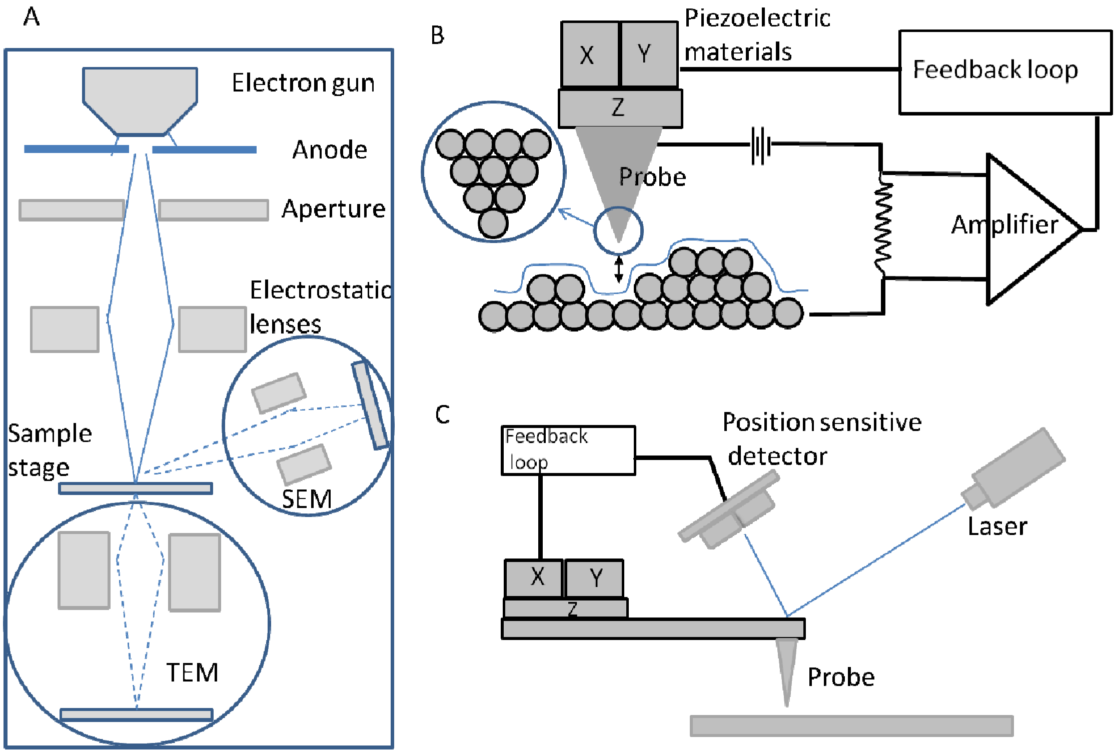
A
Electron gun
Anode
Aperture
Electrostatic lenses
Sample stage
SEM
TEM
B
X
Y
Z
Piezoelectric materials
Feedback loop
Probe
Amplifier
C
Feedback loop
Position sensitive detector
X
Y
Z
Laser
Probe

Figure 1.4

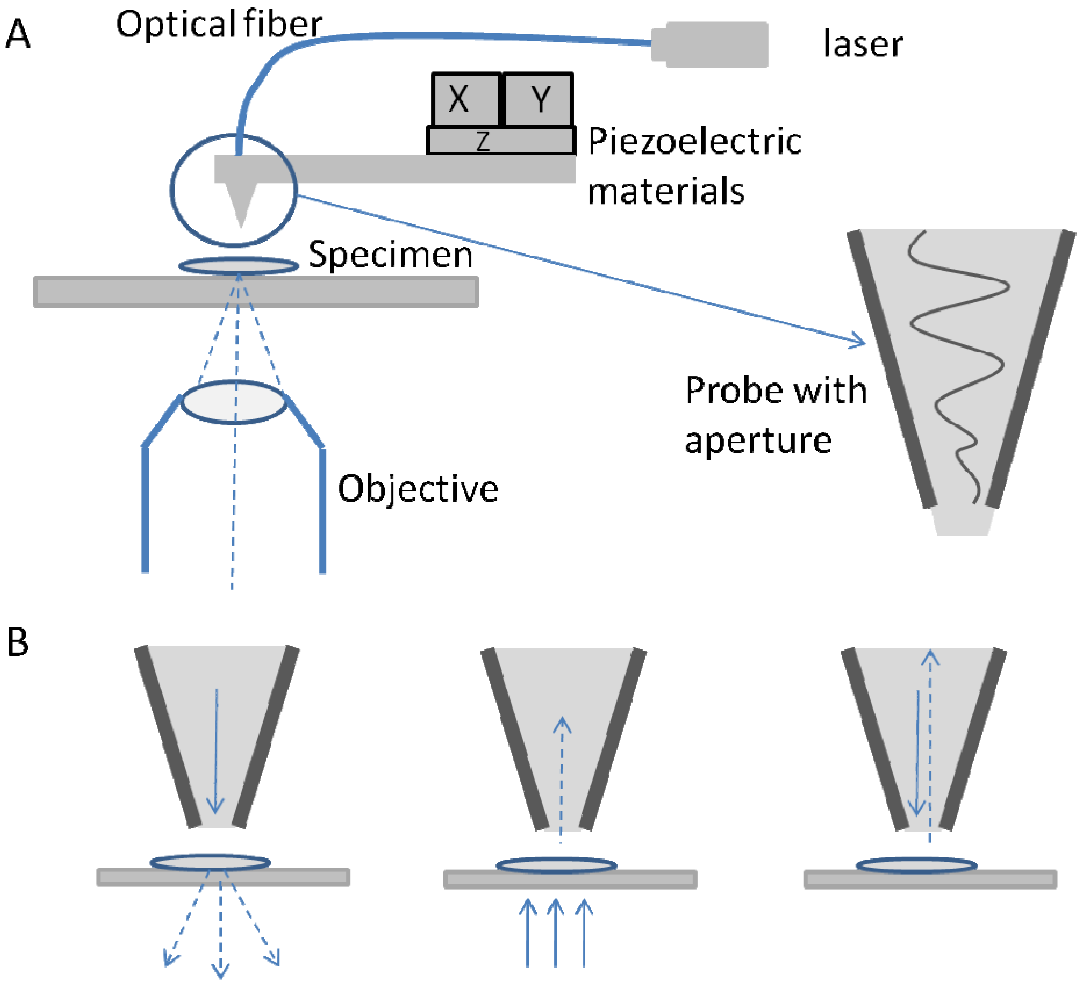
A
Optical fiber
laser
X
Y
Z
Piezoelectric materials
Specimen
Probe with aperture
Objective
B

Figure 1.5

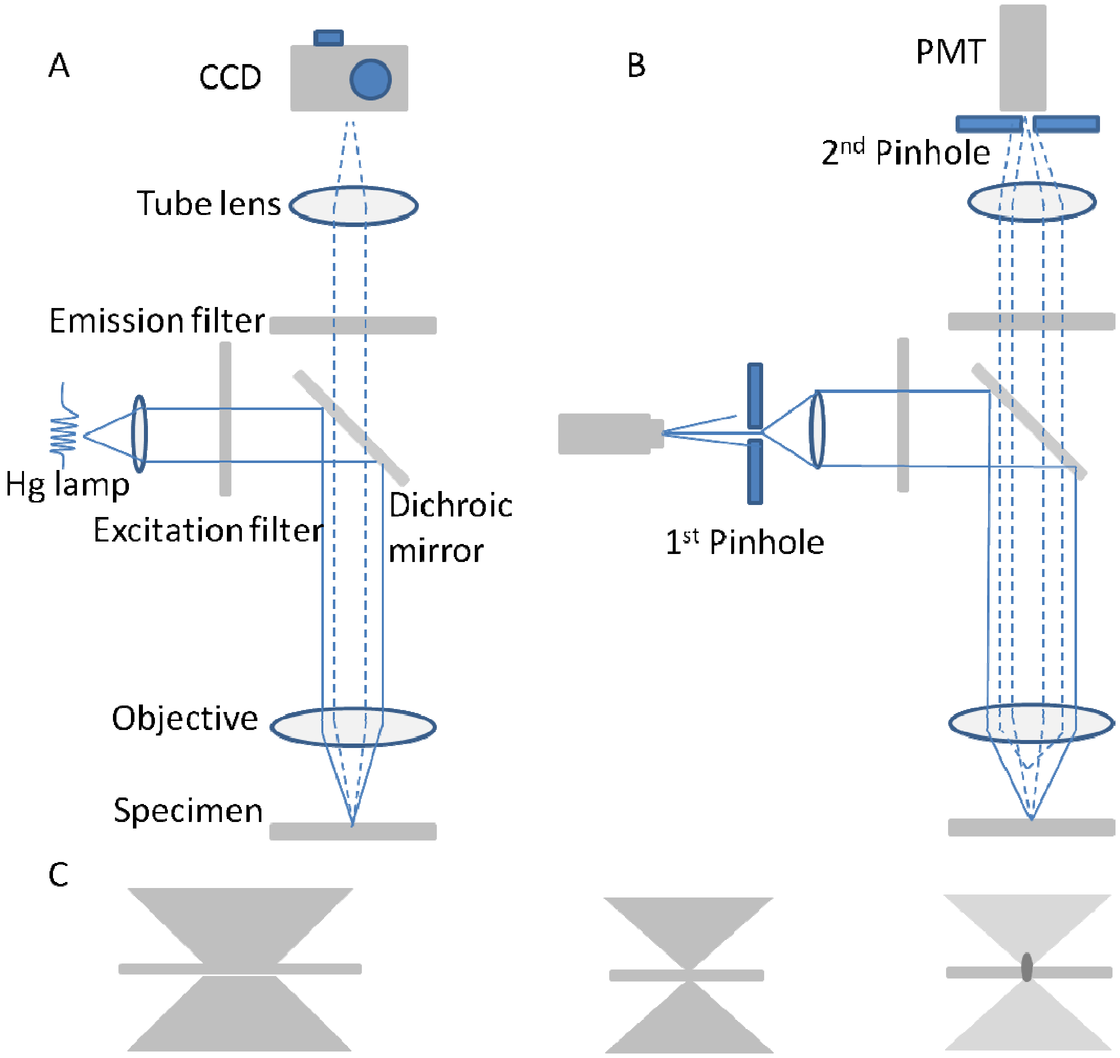
A
CCD
Tube lens
Emission filter
Hg lamp
Excitation filter
Dichroic mirror
Objective
Specimen
B
PMT
2nd Pinhole
1st Pinhole
C

Figure 1.6

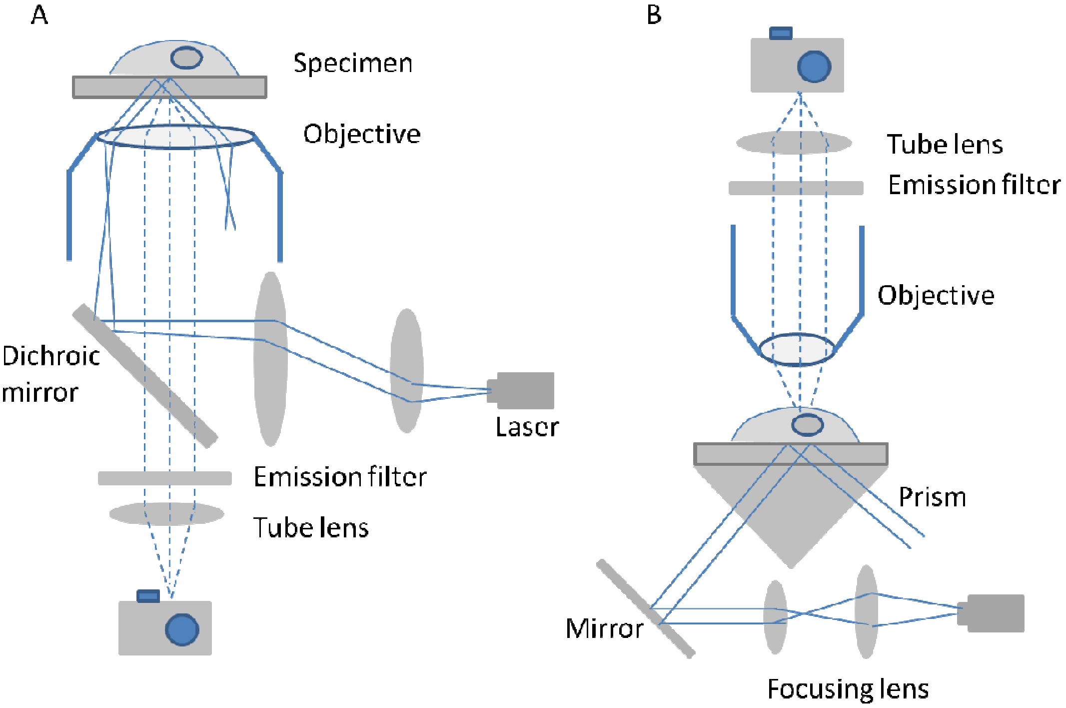
A
Specimen
Objective
Dichroic mirror
Laser
Emission filter
Tube lens
B
Tube lens
Emission filter
Objective
Prism
Mirror
Focusing lens

Figure 1.7

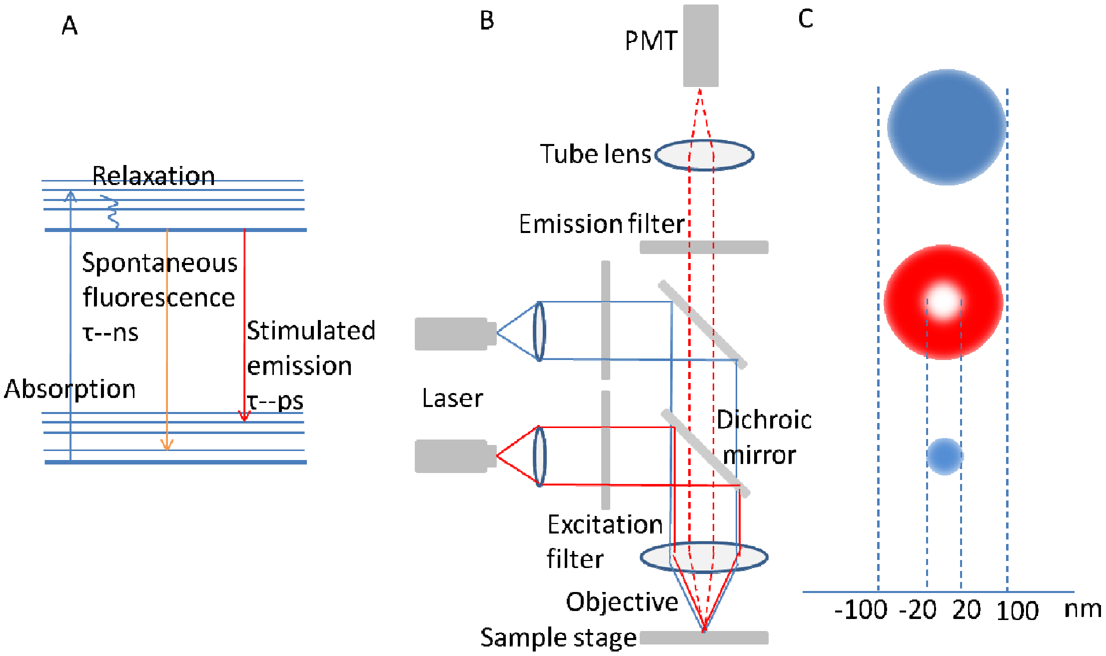
A
Relaxation
Spontaneous
fluorescence
τ--ns
Stimulated
emission
τ--ps
Absorption
B
PMT
Tube lens
Emission filter
Laser
Dichroic
mirror
Excitation
filter
Objective
Sample stage
C
-100
-20
20
100
nm

Figure 1.8

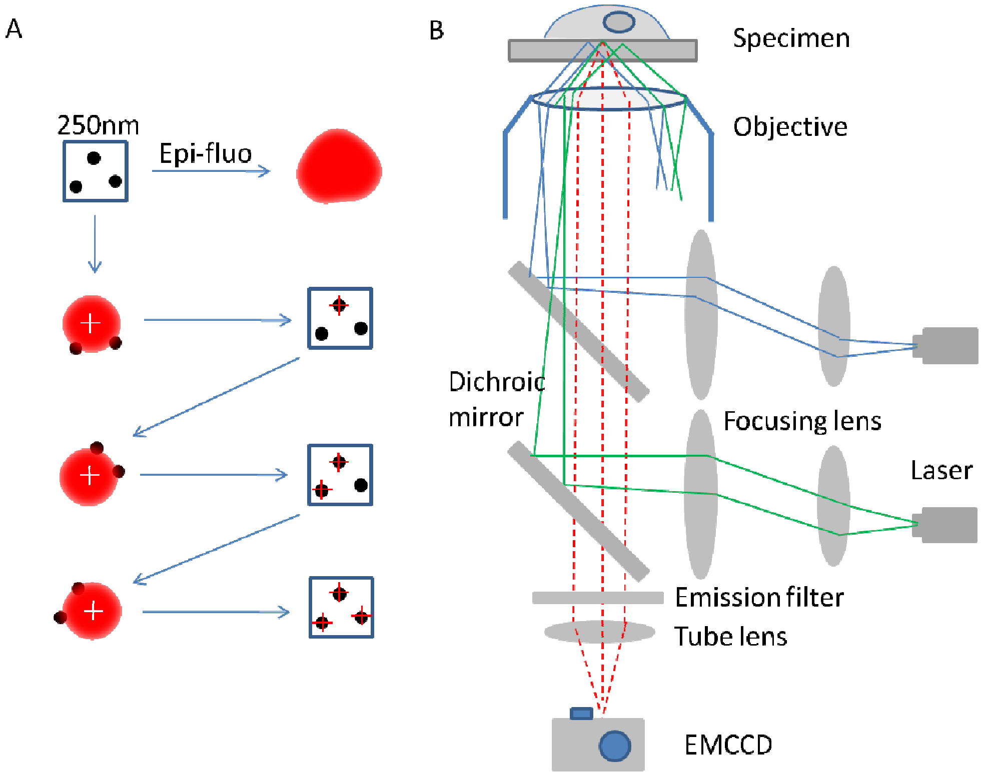
A
250nm
Epi-fluo
B
Specimen
Objective
Dichroic
mirror
Focusing lens
Laser
Emission filter
Tube lens
EMCCD

# CHAPTER 2. ENDOCYTOSIS OF SINGLE MESOPOROUS SILICA NANOPARTICLE INTO LIVING HUMAN LUNG CANCER CELL (A549) OBSERVED BY DIFFERENTIAL INTERFERENCE CONTRAST MICROSCOPY

Wei Sun, Ning Fang, Brian G. Trewyn, Makoto Tsunoda, Igor I. Slowing, Victor S.Y. Lin, Edward S. Yeung

Published in Analytical and Bioanalytical Chemistry*

## Abstract

The unique structural features of mesoporous silica nanoparticles (MSN) have made them very useful in biological areas, such as gene therapy and drug delivery. Flow cytometry, confocal microscopy, and electron microscopy have been used for observing the endocytosis of MSN; however, flow cytometry cannot directly observe the process of endocytosis; confocal microscopy needs to stain cells; electron microscopy requires fixed cells. In the present work, we demonstrate for the first time that differential interference contrast (DIC) microscopy can be used to observe the entire endocytosis process of MSN into living human lung cancer cell (A549) without staining. There are 3 physical properties (observations) that characterize the locations of MSN and the stages of the endocytosis process: motion, shape, and vertical position. When it was outside the cell, the MSN underwent significant Brownian motion in the cell growth medium. When trapped on the cell membrane, the motion of MSN was greatly limited. After the MSN got inside, it resumed motion at a much slower speed because the cytoplasm is more viscous than the cell growth medium and the cellular cytoskeleton networks are present as obstacles. Moreover, there were shape changes around the MSN due to the formation of vesicle after the MSN was trapped on the cell membrane. Finally, by coupling a motorized vertical stage

---

* Reprint with permission from Analytical and Bioanalytical Chemistry, **2008**, 391(6), 2119-2125. Copyright © Springer

to the DIC microscope, we recorded the locations of the MSN three-dimensionally. The accurate 3D particle tracking ability in living cells is essential for studies of selectively targeted drug delivery.

## Introduction

Mesoporous silica nanoparticle (MSN) materials have many unique features, such as chemical stability, tunable pore diameter (2-30 nm), narrow pore size distribution, and high surface area (>700 $m^2$ $g^{-1}$). Moreover, the pores inside MSN are independent parallel channels that can be capped and opened at controllable chemical,[1] photo,[2] or pH stimulation.[3] The premature release of guest-molecules can be avoided because guest-molecules are protected from enzymatic digestion before they reach destinations. Furthermore, compared to viral vectors, MSNs cause fewer pathogenic risks;[4] compared to polymer nanoparticles, MSNs are more resistant to organic solvents.[5] It has already been demonstrated that MSNs are biocompatible and can be endocytosed by animal and plant cells.[6, 7]

Because of these unique features, MSNs have been used as carriers in controlled-release delivery system to transfer cell membrane impermeable molecules.[8] In order to increase cell recognition and selective endocytosis of MSN, it is of great importance to observe and understand the entire process of endocytosis of MSN. Flow cytometry, confocal microscopy, and electron microscopy have been employed previously for this purpose.[8-11] Flow cytometry can be used to study the efficiency of endocytosis by converting the measured fluorescence intensity into the amount of MSNs present inside the cell, but it cannot provide information during the process of endocytosis or show the distribution of MSNs inside the cell. Confocal microscopy can be used for live cell imaging, but cells need to be stained and its operation is not fast enough for real-time particle tracking. In electron microscopy, more detailed information can be extracted, including the distribution of MSNs; however, because the cells are fixed and dead, this technique cannot track continuous movement of MSNs inside living cells directly.

In the present study, various modes of optical microscopy were tested for non-intrusive, continuous tracking of sub-diffraction-limited MSN during the entire endocytosis process in living cells. The application of bright field microscopy is limited because there is too little contrast between MSNs, cells and the surrounding medium. The contrast can be greatly improved by using phase contrast microscopy, dark-field microscopy, or differential interference contrast (DIC) microscopy. These three techniques have been compared previously for horizontal resolving power and vertical sectioning ability.[12] Here we evaluated their performance for observing the endocytosis of single MSN, and demonstrated that DIC sectioning microscopy was a direct, straightforward, and high-throughput method for monitoring endocytosis or other dynamic biological events at the single-cell level.

In phase contrast microscopy, halos were always seen around the edges of cell membrane and intracellular organelles, blurring some details. In dark-field microscopy which mainly depends on light scattering of objects, we noticed that inside eukaryotic cells, especially around cell nuclei, the scattering light was too strong to resolve particles of sub-200 nm in diameter. In addition, dark-field microscopy needs strong incident light, which is not suitable for long-time observation of living cells.

DIC microscopy not only increases the contrast between cells and the surrounding medium, but also has some other advantages over phase contrast and dark-field microscopy.[13] DIC microscopy does not have the “halo” edge effect, and it does not cause much scattering inside the cell. DIC microscopy makes full use of the numerical aperture of the system and has a shallow depth of focus, leading to a much better vertical resolution and thus good optical sectioning. Moreover, DIC microscopy utilizes the interference of light instead of the opacity of specimen; it can resolve objects which are smaller than theoretical resolution limit of optical microscopy. The MSN of around 100 nm in diameter used in our experiment is one example.

DIC microscopy is useful for single particle tracking in living cells. In our experiment, we used DIC microscopy to record the entire process of endocytosis of single MSN by living human lung cancer cell (A549) without staining the cell. Unlike in electron microscopy, the cells were alive during the entire recording period and the endocytosis process was tracked continuously from start to finish. Three physical properties (observations) – motion speed, shape, and vertical position – were used to characterize the locations of MSN (inside/outside the cell or on the cell membrane) and the stages of the endocytosis process.

## Experimental

**Synthesis of fluorescein isothiocyanate (FITC) labeled and tri(ethylene glycol) organic linker modified MSNs.** Tetraethylorthosilicate was purchased from Gelest (Philadelphia, PA). Fluorescein isothiocyanate isomer I, anhydrous DMSO, 3-aminopropyltrimethoxysilane, and cetyltrimethylammonium bromide were purchased from Sigma-Aldrich (St. Louis, MO). All chemicals were used as received. FITC labeled MSNs were prepared by reacting 5.0 mg (1.284 mmol) of FITC with 40 µl (1.146 mmol) of 3-aminopropyltrimethoxysilane (APTMS) in anhydrous DMSO under inert atmosphere for 2 hours, and then co-condensing the resulting product with 5.0-ml (32.5-mmol) tetraethyl orthosilicate (TEOS) by the hydrothermal method previously reported.[11] To a mixture of 1.0-g (2.75-mmol) cetyltrimethylammonium bromide (CTAB), 480-ml water and 3.5-ml 2M sodium hydroxide, heated at 80°C, under vigorous stirring, the TEOS and the product of FITC and APTMS reaction were added dropwise. The reaction mixture was maintained at 80°C for 2 hours, after which the resulting orange colored solid was filtered, washed thoroughly with water and methanol and dried under vacuum at 80°C for 20 hours. The synthesis of the organic ligand was achieved by modifying a procedure previously reported.[14] Specifically the synthesis of 1-[2-(2-bromo-ethoxy)-ethoxy]-2-methoxy-ethane was followed directly, then this molecule was attached to 3-aminopropyltrimethoxysilane via an SN$^2$ reaction in refluxing ethanol overnight. This crude product was directly grafted to as-synthesized FITC-MSNs (still containing surfactant template). Once grafted the surfactant template was removed via our previously published method.[15] The average diameter of these FITC-labeled spherical MSNs measured by transmission electron microscopy (TEM) was around 100 nm (Figure 1).

**Cell culture.** Human lung cancer cell (A549) was purchased from American Type Culture Collection (ATCC, Baltimore, USA, CCL-185). The cells were plated in a T25 cell culture flask (Corning). 4-ml Kaighn's Modification of Ham's F-12 medium (F-12K medium, ATCC) supplemented with 10% fetal bovine serum was added to the flask. The flask was put in cell culture oven (37°C, 5% CO$_2$). The cells were subcultured every 2 to 3 days on a ratio of 1:3. When subculturing, 200 µl of cell suspension solution was mixed well with 800 µl of F-12K medium (supplemented with 10% fetal bovine serum). Then 150 µl of such cell suspension solution was transferred to a 22mm×22mm No.1 poly-L-lysine coated coverslip, which was then put into a Petri dish (50mm×12mm, Corning). The Petri dish was left in cell culture oven for 1 hour to let cells attach to the coverslip. After 1 hour, 1.5 ml of F-12K medium (supplemented with 10% fetal bovine serum) was added into the Petri dish to immerse the whole coverslip. Finally, the Petri dish was put back in the cell culture oven for 24 hours.

**Sample preparation for DIC microscopy.** Figure 2 is the schematic diagram of the experimental setup. Two pieces of double-sided tape were stuck parallel on the top of a pre-cleaned glass slide. The distance between the two pieces of tape was about 15 mm. A coverslip was taken out from the Petri dish which was prepared in the last step, and the side without cells was cleaned and dried by kimwipe. The coverslip was placed carefully on the top of the tapes, with the poly-L-lysine-coated side facing the glass slide. Then 20-µl MSN suspension solution (30-µg/ml F-12K medium without fetal bovine serum, sonicate for 30 min before use) was added to the chamber formed between the glass slide and the coverslip. The other two open edges of the chamber were sealed by nail oil to prevent evaporation. This sample slide was placed on the stage of the DIC microscope for observation. Because the cells were hung on the ceiling of the chamber, the endocytosed MSN actually moved up from the bottom of the cell against the direction of gravity.

It is crucial to keep the cells alive during the recording period. In our observation, when the ell was dying, the cell membrane would usually break, the cell could no longer stretch out on the coverslip, and lots of cell cytoplasm materials bubbled out. None of these phenomena were observed while the endocytosis event was recorded. Besides, the intracellular organelles, such as granules and mitochondria, were moving around. All these observations confirmed that the cells were still alive even after the recording was finished.

**DIC microscopy.** An upright Nikon Eclipse 80i microscope equipped with a DIC slider was used for investigations. A 100× objective lens (Nikon Plan Apo/1.40 oil) was used. The fine focusing adjustment of the microscope is 0.1 mm/rotation. A motorized rotary stage from Sigma Koki (model no. SGSP-60YAM) was coupled to the fine-adjustment knob on the microscope. The motor was controlled by Intelligent Driver, CSG-602R (Sigma Koki). The travel for each pulse is 0.0025°. A CCD camera (Cool SNAP ES, Photometrics, Tucson, AZ, pixel size 6.4 µm) was mounted on the microscope. The CCD exposure time was 200 ms at 20-MHz digitization speed unless otherwise specified. Winview32 (Roper Scientific, Princeton, NJ) was used for cell image collection and data processing.

We first distinguished the MSNs from cellular organelles of similar size and shape by fluorescence microscopy equipped with a typical FITC filter set and then switched to DIC microscopy to track the movements. The tracking was accomplished by manually adjusting the focus to the same plane as the MSN. At the same time, vertical sectioning through the entire cell was performed every 5-10 min or when a change in the MSN's vertical position was noticed.

## Results and Discussion

Generally speaking, to carry out endocytosis, the invaginations or pits of cell membrane form vesicles which contain foreigner materials, and then these vesicles pinch off from cell membrane, move into cytosol, and travel towards their final destinations.[16] MSNs are endocytosed by the cell in a similar manner. The whole endocytosis process of a single MSN was recorded by DIC microscopy. To characterize the locations of the MSN and the stages of the endocytosis process, three physical properties were studied: motion speed, shape, and vertical position.

**Motion speed.** During the whole process of endocytosis, the MSN, a hard spherical particle with pores, went through 3 kinds of environment: cell growth medium, cell membrane surface, and cell cytoplasm. They were also the 3 main stages of endocytosis. The MSN had different motion speeds in each stage.

In the first stage, the MSN underwent significant Brownian motion in the cell growth medium. To have a more quantitative knowledge of the motion, we calculated the diffusion coefficient ($D$) in two dimensions. The lateral displacements ($r$) of the MSN between two successive steps were calculated by reading out the x-y coordinates of the MSN in a trajectory. The time interval ($t$) between the two successive steps was 0.2 s. The distribution of lateral displacement is shown in Figure 3A.

The probability density that a particle diffuses a distance $r$ in a constant time interval $t$ can be expressed in eq.1[17]:

$$P(r)dr = \frac{2rdr}{<r^2>}\exp\left[-\frac{r^2}{<r^2>}\right] \qquad (1)$$

where $<r^2>$, the mean-square displacement, is equal to $4Dt$. Note that the probability $P(r)$ is interchangeable with the number of counts used as the y-axis in Figure 3, where the total number of measurements was known. Naturally, a large number of displacement measurements – usually generated by Monte Carlo simulation[17] – are required to have a good fit with eq.1. Due to relatively small sample size from actual experiments, the mean lateral displacement ($<r>$) was estimated to be $7.6\times10^{-5}$ cm by fitting the histogram with a typical Gaussian function, instead of eq.1. Then by using formula $<r^2> = 4Dt$ with $t = 0.2$ s, the diffusion coefficient $D$ was calculated to be $2.9\times10^{-8}$ cm$^2$s$^{-1}$.

In order to confirm whether this diffusion coefficient had the right order of magnitude, a theoretical diffusion coefficient $D^*$ was calculated from the Stokes-Einstein equation:

$$D^* = \frac{k_B T}{3\pi\eta d} \qquad (2)$$

where $k_B$ is the Boltzmann constant, $T$ is temperature (295 K), $\eta$ is the viscosity of cell growth medium (0.98 cp, Material Safety Data Sheet of Minimum Essential Medium, Invitrogen, Carlsbad, CA), and $d$ is the particle diameter (100 nm). The value of $D^*$ is $4.4\times10^{-8}$ cm$^2$s$^{-1}$, and $D$ and $D^*$ are indeed on the same order of magnitude.

Before the MSN settled down on the cell membrane, it was very close to but not on the cell membrane and still moved quickly outside of the cell. The diffusion coefficient in this intermediate stage was $1.0\times10^{-9}$ cm$^2$s$^{-1}$ (Figure 3B), which was one order of magnitude smaller than the diffusion coefficient in the first stage. It is believed that the attractive force between the ligands on the MSN surface and the corresponding receptors on the cell membrane surface limited Brownian motion of the MSN. When the force was strong enough, the MSN was finally trapped on the cell membrane surface. The MSN eventually crossed cell membrane (usually less than 10 nm in thickness [18]) to get inside the cell. This was the second stage.

After the MSN got inside, it resumed motion in cytoplasm, but at a much lower speed compared to the speed in the first stage. This was the third stage. By using the same method mentioned before, we plotted the lateral displacement distribution in Figure 3C. The diffusion coefficient calculated was $6.4\times10^{-10}$ $cm^2s^{-1}$, two orders of magnitude smaller than the diffusion coefficient in the first stage, which cannot be explained solely from the viscosity difference between cell cytoplasm and cell growth medium, because the aqueous phase viscosity of cell cytoplasm is only slightly larger than the viscosity of water (1 cp).[19, 20] For example, the cell cytoplasmic viscosity of Chinese hamster ovary cell (an epithelial cell) is 1.0-1.4 cp;[19] therefore, we can assume that A549 cell, which is also an epithelial cell, has a similar cytoplasmic viscosity. This large difference in diffusion coefficients can be attributed to other properties of cell cytoplasm. It is well-known that cell cytoplasm is not just homogenous salt buffer solution containing proteins; instead, cell cytoplasm has mesh-like networks composed of small cytoskeletons, such as microtubules (25 nm in diameter), microfilaments (4-6 nm in diameter) and intermediate filaments (7-11 nm in diameter),[21, 22] which are all too small to be resolved by our DIC microscopy. Cytoskeleton dense networks can function as physical obstacles to limit the free diffusion of macromolecules inside cytoplasm.[23] The reported mesh size in cytoskeleton networks was 20-40 nm,[23] or on the order of 100 nm.[24] Considering that the MSN used in our experiment had a diameter of 100 nm, it is reasonable to assume that Brownian motion of the MSN inside cytoplasm was greatly constrained. Besides, cell cytoskeletons are well-known for their importance in transportation inside the cell.[25] Although there is no report about the requirement of microtubules or small filaments for transportation of MSN inside the cell, we cannot exclude the possibility. If the MSN was bound to cytoskeletons and was selectively directed to some subcellular domains along microtubules or filaments, its motion could no longer be described by free-space Brownian motion.

**Shape change.** The video recorded by DIC microscopy clearly showed that the MSN was enveloped by a vesicle and engulfed into the cell. There were obvious shape changes around the MSN during the process of endocytosis. As shown in Figure 4, after it was trapped on cell membrane, the MSN diffused laterally in the first 15 min, and the shape around MSN did not change noticeably. In the next 15 min, the volume of the MSN containing body increased significantly, indicating the cell had formed a vesicle (endosome) to engulf the MSN. From that time on, the MSN continued to go further inside the cell, and the volume of the MSN containing vesicle decreased. Further investigation may be needed to distinguish the MSN itself from the vesicle.

**Vertical position.** In the recorded endocytosis event, the MSN was first trapped on the membrane near the bottom of the cell. Then the MSN moved up and got further inside the cell. This moving direction was against gravity, which helped to prove that the MSN got inside the cell by endocytosis instead of gravity. The vertical positions of the MSN were measured through optical sectioning accomplished by coupling DIC microscope with a motorized stage.[12] The vertical position of the MSN was plotted against the recording time in Figure 5. The MSN traveled about 1.2 μm from the cell membrane towards the nucleus, while the thickness of the entire cell was about 6 μm.

Shape changes (Figure 4) and vertical position changes (Figure 5) can be correlated to provide more detailed information. In the first 15 min, the position and shape of the MSN did not change much, meaning the MSN was still on the cell membrane surface. The granules inside the cell were out of focus because they were not at the same plane as the MSN. From then on till 31 min, there were steep changes in vertical position, indicating that the MSN crossed the cell membrane to get inside. This change coincided with the shape change at 20, 27, and 31 min. The volume of the MSN containing vesicle first increased and then decreased later in this period. After it got inside the cell, the MSN moved randomly in the three-dimensional space between the cell membrane and the nucleus. At the end of endocytosis, most granules and other features inside the cell could be seen clearly as they now stayed close to the same focal plane as the MSN.

## Conclusion

In this paper we demonstrate that DIC microscopy can be used to study the endocytosis of single MSN into living human lung cancer (A549) cell. The movement of MSN was observed directly and continuously without staining the cell. The process of endocytosis was characterized by the motion speed, the shape, and the vertical position of MSN. By comparing the diffusion coefficients of MSN in and outside of the cell, we confirmed that cell cytoplasm was not just homogeneous viscous solution. The cytoskeletons inside cytoplasm had big effect on free diffusion of MSN inside the cell. Since our DIC microscope had a shallow depth of focus, the accurate vertical position change of MSN can be measured by DIC optical sectioning. It provides the knowledge on the three-dimensional distribution of MSN inside the cell and helps to demonstrate the endocytosis of MSN. MSN can be a good drug delivery vector and have lots of applications in controlled drug release system. MSN may be selectively targeted to specific cellular organelles through surface modification, and drugs can be protected from enzymatic digestion in the cell cytoplasm by capping the channels in MSNs. In the future, DIC microscopy will be employed to study real-time drug release events in living cells when MSNs or other nanoparticles are used as drug delivery vector.

## References

(1) Supratim Giri, B. G. T. M. P. S. V. S. Y. L. *Angewandte Chemie International Edition* **2005**, *44*, 5038-5044.

(2) Mal, N. K.; Fujiwara, M.; Tanaka, Y. *Nature* **2003**, *421*, 350.

(3) Chiyoung Park, K. O. S. L. C. K. *Angewandte Chemie International Edition* **2007**, *46*, 1455-1457.

(4) Moghimi, S. M.; Rajabi-Siahboomi, A. R. *Advanced Drug Delivery Reviews* **2000**, *41*, 129-133.

(5) A. Stein, B. J. M. R. C. S. *Advanced Materials* **2000**, *12*, 1403-1419.

(6) Lu, J.; Liong, M.; Zink, J. I.; Tamanoi, F. *Small* **2007**, *3*, 1341-1346.

(7) Torney, F.; Trewyn, B. G.; Lin, V. S. Y.; Wang, K. *Nature Nanotechnology* **2007**, *2*, 295-300.

(8) Slowing, II; Trewyn, B. G.; Lin, V. S. Y. *Journal of the American Chemical Society* **2007**, *129*, 8845-8849.

(9) Lin, Y. S.; Tsai, C. P.; Huang, H. Y.; Kuo, C. T.; Hung, Y.; Huang, D. M.; Chen, Y. C.; Mou, C. Y. *Chemistry of Materials* **2005**, *17*, 4570-4573.

(10) Radu, D. R.; Lai, C. Y.; Jeftinija, K.; Rowe, E. W.; Jeftinija, S.; Lin, V. S. Y. *Journal of the American Chemical Society* **2004**, *126*, 13216-13217.

(11) Slowing, I.; Trewyn, B. G.; Lin, V. S. Y. *Journal of the American Chemical Society* **2006**, *128*, 14792-14793.

(12) Li, H. W.; McCloskey, M.; He, Y.; Yeung, E. S. *Analytical and Bioanalytical Chemistry* **2007**, *387*, 63-69.

(13) Salmon, E. D.; Tran, P. In *Digital Microscopy, 3rd Edition*, 2007; Vol. 81, pp 335-364.

(14) Zheng, M.; Davidson, F.; Huang, X. Y. *Journal of the American Chemical Society* **2003**, *125*, 7790-7791.

(15) Kulak, A.; Hall, S. R.; Mann, S. *Chemical Communications* **2004**, 576-577.

(16) Mellman, I. *Annual Review of Cell and Developmental Biology* **1996**, *12*, 575-625.

(17) Saxton, M. J. *Biophysical Journal* **1993**, *64*, 1766-1780.

(18) Curtis, H.; Barnes, S. N. *Biology*, 5th edition ed.; W. H. Freeman, 1989.

(19) Srivastava, A.; Krishnamoorthy, G. *Archives of Biochemistry and Biophysics* **1997**, *340*, 159-167.

(20) Fushimi, K.; Verkman, A. S. *Journal of Cell Biology* **1991**, *112*, 719-725.

(21) Lubyphelps, K. *Current Opinion in Cell Biology* **1994**, *6*, 3-9.

(22) Blum, J. J.; Lawler, G.; Reed, M.; Shin, I. *Biophysical Journal* **1989**, *56*, 995-1005.

(23) Lubyphelps, K.; Taylor, D. L.; Lanni, F. *Journal of Cell Biology* **1986**, *102*, 2015-2022.

(24) Gershon, N. D.; Porter, K. R.; Trus, B. L. *Proceedings of the National Academy of Sciences of the United States of America* **1985**, *82*, 5030-5034.

(25) Radtke, K.; Dohner, K.; Sodeik, B. *Cellular Microbiology* **2006**, *8*, 387-400.

## Figure captions

Figure 2.1. TEM image of the MSNs used in our experiments. MSN was labeled with fluorescein isothiocyanate (FITC) and functionalized by tri(ethylene glycol) organic linker. The average size of MSN was around 100 nm.

Figure 2.2. Schematic experimental setup. Cells (only one cell was drawn) grew on poly-L-lysine coated coverslip (0.17 mm). A chamber was made by connecting glass slide and coverslip with double-sided tape (0.2 mm). The cell culture medium containing MSN was added to the chamber. During the process of endocytosis, the MSN moved from bottom of cell towards top of cell against the direction of gravity. Note that the components in this figure are not drawn proportionally.

Figure 2.3. Histograms of lateral displacement of the MSN in 3 different stages. The x-axis is the lateral displacement $r$ between two successive steps (time interval 0.2 s) in the trajectory of the MSN, and the y-axis is the number of points that fall in certain range of lateral displacements. Each histogram is fitted with a typical Gaussian function to estimate a mean lateral displacement. (A) Unrestricted Brownian motion in the cell growth medium. (B) Restricted Brownian motion near the cell membrane. (C) Restricted Brownian motion inside the cell. The mean lateral displacements were $7.6\times10^{-5}$, $4.5\times10^{-5}$, and $1.1\times10^{-5}$ $cm^2$ for the three panels, respectively. Note that (A) and (B) have an identical scale from 0-35 on the x-axis, but (C) has a scale from 0-3.5. The units for all the three x-axis are the same.

Figure 2.4. Endocytosis of MSN into living human lung cancer cell. These images show part of the cell, and the large spindle-shaped object is the nucleus. In these images, the MSN were always in the DIC microscope’s focal plane. In the beginning (0 min), the MSN was trapped on the cell membrane, and most of the cell features were out of focus. The shape of the MSN changed several times during this process. Most notably, a large vesicle (endosome) was seen at 27 min. After the MSN went inside the cell, many cell features were on the same horizontal plane as the MSN and could be seen very clearly (31 and 100 min).

Figure 2.5. Plot of the vertical position vs. the recording time. The difference between highest and lowest vertical distances was ~1.2 µm. At time 0, the MSN was trapped on the cell membrane and its vertical position was 0. As the endocytosis process continued, the MSN moved deeper into the cell. After roughly 31 min, the MSN moved around inside the cell and its vertical position fluctuated in a range shown in this figure. The thickness of cell was around 6 µm.

**Figures**

Figure 1.1

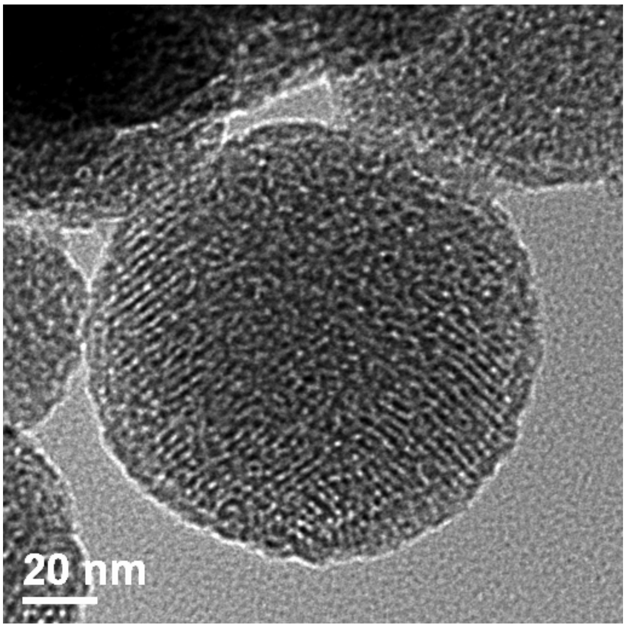

Figure 1.2

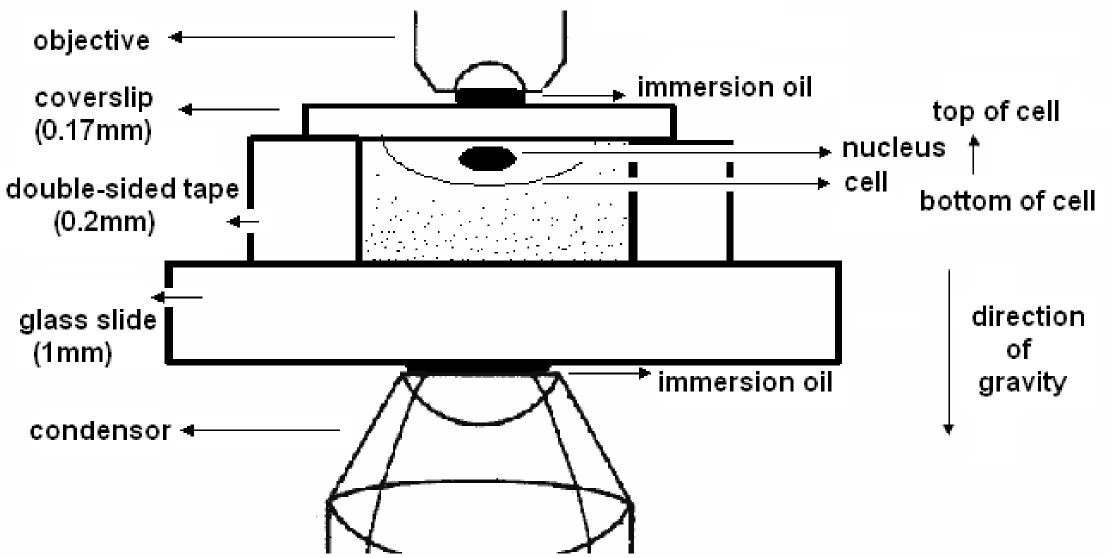
objective
coverslip
(0.17mm)
immersion oil
top of cell
nucleus
cell
bottom of cell
double-sided tape
(0.2mm)
glass slide
(1mm)
direction
of
gravity
immersion oil
condensor

Figure 1.3

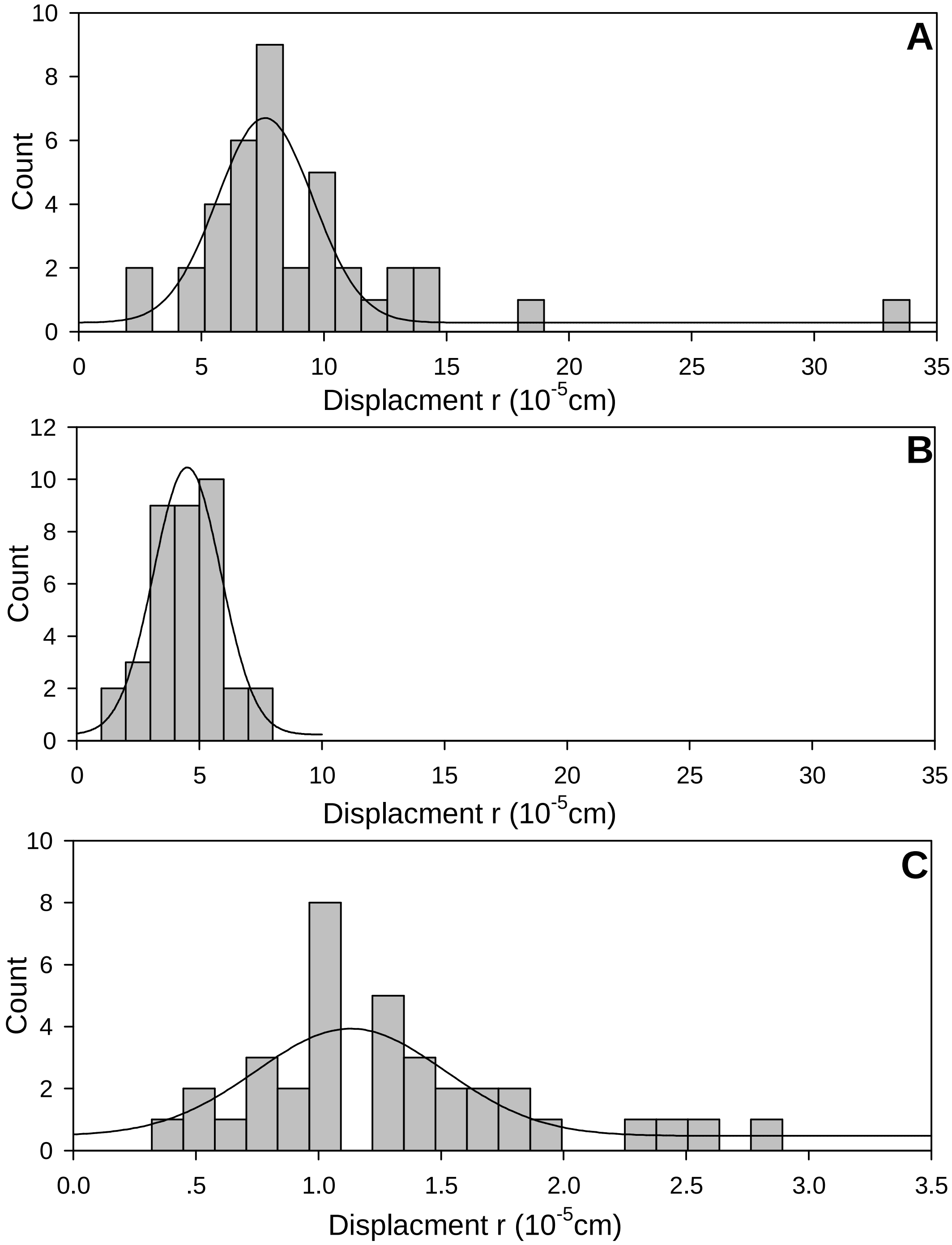
A
Count
0
2
4
6
8
10
0
5
10
15
20
25
30
35
Displacment r ($10^{-5}$cm)
B
Count
0
2
4
6
8
10
12
0
5
10
15
20
25
30
35
Displacment r ($10^{-5}$cm)
C
Count
0
2
4
6
8
10
0.0
.5
1.0
1.5
2.0
2.5
3.0
3.5
Displacment r ($10^{-5}$cm)

Figure 1.4

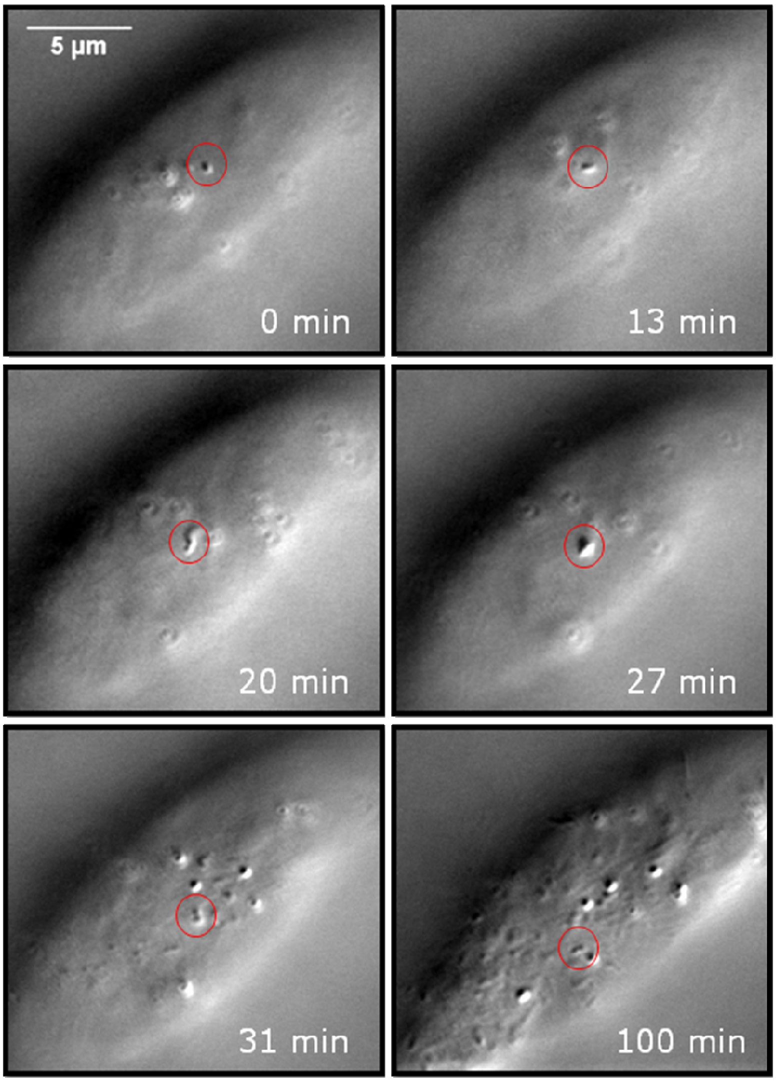

Figure 1.5

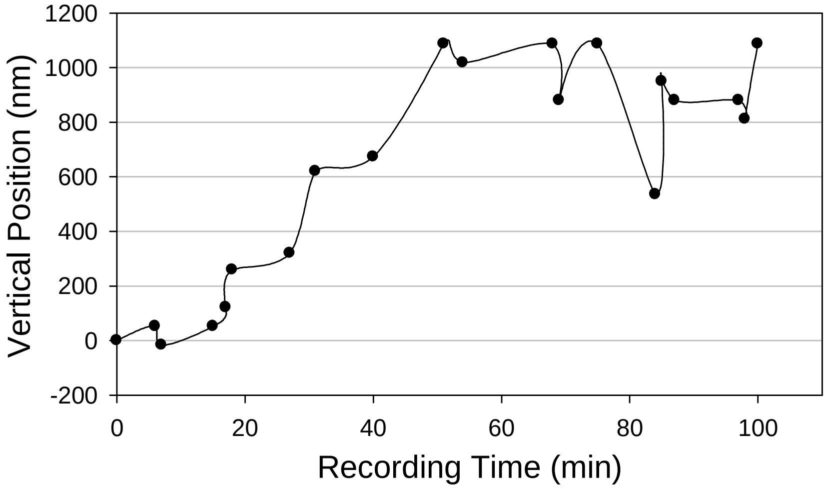
1200
1000
800
600
400
200
0
-200
Vertical Position (nm)
0
20
40
60
80
100
Recording Time (min)

# CHAPTER 3. WAVELENGTH-DEPENDENT DIFFERENTIAL INTERFERENCE CONTRAST MICROSCOPY: SELECTIVELY IMAGING NANOPARTICLE PROBES IN LIVE CELLS

Wei Sun§, Gufeng Wang§, Ning Fang, and Edward S. Yeung

§These authors contributed equally to this work.

Published in Analytical Chemistry*

## Abstract

Gold and silver nanoparticles display extraordinarily large apparent refractive indices near their plasmon resonance (PR) wavelengths. These nanoparticles show good contrast in a narrow spectral band but are poorly resolved at other wavelengths in differential interference contrast (DIC) microscopy. The wavelength dependence of DIC contrast of gold/silver nanoparticles is interpreted in terms of Mie's theory and DIC working principles. We further exploit this wavelength dependence by modifying a DIC microscope to enable simultaneous imaging at two wavelengths. We demonstrate that gold/silver nanoparticles immobilized on the same glass slides through hybridization can be differentiated and imaged separately. High-contrast, video-rate images of living cells can be recorded both with and without illuminating the gold nanoparticle probes, providing definitive probe identification. Dual-wavelength DIC microscopy thus presents a new approach to the simultaneous detection of multiple probes of interest for high-speed live-cell imaging.

---

*****Reprint with permission from Analytical Chemistry, **2009**, 81(22), 9203-9208.

## Introduction

Nanoparticle probes are becoming a powerful tool to study the dynamics in living cells. They can be located with both high spatial resolution and high temporal resolution at the individual particle level, providing valuable information in live-cell imaging. Among all nanoparticles, gold nanoparticles (AuNPs) are attractive probes for labeling applications as they display good chemical and photostability, tunable optical properties, and controllable surface chemistry for modification with a variety of chemically and biologically active molecules.[1] Due to their plasmon resonance (PR) properties, AuNPs and silver nanoparticles (AgNPs) as small as several nanometers in diameter can be detected by a variety of optical microscopy techniques, including bright-field and dark-field,[2-5] photothermal interference contrast,[6-8] and differential interference contrast (DIC) microscopies.[9]

There are still major challenges in using nanoparticle probes in live-cell imaging. Dark-field microscopies have gained much attention due to their high signal strength and temporal resolution; however, it can be difficult to identify tracer nanoparticles from cell components and other debris that scatters light in the sample medium. A recently developed technique – photothermal interference contrast – provides excellent selectivity of gold nanoparticles as small as 5 nm from cell features; however, so far the data rate is not high enough for observing dynamic processes in biological samples, and applications are limited by the undesirable temperature increase in the sample.

DIC microscopy offers excellent contrast and spatial resolution for gold nanoparticles. In addition, high quality cell images can be recorded simultaneously with the probes, eliminating the need of switching microscopy modes to correlate the cell and the probes. For these reasons, DIC has been used in high temporal resolution, high-lateral precision single particle tracking in live-cell imaging.[9-14] However, the same issue exists for DIC microscopy to distinguish nanoparticle probes from subcellular features, especially small spherical vesicles.

In this present work, we show that the image contrast of gold and silver nanoparticles varies drastically in DIC microscopy as a function of illumination wavelength and particle size. Small gold and silver nanoparticles display large apparent refractive indices, resulting in high contrast images in DIC microscopy. Moreover, they only become visible in a narrow spectral band slightly longer than their PR wavelengths, leading to the possibility of selectively illuminating different types of nanoparticles. The large apparent refractive index of gold nanoparticles near their PR wavelength is interpreted in terms of Mie's theory.[15] We further exploited the wavelength dependence of DIC contrast of gold/silver nanoparticles by modifying a DIC microscope so that it can be operated at two illumination wavelengths simultaneously. We demonstrate high-contrast, video-rate imaging of living cells both with and without illuminating the gold nanoparticle probes, providing definitive probe identification. Live-cell uptake of single 40-nm gold nanoparticles functionalized with a cell-penetrating peptide (CPP) was recorded at video rate (32 frames per second).

## Experimental

**Materials and chemicals.** Silver and citrate-capped gold colloidal solutions were purchased from BBInternational (Cardiff, UK). Gold nanoparticles that were used to conjugate with TAT peptide were purchased from Nanopartz (Salt Lake City, UT) and the capping material is proprietary. The absorption maxima of these particles were measured by a UV-VIS spectrophotometer. The size distributions were measured by transmission electron microscopy, and they agreed well with the manufacturer's data. Trans-activating transcriptional activator (TAT) 47-57 (sequence: YGRKKRRQRRR, catalog number: 60023-1) was purchased from AnaSpec (San Jose, CA).

**DIC microscope.** An upright Nikon Eclipse 80i microscope was used in this study. The DIC mode used a pair of Nomarski prisms, 2 polarizers, a 100×, 1.40 numerical aperture (NA) Plan Apo oil immersion objective, and a 1.40 NA oil immersion condenser. A Photometrics CoolSnap ES CCD camera (1392×1040 imaging array, 6.45×6.45-μm pixel size) was used to record highly detailed cell/particle images, and an Andor iXon$^{EM}$+ 897 camera (512×512 imaging array, 16×16-μm pixel size) was used to capture fast dynamics in live cells. A set of 25 filters from Thorlabs (Newton, NJ) have central wavelengths in the range of 400-780 nm and a full width at half maximum (FWHM) of 10 nm. In addition, a 387-nm bandpass filter was purchased from Semrock (Rochester, NY). When the DIC microscope was operated at one wavelength, a proper bandpass filter was inserted in the microscope’s light path. When the DIC microscope was operated at two wavelengths simultaneously, a MAG Biosystems dual-view filter (Tucson, AZ) with a 565-nm dichroic filter and two sets of filters was installed.

**Particle/cell imaging.** A computer-controlled rotary motor from Sigma Koki (model no. SGSP-60YAM) was coupled to the actuator of the microscope stage. The CCD camera and the stage were synchronized by a home-written C++ computer program. MATLAB and NIH ImageJ were used to analyze and process the collected images and videos. For imaging immobilized particles, the exposure time was adjusted to maintain the same background intensity at different wavelengths. For imaging cells incubated with gold nanoparticles, the temporal resolution was 5 Hz with the Photometrics CCD camera or 30 Hz with the Andor EMCCD camera.

**Sample preparation for investigations of plasmon resonance.** Negatively-charged nanoparticles were immobilized on positively-charged amino silane-coated glass slides (Corning, NY). The colloid solutions were first diluted with 18.2-MΩ pure water to proper concentrations. Then the diluted solution was sonicated for 15 min at room temperature. After sonication, 6 μL of the solution were added onto an amino silane-coated slide and covered with a 22 mm × 22 mm No.1.5 coverslip (Corning, NY).

**Functionalization of gold nanoparticles with TAT.** 40-nm gold nanoparticles (Nanopartz, $8.7 \times 10^{10}$ particles/mL) were modified with TAT through a linker molecule,[16] 4,7,10,13,16,19,22,25,32,35,38,41,44,47,50,53-Hexadecaoxa-28,29-dithiahexapentacontanedioic acid di-N-succinimidyl ester (NHS-PEG disulfide), which has both a disulfide and succinimidyl functionalities for the respective chemisorption onto gold and the facile covalent coupling of TAT. Briefly, 40 □L of 50 mM borate buffer and 0.2 mmol NHS-PEG disulfide was added to 1.0 mL of AuNP solution and mixed for 3 hours. The solution was then cleaned up by centrifugation and resuspension in 2 mM borate buffer. 2 μg TAT peptide was added to the gold colloid solution and react for 8 hours. The gold nanoparticles were then blocked by adding 100 mL of 2 mM borate buffer with 10% BSA for over 8 hours. Before use, the colloidal gold probes were cleaned up by centrifugation and resuspension in 500 μL of the same 2 mM borate buffer. The concentrated gold colloidal solution was diluted in the cell culture medium to a final concentration of $\sim 1.8\times10^{10}$ particles/mL when incubated with HeLa cells. The final concentration of the nanoparticles was estimated from the number of dilutions and it was assumed that no particle was lost during all the modification procedures.

**Cell culture and incubation with gold nanoparticles.** HeLa cells were purchased from American Type Culture Collection (ATCC, Baltimore, USA, CCL-2). The cells were plated in a T25 cell culture flask (Corning) and grown in cell culture medium supplemented with 10% fetal bovine serum (FBS). 150 μL of such cell suspension solution was transferred to a 22 mm × 22 mm No. 1.5 poly-L-lysine-coated coverslip, housed in a 50-mm Petri dish (Corning). The Petri dish was left in a cell culture incubator (37 °C, 5% $CO_2$) for 1 hour to let the cells attach to the coverslip. After 1.5 mL of the cell culture medium with 10% FBS supplement was added to immerse the coverslip, the Petri dish was left again in the oven for 24 hours. The purchased gold nanoparticle colloid solution was diluted in the cell culture medium to a concentration of $1.8 \times 10^{10}$ particles/mL, followed by 1-min sonication at room temperature. 1.5 mL of the diluted AuNP solution was then added to the Petri dish to replace the old cell culture medium. Incubation took place in the oven for 2-6 hours.

**Cell slide preparation.** Two pieces of double-sided tape were stuck parallel on top of a pre-cleaned glass slide. For live cell imaging, an incubated coverslip was placed carefully on top of the tapes, with the poly-L-lysine-coated side facing the glass slide. 20 μL of the cell culture medium with 10% FBS supplement was then added to the chamber formed between the glass slide and the coverslip. Finally, the two open edges of the chamber were sealed by nail polish to prevent evaporation. When cells were fixed before imaging, a coverslip with cells was put in a phosphate buffered saline (PBS) containing 3.7% formaldehyde and 0.2% glutaraldehyde at room temperature for 10 mins. Then the coverslip was washed with PBS several times, and taped to the glass slide.

## Results and Discussion

**Plasmonic nanoparticles in DIC microscopy.** We are able to detect gold and silver nanoparticles as small as 5-10 nm, one order of magnitude smaller than non-plasmonic nanoparticles. More interestingly, small gold and silver nanoparticles (≤ 40 nm) are only detectable with sufficient contrast within a narrow band of wavelengths. To illustrate this, sample images of 30-nm AuNPs and AgNPs at select illumination wavelengths are shown in Figures 1a and 1b, respectively. The gold nanoparticles give the best contrast at ~540 nm. At wavelengths below 420 nm or above 640 nm, they become undetectable. The contrast here is defined as the difference between the maximum and the minimum intensities divided by the average local background intensity. The contrast spectrum of 30 nm AuNP shows a peak very close to its PR wavelength, but slightly red-shifted (Figure 1c). Similarly, 30-nm AgNPs show the best DIC contrast at 420 nm, which is also slightly red-shifted as compared to its PR wavelength (Figure 1d).

The DIC contrast of the nanoparticles also shows strong particle size-dependency. The measured contrast spectra of 20, 30, 40, 50, and 80-nm AuNPs are displayed in Figure 2a. All of the spectra show red-shifted peak contrast compared to their maximum absorptions. Their contrast increases with an accelerating trend as their size increases (Figure 2b). Especially of interest is that for AuNPs smaller than 40 nm, they are detectable only in a small wavelength range, providing an opportunity of illuminating other components of the samples while keep these AuNP probes invisible.

The correlation between the DIC contrast maximum and the PR wavelength strongly indicates that the high contrast is related to their PR properties. The bright/dark pattern of DIC images and the red-shifted contrast peak suggest that DIC signals of gold nanoparticles are not simple absorption or scattering. In contrast, DIC microscopy works on the principle of interference by using two mutually shifted illumination beams to gain differential information about the refractive index of the sample. A refractive index difference between the sample and its surrounding medium causes a phase difference $\Delta\phi$ for the passing beams, which are recombined into a single beam to generate an interference pattern. For nanoparticles with a size smaller than the shear distance, the contrast is proportional to $\Delta\phi$ under coherent illumination:

$$\Delta\phi = \Delta n \cdot 2\pi d/\lambda. \qquad (1)$$

where $d$ is the optical path, $\lambda$ is the wavelength of the incident beam, and $\Delta n$ is the refractive index difference between the sample and the surrounding medium.

Gold nanoparticles in dielectric medium display extraordinarily large apparent refractive indices near their PR wavelengths. For example, 40 nm AuNP in aqueous solution shows a contrast of 0.183 at 550 nm illumination, close to that of 97 nm polystyrene particles (0.163) whose refractive index is 1.59 at the same wavelength. From Equation 1, we can estimate the apparent refractive index of 40 nm AuNP to be 2.04, higher than most of the conventional materials.

The large apparent refractive index of gold nanoparticles in dielectric medium near PR wavelengths can be interpreted with Mie's theory and DIC microscopy working principles. In Nomarski-type DIC,[17] the two illumination beams are spatially coherent. Assume the two beams are equally split and one of the beams illuminates a gold nanoparticle whose radius *a* is small compared to the wavelength λ. The scattering field $E_{Sc}$ in the forward direction at a distance *R* is:[15]

$$E_{Sc} = E_0 k^2 a^3 \frac{e^{ikR}}{R} r e^{-i\Delta\phi} \quad , \qquad (2)$$

where $E_0$ is the amplitude of the illumination beam, *k* is the wavenumber (2π/ $\lambda$ ), $e^{-i\Delta\phi}$ is determined by the complex dielectric function of gold and the surrounding medium:

$$r e^{-i\Delta\phi} = \frac{(\varepsilon_1 + i\varepsilon_2)^2 - \varepsilon_{\mathrm{m}}}{(\varepsilon_1 + i\varepsilon_2)^2 + 2\varepsilon_{\mathrm{m}}} \quad , \qquad (3)$$

where $\varepsilon_1$ and $\varepsilon_2$ are the real and imaginary parts of the dielectric function of gold nanoparticle and can be derived from those of bulk material;[18] $\varepsilon_{\mathrm{m}}$ is the dielectric function of the surrounding medium which is normally a constant real number. The time-dependent factor $e^{i\omega t}$ as a function of the radial frequency $\omega$ is omitted.

In the image plane, the intensity distribution of a DIC image is the square modulus of the convolution of the DIC point spread function (PSF) and the object amplitude and phase distribution, where DIC PSF is defined as:[19]

$$h(x, y) = \frac{\sqrt{2}}{2} e^{-i\theta} k(x - \Delta x, y) - \frac{\sqrt{2}}{2} e^{i\theta} k(x + \Delta x, y) \, , \qquad (4)$$

where (*x*, *y*) is a point in the image plane, *k*(*x*,*y*) is the amplitude PSF for transmission optics under coherent illumination, $2\,\theta$ is an additional phase bias, and the shear distance $2\,\Delta\,x$ is assumed to be along the *x* direction without losing generality. To simplify, we assume an ideal

PSF (Dirac delta function) for the transmission optics in the microscope. The interference pattern can be viewed as generated from the direct overlay of the sample beam ($E_{\text{Sc}}$+$E_0$) and the reference beam ($E_0$), each with a different artificial phase bias. The electric filed at the interference point is:

$$E_{\text{interfere}} = \frac{\sqrt{2}}{2}[(E_0 + E_{\text{Sc}})e^{-i\theta} - E_0 e^{i\theta}], \qquad (5)$$

while at the background:

$$E_b = \frac{\sqrt{2}}{2}E_0(e^{-i\theta} - e^{i\theta}). \qquad (6)$$

When the phase bias $2\theta$ is properly set, the intensity at interference point is:

$$I_{\text{interfere}} = 2E_0^2 + \frac{1}{2}E_0^2[4k^2a^3r\cos(\Delta\phi) + k^4a^6r^2], \qquad (7)$$

and the background intensity $I_b$ is $2E_0^2$. The DIC contrast is proportional to ($I_{\text{interfere}}$-$I_b$)/$I_b$, thus:

$$contrast \propto 4k^2a^3r\cos(\Delta\phi) + k^4a^6r^2. \qquad (8)$$

When the particle radius *a* is small, the second term in Equation 8 becomes negligible compared to the first term.

Equation 8 shows that DIC contrast is related to not only the particle size but also the phase delay introduced by the complex refractive index of the gold nanoparticles. Figure 2c shows a simulated DIC spectrum of 40 nm gold nanoparticle in water where the complex refractive index of bulk gold is adapted from Johnson.[20] The spectrum shows a red-shifted maximum apparent refractive index (~550 nm) of gold nanoparticles compared to it PR wavelength, consistent with the experimental observation.

**Selective imaging of nanoparticles in live cells.** Based on the findings that gold nanoparticles can be selectively imaged in DIC microscopy, we modified a Nikon DIC microscope so that it can be operated at two wavelengths simultaneously. The sample is illuminated with a white light source. The recombined beams after the second Nomarski prism is split into two channels by a beam splitter, each passing through a bandpass filter that selects the observation wavelength, and refocused to form two images on different portions of the same CCD camera chip. The two images are recorded simultaneously to minimize the external influence on the image quality.

To demonstrate the capability of the modified DIC microscope, 40-nm citrate-capped AuNPs were naturally endocytosed by HeLa cells after 2-hour incubation. One channel of the modified DIC microscope collects light at 540 nm to visualize both cell components and gold nanoparticles, while the other channel collects light at 720 nm to visualize cell components but not the gold nanoparticles. The use of two different wavelengths causes some vertical offset between the two channels. This vertical offset is corrected by the objective lens so that it does not affect the accuracy of particle identification. Optical sections[10, 14] of the HeLa cell along the *z*-direction were recorded by stepping a high-precision rotary motor coupled to the actuator of the microscope stage. The steps in the *z*-direction were recorded during imaging to give the absolute position of an image in the *z*-direction. An example of the *z*-sections of a HeLa cell was displayed in figure 3. Numerous particular and tubular shapes can be seen in both channels. Using the cell-only (720 nm) image as the control, we can confidently identify in the cell-plus-AuNP (540 nm) image which features are AuNP probes and which are subcellular organelles.

**Video-rate imaging of nanoparticle endocytosis.** Combined with the single-particle tracking algorithm,[11] this imaging method provides unprecedented convenience and accuracy for real-time single-particle tracking in live cells for long periods of time. We recorded at 32 frames per second (fps) live cell uptake of single 40-nm gold nanoparticles functionalized with a cell penetrating peptide (CPP): trans-activating transcriptional activator (TAT) 47-57 (sequence: YGRKKRRQRRR) from Human Immunodeficiency Virus 1 (HIV-1). CPPs can be efficiently taken up from the surrounding media by numerous cell types in culture, and therefore hold great potential as *in vitro* and *in vivo* delivery vectors.[21] A HeLa cell slide was prepared as described in the Experimental Section and placed on the microscope stage, and the TAT-functionalized gold nanoparticle solution was added. No particle aggregation was detected during the experiment. The uptake process was recorded from the beginning. Extensive information, such as particle diffusion in different media and 3D particle trajectory with nanometer precision, can be extracted from the videos. The recorded single-particle dynamics reveals that the functionalized gold nanoparticles spent several to tens of minutes in searching for the preferred spot on the membrane, and then the actual entry took place within 1 to 2 minutes.

## Conclusions

In summary, we have developed dual-wavelength DIC microscopy for plasmonic nanoparticles based on their wavelength-dependent image contrast. This dual-wavelength DIC microscopy has many potential applications. For example, Figure 5 in the Supporting Information demonstrates that 30-nm gold and 30-nm silver nanoparticles immobilized on the same glass slide through DNA hybridization can be selectively imaged at suitable wavelengths. Such a technique will open a new avenue for multiplexed detection scheme using colloidal nanoparticles. As another example, the usefulness of this approach can be further extended in live-cell imaging by functionalizing different types of particles, e.g., AuNP and AgNP, with different CPPs, mitochondria penetrating peptides (MPP),[22] viruses, or hormones. Compared to fluorescent tags, colloidal metal particles display excellent photo-stability that they can be observed over an arbitrarily long period of time. When the colloidal particles are used in combination with DIC microscopy, we are able to observe both the probe and the cell features at video rates with high signal-to-noise ratio. Thus, different particles can be identified unambiguously, and their dynamics can be studied simultaneously in one cell culture. Moreover, 3D scans of fixed cells at the appropriate wavelengths can provide accurate information on the distributions and the numbers of different nanoparticles.

## References

(1) Sperling, R. A.; Gil, P. R.; Zhang, F.; Zanella, M.; Parak, W. J. *Chemical Society Reviews* **2008**, *37*, 1896-1908.

(2) Hu, M.; Novo, C.; Funston, A.; Wang, H. N.; Staleva, H.; Zou, S. L.; Mulvaney, P.; Xia, Y. N.; Hartland, G. V. *Journal of Materials Chemistry* **2008**, *18*, 1949-1960.

(3) Sherry, L. J.; Chang, S. H.; Schatz, G. C.; Van Duyne, R. P.; Wiley, B. J.; Xia, Y. N. *Nano Letters* **2005**, *5*, 2034-2038.

(4) Rong, G. X.; Wang, H. Y.; Skewis, L. R.; Reinhard, B. M. *Nano Letters* **2008**, *8*, 3386-3393.

(5) Lee, K. J.; Nallathamby, P. D.; Browning, L. M.; Osgood, C. J.; Xu, X.-H. N. *Acs Nano* **2007**, *1*, 133-143.

(6) Boyer, D.; Tamarat, P.; Maali, A.; Lounis, B.; Orrit, M. *Science* **2002**, *297*, 1160-1163.

(7) Cognet, L.; Tardin, C.; Boyer, D.; Choquet, D.; Tamarat, P.; Lounis, B. *Proceedings of the National Academy of Sciences of the United States of America* **2003**, *100*, 11350-11355.

(8) Lasne, D.; Blab, G. A.; Berciaud, S.; Heine, M.; Groc, L.; Choquet, D.; Cognet, L.; Lounis, B. *Biophysical Journal* **2006**, *91*, 4598-4604.

(9) Tkachenko, A. G.; Xie, H.; Liu, Y. L.; Coleman, D.; Ryan, J.; Glomm, W. R.; Shipton, M. K.; Franzen, S.; Feldheim, D. L. *Bioconjugate Chemistry* **2004**, *15*, 482-490.

(10) Tsunoda, M.; Isailovic, D.; Yeung, E. S. *Journal of Microscopy-Oxford* **2008**, 207-211.

(11) Gelles, J.; Schnapp, B. J.; Sheetz, M. P. *Nature* **1988**, *331*, 450-453.

(12) Dohoney, K. M.; Gelles, J. *Nature* **2001**, *409*, 370-374.

(13) Pouget, N.; Dennis, C.; Turlan, C.; Grigoriev, M.; Chandler, M.; Salome, L. *Nucleic Acids Research* **2004**, *32*.

(14) Sun, W.; Fang, N.; Trewyn, B. G.; Tsunoda, M.; Slowing, II; Lin, V. S. Y.; Yeung, E. S. *Analytical and Bioanalytical Chemistry* **2008**, *391*, 2119-2125.

(15) Born, M.; Wolf, E. *Principles of Optics: Electromagnetic Theory of Propagation, Interference and Diffraction of Light (7th Edition)*; Cambridge University Press: New York, 1999.

(16) Narayanan, R.; Lipert, R. J.; Porter, M. D. *Analytical Chemistry* **2008**, *80*, 2265-2271.

(17) Mehta, S. B.; Sheppard, C. J. R. *Optics Express* **2008**, *16*, 19462-19479.

(18) Kreibig, U.; Vollmer, M. *Optical Properties of Metal Clusters*, *Springer Series in Materials Science , Vol. 25*; Springer: New York, 1995.

(19) Preza, C.; Snyder, D. L.; Conchello, J. A. *Journal of the Optical Society of America a-Optics Image Science and Vision* **1999**, *16*, 2185-2199.

(20) Johnson, P. B.; Christy, R. W. *Phys. Rev. B* **1972**, *6*, 4370-4379.

(21) Stewart, K. M.; Horton, K. L.; Kelley, S. O. *Organic & Biomolecular Chemistry* **2008**, *6*, 2242-2255.

(22) Horton, K. L.; Stewart, K. M.; Fonseca, S. B.; Guo, Q.; Kelley, S. O. *Chemistry & Biology* **2008**, *15*, 375-382.

## Figure Captions

Figure 3.1. (a) Sample images of 30 nm AuNPs at four different wavelengths. (b) DIC contrast of four 30 nm AuNPs (color dots) as a function of illumination wavelength. (c) Sample images of 30 nm AgNPs. (d) DIC contrast of four 30-nm AgNPs. The nanoparticles are physically adsorbed on a glass slide and immersed in water. The average background contrast (red line) is 0.052, calculated as 3 times the standard deviation. The variations on DIC contrast are mainly caused by size and shape differences among individual particles.

Figure 3.2. DIC contrast spectra of 20, 30, 40, 50, and 80 nm gold nanoparticles. (a) Spectra from experimental measurements. (b) DIC intensity of gold nanoparticles as a function of size at 550 nm. Gold nanoparticles were physically adsorbed on a glass slide and immersed in deionized water. Each data point is the average contrast measured from 20 particles. The error bar above each point shows one standard deviation. (c) Simulated DIC spectrum of 40-nm gold nanoparticles in water (solid blue) and experimental absorption spectrum of 40 nm gold nanoparticle solution in DI water (dashed red).

Figure 3.3. Turning on and off the contrast of 40 nm AuNPs inside a HeLa cell. Three AuNPs are highlighted in the white circles. Higher-magnification views of these circled regions are displayed above in the same order from left to right as they are positioned in the original image.

Figure 3.4. A TAT-coated 40 nm gold nanoparticle located outside or inside a living HeLa cell. The cell was hung on a cover slip, and the particles in the cell culture medium diffused up towards the cell membrane against gravity. The gold particle was first seen on the cell membrane at time 0, and its presence was confirmed by imaging at both 540 and 720 nm. This particle wandered around for about 10 minutes to find the preferred spot. It finally stopped at 10 min, and the endocytosis started. The particle’s vertical position at this moment was defined as 0. Within one minute, its vertical position changed noticeably, indicating the entry of the particle into the cell. The particle then diffused inside the cell, and its vertical position changed constantly. These changes were evident as indicated by the images of the nucleus in different

focal planes. The *z* positions were estimated from the movements of the vertical stage necessary to keep the particle in focus.

Figure 3.5**.** Selectively switching on and off the images of 30-nm gold and silver nanoparticles on the same glass slide. (A) The amino-silane coated glass slide first reacted with glutaldehyde, and then covalently bonded with a mixture of two types of single-strand amino functionalized DNA *a'* and *b'*. The single-strand thiol functionalized DNA *a* and *b* were conjugated to the 30-nm Au and Ag nanoparticles, respectively. The nanoparticles were then immobilized to the surface through hybridization. (B) At 540 nm, the 30-nm AuNPs appear with good contrast, while the 30-nm AgNPs are completely invisible. The red circle points out a physically adsorbed 140-nm polystyrene particle that serves as the landmark. (C) At 420 nm, the 30-nm AgNP images are turned on, while the 30-nm AuNPs become either undetectable or barely visible with low contrast. By applying a contrast threshold, AuNP residues can be distinguished from AgNP.

Table 3.1 Sequences of thio and amino functionalized DNAs

| **DNA** | **Sequence** | **Source** |
|---|---|---|
| ***a*** | 5'-ATC CTT ATC AAT ATT-3'-$(CH_2)_6$-SH | Trilink (San Diego, CA) |
| ***b*** | 5'-TAA CAA TAA TCC CTC-3'-$(CH_2)_6$-SH | Trilink (San Diego, CA) |
| ***a'*** | 5'-AAT ATT GAT AAG GAT-3'-$(CH_2)_6$-$NH_2$ | Invitrogen (Carlsbad, CA) |
| ***b'*** | 5'-GAG GGA TTA TTG TTA-3'-$(CH_2)_6$-$NH_2$ | Invitrogen (Carlsbad, CA) |

# Figures

Figure 3.1

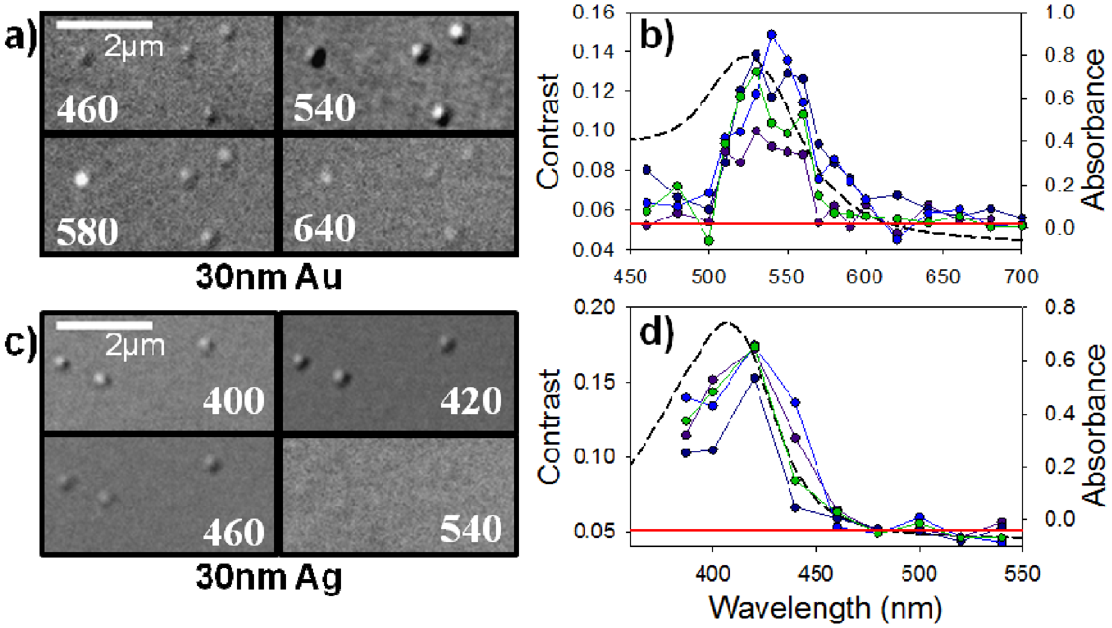

Figure 3.2

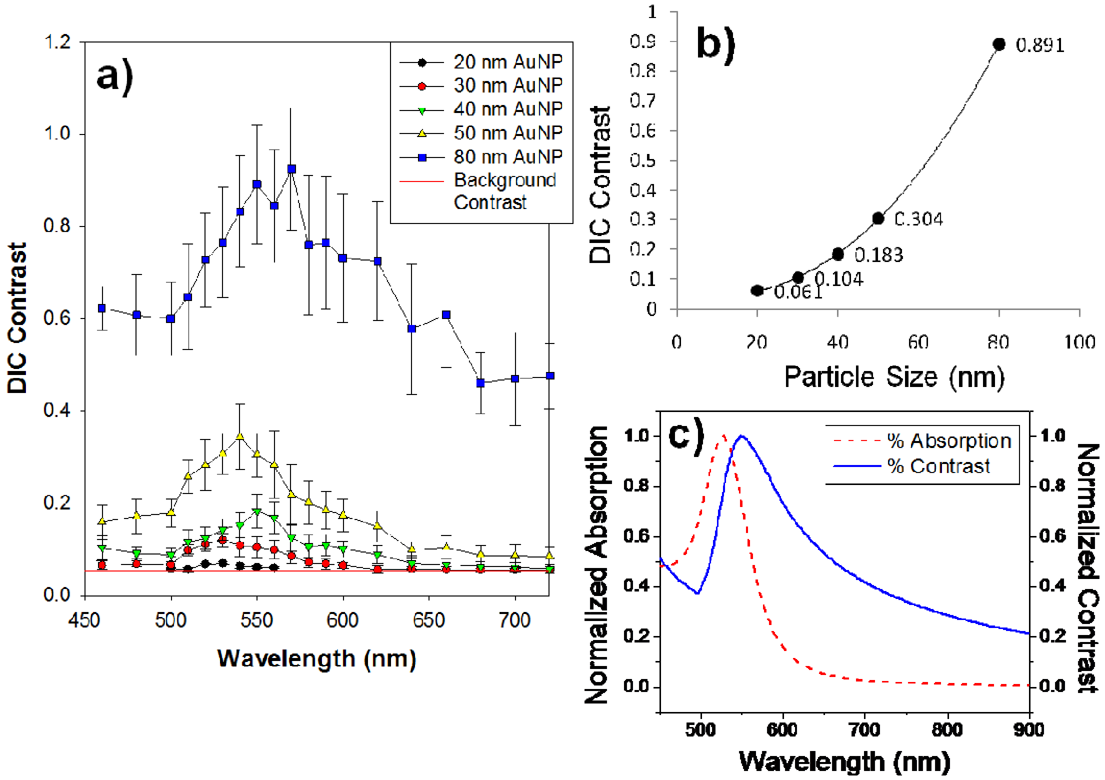
a)
DIC Contrast
Wavelength (nm)
1.2
1.0
0.8
0.6
0.4
0.2
0.0
450
500
550
600
650
700
20 nm AuNP
30 nm AuNP
40 nm AuNP
50 nm AuNP
80 nm AuNP
Background Contrast
b)
DIC Contrast
Particle Size (nm)
0.891
0.304
0.183
0.104
0.061
1
0.9
0.8
0.7
0.6
0.5
0.4
0.3
0.2
0.1
0
0
20
40
60
80
100
c)
Normalized Absorption
Normalized Contrast
Wavelength (nm)
% Absorption
% Contrast
1.0
0.8
0.6
0.4
0.2
0.0
500
600
700
800
900

Figure 3.3

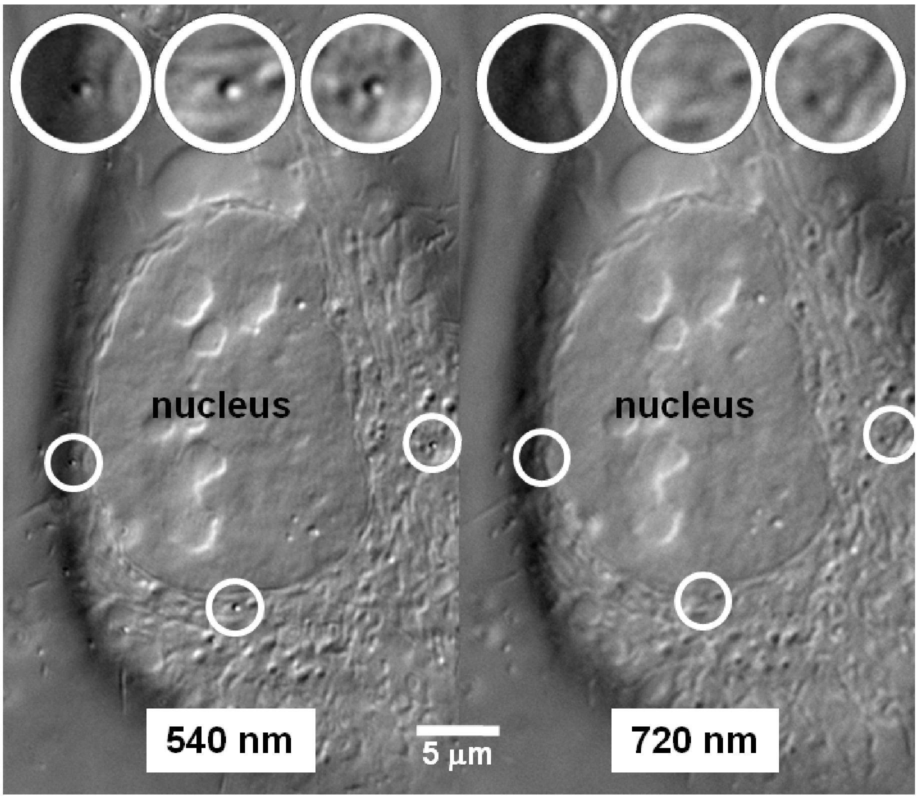

Figure 3.4

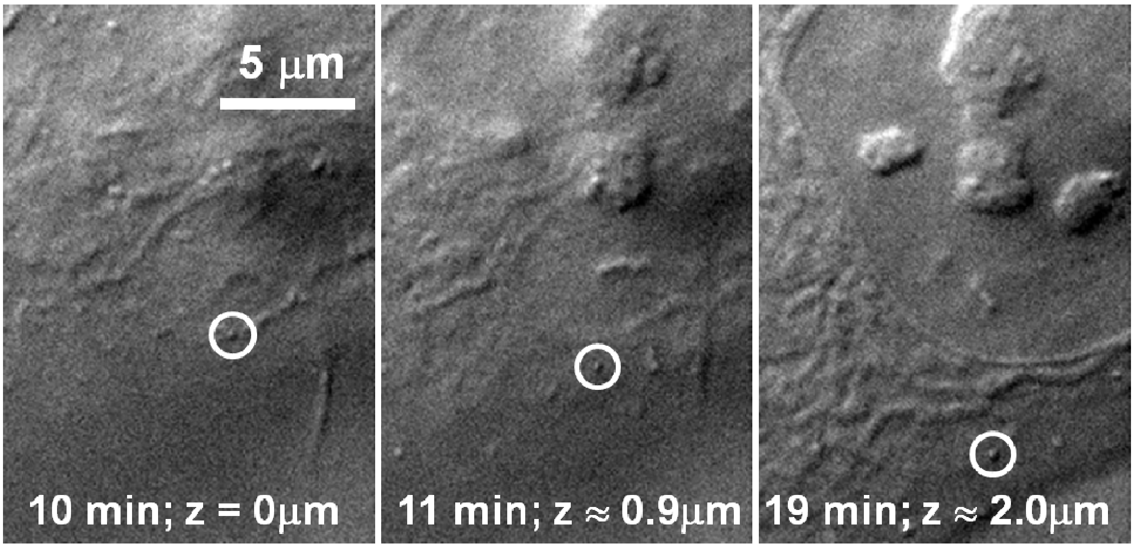

Figure 3.5

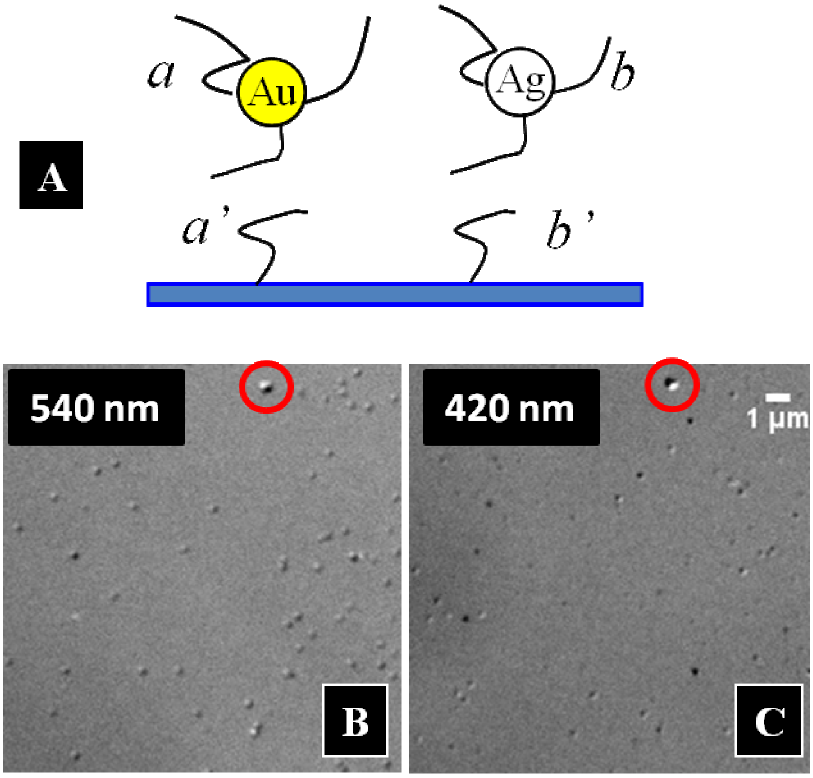

# CHAPTER 4. RESOLVING ROTATIONAL MOTIONS OF NANO-OBJECTS IN ENGINEERED ENVIRONMENTS AND LIVE CELLS WITH GOLD NANORODS AND DIC MICROSCOPY

Gufeng Wang[§], Wei Sun[§], Yong Luo, and Ning Fang

§These authors contributed equally to this work.

Published in Journal of American Chemical Society[*]

## Abstract

Gold nanorods are excellent orientation probes due to their anisotropic optical properties. Their dynamic rotational motion in the 3D space can be disclosed with Nomarski-type Differential Interference Contrast (DIC) Microscopy. We demonstrate that by using the combination of gold nanorod probes and DIC microscopy, we are able to resolve rotational motions of nano-cargos transported by motor proteins at video rate not only on engineered surfaces but also on cytoskeleton tracks in live cells.

---

[*] Reprint with permission from Journal of American Chemical Society, **2010**, 132(46), 16417-16442.Copyright © American Chemical Society

## Introduction

Numerous biological nanomachines perform various functions that keep a creature to live and prosper. How these nanomachines work, especially in cellular environments, are poorly understood to date. Since the malfunction of any of these nanomachines will lead to severe disease(s), there is an imperative need for new techniques to investigate the composition, dynamics, and working mechanism of the nanomachines from the health and medicine sectors. In addition, these nanomachines show high power and energy-efficiency. Therefore, there are always aspirations to let those bio-nanomachines step out of living organisms to find their nano-engineering applications.[1-3] This also requires a thorough understanding of these nanomachines.

Most of these nanomachines undergo motions that are essential to their functions. Understanding the characteristic translational and rotational motions is crucial to elucidate their working mechanisms. Translational motions can be revealed by a variety of single molecule/particle tracking methods.[4-10] However, rotational motions in live cells are still largely unknown due to technical limitations. The current understanding of rotational motions at the single-molecule or single-nanoparticle level was acquired mostly from *in vitro* studies. The *in vitro* methods are based either on single-molecule fluorescence polarization[11-15] or on tracking translational movement of single nanoparticle probes.[16-21] The fluorescence polarization-based methods are challenging for *in vivo* studies due to high autofluorescence background and high bleaching propensity of single fluorophores in the cellular environment. The particle tracking-based methods require specific geometries, e.g., fixed rotation center or axis, thus are also not suitable for live-cell imaging.

Gold nanorods[22] show geometrically confined plasmon resonance modes: the longitudinal mode (along the long axis) and the transverse mode (along the short axis).[23] This results in anisotropic absorption and scattering properties of gold nanorods thus allows their orientation to be determined in high precision in 2D.[24-26] Here, we show that by using Nomarski-type DIC microscopy,[27] which utilizes *two orthogonally polarized* illumination beams, the nanorod orientation can be resolved in both 2D and 3D in engineered environments and live cells.

## Experimental

**DIC/fluorescence microscope.** An upright Nikon Eclipse 80i microscope equipped with a heating stage was used in this study. This microscope can be switched between DIC mode and fluorescence mode. When the microscope was operated in DIC mode, a set of 2 Nomarski prisms, 2 polarizers and a quarter-wave plate were installed. The samples were illuminated through an oil immersion condenser (numerical aperture 1.40) and the optical signals were collected with a 100× Plan Apo/1.40 oil immersion objective. In collecting DIC intensity spectra, a set of 25 filters with central wavelengths in the range of 400-780 nm and a full width at half maximum (FWHM) of 10 nm were used. The optical filters were obtained from Thorlabs (Newton, NJ) or Semrock (Rochester, NY). The DIC images at a selected wavelength were collected by inserting the corresponding bandpass filter into the light path in the microscope. An Andor iXon$^{EM}$+ camera or a Photometrics Evolve camera (512×512 imaging array, 16×16-µm pixel size) was used to record the dynamic *in vivo* and *in vitro* transport at 32 frames per second. A Photometrics CoolSnap ES CCD camera (1392×1040 imaging array, 6.45×6.45-µm pixel size) was used to image immobilized gold nanorods in detail. When the Nikon microscope was operated in epi-fluorescence mode, samples were excited with a mercury lamp with proper bandpath filters applied in the excitation and emission channels. A rotary motor from Sigma Koki (model no. SGSP-60YAM) was coupled to the microscope stage to control the *z*-position of the sample. The CCD camera and the stage were synchronized by a home-made C++ computer program. MATLAB and NIH ImageJ were used to analyze the collected images and videos.

**Preparation of surface-modified gold nanorods for cell experiments.** Neutravidin-modified gold nanorods (10×35 nm) were purchased directly from Nanopartz (Salt Lake City, UT). TAT-coated gold nanorods were modified from cetyl trimethylammonium bromide (CTAB)-capped (25×73 nm, $1.3\times10^{11}$ particles/mL, Nanopartz) gold nanorods. The size distribution and geometric profile were evaluated with transmission electron microscopy and agreed well with the manufacturer's data. The absorption spectrum of the particles in bulk solution (Fig. 1b) was measured with a Cary 300 UV-VIS spectrophotometer (Varian, Palo Alto, CA). To functionalize the surface of CTAB-coated gold nanorods with TAT 47-57 peptide (sequence: YGRKKRRQRRR; AnaSpec, San Jose, CA), a NHS-PEG disulfide linker (Sigma-Aldrich) was used by following a published protocol.[39] The NHS-PEG disulfide linker has both disulfide and succinimidyl functionalities for respective chemisorption onto gold and facile covalent coupling of TAT peptide. Briefly, excessive surfactant was first removed from 1.0 mL gold nanorod solution by centrifugation at 3000 g for 10 minutes and the particles were resuspended in 1.0 mL 2 mM borate buffer. A proper amount of fresh NHS-PEG disulfide solution (in dimethyl sulfoxide) was added to reach a final thiol concentration of 0.2 mM and reacted with gold nanorods for 2 hours. The solution was then cleaned up by centrifugation and resuspended in 2 mM borate buffer. For TAT modified gold nanorods, 2.0 μg TAT peptide was added to the gold colloidal solution and reacted for 8 hours. The gold nanorods were then blocked by adding 100 μL 10% BSA solution (2 mM borate buffer) for over 8 hours. Before use, the colloidal gold nanorod probes were cleaned up by centrifugation and resuspended in 500 μL 1% BSA (2 mM borate buffer). The concentrated gold colloidal solution was diluted in cell culture medium to a final concentration of $4.3\times10^9$ particles/mL for incubation with cells.

**Imaging of immobilized gold nanorods.** The purchased gold nanorod solution was cleaned up and diluted with 18.2-MΩ pure water to a proper concentration and sonicated for 15 min at room temperature. 6 μL of the diluted solution was added onto a freshly cleaned glass slide and covered with a 22×22 mm No.1.5 coverslip (Corning, NY). The positively charged gold nanorods were immobilized on the negatively charged surface of the glass slide by electrostatic forces. The glass slide was then placed on a 360°-rotating mirror holder affixed onto the microscope stage. By rotating the mirror holder 5° or 10° per step, the nanorods were positioned in different orientations, and their DIC images at 540 or 720 nm were taken with the Photometrics CoolSnap ES CCD camera. The exposure time was adjusted to maintain the same background intensity at different wavelengths.

**Full length kinesin motor proteins.** BL21 (DE3) *E. coli* bacteria with the full-length His-tagged kinesin plasmid were kindly provided to us by Dr. Will Hancock in Pennsylvania State University. The *E. coli* bacteria were induced to express kinesin with isopropyl β-D-1-thiogalactopyranoside (IPTG). And the kinesin was purified on a Ni column according to published protocol.[40]

**Preparation of microtubule.** All the tubulin proteins, GTP and taxol were purchased from Cytoskeleton (Denver, CO). Tubulin proteins were mixed and aliquoted with ratio as following: 86% unlabeled tubulin, 7% Rhodamine labeled tubulin, and 7% biotinylated tubulin. Microtubules with 12 protofilaments were prepared according to published protocol:[41,42] 10 μL BRB80 buffer supplemented with 9 μM tubulin, 4 mM $MgCl_2$, 0.5 mM GTP and 10 μM taxol inside was incubated at 37°C for 3 hrs; microtubules were then diluted and stabilized in 100 μL BRB80 buffer supplemented by 10 μM taxol. Before introducing the microtubules into the chamber for gliding assay, the microtubule solution was pipette up and down to shorten the microtubules to proper length.

**In vitro transport.** Two strips of double-sided tape were put on a clean glass slide to serve as the spacers, and one clean coverslip was placed on top to form a chamber. BRB80 solution containing 0.5 mg/mL casein (Sigma, St. Louis, MO) was flowed into the chamber and the chamber was kept at room temperature for 5 min. BRB80 solution containing 0.2 mg/mL casein, 0.2 mM MgATP and kinesin was then introduced into the chamber to replace the previous liquid. After 5 min, BRB80 solution containing 0.2 mg/mL casein, 0.2 mM MgATP, 10 μM Taxol and microtubules was introduced into the chamber and was kept at room temperature for 5 min. Next, BRB80 solution containing 0.2 mg/mL casein, 0.2 mM MgATP, 10 μM Taxol and neutravidin modified gold nanorod (10×35 nm, Nanopartz, Salt Lake City, UT) was flowed into the chamber and was kept at room temperature for 7 min. Finally, the chamber was filled with BRB80 solution containing 0.2 mg/mL casein, 1 mM MgATP and 10 μM Taxol with oxygen scavenging system [50 μg/mL glucose oxidase (Sigma), 4 μg/mL catalase (Sigma), 1% (w/v) glucose (Sigma) and 0.1% (v/v) β-mercaptoethanol (Fluka)]. Between each step, the chamber was washed twice with BRB80 solution containing 0.2 mg/mL casein and 0.2 mM MgATP. The sample slide was then observed under a DIC microscope.

**Cell culture and intracellular transport of gold nanorods.** A549 human lung cancer cell line was purchased from American Type Culture Collection (CCL-185, ATCC, Manassas, VA). The cells were plated in a T25 cell culture flask (Corning) and grown in cell culture medium supplemented with 10% fetal bovine serum (FBS) in a cell culture incubator (37°C, 5% CO2). When subculturing, 150 μL of cell suspension solution was transferred to a 22×22 mm poly-L-lysine (PLL)-coated coverslip, housed in a 35-mm Petri dish (Corning). The Petri dish was left in the incubator for 1 hour to let the cells attach to the coverslip. After 1.5 mL of the cell culture medium with 10% FBS supplement was added to immerse the coverslip, the Petri dish was left again in the incubator for 24 hours. Gold nanorods were diluted in cell culture medium to proper concentration and incubated with cells from 1 hour to 8 hours as desired. After incubation, the microtubules were stained with Tubulin Tracker Green Reagent (T34085, Invitrogen, Carlsbad, CA) for 30 mins in the incubator according to protocol provided by Invitrogen. Then the coverslip with cells was put on glass slide with two strips of double-sided tape as spacers to form a chamber, and was put on microscope for observation.

**Simulation of DIC intensity changing pattern of a nanorod during rotation.** To validate the interpretation from the experimental DIC intensity traces, we used computer simulation to illustrate the theoretical DIC intensity changing patterns as the nanorod rotates in the 3D space. The relative DIC intensities of the bright part $\Delta I/\Delta I_{max}$ and the dark part $\Delta I'/\Delta I'_{max}$ were calculated using Eq. A33 and A34 (see theory part). In the simulation (Figure 3e and Figure 4), the phase delay $\delta_1$ was set to 90°, $\delta_2$ was set to 0° for simplicity. Since we are focusing on the DIC intensity variation profile and periodicity, the maximum DIC intensities ($\Delta I/\Delta I_{\mathrm{max}}$ and $\Delta I'/\Delta I'_{\mathrm{max}}$) of the nanorods were normalized to unit.

## Results and Discussion

**2D and 3D orientation of gold nanorods.** Nomarski-type DIC microscopes are in principle two-beam interferometers. Each of the two orthogonally polarized illumination beams creates an *independent* intermediate image. One such image is shifted laterally by ~100 nm, and then overlapped with the other to generate the final interference image. For *isotropic* samples, such as nanospheres, the two intermediate images are *identical*, thus leading to evenly distributed bright and dark intensities. For optically *anisotropic* samples, such as gold nanorods, the two intermediate images are different because the two illumination beams are phase-delayed to different extent depending on the relative orientation of the nanorod to the two polarization directions. Therefore, the DIC images of gold nanorods appear as diffraction-limited spots with disproportionate bright and dark parts. Figure 1a shows the DIC images of two 25×73 nm gold nanorods positioned at different orientations and illuminated at their plasmon resonance wavelength: 540 nm for the transverse mode or 720 nm for the longitudinal mode (Figure 1c).

The orientation of a gold nanorod, i.e., the angle $\phi$ between the nanorod's long axis and the *x*-polarization direction as defined in Figure 1b, can be determined using the bright *or* dark intensities of its DIC images collected at 720 nm. The relative brightness $\Delta I/\Delta I_{max}$ (defined in Figure 1d) adopts a *sin*$^4$ relationship with $\phi$(for details, please see the Supplementary Data)□

$$\phi = \mathrm{asin}(\Delta I / \Delta I_{max})^{1/4} \qquad ..1$$

Similarly, the relative darkness $\Delta I'/\Delta I'_{max}$ adopts a *cos*$^4$ relationship with $\phi$□.

$$\phi = \mathrm{acos}(\Delta I' / \Delta I'_{max})^{1/4} \qquad .□.$$

It is worthwhile to mention that the relative brightness and relative darkness are measures of effective projections of the nanorod onto the two polarization directions.

The errors of the angle determination are directly related to the precision of DIC intensity measurement. For example, when the relative error of intensity measurement is ~0.5% (as in Figure 1d), the standard deviation of $\phi$ determined for a 25×73 nm gold nanorod is ~0.8°, that is, a 2-3° angular resolution in nearly the entire range. We also estimated the error of angle determination when these gold nanorods are used in live cells as orientation probes to track highly dynamic processes. For imaging live cells at video rates (32 frames/s) with an Andor EMCCD camera on a Nikon Eclipse 80i microscope, the relative error of intensity measurement under optimized conditions rises to ~1.5%, resulting in a standard deviation of the angle determination less than 3° (or an angular resolution of ~9°) for a 25×73 nm gold nanorod.

When a gold nanorod is arbitrarily positioned in the 3D space, its 3D orientation (the elevation angle $\psi$ and the azimuth angle $\phi$, as defined in Figure 2) can be resolved due to the two *independent* measurements of the bright and dark intensities in *each* DIC image. In practice, the accuracy of the nanorod orientation determination in 3D is directly related to the signal-to-noise ratio of the bright/dark intensities, which declines when the projection of the nanorod on either of the polarization directions approaches zero.

**Rotational motion of gold nanorods attached on gliding microtubules.** It is also possible to identify the nanorod rotational patterns from the dynamic rotation context. For example, when a nanorod rotates around a fixed axis, its orientations and the resulting DIC intensities must follow a characteristic pattern. A rotating nanorod goes through positions that can be resolved with either high or low confidence; thus, when the nanorod is followed continuously, the positions of low confidence can be resolved in the chronological context of the positions of high confidence, giving a better overall understanding of nanorod orientations in the time course.

Here we demonstrate that by using the combination of gold nanorod probes and DIC microscopy, we are able to resolve rotational motions of nano-cargos transported by motor proteins in 3D space. Motor proteins are essential to cellular functions by generating both translational and rotational motions, and they have shown great potential to serve as components of nanomachines to sort and shuttle cargos to designated locations both in engineered and biological environments.[28-29] Depending on the composition of the microtubules (number of protofilaments), the microtubule may rotate or not rotate around its longitudinal axis[30] when being driven to move laterally. Apparently, such self-rotating motion is not readily resolved with conventional fluorescence microscopy. With carefully designed experiments and recently developed techniques, e.g., microtubules with a side arm,[30-31] quantum dot assisted fluorescence interference contrast (FLIC) microscopy,[19] or fluorescence microscopy with a wedged prism at the back-focal-plane of the objective,[21] etc., it becomes possible for researchers to detect the self-rotation of gliding microtubules. Till now, the majority of reports were accomplished under ideal conditions, i.e., on clean, smooth surfaces. Here we show that by using the combination of gold nanorod probes and DIC microscopy, we are able to report rotational motions of nano-cargos during transport at video rate not only on *in vitro* engineered surfaces but also on cytoskeletons in live cells.

It is worthy of mention that small gold nanorods (10×35 nm) were used as reporters to track the self-rotation of gliding microtubules on flat substrates coated with full-length kinesin to avoid steric hindrance.[32] The observation wavelength was adjusted to 760 nm accordingly. By using a smaller probe, the signal strength was sacrificed, leading to lower signal to noise ratios. However, since the largest dimension of the gold nanorods is much smaller than the length of a full-length kinesin motor protein (70 nm),[32] the continuous movement of the microtubule was not affected in the presence of the nanorod probe.

As mentioned earlier, the bright/dark DIC pattern of a gold nanorod is determined by the effective projections of the nanorod onto the two polarization directions of the two illumination beams. The two polarization directions are named the *bright axis* and the *dark axis* in the following discussion. When a nanorod is firmly bound to a non-13-protofilament microtubule through multiple strong biotin-neutravidin linkages, its rotation along with the microtubule on kinesin-coated substrate gives rise to periodic image patterns, which is dependent on the *transport angle* $\beta$ between the microtubule advancement direction and the bright axis and the nanorod *binding angle* $\alpha$ between the microtubule and the long axis of the nanorod (Figure 3b). Judging from the DIC intensity changing patterns, the details of the microtubule rotation, e.g., the periodical length of protofilament helices, can be obtained. Figure 3cde shows an example of a nanorod binding to a gliding and self-rotating microtubule on a kinesin-coated glass substrate. The nanorod was transported in a direction of ~151° to the bright axis (Figure 3c). The nanorod show bright and dark images alternatively (Figure 3cd), indicating that the projections of the nanorod onto the two polarization axes change periodically as it rotated along with the self-rotating microtubule. The peak-to-peak distance is 3.4 μm, suggesting the microtubule is most likely composed of 12 protofilaments.[19,30]

We further simulated the DIC intensities of the nanorod as a function of time as it glides with a microtubule on the substrate with a transport angle $\beta$ of 151° (Figure 3e). The gliding velocity was assumed to be 0.68 μm/s as in the experiment and the nanorod binding angle $\alpha$ was assumed to be 45°. Since we focused on the DIC intensity variation profile and periodicity in the simulation, the DIC intensities ($\Delta I/\Delta I_{\max}$ and $\Delta I'/\Delta I'_{\max}$) of the nanorods were normalized to between zero and unit. The simulated DIC intensity pattern is consistent with that from the experiment, showing that the periodical changing pattern is caused by the self-rotating of the gliding microtubule.

As a comparison, Figure 4 shows an example of a nanorod being transported by a non-rotating microtubule. The nanorod traveled a distance of ~15 μm along the direction of ~66° to the bright axis, showing slightly curved bright intensities and nearly constant, negligible dark intensities. The mostly bright image of the nanorod indicates that it binds to the microtubule at a very large angle (α close to $90^o$), yielding a large projection on the bright axis and a small projection on the dark axis. The situation that the nanorod binds in parallel to the microtubule axis (α close to $0^o$) thus can be excluded. In addition, the little variation in the DIC intensity indicates that the orientation of the nanorod did not change significantly over the whole period and the microtubule was not rotating periodically over a distance of ~15μm. Furthermore, we simulated the DIC intensity changing patterns with a microtubule transport angle β= $67.5^o$ at different nanorod binding angles α. None of the simulated curves look similar to the experimental curves shown in Figure 4b, which further confirms that this is a non-rotating microtubule.

The DIC bright intensity does show a small curvature during the whole transport period, which is correlated with the curvature of the trace. The microtubule walked a backward “s” shape (Figure 4a). For a nanorod binding to the microtubule with a large angle (a large $\alpha$), it will have relatively smaller projections on the bright axis at the two ends while larger projection in the middle of the trace. The corresponding DIC intensity will display lower bright intensities at the two ends and higher intensity in the middle, consistent with the experimental data. This shows that the variation of the DIC intensities is caused by the microtubule advancing direction rather than the self-rotation.

To assess the dependence of DIC intensity changing patterns on the transport angle β and the nanorod binding angle α, the DIC intensity changing patterns for different transport situations were simulated and plotted in the Figure 5. We noticed that when the nanorod is parallel to the microtubule (α=0), the nanorod will not report the self-rotation of the microtubule at any transport angle. However, when α is larger than 10°, we shall see the periodic DIC intensity changing pattern at most of the transport directions. This means that using gold nanorods as reporters, we will miss ~11% of the rotating cases given that the nanorod has no preferred orientation when binding to the microtubule. In our experiments, we followed a procedure which favors the formation of 12-protofilament.[19] A total number of 98 cases were recorded and analyzed. Among them, 39 cases show clear periodic patterns and the distribution of rotation period is plotted in Figure 6.

It also should be cautioned that in order for gold nanorods to be a reliable rotation probe, they must be bound to the target firmly through multi-valent bonds. In this study, in order to achieve a multi-point attachment of the nanorod to the microtubule, we purposely increased the fraction of the biotin-labeled tubulins during the microtubule polymerization process.

**Rotational motion of gold nanorods being transported in live cells.** We further show that gold nanorod probes can disclose the rotational motions of nanorod-containing vesicles as they were being pulled on cytoskeleton tracks in live cells. TAT-modified gold nanorods with a dimension of 25×73 nm were naturally internalized by A549 human lung cancer cells, and their subsequent transport on cytoskeleton tracks was followed with DIC microscopy with an observation wavelength of 720 nm. The large gold nanorods (25×73 nm) were used to improve the signal to background noise ratio in the complex cellular environment. A selected transport event where a nanorod-containing vesicle traveled a long distance (> 6 μm) on multiple tracks toward different directions was recorded. The relatively fast transport velocity (average velocity 1.2 μm/s) suggests that the nanorod-containing vesicle was most likely transported on the microtubule tracks.[33] The nanorod gave nearly constant bright/dark intensities in the time course when being transported linearly. More interestingly, when the nanorod's moving direction changed ~90°, the DIC intensity pattern changed from completely dark to completely bright, indicating a ~90° turn in the focal plane also for the cargo's orientation. These suggest that the relative orientation of the cargo to the microtubule tracks are tightly controlled, resulting in a conveyor-like movement of vesicles on the microtubule network. Figure 7 shows the traces and the presumed orientation of the nanorod.

It is assumed that the nanorod is stationary with respect to the vesicle. There are several reasons that this assumption is valid. Endocytic vesicles are usually several tens of nanometers in diameter.[34] Considering the size of the nanorod (25×73 nm) and multiple assisting proteins and receptors, there is little room for the nanorod to diffuse randomly. More importantly, we observed that the nanorod showed a fixed orientation during the transport, indicating that the nanorod cannot experience active random rotational diffusion relative to the vesicle. Thus, we are observing the rotational motions of the vesicle during a transport process rather than the random motions of the nanorod inside the vesicle.

The new approach may shed new light on many live-cell transport mysteries, such as the question whether molecular motors with different directionalities work in coordination or fight a "tug of war" to reverse the transport direction.[35-38]

## Conclusions

We demonstrated that by using gold nanorod probes and DIC microscopy, rotational motions of nano-objects can be resolved at video rates in both engineered environments and live cells. Compared to single molecule fluorescence polarization imaging, this method is more robust in terms of resistance to photobleaching and background noise. In our vision, this technique has great potentials to investigate the working mechanisms of nanomachines by revealing their dynamic rotational motions in both micro- and nano-engineered structures and in live cells.

## References

(1) Hess, H.; Bachand, G. D.; Vogel, V. *Chem.-Eur. J.* **2004**, *10*, 2110.

(2) van den Heuvel, M. G. L.; Dekker, C. *Science* **2007**, *317*, 333.

(3) Jia, L. L.; Moorjani, S. G.; Jackson, T. N.; Hancock, W. O. *Biomed. Microdevices* **2004**, *6*, 67.

(4) Saxton, M. J.; Jacobson, K. *Annu Rev Bioph Biom* **1997**, *26*, 373.

(5) Kusumi, A.; Nakada, C.; Ritchie, K.; Murase, K.; Suzuki, K.; Murakoshi, H.; Kasai, R. S.; Kondo, J.; Fujiwara, T. *Annu Rev Bioph Biom* **2005**, *34*, 351.

(6) Thompson, R. E.; Larson, D. R.; Webb, W. W. *Biophys J* **2002**, *82*, 2775.

(7) Katayama, Y.; Burkacky, O.; Meyer, M.; Brauchle, C.; Gratton, E.; Lamb, D. C. *Chemphyschem* **2009**, *10*, 2458.

(8) Joo, C.; Balci, H.; Ishitsuka, Y.; Buranachai, C.; Ha, T. *Ann. Rev. Biochem.* **2008**, *77*, 51.

(9) Toprak, E.; Balci, H.; Blehm, B. H.; Selvin, P. R. *Nano Lett.* **2007**, *7*, 2043.

(10) Jaqaman, K.; Loerke, D.; Mettlen, M.; Kuwata, H.; Grinstein, S.; Schmid, S. L.; Danuser, G. *Nat Methods* **2008**, *5*, 695.

(11) Sase, I.; Miyata, H.; Ishiwata, S.; Kinosita, K. *Proc. Natl. Acad. Sci. U. S. A.* **1997**, *94*, 5646.

(12) Forkey, J. N.; Quinlan, M. E.; Shaw, M. A.; Corrie, J. E. T.; Goldman, Y. E. *Nature* **2003**, *422*, 399.

(13) Toprak, E.; Enderlein, J.; Syed, S.; McKinney, S. A.; Petschek, R. G.; Ha, T.; Goldman, Y. E.; Selvin, P. R. *Proc. Natl. Acad. Sci. U. S. A.* **2006**, *103*, 6495.

(14) Xiao, L. H.; Qiao, Y. X.; He, Y.; Yeung, E. S. *Anal Chem* **2010**, *82*, 5268.

(15) Ha, T.; Laurence, T. A.; Chemla, D. S.; Weiss, S. *J. Phys. Chem. B* **1999**, *103*, 6839.

(16) Yasuda, R.; Noji, H.; Kinosita, K.; Yoshida, M. *Cell* **1998**, *93*, 1117.

(17) Itoh, H.; Takahashi, A.; Adachi, K.; Noji, H.; Yasuda, R.; Yoshida, M.; Kinosita, K. *Nature* **2004**, *427*, 465.

(18) Adachi, K.; Oiwa, K.; Nishizaka, T.; Furuike, S.; Noji, H.; Itoh, H.; Yoshida, M.; Kinosita, K. *Cell* **2007**, *130*, 309.

(19) Nitzsche, B.; Ruhnow, F.; Diez, S. *Nat. Nanotechnol.* **2008**, *3*, 552.

(20) Kukura, P.; Ewers, H.; Muller, C.; Renn, A.; Helenius, A.; Sandoghdar, V. *Nat Methods* **2009**, *6*, 923.

(21) Yajima, J.; Mizutani, K.; Nishizaka, T. *Nat. Struct. Mol. Biol.* **2008**, *15*, 1119.

(22) Jana, N. R.; Gearheart, L.; Murphy, C. J. *J. Phys. Chem. B* **2001**, *105*, 4065.

(23) Gans, R. *Ann Phys-Berlin* **1915**, *47*, 270.

(24) Sonnichsen, C.; Alivisatos, A. P. *Nano Lett.* **2005**, *5*, 301.

(25) Spetzler, D.; York, J.; Daniel, D.; Fromme, R.; Lowry, D.; Frasch, W. *Biochemistry* **2006**, *45*, 3117.

(26) Chang, W. S.; Ha, J. W.; Slaughter, L. S.; Link, S. *P Natl Acad Sci USA* **2010**, *107*, 2781.

(27) Pluta, M. *Advance light microscopy*; Elsevier Science Publishing Co. Inc.: New York, 1989; Vol. 2.

(28) Hess, H.; Matzke, C. M.; Doot, R. K.; Clemmens, J.; Bachand, G. D.; Bunker, B. C.; Vogel, V. *Nano Lett.* **2003**, *3*, 1651.

(29) van den Heuvel, M. G. L.; De Graaff, M. P.; Dekker, C. *Science* **2006**, *312*, 910.

(30) Ray, S.; Meyhofer, E.; Milligan, R. A.; Howard, J. *J. Cell Biol.* **1993**, *121*, 1083.

(31) Yajima, J.; Cross, R. A. *Nat. Chem. Biol.* **2005**, *1*, 338.

(32) Kerssemakers, J.; Howard, J.; Hess, H.; Diez, S. *Proc. Natl. Acad. Sci. U. S. A.* **2006**, *103*, 15812.(33) Lakadamyali, M.; Rust, M. J.; Zhuang, X. W. *Cell* **2006**, *124*, 997.

(34) Conner, S. D.; Schmid, S. L. *Nature* **2003**, 422, 37.

(35) Kural, C.; Kim, H.; Syed, S.; Goshima, G.; Gelfand, V. I.; Selvin, P. R. *Science* **2005**, *308*, 1469.

(36) Gross, S. P.; Welte, M. A.; Block, S. M.; Wieschaus, E. F. *J. Cell Biol.* **2002**, *156*, 715.

(37) Muller, M. J. I.; Klumpp, S.; Lipowsky, R. *Proc. Natl. Acad. Sci. U. S. A.* **2008**, *105*, 4609.

(38) Gennerich, A.; Vale, R. D. *Curr. Opin. Cell Biol.* **2009**, *21*, 59.

(39) Narayanan, R.; Lipert, R. J.; Porter, M. D. *Anal. Chem.* **2008**, 80, 2265.

(40) Hancock, W. O.; Howard, J. *J. Cell Biol.* **1998**, 140, 1395.

(41) Ray, S.; Meyhofer, E.; Milligan, R. A.; Howard, J. *J. Cell Biol*. **1993**, 121, 1083.

(42) Nitzsche, B.; Ruhnow, F.; Diez, S. *Nat. Nanotech*. **2008**, 3, 552.

## Figure captions

Figure 4.1. Gold nanorod orientations in 2D space. (a) DIC images of two 25×73 nm gold nanorods at different orientations in 2D space. The same nanorods were illuminated at their transverse (540 nm) or longitudinal plasmonic resonance wavelengths (720 nm). The gold nanorods were positively charged and physically adsorbed on a negatively charged glass slide, and submerged in deionized water. The glass slide was fixed on a rotating stage that allows 360° rotation. (b) Definition of the 2D orientation (*azimuth angle* □ of a nanorod with respect to the polarization directions of the two illumination beams in a DIC microscope. Other symbols are explained in the Supplementary Data. (c) UV-Vis spectrum of the gold nanorod suspension in deionized water (red) and DIC spectrum of an immobilized, randomly orientated gold nanorod (blue). The DIC contrast is defined as the difference between the maximum and the minimum intensities divided by the average local background intensity. The two DIC peaks are red-shifted compared to their plasmon resonance wavelengths. (d) Periodic changes of the bright/dark intensities of a gold nanorod when rotated under a DIC microscope and illuminated at the two DIC peak wavelengths. All intensities are relative to the background level. The periodic patterns at these two illumination wavelengths are shifted by ~90°, consistent with the relative orientation between the transverse and longitudinal plasmonic resonance modes.

Figure 4.2. Definitions of the orientation angles of a nanorod in 3D space: the *elevation angle* □ and the *azimuth angle* □.

Figure 4.3. Cargo transport in engineered environments. (a) Scheme of a piece of gliding microtubule serving as the transport vehicle on kinesin coated glass slide. The 10×35 nm gold nanorod serves as the probe to detect the rotational motion of the microtubule. (b) Definition of the microtubule *transport angle* β and the nanorod *binding angle* α. (c-e): An example of a gliding and self-rotating microtubule (β≈151°) as reported by the attached nanorod probe. (c) The trace and alternative bright-and-dark DIC images of the nanorod. (d) The measured DIC intensities as a function of time. (e) The simulated DIC intensities as a function of time. The microtubule was assumed to be gliding with a transport angle β of 151° with a velocity of 0.68

µm/s. The nanorod binding angle αwas assumed to be 45°. The simulated DIC intensity pattern is consistent with that from the experiment.

Figure 4.4. An example of a gliding and non-rotating microtubule (β≈66°). (a) The trace of the nanorod. (b) The measured DIC intensities as a function of time.

Figure 4.5. Simulated DIC intensity changing pattern when a microtubule carrying a nanorod is transported. The transport direction is along the dark axis.

Figure 4.6. Statistics of the rotation period of gliding microtubules probed with 10×35 nm gold nanorods. A total of 98 cases were recorded and analyzed. Among them, 39 cases show clear periodic patterns and the distribution of their rotation periods is plotted.

Figure 4.7. Cargo transport in live cells. (a) Schematics of the intracellular microtubule transport of a gold nanorod-containing vesicle. (b) Traces and presumed orientations of the gold nanorod during the transport.

# Figures

Figure 4.1

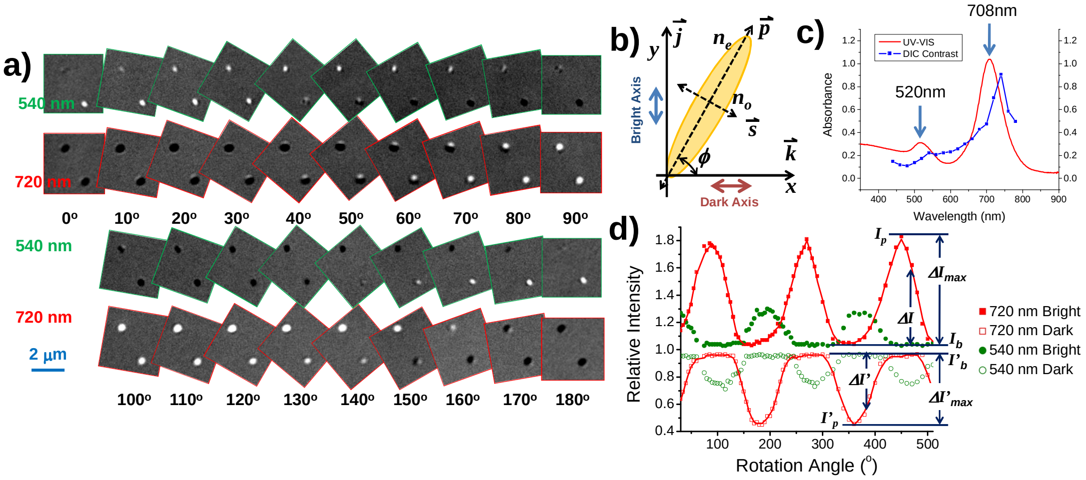

Figure 4.2

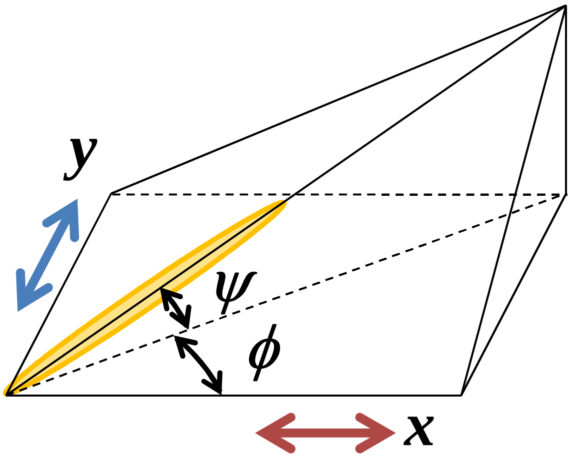

Figure 4.3

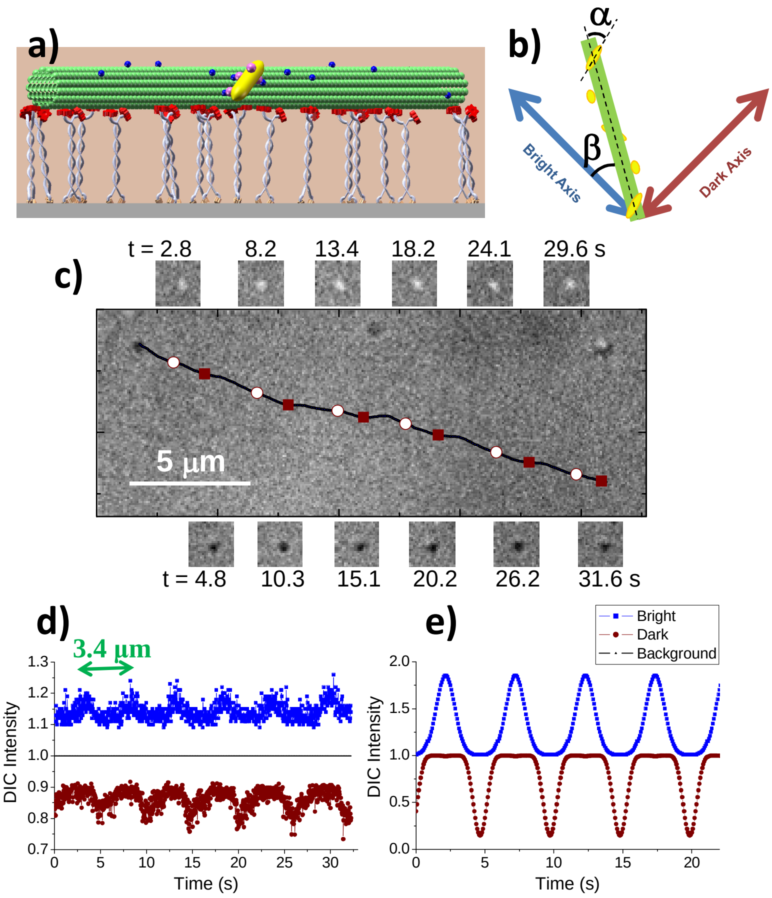
a)
b)
α
β
Bright Axis
Dark Axis
c)
t = 2.8
8.2
13.4
18.2
24.1
29.6 s
5 μm
t = 4.8
10.3
15.1
20.2
26.2
31.6 s
d)
3.4 μm
DIC Intensity
1.3
1.2
1.1
1.0
0.9
0.8
0.7
0
5
10
15
20
25
30
Time (s)
e)
Bright
Dark
Background
DIC Intensity
2.0
1.5
1.0
0.5
0.0
0
5
10
15
20
Time (s)

Figure 4.4

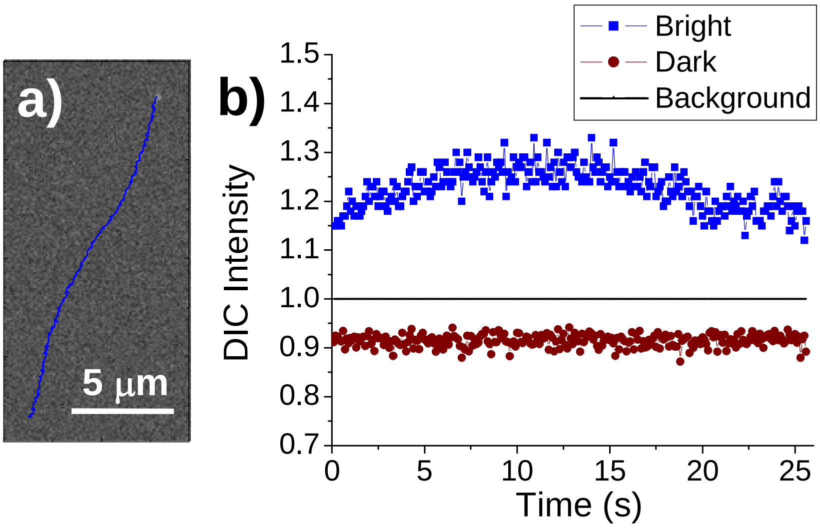
a)
5 μm
b)
Bright
Dark
Background
DIC Intensity
1.5
1.4
1.3
1.2
1.1
1.0
0.9
0.8
0.7
0
5
10
15
20
25
Time (s)

Figure 4.5

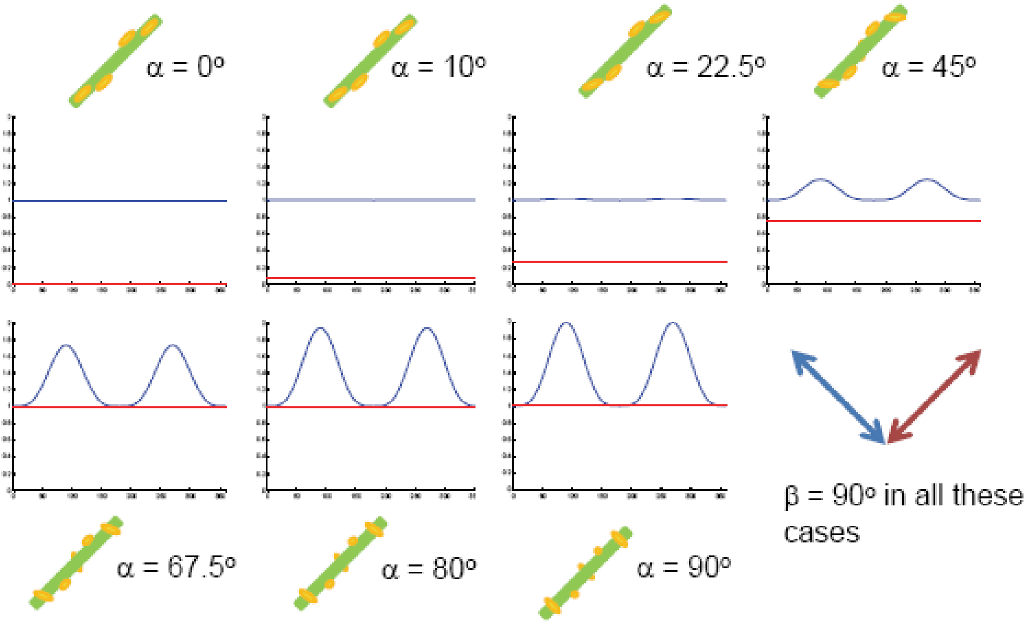

Figure 4.6

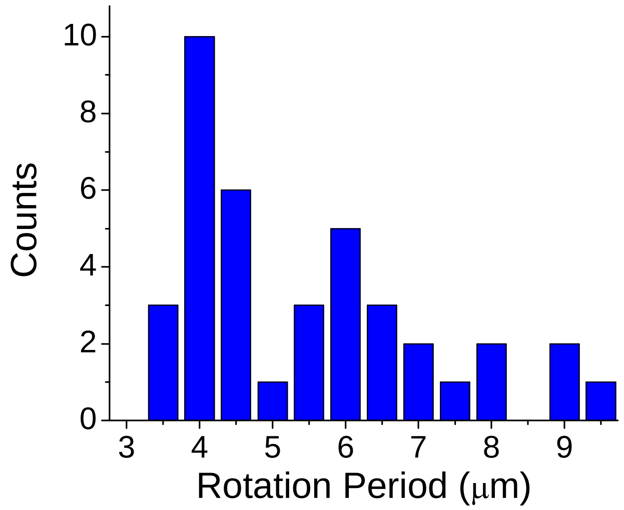

Figure 4.7

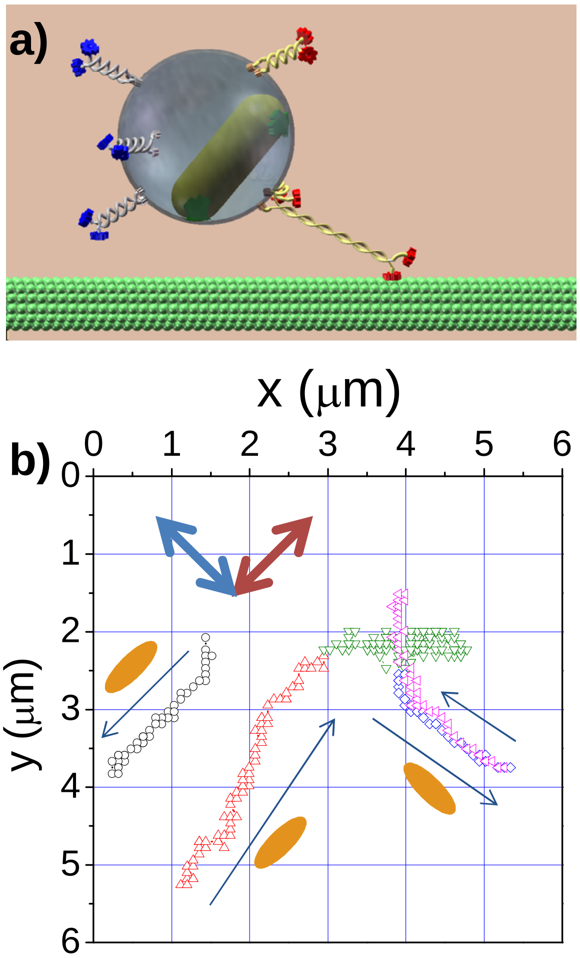

# Theory

## 1. DIC principles and imaging of optically isotropic nanoparticles

DIC microscopy works on the principle of interference to gain information about differences in refractive index and optical path length of specimen components. A Nomarski-type DIC microscope contains 2 Nomarski prisms. The incident light is split by the first Nomarski prism into two orthogonally polarized, laterally shifted beams for illumination. For non-absorbing, optically isotropic samples, two identical intermediate images with different polarizations form behind the objective, each with a flat intensity profile but a curved phase profile. The two identical images are shifted and summed in the presence of the second Nomarski prism to generate the interference pattern of the final DIC image.

Specifically, when a non-absorbing, isotropic nanoparticle that has a diameter smaller than the shear distance ($2\Delta x$) is on the object plane, the phase profiles of the two intermediate images are the same. Without losing generality, assume the image polarized along the *y*-direction was laterally shifted $\Delta x$ by the second Nomarski prism toward the negative direction of the *x*-axis, and the image polarized along the *x*-direction was shifted $\Delta x$ toward the positive direction. Assuming a perfect point spread function for the optical system (the Delta function), the brightest and the darkest intensities in the final image will appear at $-\Delta x$ and $+\Delta x$, where the phase difference between the two mutually shifted images assumes the peak values $+\gamma$and $-\gamma$. $\gamma$ is the phase delay of the illumination beam caused by the nanoparticle:

$$\gamma = \frac{2\pi L}{\lambda}\Delta n, \qquad \text{(A1)}$$

where *L* is the optical path (in this case the particle diameter); $\lambda$ is the wavelength of the incident beam; $\Delta n$ is the refractive index difference between the nanoparticle and the surrounding medium. The amplitude of the electric vector at $-\Delta x$ and $+\Delta x$ in the final image plane are:

$$E_{-\Delta x} = \frac{\sqrt{2}}{2}E_0[e^{-i\gamma}e^{-i\theta} - e^{i\theta}], \qquad \text{(A2)}$$

$$E_{+\Delta x} = \frac{\sqrt{2}}{2}E_0[e^{-i\theta} - e^{-i\gamma}e^{i\theta}]. \qquad \text{(A3)}$$

$E_0$ is the amplitude of the electric vector of one of the two illumination beams on the object plane and the intensity of the two illumination beams are assumed to be the same. 2θ is an additional phase bias introduced by the manufacturer of the microscope to give an optimal image contrast. The amplitude of the electric vector in the background is:

$$E_b = \frac{\sqrt{2}}{2} E_0[e^{-i\theta} - e^{i\theta}] . \qquad \text{(A4)}$$

By adjusting the phase bias 2θ to be $90^{\circ}$, the DIC image of an isotropic sphere can be tuned to show even bright and dark parts, and the relative bright and dark intensities are calculated by the following equations:

$$\frac{I_{-\Delta x}}{I} = 1 + \sin\gamma , \qquad \text{(A5)}$$

$$\frac{I_{+\Delta x}}{I} = 1 - \sin\gamma . \qquad \text{(A6)}$$

## 2. Optically anisotropic nanoparticles and their DIC images

The gold nanorods used in the paper have a dimension of 25×73 nm. The plasmon resonance wavelengths of these gold nanorods are at 520 nm and 708 nm, respectively (Fig. 1c). The maximum DIC contrasts appear at wavelengths slightly red-shifted to the corresponding plasmon resonance wavelengths, which is consistent with the Kramers-Kronig relations (Kreibig, U.; Vollmer, M. *Optical Properties of Metal Clusters, Springer Series in Materials Science , Vol. 25*; Springer: New York, 1995; Vol. 25)..

One special characteristic of gold nanorods is that their plasmon resonance modes are aligned with their geometric profiles: one along the long axis (longitudinal mode) and the other along the short axis (transverse mode). This results in wavelength-dependent anisotropic refractive indices of the gold nanorods. When a gold nanorod is imaged under a DIC microscope, the phase delays on the two polarized, intermediate images are different, resulting in uneven bright/dark images of gold nanorods. In fact, the phase delay caused by the nanorod depends on the angle between the optical axis of the nanorod and the corresponding polarization direction of the illumination beam. For example, when the nanorod is illuminated at 720 nm and is oriented so that its corresponding optical axis (the long axis) is perfectly in line with the *y*-axis direction, it generates the largest phase delay (determined by the extraordinary refractive index $n_e$) on the image polarized in the *y*-direction and the minimum phase delay (the ordinary refractive index $n_o$) on the other image polarized in the *x*-direction. The DIC image of the gold nanorod will have the highest bright intensity ($\Delta I$) and the lowest dark intensity ($\Delta I'$), resulting in a mainly bright spot in the DIC image. Similarly, when the nanorod is rotated to align with the *x*-axis direction, the result is a mainly dark spot in the DIC image. At any angle in between, both the dark and bright parts with different proportionalities are observed. (See Supplementary Fig. 2 for illustrations.)

In this paper, the optimal observation wavelengths were selected to be 540 nm and 720 nm for individual gold nanorods. Apparent periodicities of 180° were observed at these two wavelengths. In 2D and 3D orientation determination, 720 nm illumination was used.

### 3. Determination of the 2D orientation angle □

The periodic change provides an opportunity to determine the absolute orientation of a gold nanorod. When the phase bias $2\theta$ is adjusted to be $90^o$, the bright intensity in a nanoparticle DIC image is the result of the interference between the phase-delayed *y*-polarization image and the non-phase-delayed *x*-polarization background. Correspondingly, the dark intensity is the result of the overlay between the phase-delayed *x*-polarization image and the non-phase-delayed *y*-polarization background.

For the illumination beam that is polarized in the *y*-direction, it can be decomposed into two orthogonal components, with electric vectors perpendicular and parallel to the corresponding optical axis of the nanorod, respectively:

$$\vec{E}_0 = \vec{p}E_0 \sin\phi + \vec{s}E_0 \cos\phi \, . \tag{A7}$$

After passing through the sample plane, the two components will be delayed to different extent due to the optical birefringence of the nanorod:

$$\vec{E}_1 = \vec{p}E_0 \sin\phi e^{-i\delta_1} + \vec{s}E_0 \cos\phi e^{-i\delta_2} \, , \tag{A8}$$

where $\delta_1 = (n_e\text{-}n_m)\pi L/\lambda$ and $\delta_2 = (n_o\text{-}n_m)\pi L/\lambda$; $n_e$ and $n_o$ are the extraordinary and ordinary refractive indices, respectively; $n_m$ is the refractive index of the medium; $L$ is the optical path in sample (the nanorod's short axis). Projecting back to the original coordinates:

$$\vec{E}_1 = \vec{j}E_0(\sin^2\phi e^{-i\delta_1} + \cos^2\phi e^{-i\delta_2}) + \vec{k}E_0 \cos\phi \sin\phi (e^{-i\delta_1} + e^{-i\delta_2}) \, . \tag{A9}$$

Due to the working principle of the Nomarski prism, the electric vector polarized in the *x*-direction does not contribute to the interference pattern of the sample image (Supplementary Fig. 2b) and can be ignored:

$$\vec{E}_1 = \vec{j}E_0(\sin^2\phi e^{-i\delta_1} + \cos^2\phi e^{-i\delta_2}). \qquad \text{(A10)}$$

The electric vector of the *y*-component after the second polarizer can be written as:

$$\vec{E}_{2y} = \frac{\sqrt{2}}{2}\vec{j}E_0(\sin^2\phi e^{-i\delta_1} + \cos^2\phi e^{-i\delta_2}). \qquad \text{(A11)}$$

Correspondingly, the electric vector of the *x*-component at the same location is:

$$\vec{E}_{2x} = \frac{\sqrt{2}}{2}\vec{k}E_0. \qquad \text{(A12)}$$

The electric field is the summation of Eq. A11 and A12 with an additional phase bias 2θ:

$$\vec{E}_{-\Delta x} = \frac{\sqrt{2}}{2}E_0(\sin^2\phi e^{-i\delta_1} + \cos^2\phi e^{-i\delta_2})e^{-i\theta} - \frac{\sqrt{2}}{2}E_0 e^{i\theta}. \qquad \text{(A13)}$$

The intensity at the interference point is:

$$I_{-\Delta x} = |E_{-\Delta x}|^2 = 2E_0^2[\sin^4\phi\sin^2\frac{(2\theta+\delta_1)}{2} + \cos^4\phi\sin^2\frac{(2\theta+\delta_2)}{2} +$$

$$2\sin^2\phi\cos^2\phi\sin\frac{(2\theta+\delta_1)}{2}\sin\frac{(2\theta+\delta_2)}{2}\cos\frac{(\delta_1-\delta_2)}{2}]. \qquad \text{(A14)}$$

Similarly, the background $E_b$ can be derived as:

$$E_b = \frac{\sqrt{2}}{2}E_0 e^{-i\theta} - \frac{\sqrt{2}}{2}E_0 e^{i\theta}, \qquad \text{(A15)}$$

and the background intensity $I_b$ is:

$$I_b = |E_b|^2 = 2E_0^2\sin^2\theta. \qquad \text{(A16)}$$

When the phase bias 2θ is set at 90°, the relative DIC intensity of the bright part is:

$$\frac{I_{-\Delta x}}{I_b} = 1 + \sin^4\phi\sin\delta_1 + \cos^4\phi\sin\delta_2 + \sin^2\phi\cos^2\phi[\cos(\delta_1-\delta_2) + \sin\delta_1 + \sin\delta_2 - 1].$$

(A17)

Eq. A17 gives the analytical solution of the DIC intensity as a function of the orientation angle □. In practice, we found that applying a large birefringence approximation, we can simplify Eq. A17 to a $\sin^4\phi$ relationship while maintaining satisfactory results for □ greater than 30°:

$$\frac{I_{-\Delta x}}{I_b}-1=\frac{I_{-\Delta x}-I_b}{I_b}=\frac{\Delta I}{I_b}\approx\sin^4\phi\sin\delta_1 . \tag{A18}$$

At ϕ= 90°, the intensity is at its maximum value, that is, $I_{-\square x} = I_p$.

$$\frac{I_{-\Delta x}}{I_b}-1=\frac{I_p}{I_b}-1=\frac{I_p-I_b}{I_b}=\frac{I_{\max}}{I_b}\approx\sin\delta_1 . \tag{A19}$$

Take the ratio of Eq. A18 and A19:

$$\frac{\Delta I}{I_{\max}}\approx\sin^4\phi . \tag{A20}$$

Rearrange:

$$\phi=\mathrm{asin}(\Delta I/\Delta I_{\max})^{1/4} , \tag{A21}$$

Thus, □ can be determined from the bright part of the DIC image, where $\Delta I$ and $\Delta I_{\max}$ are defined in Fig. 1d. Considering the $sin^4$ relationship, the relative brightness ($\Delta I/\Delta I_{\max}$) of the nanorod image can be viewed as a measure of the projection of the nanorod onto the *y*-polarization direction.

The large birefringence approximation requires that $\delta_1$ is large ($\sin\delta_1$ approaches 1), while $\delta_2$ is close to 0. The rationale is given below. For a noble metal spheroid, the phase delay $\delta_1$ due to the extraordinary refractive index $n_e$ is usually much larger than the phase delay $\delta_2$ due to the ordinary refractive index $n_o$. Under this condition, Eq. A17 gives a periodical relative intensity as a function of □ with a minimum relative intensity equals to $1 + \sin\delta_2$. From the experimentally collected rotation data of 25 × 73 nm gold nanorod (Fig. 1d), we know that the relative background intensity ($I_b$) is ~1.03, so $\sin\delta_2 \approx 0.03$ and $\delta_2 \approx 1.7°$. Thus, all $\delta_2$ and $\sin\delta_2$ can be ignored from Eq. A17. Rearranging Eq. A17, we have:

$$\frac{\Delta I}{I_b}=\sin^4\phi\sin\delta_1+\sin^2\phi\cos^2\phi(\cos\delta_1+\sin\delta_1) . \tag{A22}$$

When $\sin\delta_1$ is large (approaching 1), Eq. A22 can be reduced to $\sin^4$□$\sin\delta_1$ (Eq. A18). When

$\sin\delta_1$ is small, Eq. A22 can be reduced to $\sin^2\phi\sin\delta_1$. Under our experimental conditions, the 25×73 nm nanorod gives a fairly large phase delay $\delta_1$ at 720 nm illumination. The $\Delta I/I_{max}$ curve is closer to that of the $\sin^4\phi$ model by showing a large flat region at the lower portion of the curve (Fig. 1d). Also, the calculated angles using the $\sin^4\phi$ model are consistent with physically rotated angles, showing a linear correlation at most angles (Supplementary Fig. 3a). Thus, using Eq. A18 instead of A17 in determining the orientation angle is valid.

The errors of the angle determination can be estimated from:

$$\sigma_\phi^2 = (\frac{\partial\phi}{\partial I})^2\sigma_I^2 + (\frac{\partial\phi}{\partial I_\mathrm{p}})^2\sigma_\mathrm{p}^2 + (\frac{\partial\phi}{\partial I_\mathrm{b}})^2\sigma_\mathrm{b}^2 . \qquad \text{(A23)}$$

The standard deviations of measured ($\sigma_I$), maximum ($\sigma_\mathrm{p}$), and background ($\sigma_\mathrm{b}$) intensities are all on the same level due to the high background of DIC microscopy. Supplementary Fig. 3b shows the standard deviation of the measured orientation angles from the “720 nm bright” curve in Fig. 1d. The relative error of the intensity measurement was ~0.5% for the immobilized nanorods submerged in water. Above 30°, the recovered angle $\phi$ is satisfactory, with a standard deviation less than 1.0° between 30°~80°. Below 30°, the signal becomes too weak due to the $\sin^4\phi$ relationship.

Similarly, $\phi$ can also be determined from the dark part of the DIC image:

$$\phi = \mathrm{acos}\left(\Delta I' / \Delta I'_\mathrm{max}\right)^{1/4} , \qquad \text{(A24)}$$

and the relative darkness ($\Delta I'/\Delta I'_\mathrm{max}$) of the nanorod image can be viewed as a measure of the projection of the nanorod onto the *x*-polarization direction. When the nanorod is lying in the object plane, the dark part yields the same information about $\phi$ but that it gives better signals at $\phi$ between below 60° (Supplementary Fig. 3cd). Combine Supplementary Fig. 3a and 3c to give Supplementary Fig. 3e, which demonstrates the satisfactory angle determination in nearly the entire range.

The relative error of the angle determination is undoubtedly relevant to the precision of the intensity measurement. In above discussion (Fig. 1d and Supplementary Fig. 3a-d), the precision of the intensity measurement was ~0.5% for the immobilized nanorods submerged in water. At this noise level, the standard deviation is ~1° in the range of 30-80° from the bright part using

Eq. A21 (Supplementary Fig. 3b) and 10-60° from the dark part using Eq. 24 (Supplementary Fig. 3d). Thus, using both the bright and dark parts, we can resolve the 2D orientation of immobilized nanorod with ~2° resolution in nearly the entire range (10-80°, Supplementary Fig. 3e).

When the nanorod is used to probe dynamics inside live cells, the background becomes noisier. In the current setup for live-cell imaging, an exposure time of 0.031 s was used to image both the cells and the gold nanorod probes. The relative error of the intensity measurement was found to be less than 1.5%, resulting in a standard deviation of less than 3°. Note that $\Delta I_{max}$ and $\Delta I'_{max}$ for each individual nanorod must be calibrated before the absolute orientation angles can be calculated from live-cell images. The current strategy is to follow the same nanorod for a long period of time, and the averages of the 10 brightest intensities and the 10 darkest intensities out of several thousand images are treated as $\Delta I_{max}$ and $\Delta I'_{max}$, respectively.

## 4. 3D orientation and rotation pattern of a nanorod

When the nanorod's long axis is pointing toward outside of the image plane, an additional variable - the elevation angle $\psi$- is needed to determine the 3D orientation of the nanorod. The illumination beam polarized at the $y$-direction can be decomposed in a similar way:

$$\vec{E}_0 = \vec{p}E_0 \sin\phi + \vec{s}E_0 \cos\phi\,, \qquad \text{(A25)}$$

where $p$- and $s$- directions are defined according to the projection of the nanorod on the image plane. The optical path will be longer than that of the rod lying in the image plane. For a spheroid, the new optical path is:

$$L = \sqrt{\frac{a^2 b^2}{a^2 \sin^2\psi + b^2 \cos^2\psi}}\,, \qquad \text{(A26)}$$

where $a$ and $b$ are the short axis and the long axis of the spheroid, respectively. For the $s$-component of the electric vector, it will be delayed according to the ordinary refractive index $n_o$. The phase delay of the $s$-component of the electric vector $\delta'_2$ is:

$$\frac{\delta'_2}{\delta_2} = \sqrt{\frac{b^2}{a^2 \sin^2\psi + b^2 \cos^2\psi}}\,. \qquad \text{(A27)}$$

For the $p$-component of the electric vector, the propagation velocity of the light is a function of the angle between the wave propagation direction and the optical axis of the nanorod:

$$v_p^2 = v_o^2 \sin^2\psi + v_e^2 \cos^2\psi \quad , \tag{A28}$$

where $v_o$ and $v_e$ are the velocities of the ordinary wave and the extraordinary wave, respectively. Thus, the phase delay of the *p*-component of the electric vector is:

$$\frac{\delta_1'}{\delta_1} = \frac{\left(\dfrac{n_e n_o}{\sqrt{n_e^2 \sin^2\psi + v_o^2 \cos^2\psi}} - n_m\right)\sqrt{\dfrac{b^2}{a^2 \sin^2\psi + b^2 \cos^2\psi}}}{n_e - n_m} \, . \tag{A29}$$

Two special cases: (1) When ψ= 0°, δ’$_1$ = δ$_1$, and δ’$_2$ =δ$_2$. This situation is equivalent to the nanorod in the image plane and has been considered in Theory Section 3. (2) When ψ= 90°, δ’$_1$ = δ’$_2$ =δ$_2$*b*/*a*. Under this condition, the particle is standing straight on the image plane and shows even bright and dark parts in the DIC image as an isotropic particle.

After passing through the sample plane, the two electric vector components (*p* and *s*) will be delayed to different extent due to the optical birefringence of the nanorod:

$$\vec{E}_1 = \vec{p}E_0 \sin\phi e^{-i\delta_1'} + \vec{s}E_0 \cos\phi e^{-i\delta_2'} \, , \tag{A30}$$

where δ’$_1$ and δ’$_2$ are determined from Eq. A27 and A29.

Using the similar treatment of Eq. A8-A21, we can reach Eq. A31 to characterize the relative intensity of DIC image:

$$\frac{\Delta I}{I_b} = \sin^4\phi \sin\delta_1' + \sin^2\phi \cos^2\phi (\cos\delta_1' + \sin\delta_1' - 1) \, . \tag{A31}$$

The fraction of the relative intensity to the overall maximum intensity (when the nanorod is perfectly aligned with the *y*-polarization and in the image plane) is:

$$\frac{\Delta I}{I_{\max}} = \frac{\sin^4\phi \sin\delta_1'}{\sin\delta_1} + \frac{\sin^2\phi \cos^2\phi (\cos\delta_1' + \sin\delta_1' - 1)}{\sin\delta_1} \tag{A32}$$

Taking a similar approximation as in the Theory Section 3:

$$\frac{\Delta I}{I_{\max}} = \frac{\sin^4\phi \sin\delta_1'}{\sin\delta_1} \, . \tag{A33}$$

Similarly, we can get the formula for the intensity for the dark part of the DIC image.

$$\frac{\Delta I^{'}}{I_{\max}^{'}} = \frac{\cos^4 \phi \sin \delta_1^{'}}{\sin \delta_1} . \qquad \text{(A34)}$$

In theory, when the $I_{max}$ and $I'_{max}$ for each nanorod are properly calibrated, we are able to determine the 3D orientation angles □ and ψ from each DIC image of the nanorod. Thus, we can track the nanorod movement in five dimensions (5D): three spatial coordinates and two orientation angles.

In practice, the current instruments only provide enough signal-to-noise ratios for accurate determination of 3D orientation angles within a limited range. In the present work, we demonstrate that the characteristic rotational motions of the nanorod can be identified from a series of DIC images even though the exact orientation of the nanorod at a given moment cannot be determined accurately.

# CHAPTER 5. ROTATIONAL MOTIONS OF ENDOCYTIC CARGOS

## Abstract

Single-particle tracking (SPT) is a powerful approach to probe biological processes at individual molecule level in live cells. However, conventional SPT techniques are still having difficulties in reporting the orientation and rotation motions of the probe thus the target molecules of interest. Here, we present an integrated imaging platform based on the combination of birefrigent gold nanorod probes and Differential Interference Contrast (DIC) Microscopy that can achieve single particle orientation and rotation tracking (SPORT). This new technique allows us to resolve translational and rotation motions of gold nanorod probes at each stage throughout the whole endocytosis processes, leading to the disclosure of their binding status on cell membrane and characteristic rotational motions generated by protein modules during the endocytosis.

## Introduction

Cell can be conceived as a highly interconnected network where numerous hierarchic nanomachines interact with biochemical compounds, cellular organelles and each other to carry out all kinds of biological functions. There is an imperative need for new techniques to investigate the composition, dynamics, and working mechanism of the nanomachines from both the fundamental biological sciences and the health and medicine sectors. Understanding the characteristic translational and rotational motions is crucial to elucidate their working mechanisms because most of these nanomachines undergo motions that are essential to their functions.

A variety of single molecule/particle tracking methods can resolve translational motions to a few nanometers with millisecond temporal resolution[1-7]. These techniques have been demonstrated to be useful in live-cell studies. However, detecting rotational motions in live cells is still challenging. Through the development of new techniques and carful design of the experiments, researchers are able to track rotational motions of nano-objects in *in vitro* studies. For example, single-molecule fluorescence polarization is frequently used to acquire orientation information of a target molecule[8-11]; however, its usefulness in live cells is limited by high cellular auto-fluorescence background and bleaching propensity of single fluorophores. Rotational motions can also be resolved by tracking the 3D translational motion of a large probe with high precision[12-15]; however, the translation tracking-based methods require specific geometries of the studied system, e.g., fixed rotation center or axis, thus are also not suitable for live-cell imaging.

To overcome these limitations, we recently developed an integrated single particle orientation and rotation tracking (SPORT) platform that allows us to resolve not only translational but also rotational motions of nanoprobes inside live cells[16]. This technique takes advantage of the plasmon resonance-associated birefringence of gold nanorods[17-20] and Nomarski-type DIC microscopy[21, 22], which utilizes *two orthogonally polarized* beams for illumination. DIC images are generated by the interference of the two mutually shifted intermediate images. Optically *anisotropic* nanoparticles show as diffraction limited spots with bright and dark peaks on a gray background in DIC images (**Fig. 1**), and the relative bright and dark intensities are *independent* measures of the effective projections of the nanorods onto the two polarization axes. Thus, we are able to resolve the 3D orientation of gold nanorod (the elevation angle and the azimuth angle as defined in **Fig. 2a**) in each DIC image[16]. In practice, the accuracy and precision of the calculated nanorod orientation in 3D is directly related to the signal-to-noise ratio of the bright/dark intensities, which declines when the projection of the nanorod approaches either of the polarization directions. However, it is important to note that in a continuous orientation tracking experiment, identifying the nanorod's rotation patterns from the dynamic rotation context is possible as the rotating nanorod goes through positions that can be resolved with either high or low confidence alternatively.

## Experimental

**DIC and fluorescence microscopy.** An upright Nikon Eclipse 80i microscope equipped with a heating stage was used in this study. When the microscope is operated in DIC mode, a set of 2 Nomarski prisms, 2 polarizers and a quarter-wave plate were installed. The samples were illuminated through an oil immersion condenser (numerical aperture 1.40) and the optical signals were collected with a 100× Plan Apo/1.40 oil immersion objective. In collecting DIC spectra, a set of 25 filters with central wavelengths in the range of 400-780 nm and a full width at half maximum (FWHM) of 10 nm were used. The optical filters were obtained from Thorlabs (Newton, NJ) or Semrock (Rochester, NY). The DIC images at a selected wavelength were collected by inserting the corresponding bandpass filter into the light path in the microscope. In collecting images of individual immobilized gold nanorods, a Photometrics CoolSnap ES CCD camera (1392×1040 imaging array, 6.45×6.45-μm pixel size) was used.

When the microscope is operated in epi-fluorescence mode, the sample was excited by a mercury lamp. In dynamic tracking individual endocytosis events, the microscope needs to be toggled between DIC mode and fluorescence mode. This was achieved by installing proper optical filters on the modular filter wheel of the Nikon microscope. Two shutters were used to select the illumination of the sample and the optical filter wheel was rotated manually to select DIC or fluorescence imaging mode. In recording the dynamics of individual endocytosis events, an Andor iXon$^{EM}$+ camera or a Photometrics Evolve camera (512×512 imaging array, 16×16-μm pixel size) was used at 32 frames per second (fps) when using full image size or 200fps when choosing small region of interest. A rotary motor from Sigma Koki (model no. SGSP-60YAM) was coupled to the microscope stage to control the *z*-position of the sample. MATLAB and NIH ImageJ were used to analyze the collected images and videos.

**Preparation of surface-modified gold nanorods for cell experiments.** Cetyl trimethylammonium bromide (CTAB)-capped (25×73 nm, $1.3\times10^{11}$ particles/mL) gold nanorods were obtained from Nanopartz (Salt Lake City, UT). The size distribution and geometric profile were evaluated with transmission electron microscopy (**Supplementary Fig. 1a**) and agreed well with the manufacturer's data. The absorption spectrum of the particles in bulk solution (**Supplementary Fig. 1b**) was measured with a Cary 300 UV-VIS spectrophotometer (Varian, Palo Alto, CA).

To functionalize the surface of gold nanorods with transferrin (Sigma-Aldrich), a NHS-PEG disulfide linker (Sigma-Aldrich) was used by following a published protocol.[1] The NHS-PEG disulfide linker has both disulfide and succinimidyl functionalities for respective chemisorption onto gold and facile covalent coupling of transferring or other proteins. Briefly, excessive surfactant was first removed from 1.0 mL gold nanorod solution by centrifugation at 3000 g for 10 minutes and the particles were resuspended in 1.0 mL 2 mM borate buffer. A proper amount of fresh NHS-PEG disulfide solution (in dimethyl sulfoxide) was added to reach a final thiol concentration of 0.2 mM and reacted with gold nanorods for 2 hours. The solution was then cleaned up by centrifugation and resuspended in 2 mM borate buffer. For transferrin-modified gold nanorods, 20 µg transferrin was added to the gold colloidal solution and reacted for 8 hours. The gold nanorods were then blocked by adding 100 mL 10% BSA solution (2 mM borate buffer) for over 8 hours. Before use, the colloidal gold nanorod probes were cleaned up by centrifugation and resuspended in 500 µL 1% BSA (2 mM borate buffer). The concentrated gold colloidal solution was diluted in cell culture medium to a final concentration of $4.3\times10^{9}$ particles/mL for incubation with cells.

**Imaging of immobilized gold nanorods.** The purchased gold nanorod solution was diluted with 18.2-MΩ pure water to a proper concentration and sonicated for 15 min at room temperature. 6 µL of the diluted solution was added onto a freshly cleaned glass slide and covered with a 22×22 mm No.1.5 coverslip (Corning, NY). The positively charged gold nanorods were immobilized on the negatively charged surface of the glass slide by electrostatic forces. The glass slide was then placed on a 360°-rotating mirror holder affixed onto the microscope stage. By rotating the mirror holder 5° or 10° per step, the nanorods were positioned in different orientations, and their DIC images under 540 or 720 nm illumination were taken with the Photometrics CoolSnap ES CCD camera. The exposure time was adjusted to maintain the same background intensity at different wavelengths.

**Cell culture.** Human lung cancer cell line was purchased from American Type Culture Collection (ATCC, Manassas, VA; catalog number: CCL-185). The cells were plated in a T25 cell culture flask (Corning) and grown in cell culture medium supplemented with 10% fetal bovine serum (FBS). When subculturing, 150 μL of cell suspension solution was transferred to a 22×22 mm poly-L-lysine (PLL)-coated coverslip, housed in a 35-mm Petri dish (Corning). The Petri dish was left in a cell culture incubator (37°C, 5% CO2) for 1 hour to let the cells attach to the coverslip. After 1.5 mL of the cell culture medium with 10% FBS supplement was added to immerse the coverslip, the Petri dish was left again in the incubator for 24 hours. For the hypertonic treatment, the cells were preincubated for 30 min in the cell culture medium and supplemented with 0.45 M sucrose before exposure to the surface-modified gold nanorods.

**Transfection of cell to express Clathrin-LCa-EYFP.** E. Coli bacteria with clathrin-LCa-EYFP plasmid were provided by Professor Zhuang Xiaowei through Addgene (Plasmid 21741, Cambridge, MA)[2]. The plasmid was extracted from the bacteria by using plasmid extraction kit (cat. 27104) and the corresponding protocol from QIAGEN (Valencia, CA). The human lung cancer cells were grown on coverslip in a petridish for 24 hours in cell culture incubator (37℃, 5% $CO_2$). Then the EYFP-clathrin plasmid was mixed with the transfection reagent (Fugene 6, Roche Applied Science, Indianapolis, IN) in serum free cell culture media first. Later the mixture solution was introduced into the petridish containing the cells. After additional 24 to 48 hours in the incubator, the cells were ready to use.

**Live-cell imaging of endocytosis.** The microscope stage was pre-heated to 37°C if desired. Two pieces of double-sided tape served as spacers on top of a pre-cleaned glass slide. A coverslip with cells was placed carefully on top of the tapes to form a chamber, with the cell side facing the glass slide. 20 μL of the surface-modified gold nanorod solution ($4.3\times10^9$ particles/mL) were added to the chamber. The two open sides of the chamber were sealed by nail polish to prevent evaporation. The observation started immediately using the Andor camera at 32 fps or 200 fps. The endocytic events were followed within two hours of the slide preparation.

## Results and Discussion

To help correlate recorded DIC intensity traces with real nanorod rotational motions, computer simulation was employed to generate the DIC intensity changing patterns as the nanorod rotates in the 3D space. There are two most fundamental rotation modes: the in-plane rotation in which the rotation axis is perpendicular to the object plane and the nanorod rotates within the plane, and the out-of-plane rotation in which the rotation axis is in the object plane and the nanorod swings out of the plane. Any other rotation motion with a fixed axis can be decomposed into these two fundamental modes. The simulated intensities show distinctive changing patterns for these two modes (**Fig. 2bc**): the anti-correlated changes of the bright and dark intensities for the in-plane rotation mode, where the bright intensity increases as the dark intensity decreases; and the correlated intensity changes for the out-of-plane rotation mode, where the bright and dark intensities increase/decrease at the same time. When the rotation axis is aligned with one of the illumination polarization directions (**Fig. 2de**), only the bright or dark intensity changes. In reality, a nanorod can show complicated rotational motions as the rotation axis changes its direction continuously due to Brownian motion. These simulated DIC intensity changing patterns help us identify simple rotations from real DIC intensity traces in short periods of time, thus leading to possible disclosure of the restraining factors for brief moments.

We next tracked the rotational motions of gold nanorods on the cell membrane and during the subsequent endocytosis by A549 human lung cancer cells. Endocytosis is a fundamental biological process underlying many other cell activities ranging from regulation of intercellular signaling to nutrient uptake[23-29]. Among various endocytic pathways, clathrin-mediated endocytosis (CME) is one of the most important routes for cell to internalize a wide range of biological compounds by engulfing them with cell membrane. Current view for CME is that many proteins are sequentially recruited and grouped into functional modules to drive endocytosis through a series of steps: coat formation, membrane invagination, actin-meshwork assembly, and vesicle scission[30-33]. Despite extensive work mentioned above, there are still controversies concerning how these functional protein modules cooperate to accomplish their functions. For example, dynamin assembly is believed to provide a mechanochemical function for fission in the last step of endocytosis[34]. Different models have been proposed to explain how dynamin breaks the neck of the clathrin-coated pit (CCP): constriction[35], expansion[36], twisting[37], and stochastic cycling[38, 39]. Herein we provide new *live-cell* observations on the translational and rotational motions of gold nanorod cargos during the complete endocytosis processes.

To facilitate cellular uptake, the nanorods were conjugated with transferrin[40] through PEG linker molecules. Recent studies show that CME plays a key role in cellular uptake of transferrin-coated gold nanospheres and nanorods of ~50 nm in size[41]. In the present study, we visualized the dynamic internalization of transferrin-coated gold nanorods by transfected A549 cells that expressed enhanced yellow fluorescent protein (EYFP) tagged clathrin. The co-localization of gold nanorods and the fluorescence from EYFP-clathrin gives direct evidence that CME is involved in the internalization of transferrin-coated gold nanorods with a size of 25×73 nm. **Fig. 3** shows such a case where 3 out of 8 transferrin-coated gold nanorods binding to the membrane of a transfected A549 cell display co-localized EYFP fluorescence after a 30-min incubation in the colloidal nanorod solution. In addition, we observed that the internalization of transferrin-coated gold nanorods is strongly dependent on the ambient temperature and osmotic pressure. After a long incubation at 4°C, a significant amount of gold nanorods were observed binding to the cell membrane, but not being endocytosed. Then the temperature was raised to 37°C, and over half of the nanorods initially spotted on the cell membrane were internalized within the first two hours. In another control experiment, when the cells were treated with a hypertonic media (sucrose) at 37°C, significant decreases in the uptake of the nanorods within the first two hours were observed, compared to the nanorod uptake by the cells not treated with the hypertonic media. The temperature dependence and the response to the hypertonic treatment, which disrupts the formation of clathrin-coated vesicles (CCV), are consistent with previous reports that CME is the key pathway for the cellular uptake of nanometer-sized particles[41-43].

We followed the dynamic uptake of each nanorod continuously from its abrupt appearance on the cell membrane until the nanorod was linearly transported over long distances – convincing evidence of the nanorod being inside the cell. Unlike conventional single-particle tracking probes, gold nanorod probes disclose not only translational but also rotational motions on the cell surface, giving flickering images for easy probe identification. More importantly, the nanorods display characteristic rotational motions at different endocytic stages. **Fig. 4** shows such an example of a complete process of nanorod endocytosis by an A549 cell.

The motions of nanorod at the early stage of binding were characterized by active lateral diffusion in a relatively large area on the cell membrane (e.g., **Fig. 4a-c**) and fast and random rotation as revealed by the DIC intensity changing patterns. For example, during the framed period (472.7 – 473.2 s) in **Fig. 4c**, the nanorod likely rotated around one of the polarization direction in an out-of-plane rotation mode (similar to the simulated case in **Fig. 2d**) while its DIC image changed quickly from completely bright to gray and then to completely bright again, without going through a completely dark state.

The nanorod gradually lost its translational and rotational freedoms on the cell membrane. The lateral movement quickly became restrained and came to a complete stop at 497.9 s. The rotational motion also became much slower, giving much less frequent fluctuations in the DIC intensities (**Fig. 4d**). From the DIC intensities, we can identify that a component of in-plane rotation mode became more pronounced. For example, from 500.4 to 501.1 s in **Fig. 4d**, the nanorod's DIC intensities changed in an anti-correlation manner from completely dark to completely bright and then to completely dark again, showing a typical in-plane rotation mode. The gradual loss of translational and rotational freedoms and the increase of the in-plane rotation component were an indication of the assembling of the endocytic machinery around the gold nanorod. This is also supported by the fluorescence observation: at 531.4 s, a clathrin coat has already been assembled around the gold nanorod (**Fig. 4e**), suggesting that the nanorod was on the way to be enveloped by a CCP which limited the nanorod from rotating out of the membrane plane.

For all nanorods that were eventually internalized, their rotational motions ceased at a certain point of time, an indication that the nanorods were completely locked up by receptors and other assisting proteins on the membrane, or enclosed by CCPs. The nanorods then all experienced a quiet period of several tens of seconds, during which the nanorod showed little or no rotation. Finally, the nanorods *abruptly* regained rotational and translational freedoms, indicating that the vesicles were detached from the cell membrane. In **Fig. 4f**, the detachment of this nanorod-containing vesicle occurred at 553.7 s. The nanorod's DIC image changed rapidly from dark to bright at the first moment, likely due to its sudden release from restraining forces, as well as random rotational diffusion. The translational motion followed almost immediately, showing a slow drifting away from the original entry spot. At 570.2 s (16.5 s after the detachment event), we observed that the clathrin coat already disassembled from the vesicle. This nanorod-containing vesicle was continuously followed until it was actively transported inside the cell at 599.4 s.

These findings disclose characteristic rotational motions of nanorod cargos at different endocytic stages (**Fig. 5**): translation and rotation, rotation at a fixed spot, little or no rotation during the quiet period, and re-rotation with diffusion and transportation. Combining with dynamic clathrin aggregation observed in fluorescence mode, this rotation-based model not only supports the current endocytosis models derived from the spatial and temporal organization of modular protein molecule groups[23, 32, 44, 45], but also provides new insights in the understanding of endocytosis progression.

The SPORT platform reveals for the first time that the loss of translational freedom of a cargo does not coincide with the loss of rotational freedom during the early stage of endocytosis. The fluorescence observations show clear evidence that clathrin molecules aggregate after the cargo's translation has already ceased. The rotational motion of the nanorod cargo slows down gradually, which is in line with the view that the coat formation is a gradual process, and finally comes to a complete stop, which is likely caused by either the sequentially recruited receptors/assisting proteins firmly attach the whole nanorod onto the cell membrane, or the cell membrane fully wraps around the nanorod to form a CCP, or both. Depending on the cargo's motion status, the SPORT platform provides a new approach to study the functions of different assisting proteins and how different coatings facilitate or inhibit endocytosis.

Our most important discovery is that before a nanorod cargo is endocytosed, it *always* experiences a "*quiet*" period during which the nanorod is poised without active translational and rotational motions. The nanorod then abruptly regains both rotational and translational freedoms. In the current models, endocytosis can be viewed as a series of distinct sub-steps completed by groups of interacting proteins[46]. During invagination, the CCP moves slowly toward the inside of the cell body under multiple protein modules that are involved in accelerating actin-filament assembly and stabilizing new filaments. The vesicle scission module (dynamin proteins) then assembles around the neck of the CCP and cut it off the membrane. This whole process was reported to have an average time of ~40 s[47]. In the present study, 20 complete endocytosis events were recorded, and the average "quiet" time was 59.8 s (ranging from 17.2 to 102 s), starting from the nanorod losing rotational freedom to re-rotating again. This "quiet" period clearly corresponds to the invagination of the CCP, or at least overlaps with the invagination process from the scission point retrograde. Moreover, it was reported that dynamin assembling lasts ~20 s and peaks just before the scission point[47]. Our observation shows that there is little or no rotational motion of the nanorod cargo in this period, indicating dynamin assembling does *not* introduce continuous rotational motion on the membrane pits. This observation implies that the dynamin-induced stretching force[48] is the main contributor for breaking the vesicle neck in live cells.

Finally, the SPORT platform can easily capture the scission point when the gold nanorod-containing vesicle restores active rotation and immediately followed by active transportation. The exact timing of scission is usually difficult to determine with other single-particle/molecule imaging techniques[49]. For example, using a combination of total-internal reflection and epi-fluorescence fluorescence microscopies, the small inward movement of a clathrin-coated pits at the late stage of endocytosis can be monitored dynamically[50]. However, it is often unclear whether the inward movement is caused by free diffusion of nascent endocytic vesicles or invagination of receptor-coated pits driven by the endocytic machinery[51]. Therefore, a pH sensitive dye-tagged cargo together with a buffer-exchange system were employed to probe the accessibility of the interior of the vesicle to the extracellular buffer thus the timing of scission, at the expense of a reduced temporal resolution in the time scale of seconds[47]. With gold nanorods as reporters, it becomes simple to resolve the moment of scission in the time scale of tens of milliseconds as the gold nanorods regain abrupt rotational and translational freedoms, evidenced by the moving and flickering DIC images of the nanorods.

## Conclusion

In summary, we demonstrated single particle orientation and rotation tracking in live cells with the combination of DIC microscopy and rod-shaped gold nanoprobes. The characteristic translational and rotational motions of the gold nanorod cargos were resolved in detail at each stage throughout the whole internalization process, shedding new light toward revealing functions of protein nanomachines. Due to the non-bleaching nature of gold nanoparticle probes, the observation time can be extended much longer than fluorescence-based techniques. Combined with super-localization techniques, especially in the z-direction, this method can potentially be developed into a high-precision 5D (three spatial coordinates and two orientation angles) tracking technique. Working mechanisms of various cellular nanomachines may be resolved with the SPORT platform.

## References

(1) Kusumi, A.; Nakada, C.; Ritchie, K.; Murase, K.; Suzuki, K.; Murakoshi, H.; Kasai, R. S.; Kondo, J.; Fujiwara, T. *Annual Review of Biophysics and Biomolecular Structure* **2005**, *34*, 351-U354.

(2) Thompson, R. E.; Larson, D. R.; Webb, W. W. *Biophysical Journal* **2002**, *82*, 2775-2783.

(3) Saxton, M. J.; Jacobson, K. *Annual Review of Biophysics and Biomolecular Structure* **1997**, *26*, 373-399.

(4) Joo, C.; Balci, H.; Ishitsuka, Y.; Buranachai, C.; Ha, T. *Annual Review of Biochemistry* **2008**, *77*, 51-76.

(5) Toprak, E.; Balci, H.; Blehm, B. H.; Selvin, P. R. *Nano Letters* **2007**, *7*, 2043-2045.

(6) Jaqaman, K.; Loerke, D.; Mettlen, M.; Kuwata, H.; Grinstein, S.; Schmid, S. L.; Danuser, G. *Nature Methods* **2008**, *5*, 695-702.

(7) Katayama, Y.; Burkacky, O.; Meyer, M.; Brauchle, C.; Gratton, E.; Lamb, D. C. *Chemphyschem* **2009**, *10*, 2458-2464.

(8) Sase, I.; Miyata, H.; Ishiwata, S.; Kinosita, K. *Proceedings of the National Academy of Sciences of the United States of America* **1997**, *94*, 5646-5650.

(9) Forkey, J. N.; Quinlan, M. E.; Shaw, M. A.; Corrie, J. E. T.; Goldman, Y. E. *Nature* **2003**, *422*, 399-404.

(10) Toprak, E.; Enderlein, J.; Syed, S.; McKinney, S. A.; Petschek, R. G.; Ha, T.; Goldman, Y. E.; Selvin, P. R. *Proceedings of the National Academy of Sciences of the United States of America* **2006**, *103*, 6495-6499.

(11) Xiao, L. H.; Qiao, Y. X.; He, Y.; Yeung, E. S. *Analytical Chemistry* **2010**, *82*, 5268-5274.

(12) Yasuda, R.; Noji, H.; Kinosita, K.; Yoshida, M. *Cell* **1998**, *93*, 1117-1124.

(13) Itoh, H.; Takahashi, A.; Adachi, K.; Noji, H.; Yasuda, R.; Yoshida, M.; Kinosita, K. *Nature* **2004**, *427*, 465-468.

(14) Adachi, K.; Oiwa, K.; Nishizaka, T.; Furuike, S.; Noji, H.; Itoh, H.; Yoshida, M.; Kinosita, K. *Cell* **2007**, *130*, 309-321.

(15) Nitzsche, B.; Ruhnow, F.; Diez, S. *Nature Nanotechnology* **2008**, *3*, 552-556.

(16) Wang, G. F.; Sun, W.; Luo, Y.; Fang, N. *J. Am. Chem. Soc.*, Submitted on 7/19/2010.

(17) Gans, R. *Annalen Der Physik* **1915**, *47*, 270-284.

(18) Sonnichsen, C.; Alivisatos, A. P. *Nano Letters* **2005**, *5*, 301-304.

(19) Spetzler, D.; York, J.; Daniel, D.; Fromme, R.; Lowry, D.; Frasch, W. *Biochemistry* **2006**, *45*, 3117-3124.

(20) Chang, W. S.; Ha, J. W.; Slaughter, L. S.; Link, S. *Proceedings of the National Academy of Sciences of the United States of America* **2010**, *107*, 2781-2786.

(21) Sun, W.; Wang, G. F.; Fang, N.; Yeung, E. S. *Analytical Chemistry* **2009**, *81*, 9203-9208.

(22) Pluta, M. *Advanced Light Microscopy Vol. 2. Specialized Methods*; Elsevier, New York: New York, 1989.

(23) Doherty, G. J.; McMahon, H. T. *Annual Review of Biochemistry* **2009**, *78*, 857-902.

(24) Maldonado-Báez, L.; Wendland, B. *Trends in Cell Biology* **2006**, *16*, 505-513.

(25) Miaczynska, M.; Pelkmans, L.; Zerial, M. *Current Opinion in Cell Biology* **2004**, *16*, 400-406.

(26) D'Hondt, K.; Heese-Peck, A.; Riezman, H. *Annual Review of Genetics* **2000**, *34*, 255-295.

(27) Mellman, I. *Annual Review of Cell and Developmental Biology* **1996**, *12*, 575-625.

(28) Le Roy, C.; Wrana, J. L. *Nature Reviews Molecular Cell Biology* **2005**, *6*, 112-126.

(29) Walther, T. C.; Brickner, J. H.; Aguilar, P. S.; Bernales, S.; Pantoja, C.; Walter, P. *Nature* **2006**, *439*, 998-1003.

(30) Yarar, D.; Waterman-Storer, C. M.; Schmid, S. L. *Molecular Biology of the Cell* **2004**, *16*, 964-975.

(31) Roth, M. G. *Nature Reviews Molecular Cell Biology* **2006**, *7*, 63-68.

(32) Kaksonen, M.; Toret, C. P.; Drubin, D. G. *Cell* **2005**, *123*, 305-320.

(33) Ayscough, K. R. *Cell* **2005**, *123*, 188-190.

(34) Praefcke, G. J. K.; McMahon, H. T. *Nature Reviews Molecular Cell Biology* **2004**, *5*, 133-147.

(35) Sweitzer, S. M.; Hinshaw, J. E. *Cell* **1998**, *93*, 1021-1029.

(36) Stowell, M. H. B.; Marks, B.; Wigge, P.; McMahon, H. T. *Nature Cell Biology* **1999**, *1*, 27-32.

(37) Roux, A.; Uyhazi, K.; Frost, A.; De Camilli, P. *Nature* **2006**, *441*, 528-531.

(38) Pucadyil, T. J.; Schmid, S. L. *Cell* **2008**, *135*, 1263-1275.

(39) Bashkirov, P. V.; Akimov, S. A.; Evseev, A. I.; Schmid, S. L.; Zimmerberg, J.; Frolov, V. A. *Cell* **2008**, *135*, 1276-1286.

(40) Qian, Z. M.; Li, H. Y.; Sun, H. Z.; Ho, K. *Pharmacological Reviews* **2002**, *54*, 561-587.

(41) Chithrani, B. D.; Chan, W. C. W. *Nano Letters* **2007**, *7*, 1542-1550.

(42) Daukas, G.; Zigmond, S. H. *Journal of Cell Biology* **1985**, *101*, 1673-1679.

(43) Kam, N. W. S.; Liu, Z. A.; Dai, H. J. *Angewandte Chemie-International Edition* **2006**, *45*, 577-581.

(44) Conner, S. D.; Schmid, S. L. *Nature* **2003**, *422*, 37-44.

(45) Robertson, A. S.; Smythe, E.; Ayscough, K. R. *Cellular and Molecular Life Sciences* **2009**, *66*, 2049-2065.

(46) Schmid, E. M.; McMahon, H. T. *Nature* **2007**, *448*, 883-888.

(47) Merrifield, C. J.; Perrais, D.; Zenisek, D. *Cell* **2005**, *121*, 593-606.

(48) Marks, B.; Stowell, M. H. B.; Vallis, Y.; Mills, I. G.; Gibson, A.; Hopkins, C. R.; McMahon, H. T. *Nature* **2001**, *410*, 231-235.

(49) Schmid, S. L.; Smythe, E. *Journal of Cell Biology* **1991**, *114*, 869-880.

(50) Merrifield, C. J.; Feldman, M. E.; Wan, L.; Almers, W. *Nature Cell Biology* **2002**, *4*, 691-698.

(51) Engqvist-Goldstein, A. E. Y.; Drubin, D. G. *Annual Review of Cell and Developmental Biology* **2003**, *19*, 287-332.

## Figure Captions

Figure 5.1. Illustration to show the image formation of an optically birefringence nanoparticle under a DIC microscope.

Figure 5.2. Computer simulated DIC intensity changing patterns of a gold nanorod. (**a**) Definitions of the elevation angle □ and the azimuth angle □̃ (**b**) In-plane rotation mode. (**c**) Out-of-plane rotation mode in a vertical plane $45^{o}$ to both *x*- and *y*-polarization directions. (**d**) Out-of-plane rotation mode in a vertical plane with an azimuth angle of $90^{o}$. (**e**) Out-of-plane rotation mode in a vertical plane with an azimuth angle of $0^{o}$.

Figure 5.3. Co-localization of the gold nanorods and EYFP-clathrin-coated pits on a transfected A549 cell membrane. (**a**) DIC image, (**b**) fluorescence image, (**c**) overlapped DIC and fluorescence image, and (**d**) expanded images of the framed areas in (c). The three nanorods co-localized with fluorescent clathrin coats were labeled with red arrows and the other five nanorods without co-localized fluorescence were labeled with orange arrows. Considering that coating of clathrin on endocytic pits is a transient process, this observation suggests that clathrin-mediated endocytosis is a key pathway for the internalization of transferrin-coated gold nanorods. The integration time was 310 ms for the fluorescence image and 31 ms for the DIC image.

Figure 5.4. A complete CME event of a gold nanorod by an A549 cell. Time 0 is set to the moment when the nanorod first appeared on the membrane. (**a**) The cell and the location of the gold nanorod probe on the cell membrane. The nanorod was beside a cell feature that showed a constant contrast throughout the recording. (**b**) The trace of the nanorod’s active translational movement at an early binding stage. (**c**) DIC intensities of the nanorod in the same period as (b). The framed period shows typical out-of-plane rotations. (**d**) DIC intensities of the nanorod at a late stage. The framed period shows typical in-plane rotations. (**e**) Sequential DIC and fluorescence images captured in tandem showing that the gold nanorod co-localized with a CCP. The movie was acquired at 32 frames per second continuously and the displayed fluorescence images were the average of 10 consecutive images from the movie. (**f**) DIC intensities of the

nanorod before and after scission of the nanorod-containing vesicle. The nanorod lost active rotation at 536.5 s and regained rotational and translational freedoms at 553.7 s. The same particle was observed to lose co-localization of fluorescence from EYFP-clathrin, indicating the clathrin disassembly.

Figure 5.5. Rotational and translational motions of a nanorod cargo during endocytosis and presumed correlation with current modular endocytosis models.

# Figures

Figure 5.1

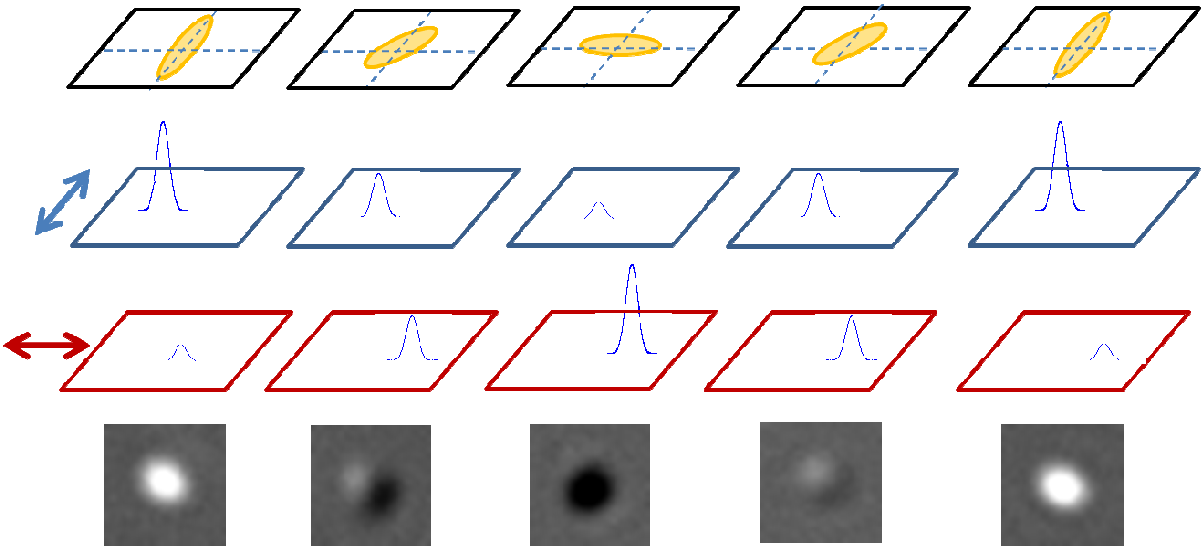

Figure 5.2

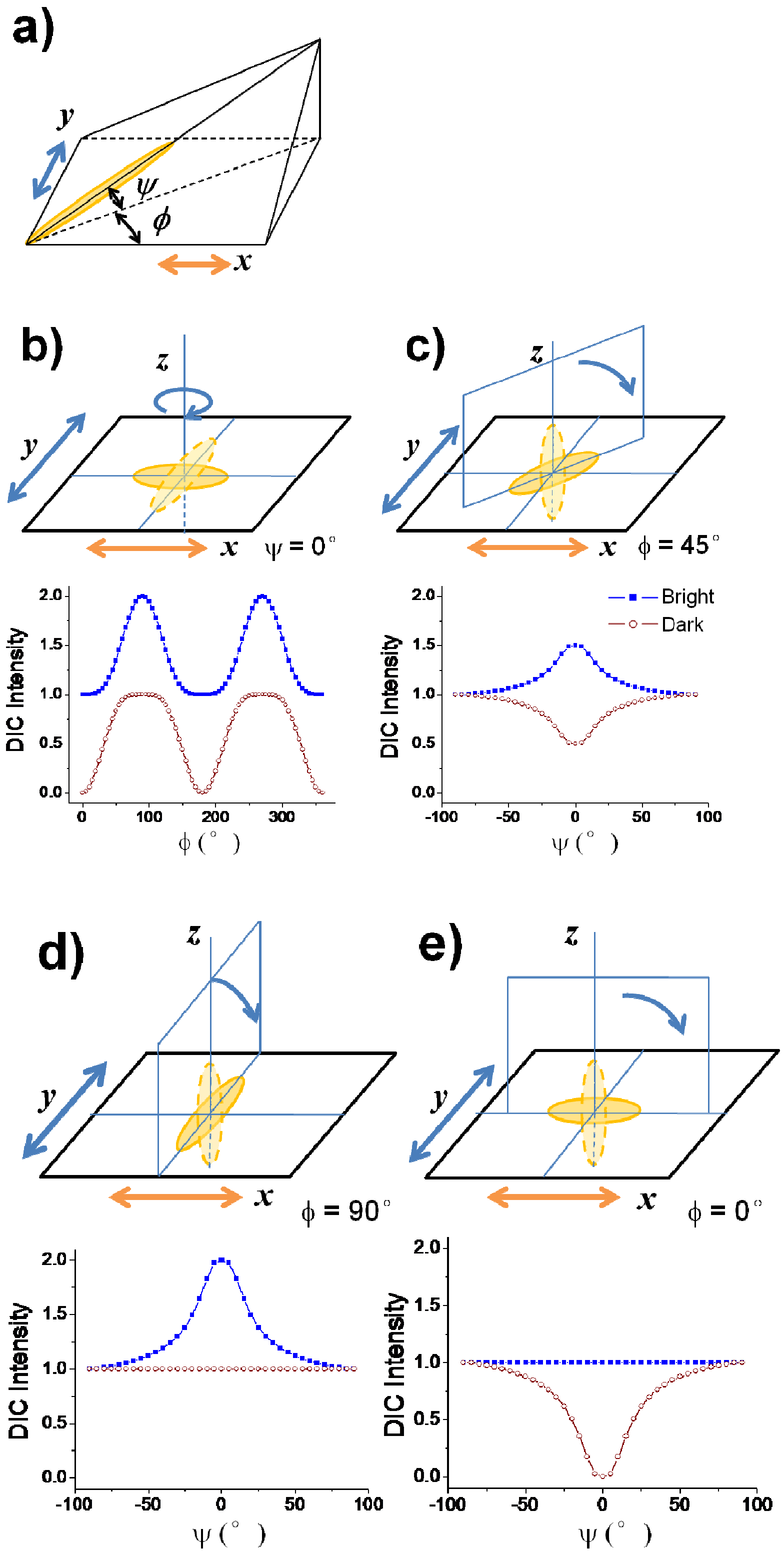
a)
y
ψ
φ
x
b)
z
y
x
ψ = 0°
c)
z
y
x
ϕ = 45°
DIC Intensity
2.0
1.5
1.0
0.5
0.0
0
100
200
300
ϕ (°)
Bright
Dark
-100
-50
0
50
100
ψ (°)
d)
z
y
x
ϕ = 90°
e)
z
y
x
ϕ = 0°

Figure 5.3

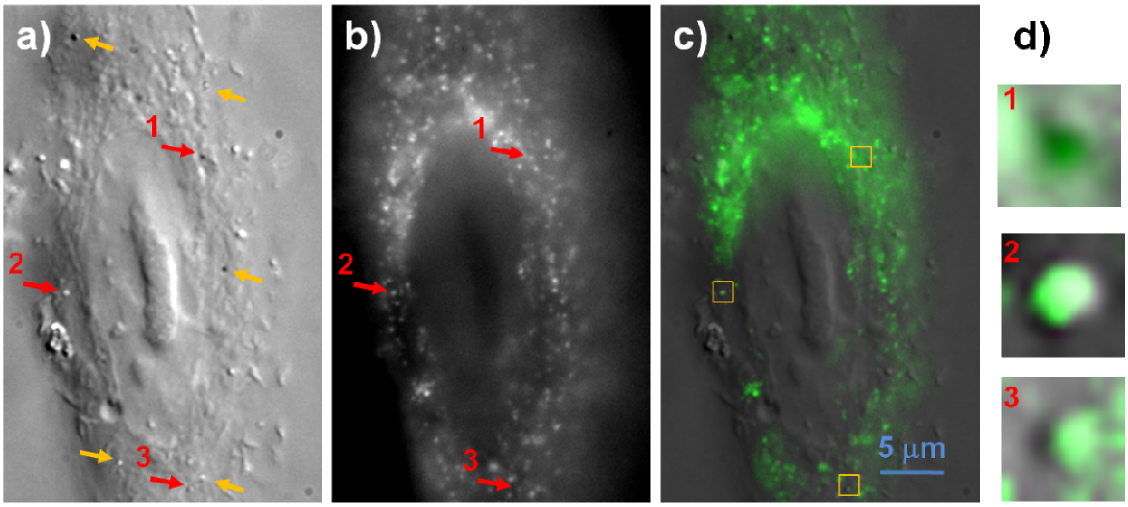

Figure 5.4

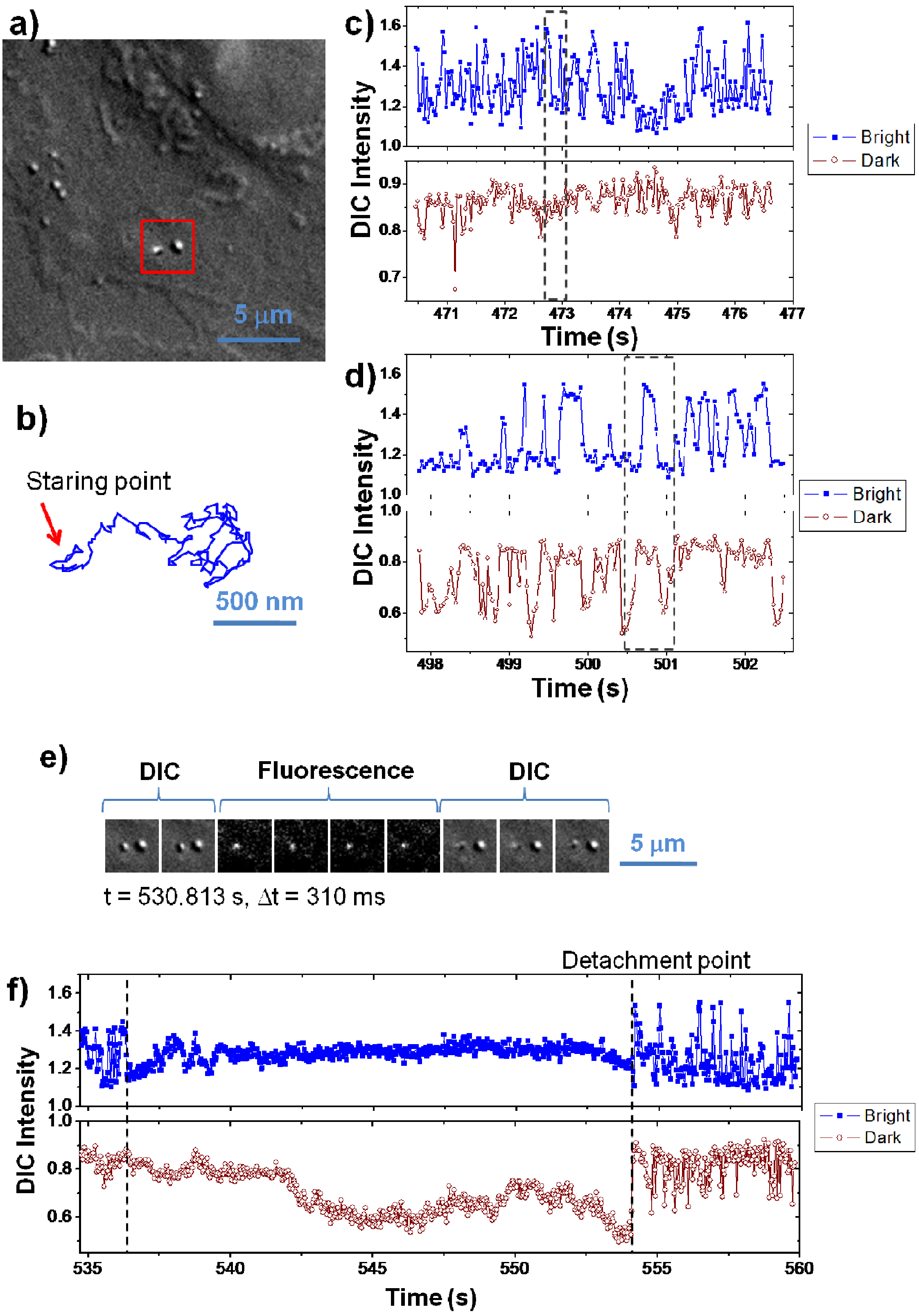
a)
5 μm
b)
Staring point
500 nm
c)
DIC Intensity
1.6
1.4
1.2
1.0
0.9
0.8
0.7
471
472
473
474
475
476
477
Time (s)
Bright
Dark
d)
1.6
1.4
1.2
1.0
1.0
0.8
0.6
DIC Intensity
498
499
500
501
502
Time (s)
Bright
Dark
e)
DIC
Fluorescence
DIC
5 μm
t = 530.813 s, Δt = 310 ms
f)
Detachment point
1.6
1.4
1.2
1.0
1.0
0.8
0.6
DIC Intensity
535
540
545
550
555
560
Time (s)
Bright
Dark

Figure 5.5

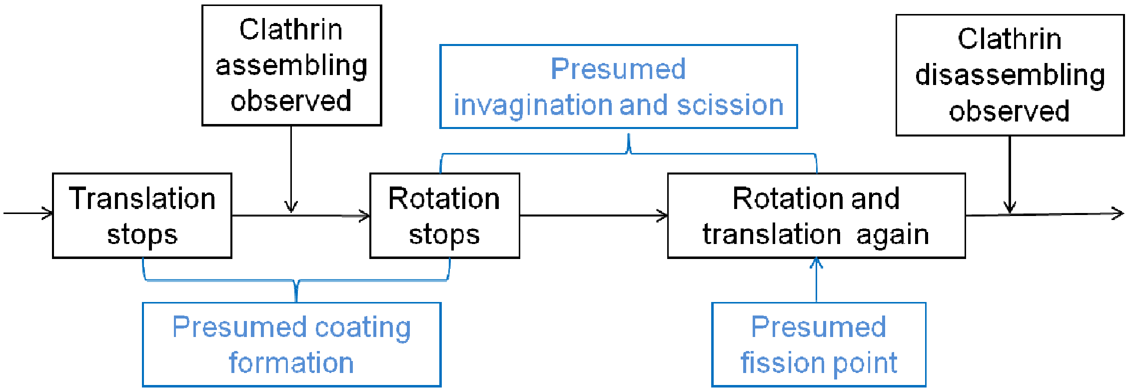

Scheme 1

# CHAPTER 6. DYNAMIC ORIENTATION OF NANO-CARGOS DURING MICROTUBULE-BASED INTRACELLULAR TRANSPORT

## Abstract

We demonstrated that by using gold nanorod probes and DIC microscope, dynamic orientation of nanometer-sized cargos during microtubule-based intracellular transport can be resolved at video rates. The vesicles containing cargos tend to have a train-like movement, with a fixed vesicle-to-microtubule orientation in the transport. Especially, the vesicles' orientation shows little change during transition points, after which the vesicle continues to move forward or reverse transport direction. This indicates that the orientation of the cargo-containing vesicle is tightly controlled at temporary stops during transport. These new observations may help to understand resolved questions in intracellular transport such as whether motor molecules with different directionalities work in coordination or fight a "tug of war".

## Introduction

Microtubules are one component of the cytoskeleton network within the cytoplasm of mammalian cells.[1] They not only maintain a cell's shape, but also sustain specific cellular functions through serving as moving tracks in intracellular transport.[2-3] For example, in neuron cells, specialized proteins manufactured for signaling processes are transported from cell bodies towards axon tips, while endocytic vesicles at axon tips move towards cell bodies through retrograde transport.[4] These transport processes are accomplished by kinesin and dynein motor proteins through converting chemical energy from hydrolysis of adenosine triphosphate (ATP) into mechanical work. Kinesin and dynein motor proteins transport cargos in opposite directions to different destinations by "walking" on the intracellular microtubule network.[4] The dysfunction of intracellular transport may cause serious diseases, such as neurodegenerative Alzheimer's disease.[5]

The complete understanding of the working mechanisms of microtubule-associated motor proteins is imperative in order to realize the ultimate goal of the applications of intracellular transport in human health and medicines. This involves resolving motor proteins' motions accurately and precisely, which has spurred researchers in the fields of biology, chemistry and physics for many years. The *in vitro* transport behavior of motor proteins has been studied extensively.[6-13] For example, kinesin and dynein step on the microtubule with a predominant step size of 8 nm;[9,14-15] kinesin tracks the same protofilament of microtubule,[16-18] while dynein may step off one protofilament to neighboring protofilaments.[19] These *in vitro* models paved the way for the understanding of much more complicated *in vivo* transport, which involves multiple intracellular regulation pathways and multi-motor coordination in a single transport event.[10,20] With the fast development of imaging techniques, researchers are able to track translational motions with high precision at individual molecule/particle level in highly auto-fluorescent cell environments.[21-23] The 8 nm step-by-step movement of motor proteins became detectable in live cells.[24-25]

In contrast to translational motions, rotational motions generated by motor proteins are still largely unknown due to technical difficulties. For example, little has been known for the dynamic cargo orientation during a linear transport, or during the pauses, direction-reversing, and changing transport tracks. All of these are crucial to understand the motor-regulator or motor-motor interactions, which is currently under intensive investigation.[10,20] Single molecule polarization imaging is a potential method to probe dynamic orientation – or rotation – of the cargo in nanometer sizes. However, the autofluorescence background and high bleaching propensity make it challenging from being successfully employed in cellular environments. The orientation and rotation information can also be obtained by tracking translational motions of a relatively large particle with high precision. For example, with carefully designed experiments and recently developed techniques, e.g., microtubules with a side arm,[16,26] quantum dot-assisted fluorescence interference contrast (FLIC) microscopy,[18] and fluorescence microscopy with a wedged prism at the back-focal-plane of the objective,[17] it becomes possible to detect the self-rotation of gliding microtubules with a diameter of ~25 nm. These methods have not yet been reported in the literature to study motor proteins in live cells.

We recently introduced a new technique based on the combination of gold nanorod probes and differential interference contrast (DIC) microscopy to achieve single particle orientation and rotation tracking (SPORT). Gold nanorods, which have anisotropic refractive indices,[27-29] show bright-and-dark interference patterns in Nomarski-type DIC microscopy.[30] The bright and dark intensities are effective projections of a nanorod onto the two mutually orthogonal polarization directions of the two illumination beams used in a DIC microscope.[30-32] Thus, we were able to resolve the dynamic orientation of gold nanorod probes bound to gliding microtubules on kinesin-coated glass slides.

## Experimenatl

**Dual mode DIC/fluorescence microscopy.** An upright Nikon Eclipse 80i microscope equipped with a heating stage was used in this study. This microscope was modified that it can be operated in DIC mode, epi-fluorescence mode, or DIC/fluorescence dual-mode. When the microscope was operated in DIC mode, a set of 2 Nomarski prisms, 2 polarizers and a quarter-wave plate were installed. The samples were illuminated through an oil immersion condenser (numerical aperture 1.40) and the optical signals were collected with a 100× Plan Apo/1.40 oil immersion objective. The DIC images at a selected wavelength were collected by inserting the corresponding bandpass filter into the light path in the microscope. The optical filters were obtained from Thorlabs (Newton, NJ) or Semrock (Rochester, NY). When the Nikon microscope was operated in epi-fluorescence mode, samples were excited with a mercury lamp with proper bandpath filters applied in the excitation and emission channels. When the microscope was operated in DIC/fluorescence dual-mode, the instrument was set up as in Supplementary Figure 1. A dual-view filter cube (MAG Biosystems, Tucson, AZ) was installed at the microscope exit port to split the output image into two images at selected wavelengths: one for the DIC image and the other for the fluorescence image. The two images were then projected onto different portions of the same camera chip and collected simultaneously. An Andor iXon$^{EM}$+ camera or a Photometrics Evolve camera (512×512 imaging array, 16×16-µm pixel size) was used to record the dynamic *in vivo* and *in vitro* transport at 32 frames per second. A rotary motor from Sigma Koki (model no. SGSP-60YAM) was coupled to the microscope stage to control the *z*-position of the sample. The CCD camera and the stage were synchronized by a home-made C++ computer program. MATLAB and NIH ImageJ were used to analyze the collected images and videos.

**Preparation of surface-modified gold nanorods for cell experiments.** Neutravidin-modified gold nanorods (10×35 nm) were purchased directly from Nanopartz (Salt Lake City, UT). TAT-coated gold nanorods were modified from cetyl trimethylammonium bromide (CTAB)-capped (25×73 nm, $1.3\times10^{11}$ particles/mL, Nanopartz) gold nanorods. The size distribution and geometric profile were evaluated with transmission electron microscopy and agreed well with the manufacturer's data. To functionalize the surface of CTAB-coated gold nanorods with TAT 47-57 peptide (sequence: YGRKKRRQRRR; AnaSpec, San Jose, CA), a NHS-PEG disulfide linker (Sigma-Aldrich) was used by following a published protocol[37]. The NHS-PEG disulfide linker has both disulfide and succinimidyl functionalities for respective chemisorption onto gold and facile covalent coupling of TAT peptide. Briefly, excessive surfactant was first removed from 1.0 mL gold nanorod solution by centrifugation at 2000 g for 10 minutes and the particles were resuspended in 1.0 mL 2 mM borate buffer. A proper amount of fresh NHS-PEG disulfide solution (in dimethyl sulfoxide) was added to reach a final thiol concentration of 0.2 mM and reacted with gold nanorods for 2 hours. The solution was then cleaned up by centrifugation and resuspended in 2 mM borate buffer. For TAT modified gold nanorods, 2.0 μg TAT peptide was added to the gold colloidal solution and reacted for 8 hours. The gold nanorods were then blocked by adding 100 mL 10% BSA solution (2 mM borate buffer) for over 8 hours. Before use, the colloidal gold nanorod probes were cleaned up by centrifugation and resuspended in 500 μL 1% BSA (2 mM borate buffer). The concentrated gold colloidal solution was diluted in cell culture medium to a final concentration of $4.3\times10^9$ particles/mL for incubation with cells.

**Cell culture and intracellular transport of gold nanorods.** A549 human lung cancer cell line was purchased from American Type Culture Collection (CCL-185, ATCC, Manassas, VA). The cells were plated in a T25 cell culture flask (Corning) and grown in cell culture medium supplemented with 10% fetal bovine serum (FBS) in a cell culture incubator (37°C, 5% CO2). When subculturing, 150 μL of cell suspension solution was transferred to a 22×22 mm poly-L-lysine (PLL)-coated coverslip, housed in a 35-mm Petri dish (Corning). The Petri dish was left in the incubator for 1 hour to let the cells attach to the coverslip. After 1.5 mL of the cell culture medium with 10% FBS supplement was added to immerse the coverslip, the Petri dish was left again in the incubator for 24 hours. Gold nanorods were diluted in cell culture medium to proper concentration and incubated with cells from 1 hour to 8 hours as desired. After incubation, the microtubules were stained with Tubulin Tracker Green Reagent (T34085, Invitrogen, Carlsbad, CA) for 30 mins in the incubator according to protocol provided by Invitrogen. Then the coverslip with cells was put on glass slide with two strips of double-sided tape as spacer to form a chamber, and was put on microscope for observation.

## Results and Discussion

In the present study, the SPORT technique is employed to resolve the dynamic orientation of nanometer-sized cargos during microtubule-based transport in live cells. Gold nanorod probes with a dimension of 25×73 nm were naturally internalized by A549 human lung cancer cells to form endocytic vesicles, and their subsequent intracellular transport on cytoskeleton tracks was followed with fluorescence and DIC microscopy.

Fig. 1 shows a complete intracellular transport process of a nanorod-containing vesicle starting from the beginning of the transport to a point where the transport was stopped. To ensure that microtubule-based transport is observed, we modified a DIC microscope so that it can collect fluorescence and DIC images simultaneously (figure 2). The microtubule tracks inside a living cell were dyed with Oregon Green 488-tagged taxol molecules. Fig. 1b shows the overlapped DIC and fluorescence images. The trajectory of the translational movement of the nanorod was also plotted in blue to show that the nanorod was transported on the microtubule tracks.

Based on the information on both translational and rotational motions of the nanorod probe, 5 different stages in this transport process are identified and labeled in Fig. 1c. We are able to draw more detailed physical pictures of each stage with anisotropic gold nanorod probes than with isotropic probes like gold spheres or quantum dots.

During the first half of Stage 1, the DIC intensities of the nanorod fluctuated drastically, most likely representing rotational diffusion within a restricted location. The fast rotation slowed down in the second half of Stage 1, possibly indicating that a partial attachment of the nanorod-vesicle to the microtubule was established. Next in Stage 2, the nanorod-containing vesicle was transported on a microtubule for 0.8 μm with an average speed of 0.8 μm/s, consistent with the reported values.[21] It is interesting to note that the nanorod's DIC image changed from almost completely dark to almost completely bright at the beginning of the transport, a ~ 90° turn of the nanorod-containing vesicle. This reorientation should be ascribed to the pulling force generated by motor proteins during transport that the vesicle changed from a relaxed state to a state under tension. In State 3, the vesicle paused for 2.5 s at the same location. The nanorod probe showed an almost constant bright image, indicating the orientation of the vesicle was fixed during the pause. It should be noted that it was only with the orientation probe that we were able to tell the difference between the pause in Stage 3 and the rotational diffusion in Stage 1. The lack of rotational motion suggests that the vesicle was still under tension during the temporary pause. This observation depicts a new image that the nanorod-containing vesicle was tightly bound to the microtubule by multiple motor proteins, most likely with both directionalities (both kinesin and dynein), before it proceeded forward translational motion. In Stage 4, the vesicle was transported again on the microtubule tracks at 0.8 μm/s. In Stage 5, the vesicle came to a stop gradually and restored to a relaxed state with active rotation within a small region, indicating it was likely detached from the microtubule track.

An important finding of using gold nanorods and DIC microscopy to probe intracellular transport is that vesicles tend to keep their orientation with the underneath microtubule during the transport, showing a train-like movement. This can be identified when the nanorod-containing vesicles are transported along a straight line, giving relatively constant bright/dark images as in Stages 2 and 4 in Figure 1. Fig. 3 shows a further example that this relative orientation was locked even when the transport direction changed. A nanorod-containing vesicle was transported first to the northeast direction and then made a ~90° turn onto the southeast direction. The nanorod gave mostly dark images on the northeast track (Stage 1 in Fig. 3b) and mostly bright images on the southeast track (Stage 3). During the transition Stage 2, the DIC image of the nanorod changed gradually from completely dark to completely bright in ~1 s, indicating the orientation of the nanorod also changed by ~90°. The train-like motion in this case implies that the same set of protein motors were employed in the transport on multiple microtubule tracks to maintain the relative orientation of the vesicle to the microtubule. The trends of the bright and dark intensities over a long period are clearly flat with noticeable fluctuations from frame to frame, which were likely caused by steric hindrance inside a living cell.[33]

A third example of transport of nanorod-containing vesicle inside a living cell was shown in figure 4. Again, the gold nanorod showed relatively constant bright images on the linear track. An interesting feature of this transport event is that the nanorod reversed its transport direction, most likely on the same microtubule track. The nanorod gave bright images throughout the event. The DIC intensity levels were slightly different for the forward and backward movement (Fig. 4b). This indicates that there was a slight orientation change of the vesicle, caused by switching sets of motor proteins with different directionality:[11] dynein in the forward movement toward the nucleus and kinesin in the backward movement away from the nucleus. Between the two segments of transport, there was a short pause of 0.4 s, during which the effective motor proteins were switched from dynein to kinesin while the vesicle stayed at the same location.

The above three ev events show for the first time the detailed orientation information of cargos in live-cell transport. The cargo-containing vesicles tend to have a train-like movement, with a fixed vesicle-to-microtubule orientation in the transport. The fixed vesicle-microtubule orientation during transport is consistent with the literature that microtubules of most mammalian cells contain 13 protofilaments.[34] We studied 41 cases of intracellular transport of nanorod-containing vesicles. A minimum traveling distance of 4 μm was applied to exclude short intracellular transport. In these 41 cases, we observed 21 cases (~50%) that the nanorod kept a relatively constant bright/dark image during a linear transportation. The rest showed irregular (no periodicity) DIC intensity changing patterns, most likely caused by steric hindrance.

Especially, event 1 and 3 disclose the orientation information of vesicles at temporary stop points, during which the cargo's next movement is determined. Event 1 shows such a transition point after which the cargo continued to move forward, while in event 3 the vesicle reversed its advance direction. The transition points are receiving more attention in recent intracellular transport studies, especially where a network of transportation tracks are involved.[10,20] How the cell signals and regulates the movements of the cargo-containing vesicle, especially the binding status of multiple motors and signaling molecules to the vesicle and the track is still unclear.[10,20] In events 1 and 3, we show the cases that the vesicles are firmly attached to the microtubule tracks throughout these pausing points, no matter whether the vesicle continues to go forward or reverses its direction. These new observations give direct evidence that the relative orientation of cargo-containing vesicles to the microtubule is tightly controlled.

## Conclusion

In summary, we demonstrate that by using gold nanorod probes and DIC microscopy, dynamic orientation of nanometer-sized cargos during microtubule-based intracellular transport can be resolved at video rates in live cells. Compared to single molecule fluorescence polarization imaging, this method is more robust in terms of resistance to photobleaching and background noise. We report for the first time that the vesicles containing cargos tend to have a train-like movement, with a fixed vesicle-to-microtubule orientation in the transport. Especially, these studies show that the vesicles' orientation is tightly controlled at temporary stops during transport. These new observations can possibly shed new light on many live-cell transport mysteries, such as the question whether molecular motors with different directionalities work in coordination or fight a “tug of war” to reverse the transport direction.[25,35-36]

## References

(1) Lubyphelps, K. *Curr. Opin. Cell Biol.* **1994**, *6*, 3.

(2) Hirokawa, N. *Science* **1998**, *279*, 519.

(3) Vale, R. D. *Cell* **2003**, *112*, 467.

(4) Hirokawa, N.; Takemura, R. *Nat. Rev. Neurosci.* **2005**, *6*, 201.

(5) Chevalier-Larsen, E.; Holzbaur, E. L. F. *Biochim. Biophys. Acta-Mol. Basis Dis.* **2006**, *1762*, 1094.

(6) Schnitzer, M. J.; Block, S. M. *Nature* **1997**, *388*, 386.

(7) Khalil, A. S.; Appleyard, D. C.; Labno, A. K.; Georges, A.; Karplus, M.; Belcher, A. M.; Hwang, W.; Lang, M. J. *Proc. Natl. Acad. Sci. U. S. A.* **2008**, *105*, 19247.

(8) Hancock, W. O.; Howard, J. *J. Cell Biol.* **1998**, *140*, 1395.

(9) Svoboda, K.; Schmidt, C. F.; Schnapp, B. J.; Block, S. M. *Nature* **1993**, *365*, 721.

(10) Ross, J. L.; Ali, M. Y.; Warshaw, D. M. *Curr. Opin. Cell Biol.* **2008**, *20*, 41.

(11) Gennerich, A.; Vale, R. D. *Curr. Opin. Cell Biol.* **2009**, *21*, 59.

(12) Block, S. M. *Biophys. J.* **2007**, *92*, 2986.

(13) Sindelar, C. V.; Downing, K. H. *Proc. Natl. Acad. Sci. U. S. A.* **2010**, *107*, 4111.

(14) Coy, D. L.; Wagenbach, M.; Howard, J. *J. Biol. Chem.* **1999**, *274*, 3667.

(15) Reck-Peterson, S. L.; Yildiz, A.; Carter, A. P.; Gennerich, A.; Zhang, N.; Vale, R. D. *Cell* **2006**, *126*, 335.

(16) Ray, S.; Meyhofer, E.; Milligan, R. A.; Howard, J. *J. Cell Biol.* **1993**, *121*, 1083.

(17) Yajima, J.; Mizutani, K.; Nishizaka, T. *Nat. Struct. Mol. Biol.* **2008**, *15*, 1119.

(18) Nitzsche, B.; Ruhnow, F.; Diez, S. *Nat. Nanotechnol.* **2008**, *3*, 552.

(19) Wang, Z. H.; Khan, S.; Sheetz, M. P. *Biophys. J.* **1995**, *69*, 2011.

(20) Miller, K. E.; Heidemann, S. R. *Exp. Cell Res.* **2008**, *314*, 1981.

(21) Cai, D. W.; Verhey, K. J.; Meyhofer, E. *Biophys. J.* **2007**, *92*, 4137.

(22) Courty, S.; Luccardini, C.; Bellaiche, Y.; Cappello, G.; Dahan, M. *Nano Lett.* **2006**, *6*, 1491.

(23) Sims, P. A.; Xie, X. S. *ChemPhysChem* **2009**, *10*, 1511.

(24) Nan, X. L.; Sims, P. A.; Chen, P.; Xie, X. S. *J. Phys. Chem. B* **2005**, *109*, 24220.

(25) Kural, C.; Kim, H.; Syed, S.; Goshima, G.; Gelfand, V. I.; Selvin, P. R. *Science* **2005**, *308*, 1469.

(26) Yajima, J.; Cross, R. A. *Nat. Chem. Biol.* **2005**, *1*, 338.

(27) Lee, K.-S.; El-Sayed, M. A. *J. Phys. Chem. B* **2006**, *110*, 19220.

(28) Sonnichsen, C.; Alivisatos, A. P. *Nano Lett.* **2005**, *5*, 301.

(29) Spetzler, D.; York, J.; Daniel, D.; Fromme, R.; Lowry, D.; Frasch, W. *Biochem.* **2006**, *45*, 3117.

(30) Pluta, M. *Advance light microscopy*; Elsevier Science Publishing Co. Inc.: New York, 1989; Vol. 2.

(31) Sun, W.; Wang, G. F.; Fang, N.; Yeung, E. S. *Anal. Chem.* **2009**, *81*, 9203.

(32) Wang, G. F.; Sun, W.; Luo, Y.; Fang, N. *J. Am. Chem. Soc.*, Submitted on 7/19/2010.

(33) Lubyphelps, K.; Taylor, D. L.; Lanni, F. *J. Cell Biol.* **1986**, *102*, 2015.

(34) Tilney, L. G.; Bryan, J.; Bush, D. J.; Fujiwara, K.; Mooseker, M. S.; Murphy, D. B.; Snyder, D. H. *J. Cell Biol.* **1973**, *59*, 267.

(35) Gross, S. P.; Welte, M. A.; Block, S. M.; Wieschaus, E. F. *J. Cell Biol.* **2002**, *156*, 715.

(36) Muller, M. J. I.; Klumpp, S.; Lipowsky, R. *Proc. Natl. Acad. Sci. U. S. A.* **2008**, *105*, 4609.

(37) Narayanan, R.; Lipert, R. J.; Porter, M. D. *Anal. Chem.* **2008**, *80*, 2265.

## Figure captions

Figure 6.1. An example of cargo transport process in a live cell. (a) Scheme of intracellular microtubule-based transport of a gold nanorod-containing vesicle. (b) The overlapped DIC (gray) and fluorescence images (green) of the cell containing the gold nanorod probe. The green fluorescence shows the distribution of the microtubule network. The blue curve shows the intracellular transport trace of the nanorod-containing vesicle. (c) The expanded view of the fluorescently tagged microtubules in the frame inside (b). (d) DIC intensities as a function of time during the whole process, which is divided into 5 stages at the following time points: 3.1, 4.5, 7.3, and 10.3 s. A detailed explanation of the five stages is provided in the text.

Figure 6.2. Optical path of the dual-mode DIC/fluorescence microscopy.

Figure 6.3. An example of train-like motion when a vesicle was transported on microtubule tracks. The gold nanorod showed a mostly dark images and then mostly bright images after a ~90° turn on microtubule tracks, indicating the orientation of the nanorod also changed ~ 90° after the turn. (a) The DIC image of the cell and the trace of the intracellular transport of the nanorod-containing vesicle. (b) DIC intensities as a function of time.

Figure 6.4. An example of bi-directional cargo transport in live cells (Movie 3). The nanorod-containing vesicle was transported forward and then backward on the same microtubule track inside a live cell. (a) The near-perfectly overlapped forward and backward traces of the gold nanorod-containing vesicle during the transportation. (b) The displacement and DIC intensities of the nanorod as a function of time. The displacement was defined as the distance between its positions at time *t* and time 0.

# Figures

Figure 6.1

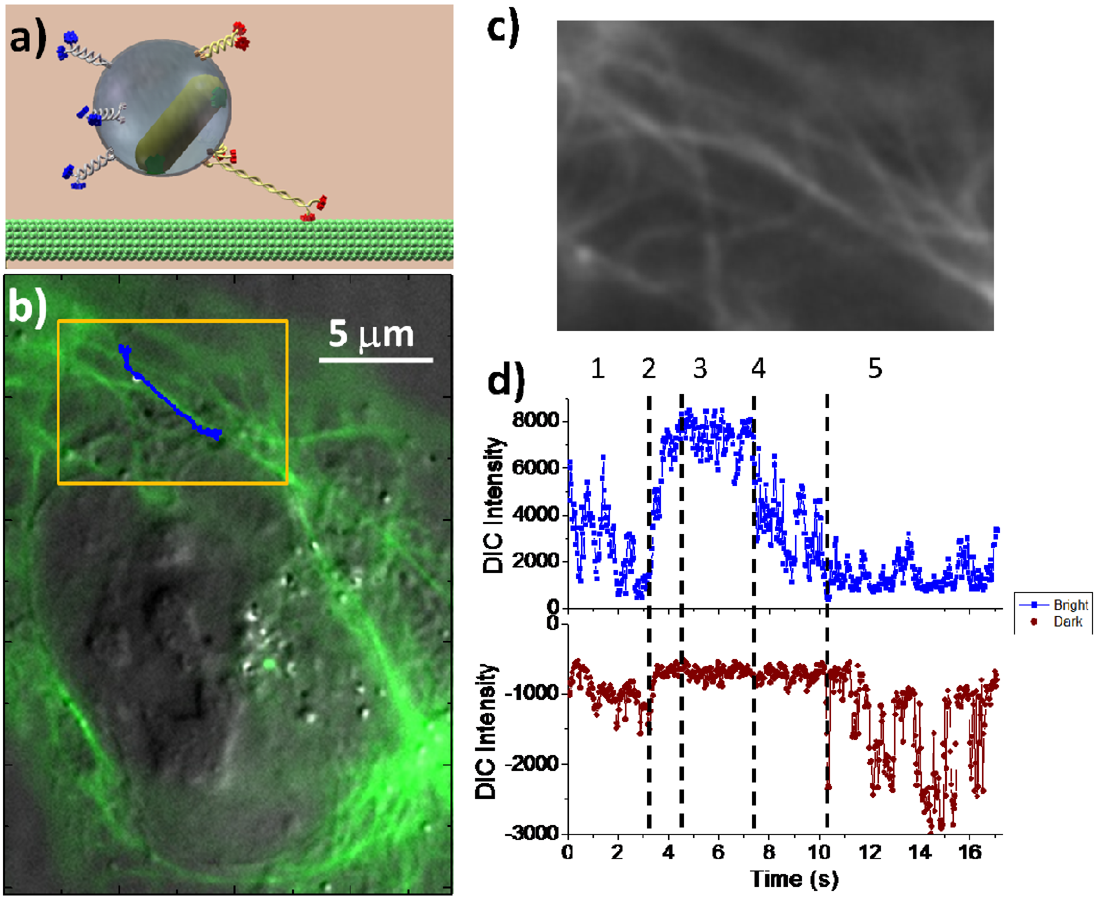

Figure 6.2

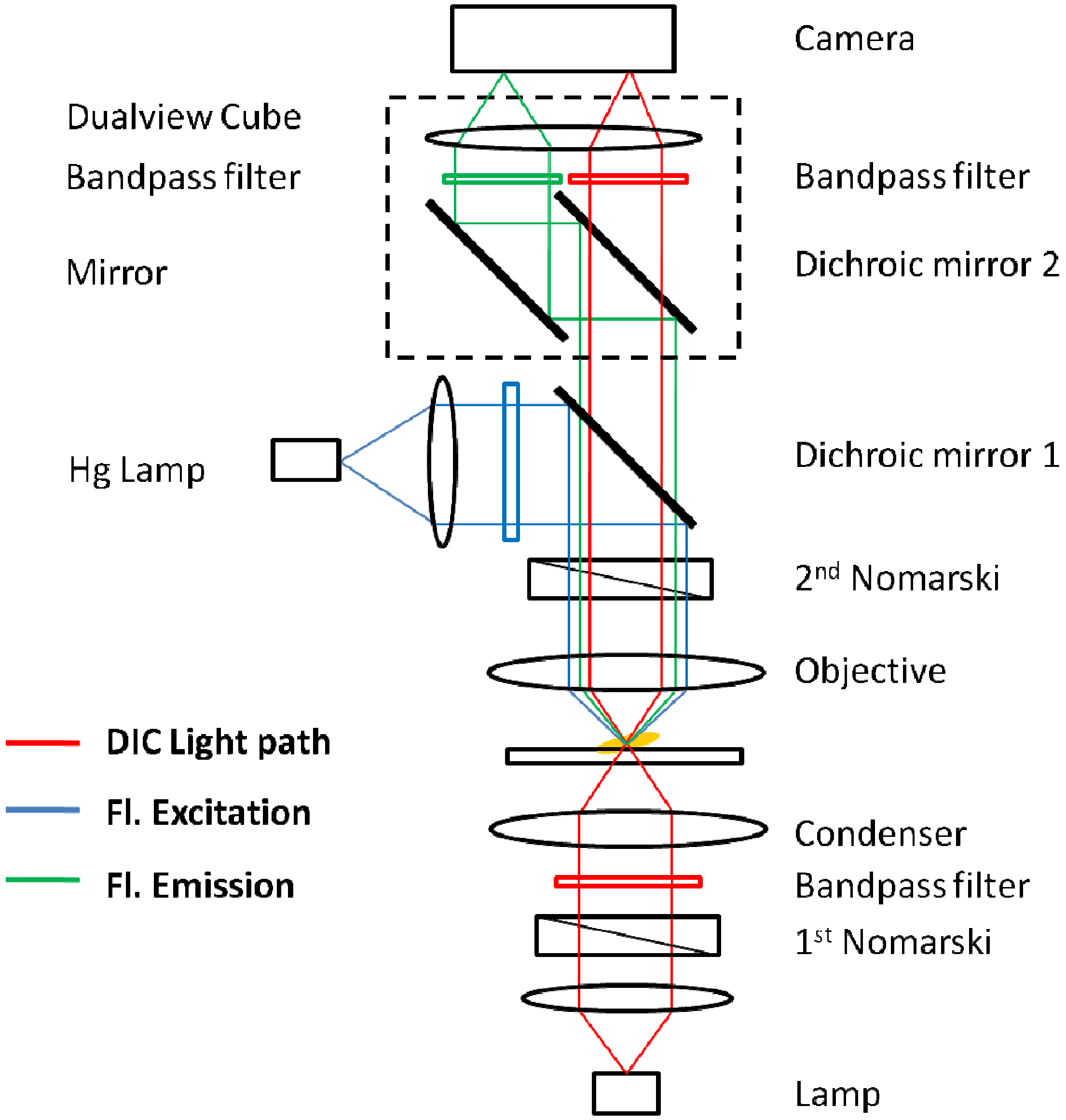
Camera
Dualview Cube
Bandpass filter
Bandpass filter
Mirror
Dichroic mirror 2
Hg Lamp
Dichroic mirror 1
2nd Nomarski
Objective
DIC Light path
Fl. Excitation
Fl. Emission
Condenser
Bandpass filter
1st Nomarski
Lamp

Figure 6.3

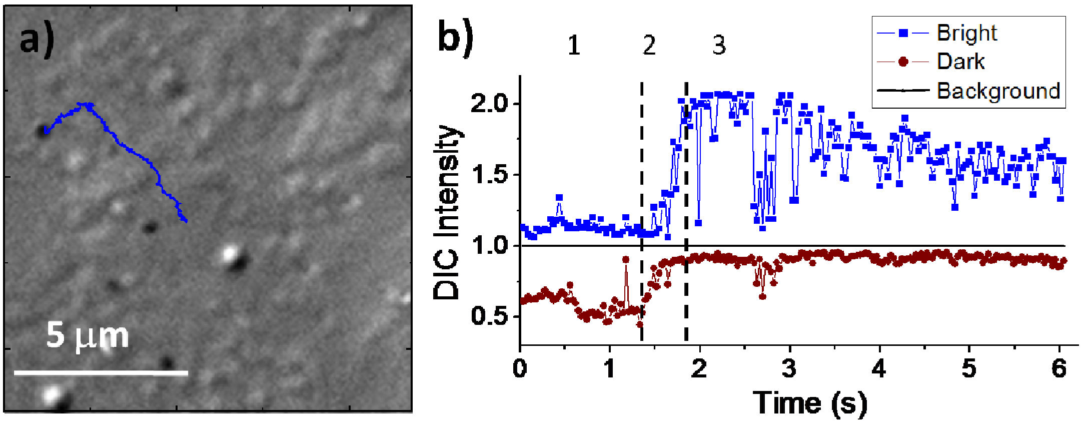
a)
5 µm
b)
1
2
3
Bright
Dark
Background
DIC Intensity
2.0
1.5
1.0
0.5
0
1
2
3
4
5
6
Time (s)

Figure 6.4

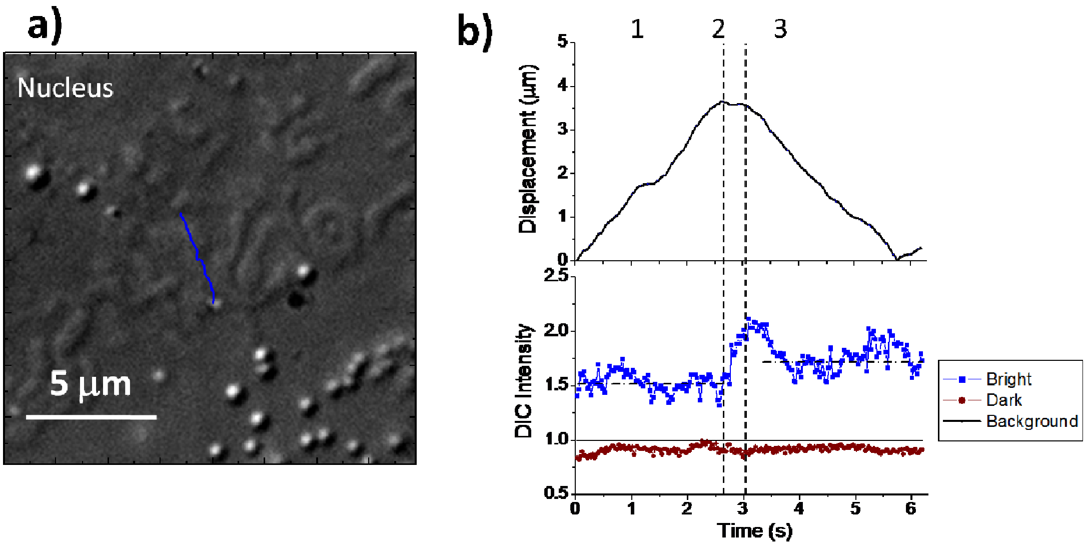
a)
Nucleus
5 µm
b)
1
2
3
Displacement (µm)
5
4
3
2
1
0
2.5
2.0
1.5
1.0
0.5
DIC Intensity
0
1
2
3
4
5
6
Time (s)
Bright
Dark
Background

# CHAPTER 7. AXONAL TRANSPORTATION OF GOLD NANORODS STUDIED WITH DIC MICROSCOPY

## Abstract

In this work, the transport of endocytosed gold nanorods in the axon was studied with DIC microscopy. The white/black intensity pattern in DIC images of both actively transported and free diffusing nanorods were analyzed and compared. Through calculating the relative mean intensity variation, it was found that the rotation freedom of cargoes during active transport was greatly reduced compared to that during free diffusion. It is because motor proteins (kinesin and dynein) that bind cargoes to microtubules restrict the cargo’s free rotation. For active transport, the short and infrequent pause phenomenon happened in both unidirectional and bidirectional movement was also observed and analyzed. During the pause stage, although the nanorods performed no translational movement, their orientation still changed. And the relative mean intensity variation value of gold nanorod during pause stage is close to that during moving stage. It shows that the cargoes were still bound to the microtubules during the pause stage of active transport. The underlying mechanism may be that different directional motor proteins work together on the cargoes during the pause stage, and the cargoes need to adjust their orientation responding to the net force change.

## Introduction

Axonal transport is a significant intracellular process taking place inside the cytoplasm of the long and slender axon which bridges its distant outposts to neuron's cell body. The importance of axonal transport is well-known to biologists[1]. For instances: proteins manufactured by ribosomes that mainly locate inside cell body need to be transported anterogradely and distributed along the axon; while endocytic vesicles are moved retrogradely from axon terminals towards cell body for degradation or reusing. The dysfunction of axonal transport can cause serious diseases such as Alzheimer's disease which is related to the abnormal depolymerization of the microtubules inside axons[2].

The axonal transport can be classified into slow and fast axonal transport that differs in average speed based on the properties of cargoes. Fast transport components include membranous organelles like mitochondria, endocytotic vesicles; whereas slow transport components are categorized into slow transport component a (such as cytoskeletal polymers) and b (such as cytosolic protein complexes)[3-7]. The average speed difference between slow and fast transport results from the diverse proportion of time cargoes spend in moving: slow transport components move in a more intermittent and bidirectional pattern and spend more time in the pause stage; while for fast transport, the frequency and time of pausing is much smaller which makes the total average speed apparently larger[8, 9]. For example, although both neurofilaments and microtubules can be transported at fast rates when moving, the average speed of movement is slow because the movements are infrequent and bidirectional[10-13].

The underlying mechanism by which the fast and slow transports are regulated spurred researchers in neurobiology for decades. Until the 1960s, it was discovered that axonal transport was active transport based on the originally designed experiments by using pulse injections of radio-labeled amino acids into the neurons of live animals[5, 14, 15]. In those experiments, transport was characterized by the movement of peaks of radio-labeled proteins instead of exponentially decay curve caused by simply diffusing through the axon. Later since the discovery and identification of two major molecular motor proteins--kinesin[16] and dynein[17-19], the underlying mechanism of axonal transport has become more and more unveiled[20, 21]. Results obtained with new techniques such as speckle microscopy or tracking photo-bleached zone[10-12, 22] helped to the falsify the initial axonal transport hypothesis that supported either the movement of axonal cytoskeletal framework[5, 6] or coherent axoplasmic streaming[23, 24]. New mechanisms such as "stop-and-go"[25, 26] and "cut-and-run"[27, 28] have been raised to postulate the slow axonal transport of cytoskeletal polymers. More and more efforts were devoted to fully solve the question: what determines a particular intracellular cargo to move or pause? Now it is widely agreed that the movement of cargoes in both slow and fast transport are driven by kinesin and dynein along microtubules[20, 29-32]. The pause during active transport may result from the varying affinities between cargoes and motor proteins[4, 29,33] Compared to fast transport components, the affinities between slow transport components and motor proteins are smaller. Thus the low efficient coupling of slow transport components to the microtubule track provides more chances for cargoes to unbind from the axonal microtubules. Although fast transport components also detach from the microtubules, the frequency is much smaller and the average speed is larger.

As reported in our previous work, the unique white/black intensity pattern in DIC images of gold nanorods helps distinguish nanorods from other intracellular organelles with similar shape and size easily. Moreover, the intensity change is directly related to the orientation of gold nanorods. By using gold nanorod as rotational probe, new perspectives can be extracted to complement the information obtained by measuring only the lateral displacement[34, 35]. In this work, the axonal transport of internalized gold nanorods through endocytosis was studied by using the new technique-SPORT. The white/black intensities of gold nanorods during free diffusing and active transport including both moving stage and pause stage were analyzed and the underlying rotational information was extracted.

## Experimental

**Preparation of transferrin surface-modified gold nanorods for cell experiments.** Cetyl trimethylammonium bromide (CTAB)-capped (25×73 nm, $1.3\times10^{11}$ particles/mL, Nanopartz) gold nanorods were used. A NHS-PEG disulfide linker (Sigma-Aldrich) was used by following a published protocol[36]. The NHS-PEG disulfide linker has both disulfide and succinimidyl functionalities for respective chemisorption onto gold and facile covalent coupling of TAT peptide. Briefly, excessive surfactant was first removed from 1.0 mL gold nanorod solution by centrifugation at 3000 g for 10 minutes and the particles were resuspended in 1.0 mL 2 mM borate buffer. A proper amount of fresh NHS-PEG disulfide solution (in dimethyl sulfoxide) was added to reach a final thiol concentration of 0.2 mM and reacted with gold nanorods for 2 hours. The solution was then cleaned up by centrifugation and resuspended in 2 mM borate buffer. 2.0 µg transferrin was added to the gold colloidal solution and reacted for 8 hours. The gold nanorods were then blocked by adding 100 mL 10% BSA solution (2 mM borate buffer) for over 8 hours. Before use, the colloidal gold nanorod probes were cleaned up by centrifugation and resuspended in 500 µL 1% BSA (2 mM borate buffer). The concentrated gold colloidal solution was diluted in cell culture medium to a final concentration of $4.3\times10^9$ particles/mL for incubation with cells.

**Cell culture**. Hippocampal cultures were obtained from brains of embryonic day 18 (E18) to E19 C57Bl/6 mice following standard protocols. The dissociated cells were plated on poly-L-lysine-coated coverslip and maintained in Neurobasal/B27 media (Invitrogen, Carlsbad, CA) supplemented with 0.5 mM glutamine. Proper amount of transferrin modified gold nanorods were diluted in cell culture media and were incubated with cells together in the incubator (37□, 5% $CO_2$) for 4 hours. Then the coverslip was taken out from the incubator and made into a chamber by using double sided tape and a clean glass slide. When it needed to destruct the microtubule network inside axons, the cells were following incubated in cell culture media containing 200µg/ml colchicine for 1 hour in the incubator (37□, 5% $CO_2$) after incubated with gold nanorods. The cells were fixed with 4% Paraldehyde in PBS solution and stained with 1st antibody--mouse anti-alpha tubulin and 2nd antibody--Alexa 488 goat anti-mouse when required.

**Microscopy and live cell imaging.** An upright Nikon Eclipse 80i microscope equipped with a heating stage was used in this study. The temperature of the heating stage was set at 37□. This microscope can be switched between DIC mode and epi-fluorescence mode. The samples were illuminated through an oil immersion condenser (numerical aperture 1.40) and the optical signals were collected with a 100×Plan Apo/1.40 oil immersion objective. One bandpass filter (Semrock, Rochester, NY) with central wavelengths in 700 nm and a full width at half maximum (FWHM) of 13 nm was inserted into the light path in the microscope. An Andor iXon$^{EM}$+ camera

(512×512 imaging array, 16×16-µm pixel size) was used to record the dynamic in vivo transport at 32 frames per second. MATLAB and NIH ImageJ were used to analyze the collected images and videos.

## Results and Discussion

The surface of gold nanorods was modified with transferrin to facilitate the nanorods' internalization into neuron cells through clathrin mediated endocytosis[37]. After entry into cells, the nanorods are enveloped by vesicles that make them as possible membranous cargoes that move at fast axonal transport mode. Movies recording the unidirectional axonal transport of such gold nanorods were taken. The average active transport speed was 1.2µm/s, which is in the reported transport speed range[9]. In addition, the infrequent and short pause phenomenon was also observed. In two such events, the gold nanorods paused for around 0.96s and 0.88s respectively at the same location inside axon before being transported again.

Through Matlab software and home-written program, the white/black intensity pattern and the absolute lateral displacement of the gold nanorods during transport process were extracted. Figure 1A shows the intensity pattern and displacement of one gold nanorod that underwent active transport. During the moving stage, the white/black intensity of the nanorod did not keep completely the same, but varied within a small range all the time and changed greatly at certain locations. During the pause stage, the nanorod performed no translational motion, but the white/black intensity also changed. Besides unidirectional movement, bi-directional axonal transport was also captured. Figure 1B shows one bidirectional transport event. In this event, the nanorod first moved towards the terminal of axon for 3µm, paused for around 1.5s and then reversed the moving direction towards cell body.

Different from the gold nanorods describes above, some nanorods performed free diffusion inside the axon. It can be judged from the moving trajectory: free diffusing gold nanorod moved in random directions and the absolute displacement was much smaller (figure 2A). In addition, the intensity of these free diffusing nanorods fluctuated more obviously than that of those actively transported nanorods. To further compare and confirm the difference between actively transported and free diffusing nanorods, the neuron cells were treated with colchicine which can destroy the intracellular microtubule network[38]. When the intracellular microtubule network is destroyed, the cargoes can’t be bound to the microtubules by motor proteins and will rotate with higher freedom inside axon. The drug effect was confirmed by carrying out immuno-labeling and fluorescence imaging (figure 3): the intact microtubule network was distributed inside normal neuron cells; while inside cells pretreated with colchicine, no intact single microtubule was observed. Figure 2B shows the white/black intensity of one nanorod moving inside the axon treated with colchicine.

To better understand how the motor proteins restrict cargoes’ free diffusing and rotating, the intensity patterns were analyzed in a semi-quantitative way. Following the method of using mean lateral displacement to calculate diffusion coefficient[39, 40], the freedom of cargo’s rotation was quantified by using the relative mean intensity variation (RMIV). The larger the RMIV is, the higher the rotation freedom will be. First, the mean intensity variation was estimated by Gaussian fitting the histograms of the intensity variation of nanorod between two successive frames in a movie recording the movement. Since the average intensity for each nanorod during different time domains was a little different, the mean intensity variation was further divided by the average intensity in the same time domain. As shown in figure 4, the histogram of intensity variation of nanorods during transport stage, pause stage and free diffusing were listed. And the corresponding RMIV values were listed in table 1.

From table 1, it is known that the RMIV values during the active transport including moving stage and pause stage are within 10%. The intensity change during active transport may result from the steric hindrance placed on the nanorod from the crowding cytoskeleton network inside the slender axon. Such impeditive force during transport process forces the gold nanorod to adjust its orientation when being dragged by motor proteins along the microtubule track. It is also known from table 1 that the RMIV values of free diffusing nanorods are ~30% which is much larger than the RMIV values of active transport. It demonstrates that the cargo’s rotation freedom was greatly reduced when being actively transported. The reduction in rotation results from the restriction placed by motor proteins.

It is also noticed that the RMIV values for both pause and moving stages in the same active transport process are close to each other. The data shows that the rotation freedom of pause stage and moving stage is at the same level--the cargoes did not rotate more during the pause stage than during moving stage. The observation is contrary to the aforementioned hypothesis--the pause comes from the detachment of cargoes from microtubule resulting from the low affinity between cargoes and motor proteins[4,29,33]. It is because the decoupling of cargoes from motor proteins can cause the detachment of cargoes from microtubules and allow the free rotation of cargoes. But this expected phenomenon did not happen during the pause stage in the experiments.

The experimental observation points out that it is most possible that the gold nanorods were still bound to the microtubules by motor proteins during the pause stage. It may be supported by the idea that different directional motor proteins work together on the cargoes[41-43]. When the driving forces in opposite directions are balanced, the motion of cargo will be ceased; when the balance is broken, the cargo will be transported again either in the original direction or opposite direction depending on the new net force direction (figure 5). The reach and break of force balance result the decelerating and accelerating process of cargo. As shown in figure 1A and 1B, the intensity patterns of both nanorods shared one common feature: the white/black intensity of nanorods changed relatively greater at the early and late part of the pause stage than during the middle part of pause stage. The greater intensity change could be the characteristic of the accelerating and decelerating process during which the net force is at the maximum.

When the nanorod was “locked” by motor proteins during the pause stage, it performed no translational movement. However, the nanorod was not complete “quiet”. The intensity pattern is similar to that when the nanorod was dragged along the microtubule track by a non-zero net force during the moving stage. It means that different directional motor proteins fight with each other to pull the nanorod away during the pause stage. Because of the restriction from motor proteins, the gold nanorod didn’t rotate freely when it stayed at the same location.

## Conclusion

In this work, the translational and rotational motions of gold nanorods in axon were studied by DIC microscopy. The white/black intensity patterns of actively transported and free diffusing nanorods were different. During the active transport process, the rotation freedom of nanorods was greatly reduced compared to that of free diffusing nanorods because of the restriction from motor proteins which bound cargoes to microtubules. In addition, by comparing the relative mean intensity variation (RMIV) for both moving and pause stages, it is known that the nanorods were still bound to the microtubules during the pause stage. The move or pause of cargoes is mainly determined by the net force placed on the cargo by different directional motor proteins.

## References

(1) Wu, C. B.; Cui, B. X.; He, L. M.; Chen, L.; Mobley, W. C. *Journal of Proteomics* **2009**, *72*, 46-55.

(2) Roy, S.; Zhang, B.; Lee, V. M. Y.; Trojanowski, J. Q. *Acta Neuropathologica* **2005**, *109*, 5-13.

(3) Dahlstrom, A. B. *Progress in Neurobiology*, *90*, 119-145.

(4) Shah, J. V.; Cleveland, D. W. *Current Opinion in Cell Biology* **2002**, *14*, 58-62.

(5) Lasek, R. J.; Garner, J. A.; Brady, S. T. *Journal of Cell Biology* **1984**, *99*, S212-S221.

(6) Black, M. M.; Lasek, R. J. *Journal of Cell Biology* **1980**, *86*, 616-623.

(7) Roy, S.; Winton, M. J.; Black, M. M.; Trojanowski, J. Q.; Lee, V. M. Y. *Journal of Neuroscience* **2007**, *27*, 3131-3138.

(8) Brown, A. *Journal of Cell Biology* **2003**, *160*, 817-821.

(9) Cui, B. X.; Wu, C. B.; Chen, L.; Ramirez, A.; Bearer, E. L.; Li, W. P.; Mobley, W. C.; Chu, S. *Proceedings of the National Academy of Sciences of the United States of America* **2007**, *104*, 13666-13671.

(10) Roy, S.; Coffee, P.; Smith, G.; Liem, R. K. H.; Brady, S. T.; Black, M. M. *Journal of Neuroscience* **2000**, *20*, 6849-6861.

(11) Wang, L.; Brown, A. *Molecular Biology of the Cell* **2001**, *12*, 3257-3267.

(12) Wang, L.; Brown, A. *Current Biology* **2002**, *12*, 1496-1501.

(13) He, Y.; Francis, F.; Myers, K. A.; Yu, W. Q.; Black, M. M.; Baas, P. W. *Journal of Cell Biology* **2005**, *168*, 697-703.

(14) Droz, B.; Leblond, C. P. *Science* **1962**, *137*, 1047-&.

(15) Grafstein, B.; Forman, D. S. *Physiological Reviews* **1980**, *60*, 1167-1283.

(16) Vale, R. D.; Reese, T. S.; Sheetz, M. P. *Cell* **1985**, *42*, 39-50.

(17) Lye, R. J.; Porter, M. E.; Scholey, J. M.; McIntosh, J. R. *Cell* **1987**, *51*, 309-318.

(18) Vallee, R. B.; Williams, J. C.; Varma, D.; Barnhart, L. E. *Journal of Neurobiology* **2004**, *58*, 189-200.

(19) Paschal, B. M.; Shpetner, H. S.; Vallee, R. B. *Journal of Cell Biology* **1987**, *105*, 1273-1282.

(20) Hirokawa, N.; Takemura, R. *Nature Reviews Neuroscience* **2005**, *6*, 201-214.

(21) Hirokawa, N.; Noda, Y. *Physiological Reviews* **2008**, *88*, 1089-1118.

(22) Chang, S. H.; Svitkina, T. M.; Borisy, G. G.; Popov, S. V. *Nature Cell Biology* **1999**, *1*, 399-403.

(23) Brady, S. T.; Lasek, R. J. *Cell* **1981**, *23*, 515-523.

(24) Gross, G. W. *Advances in Neurology* **1975**, *12*, 283-296.

(25) Brown, A.; Wang, L.; Jung, P. *Molecular Biology of the Cell* **2005**, *16*, 4243-4255.

(26) Craciun, A.; Brown, A.; Friedman, A. *Journal of Theoretical Biology* **2005**, *237*, 316-322.

(27) Baas, P. W.; Nadar, C. V.; Myers, K. A. *Traffic* **2006**, *7*, 490-498.

(28) Baas, P. W.; Karabay, A.; Qiang, L. *Trends in Cell Biology* **2005**, *15*, 518-524.

(29) Miller, K. E.; Heidemann, S. R. *Experimental Cell Research* **2008**, *314*, 1981-1990.

(30) Hirokawa, N.; Noda, Y.; Tanaka, Y.; Niwa, S. *Nature Reviews Molecular Cell Biology* **2009**, *10*, 682-696.

(31) Uchida, A.; Alami, N. H.; Brown, A. *Molecular Biology of the Cell* **2009**, *20*, 4997-5006.

(32) Francis, F.; Roy, S.; Brady, S. T.; Black, M. M. *Journal of Neuroscience Research* **2005**, *79*, 442-450.

(33) Kuznetsov, A. V.; Avramenko, A. A.; Blinov, D. G. *International Communications in Heat and Mass Transfer* **2009**, *36*, 293-296.

(34) Nan, X. L.; Sims, P. A.; Xie, X. S. *Chemphyschem* **2008**, *9*, 707-712.

(35) Courty, S.; Luccardini, C.; Bellaiche, Y.; Cappello, G.; Dahan, M. *Nano Letters* **2006**, *6*, 1491-1495.

(36) Narayanan, R.; Lipert, R. J.; Porter, M. D. *Analytical Chemistry* **2008**, *80*, 2265-2271.

(37) Qian, Z. M.; Li, H. Y.; Sun, H. Z.; Ho, K. *Pharmacological Reviews* **2002**, *54*, 561-587.

(38) Gunstream, J. D.; Castro, G. A.; Walters, E. T. *Journal of Neuroscience* **1995**, *15*, 439-448.

(39) Saxton, M. J. *Biophysical Journal* **1993**, *64*, 1766-1780.

(40) Sun, W.; Fang, N.; Trewyn, B. G.; Tsunoda, M.; Slowing, II; Lin, V. S. Y.; Yeung, E. S.

*Analytical and Bioanalytical Chemistry* **2008**, *391*, 2119-2125.

(41) Kural, C.; Kim, H.; Syed, S.; Goshima, G.; Gelfand, V. I.; Selvin, P. R. *Science* **2005**, *308*, 1469-1472.

(42) Muller, M. J. I.; Klumpp, S.; Lipowsky, R. *Proceedings of the National Academy of Sciences of the United States of America* **2008**, *105*, 4609-4614.

(43) Hendricks, A. G.; Perlson, E.; Ross, J. L.; Schroeder, H. W.; Tokito, M.; Holzbaur, E. L. F. *Current Biology*, *20*, 697-702.

## Figure captions

Figure 7.1. The white/black intensity profile and the absolute lateral displacement of gold nanorods moving through active axonal transport. Column A is for a gold nanorod doing unidirectional movement. Top graph shows the white intensity pattern along with time; the value in Y axis is the quotient—the highest intensity value in the white part of nanorod's DIC image divided by the background intensity value of the DIC image. Middle graph shows the black intensity pattern along with time. Bottom graph shows the absolute lateral displacement of the nanorod along with time; unit for Y axis is µm. Unit of X axis for all the graphs is second. Column b is for the gold nanorod doing bidirectional movement.

Figure 7.2**.** The white/black intensity profile and the absolute lateral displacement of gold nanorods moving through free diffusion. Column A is for a gold nanorod in native neuron cell. Column b is for a gold nanorod in neuron cell treated with chochicine. The units of X axis and Y axis are the same as that in figure 1.

Figure 7.3. The microtubule inside native neuron cells and. Left: native neuron cells, no colchicine treatment. Right: colchicines treated neuron cells.

Figure 7.4. The histograms of the distribution of mean intensity variation. Column A is for the actively transported gold nanorod doing unidirectional movement. Top graph is the distribution during the moving stage; bottom graph is the distribution during the pause stage. Column B is for the nanorod doing bidirectional movement. Top graph is the distribution during the moving stage; bottom graph is the distribution during the pause stage. Top graph in column C is the distribution for nanorod free diffusing in native cell; bottom graph in column c is the distribution for nanorod free diffusing in colchicine treated cell. The X axis is value range of the intensity variation times 1000. The Y axis is the probability calculated by dividing the counts in each intensity variation range by the total number of intensity variation.

Figure 7.5. The mechanism how move or pause of cargo is determined during active transport.

Table 7.1. The relative mean intensity variation (RMIV) of different gold nanorods in different moving modes.

| Particle NO. | Transport type | Movement type | RMIV |
|---|---|---|---|
| 1 | Unidirectional active | Moving stage | 5.1% |
| | | Pause stage | 5.5% |
| 2 | Bidirectional active | Moving stage | 10% |
| | | Pause stage | 3.0% |
| 3 | Free diffusing | | 32% |
| 4 | Free diffusing | | 30% |

# Figures

Figure 7.1

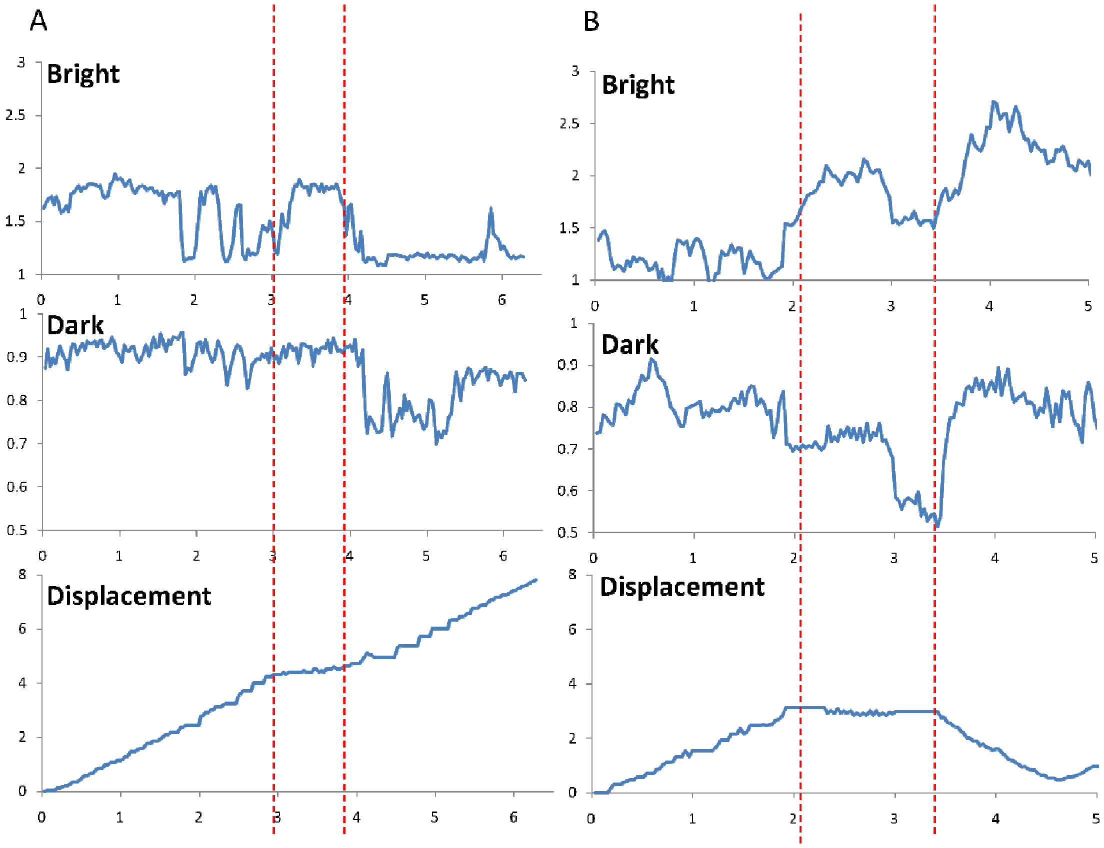

Figure 7.2

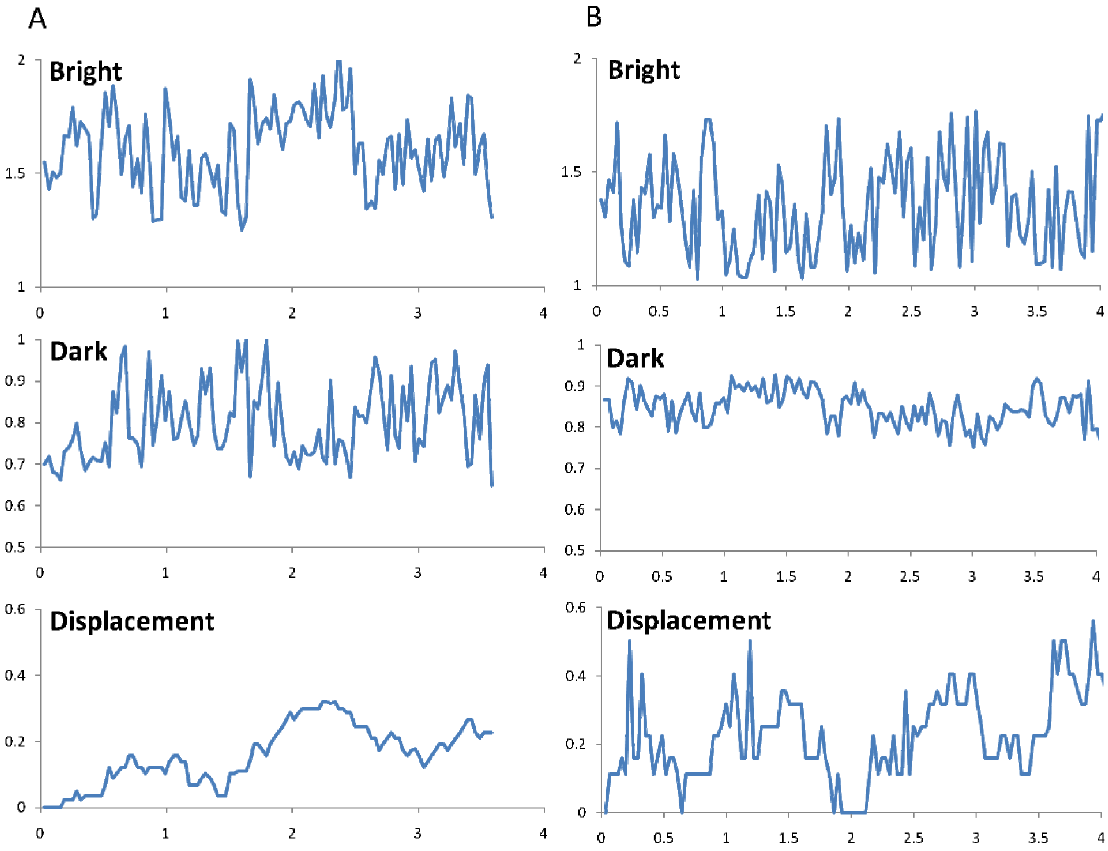
A
B
Bright
Dark
Displacement
2
1.5
1
1
0.9
0.8
0.7
0.6
0.5
0.6
0.4
0.2
0
0
0.5
1
1.5
2
2.5
3
3.5
4

Figure 7.3

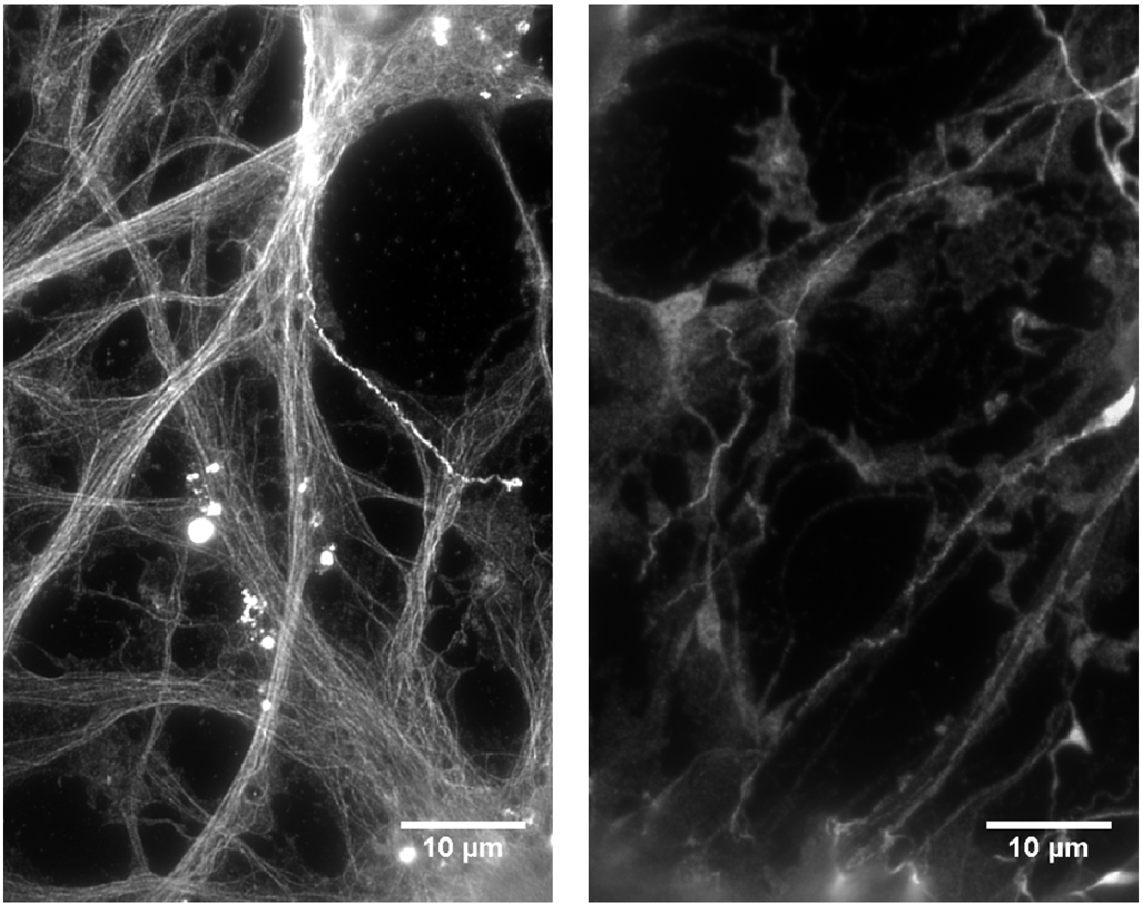

Figure 7.4

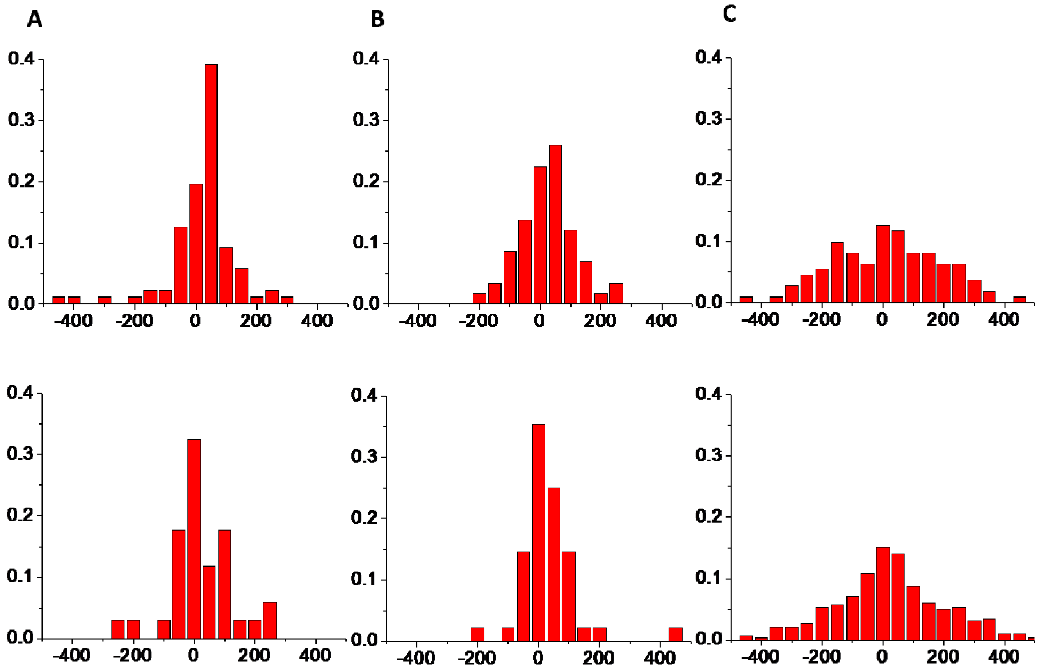

Figure 7.5

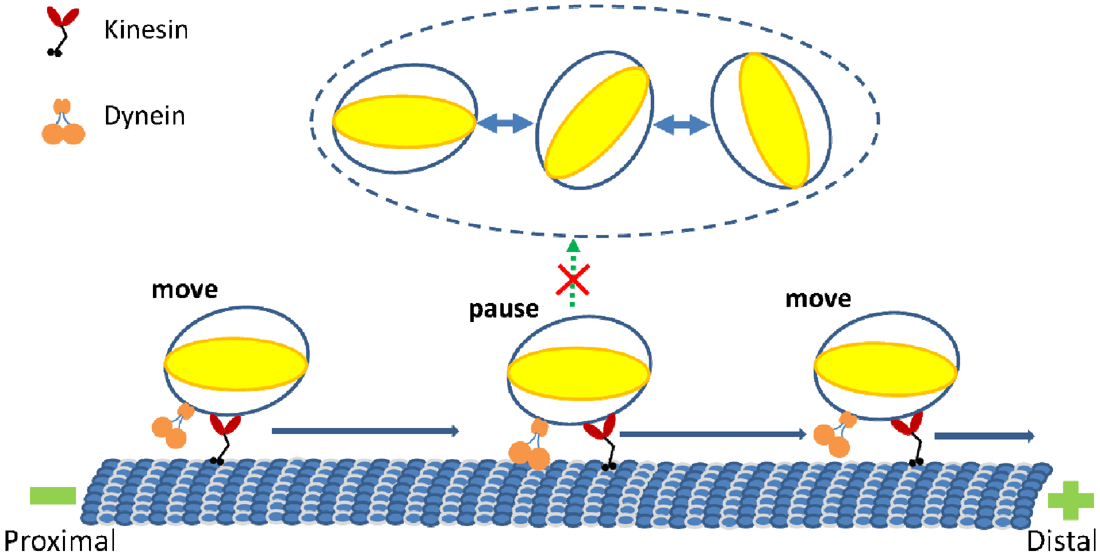

# CHAPTER 8. AUTO-CALIBRATED SCANNING-ANGLE PRISM-TYPE TOTAL INTERNAL REFLECTION FLUORESCENCE MICROSCOPY FOR NANOMETER-PRECISION AXIAL POSITION DETERMINATION

Wei Sun, Kyle Marchuk, Gufeng Wang, and Ning Fang

Published in Analytical Chemistry*

## Abstract

An automatic angle scanning prism type total internal reflection fluorescence microscopy (TIRFM) is realized. The angle of incident laser light can be changed automatically and reliably from subcritical angle to nearly 90° with interval smaller than 0.2°; and the laser illumination spot in the sample can be automatically calibrated to overlap with the center of the microscope field of view. By adjusting the penetration depth of evanescent field through changing incident angle, the fluorescence intensity decay function of 28nm diameter fluorescent nanospheres randomly distributed in agarose gel was obtained. Through correlating the experimental decay function with theoretical decay curve, the vertical positions of nanospheres were extracted and resolved. Then best axial resolution obtained was better than 10nm. And through the automatic scanning, the SPR angle for gold film enhanced TIRFM was found precisely and reproducibly. The setup was further applied to study the tilted angle for microtubules buried in agarose gel.

---

*Reprint with permission from Analytical Chemistry, **2010**, 82(6), 2441-2447.

## Introduction

Total internal reflection fluorescence microscopy (TIRFM) has become an indispensable tool to study cellular organization and dynamic processes that occur near the cell culture and glass substrate interface[1]. It has also been used extensively to study molecular dynamics, including diffusion[2-4] and absorption[5,6], at liquid/solid interfaces. All of these applications rely on TIRFM's ability to selectively excite fluorophores very close to the interface while minimizing background fluorescence from out-of-focus planes. An evanescent field (EF) is produced when an incident light beam travelling from a medium of high refractive index ($n_1$) into a medium of low refractive index ($n_2$) at an incident angle ($\theta$) greater than the critical angle ($\theta_c$), which is defined as $\theta_c = \sin^{-1}(n_2 / n_1)$. The EF intensity ($I$) exponentially decays with the vertical distance ($z$) from the interface, and drops to 1/e of the value at the interface over the penetration depth ($d$). The $d$ value is well defined for a given interface as it depends theoretically only on the incident angle and the wavelength of the incident light ($\lambda$). However, the characteristic EF depth in an actual sample may deviate from theoretical values for several reasons, including the polarization of the excitation light, the orientation of the dipoles, the unevenness of light illumination, refractive index mismatch, non-uniform fluorescence emission near a dielectric surface, and optical interference between the direct and reflected emission beams.

The calibration of the evanescent field in a homogeneous sample can be carried out with quantum dots or fluorescent beads on the tip of an AFM arm[7] or a graphite pencil[8] or a patch pipette[9], fluorescent beads attached onto a convex lens or settled on a cell surface[10], large spherical beads (8.85 μm diameter) on a flat glass slide[11], a known fluorophore distribution between a convex lens and a flat prism surface[12], or tilted microtubules in gel[13]. With the calibration data, axial distances can then be estimated with much improved accuracy in a number of different means. The ratio of fluorescence intensities from sequential acquisitions with fixed-angle TIRFM and wide-field (WF) microscopy[14,15] or from two-angle TIRFM[16] can give good estimates of axial distances, while more depth-resolved information is obtainable with prism or objective-based variable-angle (VA) TIRFM[4,12,13,17,18] in which a stack of multi-angle images contains the integrated fluorescence intensity over various thicknesses of the sample.

The prism-type VA-TIRFM generally provides several benefits over its objective-based counterpart, such as a wider range of incident angles, higher accuracy in incident angle determination, less excitation light scattering, and lower cost. In a typical prism-based VA-TIRFM system, a set of rotatable mirrors and micro-stepper motors are used to direct the center of the laser beam onto a specified spot on a sample at a wide range of incident angles. The parameters are recorded and later used to capture images at these calibrated incident angles. Re-calibration is often necessary before a new sample is imaged. The performance of the system largely depends on the accuracy, precision, and reproducibility of the tedious, time-consuming calibration procedure.

In the present work, we introduce a new auto-calibration scanning-angle (ACSA) TIRFM setup. An optimized system layout and an automatic high-precision calibration procedure were implemented to find the incident angles in the full range (from subcritical angles to nearly 90°) with an interval of 0.2°. The entire auto-calibration procedure can be finished within minutes. At each incident angle, the automatic calibration (or re-calibration) was designed to overlap the center of laser illumination spot with the center of the microscope field of view. Once calibrated, the system scans through the whole range of incident angles reliably and reproducibly, and the measured fluorescence intensities can follow the decay functions more closely with smaller relative errors than any other existing VA-TIRFM system, resulting in better practical resolution in the axial direction.

To demonstrate the precision of the system, we used ACSA-TIRFM to find the exact incident angle that produced the most intense evanescent field for a given interface between gold-film-coated coverslip and water solution while a p-polarized (in the plane of incidence formed by the incident and reflected beams) incident laser beam was used. To demonstrate the high axial resolution in practice, we resolved fluorescent nanospheres buried in agarose gel in different vertical positions. And the setup was further applied to image tilted fluorescent microtubules in agarose gel.

## Experimental

**Imaging system.** Figure 1 shows the schematic representation of the apparatus that was designed and built in the present study. A Nikon Optiphot-2 microscope equipped with a Plan Fluor 100x/NA 1.3 objective and an Andor iXon$^{EM}$+ 897 camera (Belfast, Northern Ireland; 512×512 imaging array, 16 μm × 16 μm pixel size) were used as the center piece. In order to reduce the sample drifting, the original microscope stage was replaced by a Sutter MP-285 motorized high precision three-dimensional translational stage (Novato, CA). An equilateral fused silica prism (Melles Griot, Albuquerque, NM) was housed in a home-made prism holder that was fixed on the Sutter stage. A 40-mW 640-nm solid-state continuous wave (CW) laser (Coherent, Santa Clara, CA) and a 45-mW 532-nm solid-state CW laser (Uniphase, San Jose, CA) were employed for excitation. Nearly identical arrangements of the optics and stages were set up on both sides of the prism to direct laser beams towards the imaging area. On either side, the laser beam was first pointed to a periscope, passed through a Uniblitz mechanical shutter (model LS2Z2, Vincent Associates, Rochester, NY) and a focusing lens (15-cm focal length), and then was directed towards the mirror of a galvanometer optical scanner (model 6220, Cambridge Technology, Cambridge, MA). The focusing lens was used to control the laser spot size in the imaging area. The mirror of galvanometer was coupled to a high precision motorized linear stage (model MAA-PP, Newport, Irvine, CA), and directed the focused laser beam through the equilateral prism to sample prism interface at different incident angles. Both the angle and the vertical position of the mirrors were controlled simultaneously by a home-written computer program.

### Chemical and sample preparation

**Resolving fluorescent nanospheres buried in agarose gel in different vertical positions.** 1.5% agarose gel was prepared by dissolving 1.5 mg agarose powder in 1ml 18.2 MΩ pure water containing oxygen scavenging system through heating in water bath. The gel solution was kept warm to avoid solidification. 28nm diameter fluorescent nanospheres were diluted to proper concentration in agarose gel solution. Then the gel solution of nanospheres was put on the surface of TIRF prism and was covered with a clean coverslip quickly. When the gel solution cooled to room temperature, it solidified, and trapped the nanospheres in different vertical positions randomly in the three dimensional network of gel.

**Surface plasmon resonance (SPR) angle finding for gold metal film enhanced TIRF.** Coverslips of 22mm×22mm (Zinc Titania glass, refractive index 1.523 at sodium D line, Corning, NY) were thoroughly cleaned in an ultrasonic bath twice in Contrad 70 detergent solution (Decon Labs, King of Prussia, PA), 4 times in 18.2MΩ pure water and twice in pure ethanol. Each time for sonication was 30 mins. After blown dried with pure nitrogen gas, the coverslips were deposited with 5nm of chromium followed by 30nm of gold in an Airco Temscal BJD1800 E-beam evaporator (Berkeley, CA). In order to let the negative charged 28 nm diameter fluorescent nanospheres (Duke scientific, Palo Alto, CA) be attached to gold surface, the coverslips were immersed with 100μg/ml PLL solution for 2 hours first. Nanospheres were diluted to proper concentration in 18.2MΩ water containing oxygen scavenging system, which was composed of 0.5 mg/ml glucose oxidase (Sigma), 40 μg/ml catalase (Sigma), 10% (w/v) glucose (Sigma) and 1% (v/v) β-mercaptoethanol (Fluka). The oxygen scavenging system was applied to reduce photobleaching of fluorescent nanospheres. Then the nanosphere solution was loaded on PLL modified gold coated coverslip, and was covered with a clean coverslip. The sample slide was put on prism surface and ready for imaging. When imaging with TIRF, 532nm longpass filter (Chroma, Rockingham, VT) was applied to filter away the excitation light from the emission fluorescence light.

**Imaging tilted fluorescent microtubule buried in agarose gel.** Rhodamine labeled tubulin protein was obtained from Cytoskeleton (Denver, CO). And it was polymerized to form microtubules according to the protocol provided by the company. The microtubules were diluted to proper concentration in 1.5% agarose gel solution containing oxygen scavenging system. Then the microtubule gel solution was put on the surface of prism and was covered with a clean coverslip quickly.

## Results and Discussion

### Automatic angle scanning and vertical position calibrating

Fluorescent nanospheres were used to calibrate the incident angles. These nanospheres were immobilized on the positively charged prism surface modified with poly-L-lysine (PLL).

The collected fluorescence intensity at a given incident angle also depends on the horizontal position of the laser spot on the prism surface. Only when the center of the laser spot overlaps perfectly with the center of the objective lens, the fluorescence intensity is at the highest level. Furthermore, if the overlapping of two centers is consistently achieved at every incident angle, the angle scanning process can produce highly reproducible and correlated depth information of objects located in the EF.

The horizontal position of the laser spot was adjusted through changing the vertical position of galvanometer's mirror. Then the fluorescence intensity was used as the standard to calibrate vertical position of galvanometer's mirror. A home-written computer program was used to control the angle of galvanometer's mirror and its vertical position simultaneously. After inputting certain angle for galvanometer's mirror, computer first controlled the motorized linear stage to scan the vertical position of galvanometer's mirror step by step. After each step, the fluorescence image was recorded by EMCCD and analyzed. During the first round, the distance between two successive steps was set relatively large. This step was called rough scan. After rough scan, a rough vertical position for galvanometer which gave relatively highest florescence intensity was got. Then second scan called fine tune began. During fine tune scan, computer controlled galvanometer's mirror to move around the rough position again but with a smaller step size. After fine tune, a more precise vertical position for galvanometer's mirror was obtained. And more runs of fine tune can be repeated if required. After recording the vertical position for the first angle, computer inputted following angle values, and repeated rough scan and fine tune until getting all the vertical positions for the whole angle range used in the experiment. All those data for angle and vertical position were recorded, and could be reloaded when starting new experiments.

**Determination of the *z*-position of a dye-doped nanosphere in angle-scanning TIRFM**

The exponential decay of the *EF* intensity is described[19]:

$$I(z) = I(0)e^{-z/d(\theta)} \qquad (1)$$

where *I* is the intensity of the evanescent field; *z* is axial distance from the TIR interface; $d(\theta)$ is the characterization penetration depth as a function of the incident angle $\theta$ of the illumination beam:

$$d(\theta) = \frac{\lambda}{4\pi\sqrt{(n_1 \sin\theta)^2 - n_2^2}}\ , \qquad (2)$$

where λ is the wavelength of the incident light, $n_1$ and $n_2$ are the refractive indices of the optically more condensed and less condensed media. For *s*-polarized incident light (the polarization direction perpendicular to the plane of incidence), the *EF* intensity at the interface (z = 0) is:

$$I(0) = I_{\text{in}} \frac{4\cos^2\theta}{1 - n_2^2/n_1^2}\ , \qquad (3)$$

where $I_{in}$ is the intensity of the incident light. When a dye-doped nanosphere is placed in the *EF*, the total emitted fluorescence is:

$$F(\theta) = k\varepsilon q \int_{z1}^{z2} w(z) I(0) e^{-z/d(\theta)} dz = k\varepsilon q I_{\text{in}} \frac{4\cos^2\theta}{1 - n_2^2/n_1^2} \int_{z1}^{z2} w(z) e^{-z/d(\theta)} dz\ , \qquad (4)$$

where *k* is a constant instrumentation factor; *ε* is the molar extinction coefficient of the fluorophore; *q* is the quantum efficiency; *w*(*z*) is the number of the dye molecules in the *z* + dz layer. When the size of the nanosphere is small compared to the penetration depth and the dye molecules are homogeneously doped, the geometrical center of the nanosphere nearly overlaps with the center of fluorescence.[8] The integral term in Equation 4 can be simplified:

$$F(\theta) = k\varepsilon q I_{\text{in}} \frac{4\cos^2\theta}{1 - n_2^2/n_1^2} c(z) V e^{-z/d(\theta)} = B\cos^2\theta e^{-z/d(\theta)}\ , \qquad (5)$$

where *V* is the volume of the nanosphere; *c*(*z*) is the concentration of the dye molecules in the sphere; *B* is a constant to account for all the variables that remain unchanged in Equation 4. Thus, the absolute *z*-position of a nanosphere can be determined through non-linear least squares (NLLS) fitting by measuring the fluorescence intensity at several different incidence angles of the illumination light.

**Precision of the *z*-determination**

Figure 2A shows the fluorescence intensity profile of a 28 nm, dye-doped polystyrene nanosphere on the quartz prism/water interface at 60 different incident angles between 67.2°

(critical angle) and 82.6°. Each data point was the average of 5 measurements and the signal was the integrated fluorescence from whole particle subtracting the non-fluorescence background. The center position of the nanosphere in the axial direction is determined to be 15 ± 2.8 nm by NLLS fittings using Equation 5, consistent with the geometrical center (14 nm or half of the diameter).

It is important to note that there can be significant uncertainties in the *z*-values determined through NLLS fittings. Estimation of the uncertainties of the derived values in NLLS fittings is often-ignored in the literature, yielding results of little statistical importance. Some literature report uncertainties based on asymptotic standard errors (ASEs) assumption, which usually underestimates the actual uncertainties in the recovered values.

Here, we examined the uncertainty of the fitted *z*-value by support plane analysis[20] over the $\chi^2$-surface. $\chi^2$ is defined as:

$$\chi^2 = \sum_1^m \frac{1}{\sigma_m^2}[F_{\exp} - F_{\text{theor}}]^2, \qquad (6)$$

where the summation is over *m* number of data points; $\sigma_m$ is the standard deviation obtained from 5 measurements at each incident angle; $F_{exp}$ and $F_{theor}$ are the experimental and theoretical fluorescence intensities, respectively. The detailed procedure to obtain the standard deviation of the axial position is to vary *z* close to its fitting value where $\chi^2$ reaches the global minimum - $\chi^2(min)$. At each fixed *z*-value, the minimum $\chi^2$, $\chi^2(par)$, is re-sought by floating the other parameter(s) (e.g., *B* in Equation 5). The uncertainty of *z* can then be estimated from $F_\chi$-statistic appropriate for *p* parameters and *v* degrees of freedom:

$$F_\chi = \frac{\chi^2(par)}{\chi^2(\min)} = 1 + \frac{v}{p} F(p, v, P), \qquad (7)$$

where *P* is the probability that the value of $F_\chi$ is due to random errors in the data. When *P* is smaller than 0.32, there is a 68% probability that the *z*-value yielding a corresponding $F_\chi$ is consistent with the experimental data, which is the usual definition of one standard deviation.

For our measurements, $F_\chi$ with 2 parameters (*p*) and 60 degrees of freedom (*v*) with a probability (*P*) of 0.32 is 1.039. When $\chi^2(par)$ is 1.039 times of $\chi^2(min)$, the two corresponding *z* values are 12.3 and 17.8 nm, respectively (Figure 2A inset). Thus, the corresponding standard deviation for determined *z* is 2.8 nm, which results in an axial resolution of 8.4 nm. This precision in determining the axial resolution is so far the best in the literature that were derived through a strict statistical analysis.

There are two main features of our setup that allow us to reach this high precision. The first is that our setup automatically calibrates the laser spot position when the incidence angle is changed during scanning, ensuring the laser always illuminates center of the field of view under a microscope. We are able to scan as many angles as possible with this auto-calibrated system, which is unimaginable when the angles need to be tuned manually. The second is that in the prism-type TIRFM, we can scan a wide range of angles especially for large angles toward 90º. These large angles are important in determining the z-positions and are usually unattainable in objective-type of TIRF microscopy.

To demonstrate the advantages of our setup, we show two examples of how these two features contribute to the precision of the *z*-determination. The first example simulates a manually scanning experiment that has 6 data points. Please note that it is not trivial to manually measure fluorescence intensities at only 6 incidence angles and usually it takes hours for an experienced worker to finish. The 6 data points were arbitrarily chosen from the earlier data set and spanned the whole range of angels. Figure 2B shows the NLLS fittings from these data points. The determined the *z*-values are 11 ± 9.9 nm. The standard deviation was derived similarly through *F*-statistic analysis, with a $F_{□}$ value of 1.456 for 2 parameters and 6 degrees of freedoms. Note that the center of the nanosphere did not change much but the uncertainty of the z-value increased significantly, by a factor of 3.5 (Figure 2B). This is because the fitting results are more susceptible to noises when the number of data points is limited. Apparently, it is more advantageous to scan more angles in order to achieve better axial resolution.

The second example shows that our method is more advantageous than the objective-type TIRF microscopy. The objective-type TIRFM can be automated in calibration and scanning as well and there are already commercial instruments available on the market. However, one practical drawback of objective-type TIRFM is that the incident angle of the illumination beam is limited to a very small range. The large incidence angles (approaching 90º) cannot be reached due to geometric constraints by objective. Here we show that the fluorescence intensities at these large angles are important in determining the z-positions in NLLS fittings. The data points used in the NLLS fittings were chosen from the same fluorescence intensity profile but with a limited range from the critical angle (67.2º) to 72º, a maximum angle that can be practically reached with objective-type TIRFM[13]. The NLLS fittings are shown in Figure 2C and the *z*-values are 9.3 ± 3.1 nm. The center of the nanosphere changed much due to the sampling bias but the uncertainty of the z-value did not increase significantly, only by a factor of 1.1. (Figure 2C inset).

To exam the limit of the z-determination precision with angle-scanning TIRF microscopy, we further studied the theoretical standard deviation through Monte Carlo simulations. The resolution is highly dependent on the measurement errors of the fluorescence intensity at each incident angle. In our experiments, the exposure time of each image was set at 20 ms, resulting in a total collection time of 5 repeated measurements at 60 angles to be within 6 seconds. The standard deviation of the intensity measurements is relatively constant (150 counts/frame/s), indicating the overall noise at this acquisition speed is dominated by the readout noise of the EMCCD camera. In the Monte Carlo simulation, when a flat noise at this level is added to the theoretical fluorescence intensity, the corresponding standard deviation for the determined z-value is 2.0 nm, resulting in an axial resolution of 6.0 nm (Figure 2D). The theoretical resolution is slightly better than our experimental value, which can be ascribed to the stability of the EMCCD camera, the motorized stage, or other instrument factors. (I think this paragraph is not necessary.)

In the literature[8], the axial position of a fluorescent object can also be calculated from:

$$\Delta z = z_2 - z_1 = \ln\frac{F(z_1)}{F(z_2)}, \tag{8}$$

where $F(z_1)$ and $F(z_2)$ are the fluorescence intensities of a fluorescent object at positions $z_1$ and $z_2$, respectively. This method is usually used to dynamically track the z-positions of a particle. The best resolution of this method was reported to be 8 nm[8]. However, it should be noted that this method only reports the relative position difference in the axial direction (□*z*). In order to know the absolute position of the sample at a time *t*, the absolute value of $z_1$ at the beginning time $t_1$ must be known to serve as the reference. However, this criterion is usually difficult to meet in dynamic tracking experiments.

### Resolving *z*-position of fluorescent nanospheres embedded in agarose gel

To demonstrate that we are able to resolve the absolute z-distance of fluorescent objects with angle scanning TIRFM, we buried fluorescent nanospheres in agarose gel and determine their z–distances from the TIR interface. The incident angle of illumination beams was varied to adjust the penetration depth of the evanescent field, allowing the fluorescent particles to show up layer by layer. Figure 3A shows 5 such particles that showed up sequentially as we scanned the incident angle from 90° toward the critical angle. It is obvious that the relative positions of the 3 particles labeled as 1, 2 and 3 have a relationship of $z(1) < z(2) < z(3)$. Their absolute z-positions can be determined with NLLS fittings as mention in the earlier section. Figure 3B shows the NLLS fitting results of the 3 particles, which show apparently different fluorescence intensity profiles as a function of the incident angles. The determined axial positions are 18.5 ± 4.5, 26.9 ± 5.1 and 105.8 ± 8.3 nm, respectively (Figure 3CDE). The standard deviation increases slightly as the axial position increases. This may be a result of decreased total fluorescence intensity as the particles are further away from the total internal reflection interface.

### SPR angle finding for gold metal film enhanced TIRFM

TIRFM is a very good imaging tool which provides high signal to noise ratio. To further improve the fluorescence signal, people used surface plasmon resonance enhanced TIRFM through introducing a thin metal film in the total internal reflection interface such as silver, aluminum or gold. The incident angle of excitation laser beam plays a very important role in obtaining metal film enhanced TIRFM. The angle at which fluorescence can be enhanced most is usually called SPR angle. If the incident angle is away from SPR angle, fluorescence signal can be enhanced very little, or even reduced much compared to signal from TIRFM without metal film. In this work, gold film enhanced TIRFM was studied. Normally, SPR angle was found by changing the incident angle degrees by degrees manually, which was time consuming and labor intensive. In our work, SPR angle was found quickly through automatic scanning and calibration with time less than 2mins.   Meanwhile the angle increment was 0.18°, which was much smaller than that done by other researchers [21,22], and then the SPR angle obtained in our work was more precise.

As shown in fig 4, the angle range scanned was from 60.3° to 70.2° with 55 intervals, and the SPR angle found was 66.5°. The refractive index of coverslip was 1.523, and the refractive index of buffer used in experiment was measured to be 1.346. From calculation, the theoretical critical angle was 62.1°, which is 4.9° smaller than the SPR angle, which was consistent with other researchers' observation[23]--the SPR angle was larger than the critical angle. From the experimental images, it was also found that actual total internal reflection occurred at 60.4° not at 61.6°. When incident angle was smaller than 60.4°, the 532nm excitation laser leaked into the background of images. It happened only because incident light was not 100% totally reflected, which means refraction also existed at that angle. The difference between actual critical angle value and theoretical value can be explained. Since the refractive index of coverslip was measured at wavelength around 590nm, while the laser wavelength used for in this experiment was 532nm, the refractive index of coverslip is not exactly 1.523, but is some value larger than 1.523. As a result, the actual critical angle is smaller than previously calculated theoretical value 61.6°. And through calculation, the refractive index of coverslip used in this work is 1.548 at 532nm.

The fluorescence intensity at SPR angle was around 1.16 times as that at critical angle without gold film. According to reported result[24], 20nm gold film can enhance fluorescence 1.57 times, which is larger than 1.16 times. Considering that 30nm gold film used in our experiment was 50% thicker and gold does not transmit light well, it is reasonable that more energy of excitation laser was absorbed and reflected when laser tried to pass through the gold film used in our work. Then the emission fluorescence intensity collected would be lower. As a result, the fluorescence intensity enhancement was reduced from 1.57 to 1.16.

**Imaging tilted fluorescent microtubules buried in agarose gel**

To further demonstrate the penetration depth change of this setup, tilted microtubules buried in agarose gel was studied. As shown in fig 5B, when using epi-fluorecence microscopy, the whole microtubules were illuminated. While using VA-TIRFM, the microtubules were not illuminated at the same time, but coming out section by section (fig 5B). The image result demonstrates that the particular microtubule did not lie horizontally flat in gel, but with a tilted angle. And the depth difference of different parts in one single microtubule was resolved by VA-TIRFM.

3 points in the same microtubule which were equally 635nm spaced in horizontal direction were chosen to analyze their axial positions. Through fitting their fluorescence intensity decay curve (fig 5C), their vertical positions were extracted as: 75.1 nm, 125.9 nm, and 176.3 nm. The angle of the tilted microtubule was calculated to be 4.6°.

## Conclusion

An automatic angle scanning total internal reflection microscope was built which can scan angle with increment less than 0.2°. The instrument can give axial resolution better than 10 nm. By using the instrument, SPR angle of gold film enhanced TIRFM was found quickly and precisely. And the angle of tilted microtubule in agarose gel was extracted.

When TIRF is used to study cell systems, basal membrane at the sites where cells are attached to the substrate was imaged most of the time, while the apical membrane was rarely studied[25]. There are two main reasons which make it difficult to adjust the incident angle to let TIRF occur in the apical interface: the difference between the refractive indices of the cytoplasm and the culture medium is too slight, and the apical membrane is not flat. The problem can be overcome since our instrument can change the angle with tiny increment. Additionally, when the incident angle is changed within the subcritical angle range, the instrument can be further applied to do variable-angle epi-fluorescence[26].

## References

(1) Axelrod, D. In *Biophysical Tools for Biologists, Volume Two: In Vivo Techniques*; 1 ed.; Correia, J. J., Detrich, H. W., Eds.; Academic Press: 2008; Vol. 89, p 169-221.

(2) Xu, X. H.; Yeung, E. S. *Science* **1997**, *275*, 1106-1109.

(3) Xu, X. H. N.; Yeung, E. S. *Science* **1998**, *281*, 1650-1653.

(4) He, Y.; Li, H. W.; Yeung, E. S. *Journal of Physical Chemistry B* **2005**, *109*, 8820-8832.

(5) Kang, S. H.; Shortreed, M. R.; Yeung, E. S. *Analytical Chemistry* **2001**, *73*, 1091-1099.

(6) Kang, S. H.; Yeung, E. S. *Analytical Chemistry* **2002**, *74*, 6334-6339.

(7) Sarkar, A.; Robertson, R. B.; Fernandez, J. M. *Proceedings of the National Academy of Sciences of the United States of America* **2004**, *101*, 12882-12886.

(8) Saffarian, S.; Kirchhausen, T. *Biophysical Journal* **2008**, *94*, 2333-2342.

(9) Oheim, M.; Loerke, D.; Stuhmer, W.; Chow, R. H. *European Biophysics Journal with Biophysics Letters* **1998**, *27*, 83-98.

(10) Steyer, J. A.; Almers, W. *Biophysical Journal* **1999**, *76*, 2262-2271.

(11) Mattheyses, A. L.; Axelrod, D. *Journal of Biomedical Optics* **2006**, *11*, 7.

(12) Olveczky, B. P.; Periasamy, N.; Verkman, A. S. *Biophysical Journal* **1997**, *73*, 2836-2847.

(13) Gell, C.; Berndt, M.; Enderlein, J.; Diez, S. *Journal of Microscopy-Oxford* **2009**, *234*, 38-46.

(14) Omann, G. M.; Axelrod, D. *Biophysical Journal* **1996**, *71*, 2885-2891.

(15) Merrifield, C. J.; Feldman, M. E.; Wan, L.; Almers, W. *Nature Cell Biology* **2002**, *4*, 691-698.

(16) Lanni, F.; Waggoner, A. S.; Taylor, D. L. *Journal of Cell Biology* **1985**, *100*, 1091-1102.

(17) Loerke, D.; Stuhmer, W.; Oheim, M. *Journal of Neuroscience Methods* **2002**, *119*, 65-73.

(18 ) Rohrbach, A. *Biophysical Journal* **2000**, *78*, 2641-2654.

(19) Stock, K.; Sailer, R.; Strauss, W. S. L.; Lyttek, M.; Steiner, R.; Schneckenburger, H. *Journal of Microscopy-Oxford* **2003**, *211*, 19-29.

(20) Lakowicz, J. R. *Principles of Fluorescence Spectroscopy* 3rd ed.; Springer, 2006.

(21) Matveeva, E. G.; Gryczynski, I.; Barnett, A.; Calander, N.; Gryczynski, Z. *Analytical and Bioanalytical Chemistry* **2007**, *388*, 1127-1135.

(22) Borejdo, J.; Gryczynski, Z.; Calander, N.; Muthu, P.; Gryczynski, I. *Biophysical Journal* **2006**, *91*, 2626-2635.

(23) Burghardt, T. P.; Charlesworth, J. E.; Halstead, M. F.; Tarara, J. E.; Ajtai, K. *Biophysical Journal* **2006**, *90*, 4662-4671.

(24) Yokota, H.; Saito, K.; Yanagida, T. *Physical Review Letters* **1998**, *80*, 4606-4609.

(25) Sako, Y.; Minoghchi, S.; Yanagida, T. *Nature Cell Biology* **2000**, *2*, 168-172.

(26) Konopka, C. A.; Bednarek, S. Y. *Plant Journal* **2008**, *53*, 186-196.

## Figure Captions

Figure 8.1**.** Schematic experimental setup for two color automatic angle scanning prism type total internal reflection fluorescence microscopy (TIRFM). M, mirror; S, mechanical shutter; FL, focusing lens.

Figure 8.2. Non-linear least squares (NLLS) fittings for the axial position of fluorescent nanospheres according to their fluorescence intensity profile as a function of the incidence angles of the illumination beam. The fluorescent particles are 28 nm polystyrene particles doped with dye molecules. The fluorescence intensities are the average of 5 measurements at 60 different incident angles ranging from 67.2° (the critical angle) to 82.6° degrees. The solid dots are experimental data and the red curve is the NLLS fitting according to Equation 6. The insets are the $\gamma^2$surface to show one times of the standard deviation of the fittings. The dashed line is the threshold at which there is a 68% probability that the corresponding *z*-value is consistent with the experimental data. (A) The fitting from the whole data set consisting of 60 angles ranging from 67.2° (the critical angle) to 82.6° degrees. (B) The fitting from a subset containing 6 data points to simulate a manual scanning experiment. (C) The fitting from a subset that spans from 67.2° (the critical angle) to 72° to simulate an objective-type TIRFM experiment. (D) The fitting from Monte Carlo simulation.

Figure 8.3. Fluorescent nanospheres imbedded in agarose gel. (A) Five nanospheres illuminated at the incident angles of 80.5° (a), 75.9° (b), 71.9° (c) and the critical angle 67.4° (d). Image (e) was taken when the incident angle (64.4°) was smaller than critical angle. Particles 1, 2 and 3 became detectable one by one when they were illuminated in the evanescent field with incident angle is varied toward the critical angle. (B) The fluorescence intensity profiles of particles 1, 2 and 3 as a function of the incident angle. Each curve was normalized to the intensity at the critical angle. (C), (D) and (E) are the NLLS fittings according to Equation 6. The insets show the one time of the standard deviation of the NLLS fittings. The vertical positions of particles 1, 2 and 3 are 18.5 ± 4.5, 26.9 ± 5.1 and 105.8 ± 8.3 nm, respectively.

Figure 8.4. SPR angle for gold film enhanced TIRFM. The curve with a peak is from gold film enhanced TIRFM; the angle for the peak is 66.5°. To get this curve, P-polarized laser was used as the excitation light. The curve without an obvious peak is from TIRFM without gold film. To get this curve, S-polarized light was used as the excitation light. The cartoon inserted shows the schematic setup for the experiment.

Figure 8.5. Tilted fluorescent microtubules in agarose gel illuminated when changing incident angle of excitation laser. The cartoon inserted (A) shows the schematic position of the tilted microtubule in agarose gel. The microtubule marked with * (B) was chosen to calculate tilting angle. The fluorescence decay curves (C) of 3 points which are 635 nm spaced in horizontal direction along the microtubule are fitted according to equation 6. The vertical distance differences between the 3 points are 50.8 and 50.4 nm. The angle of the tilted microtubule is $\theta=\arctan(50.6/635)=4.6^\circ$.

# Figures

Figure 8.1

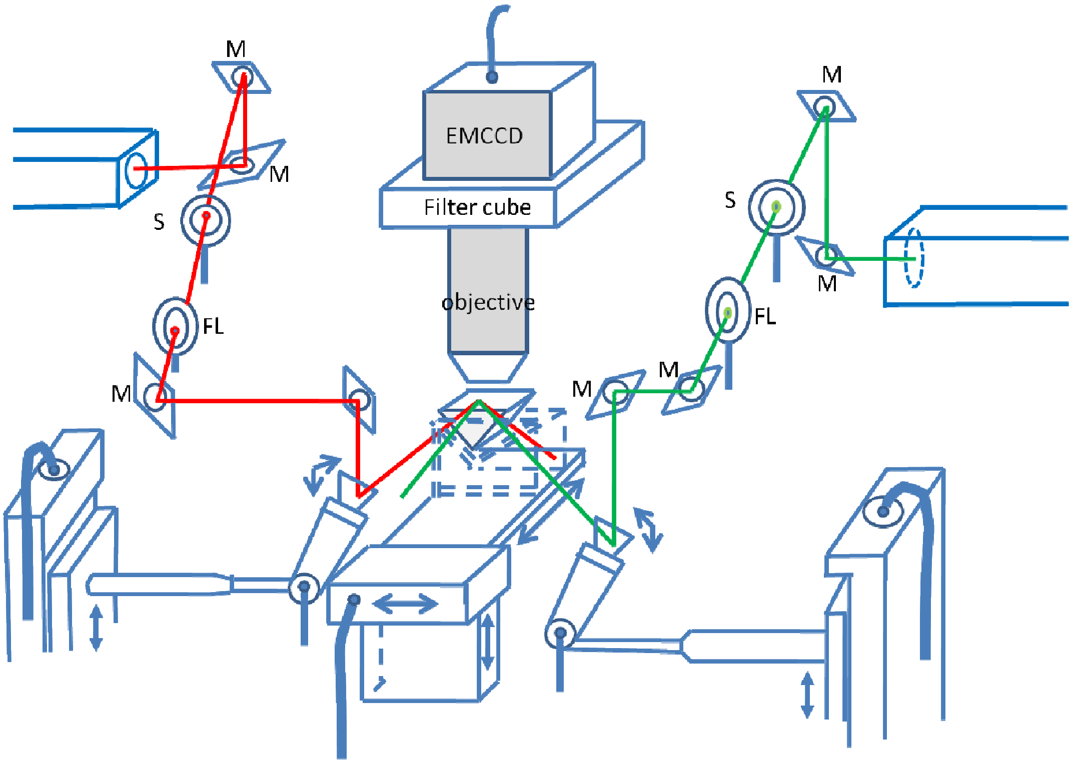

M: mirror S: shutter FL: focusing lens

Figure 8.2

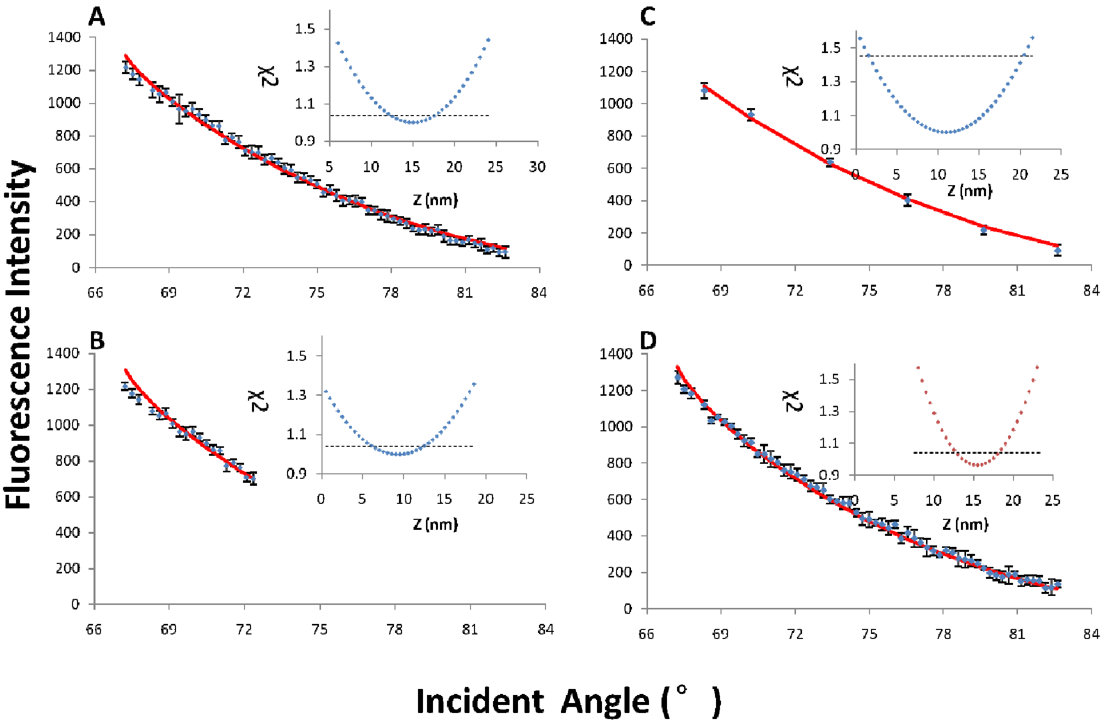
A
B
C
D
Fluorescence Intensity
Incident Angle (° )
χ2
Z (nm)
0
200
400
600
800
1000
1200
1400
66
69
72
75
78
81
84
0.9
1.1
1.3
1.5
0
5
10
15
20
25
30

Figure 8.3

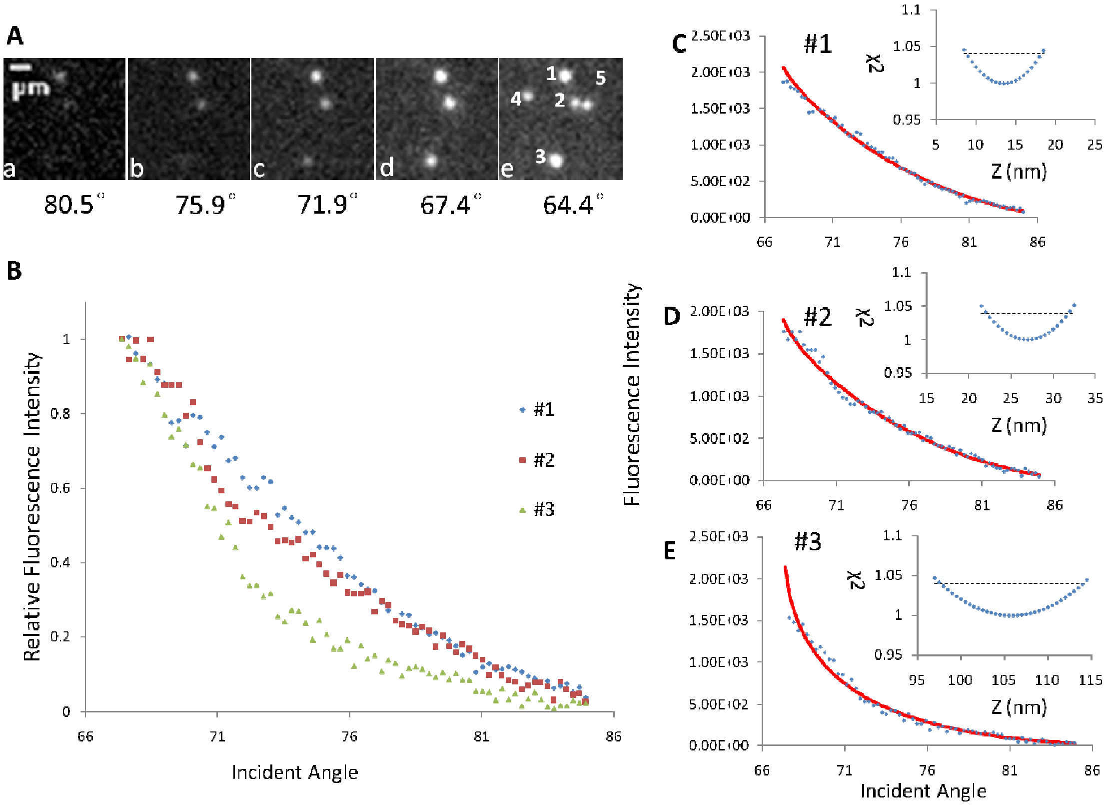
A
µm
a
b
c
d
e
1
2
3
4
5
80.5°
75.9°
71.9°
67.4°
64.4°
B
Relative Fluorescence Intensity
1
0.8
0.6
0.4
0.2
0
66
71
76
81
86
Incident Angle
#1
#2
#3
C
#1
2.50E+03
2.00E+03
1.50E+03
1.00E+03
5.00E+02
0.00E+00
66
71
76
81
86
χ2
1.1
1.05
1
0.95
5
10
15
20
25
Z (nm)
Fluorescence Intensity
D
#2
2.00E+03
1.50E+03
1.00E+03
5.00E+02
0.00E+00
66
71
76
81
86
χ2
1.1
1.05
1
0.95
15
20
25
30
35
Z (nm)
E
#3
2.50E+03
2.00E+03
1.50E+03
1.00E+03
5.00E+02
0.00E+00
66
71
76
81
86
Incident Angle
χ2
1.1
1.05
1
0.95
95
100
105
110
115
Z (nm)

Figure 8.4

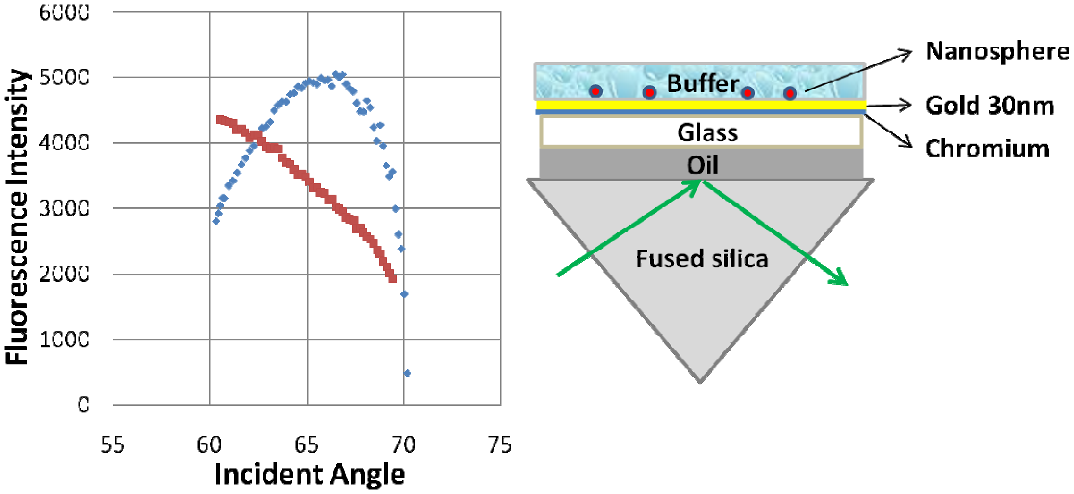
6000
5000
4000
3000
2000
1000
0
Fluorescence Intensity
55
60
65
70
75
Incident Angle
Buffer
Glass
Oil
Fused silica
Nanosphere
Gold 30nm
Chromium

Figure 8.5

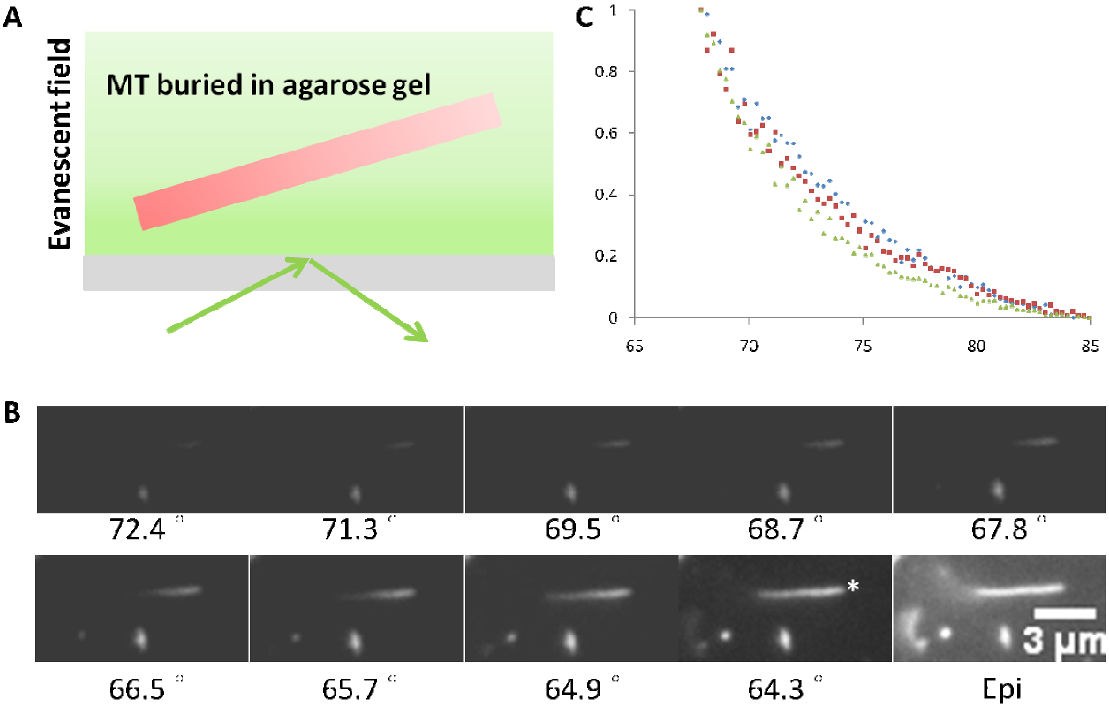
A
Evanescent field
MT buried in agarose gel
C
1
0.8
0.6
0.4
0.2
0
65
70
75
80
85
B
72.4 °
71.3 °
69.5 °
68.7 °
67.8 °
66.5 °
65.7 °
64.9 °
64.3 °
*
3 μm
Epi

# CHAPTER 9. WHOLE CELL SCAN USING AUTOMATIC VARIABLE-ANGLE AND VARIABLE-ILLUMINATION-DEPTH PSEUDO TOTAL INTERNAL REFLECTION FLUORESCENCE MICROSCOPY

Wei Sun, Aoshuang Xu, Kyle Marchuk, Gufeng Wang, and Ning Fang

Accepted by Journal of the Association for Laboratory Automation, 2010

## Abstract

An automatic calibration and angle-scanning prism-type total internal reflection fluorescence microscope (TIRFM) was modified to function both as TIRFM and pseudo TIRFM. When the incident angle of the excitation laser beam was controlled to be larger than the critical angle, the instrument served as variable-angle TIRFM. The homemade computer program automatically calibrated the laser illumination spot in the sample to overlap with the center of the microscope's field of view. Then by measuring the fluorescence intensities at different incident angles, the *z*-positions of those fluorescent nanospheres close to the cell basolateral membrane were extracted. When the incident angle was reduced to be in the subcritical range, the instrument worked as a pseudo TIRFM. And the whole cell body from bottom to top was scanned. Furthermore, the illumination field depth in the pseudo TIRFM can be controlled through changing the incident angle or the horizontal position of the laser spot.

## Introduction

A large number of biological events take place inside a living cell at any moment to keep the cell functioning properly. To have a better understanding of these biological phenomena, researchers have taken great efforts in developing a variety of imaging tools, such as epi-fluorescence, confocal fluorescence and total internal reflection fluorescence (TIRFM) microscopies,[1-3] for specific fluorescent labeling of proteins in both fixed and live cells.[4] Because of the native thin evanescent field, the background noise in TIRFM is much lower than that in epi-fluorescence microscopy.[2, 5] Additionally, unlike confocal fluorescence microscopy, TIRFM has better *z*-resolution and does not require a pinhole in the back focal plane of the objective to block the light leaking from out-of-focus planes. TIRFM has become an indispensable tool to study cellular organization and dynamic processes that occur near the interface of cell culture and glass substrate.[6]

In our previous work,[7] an auto-calibration variable-angle prism-type TIRFM setup was introduced and demonstrated to have a better practical resolution in the axial direction than any other existing variable-angle TIRFM system. An optimized system layout and an automatic high-precision calibration procedure were implemented to find the incident angles with intervals smaller than 0.2° reliably and reproducibly within minutes. Furthermore, it becomes possible to scan the widest range of incident angles from the critical angle to large angles near 90°. A larger number of data points can be collected for a better practical resolution in the axial direction. The large angles that are unattainable in objective-type TIRFM are important in determining the absolute z-positions.

Because the evanescent field is no more than a few hundred nanometers thick, TIRFM is mostly used to study dynamic processes that occur near the basolateral membrane of mammalian cells. However, these dynamic processes often continue beyond the evanescent field. For example, using TIRFM alone is impossible to answer the question about how vesicles formed during endocytosis move away from the membrane towards cell nuclear or other organelles. Another example of TIRFM's limitation in imaging depth is its inability in studies of plant cells.[8] It is difficult for the evanescent wave to penetrate the plant cell wall, because the thickness of the cell wall is usually several hundred nanometers or more, and plant cells often do not lie flat on the substrate. To help solve these technical problems, variable angle epi-fluorescence or pseudo TIRFM[8] was designed to work at subcritical angles that are smaller than yet still close to the critical angle. At a subcritical incident angle, the excitation laser beam is refracted to produce a slanted illumination path. It is possible to extend the illumination depth several micrometers into the cell body.

In the present study, we demonstrate a new microscope system that combines the variable-angle TIRFM and variable-illumination-depth pseudo TIRFM to image the whole cell from the basolateral membrane to the apical membrane. The illumination depth of the slanted refracted light just below the objective lens was regulated by varying the horizontal position of the laser spot at the interface of cell culture and glass substrate, or by adjusting the incident angle.

## Experimental

### Instrumentation

The apparatus used was similar to that described previously,[7] except for one modification: a piezo-actuated z-scanner (P-721, Physik Instrumente, Germany) was coupled to the microscope objective (figure 2A). The scanner offers the ability to change the vertical position of objective’s front focal plane with very high precision. Additionally, when observing the cell structures in bright-field microscopy, the laser for TIRFM was turned off and the illumination light source of the microscope was turned on.

The field of view of the microscope when using 100x objective was around 130µm. If the illumination spot is too large than 130µm, less laser energy can be used to excite the sample in field of view; if the spot is too small, the laser spot can’t fully cover the field of view, and the Gaussian shaped energy distribution inside the laser spot could lead to an annoying uneven illumination in the field of view. It was found that when the diameter of the illumination laser spot was adjusted to be around 150µm by controlling the relative distance between the focusing lens and the prism (figure 2A), the best compromise between laser energy distribution and even illumination in the field of view was obtained.

A computer program (Figure 1) was developed in-house to automatically optimize the horizontal position of the laser spot at each incident angle. After the user enters an incident angle range, the homemade computer program carries out the auto-calibration in two rounds: rough scan and fine-tune. To maintain high precision, the motorized linear stage travels step by step in only one direction. The fluorescence images are recorded by the EMCCD camera at each step. During the rough scan, the vertical step size is set to be relatively large to reduce the time required for a full scan, and the vertical positions of the mirror of galvanometer at all incident angles are obtained from each local maximum of the integrated fluorescence intensities in a chosen area.

Figure 2 shows the details of the scan process. When the incident angle is set at a large value, the laser spot on the prism surface is to the right of microscope objective front lens center (figure 2C-a). Then the program makes the linear vertical stage move up. The higher the stage gets, the more to the left the laser spot on the prism surface moves. During the same time, the program utilizes the EMCCD to record the fluorescence image and calculate the intensity (figure 2B). The collected fluorescence intensity at a given incident angle depends on the horizontal position of the laser spot on the prism surface. The program keeps moving the linear stage up until the laser spot is to the left of the objective front lens center (figure 2C-c) which results the collected fluorescence intensity to decrease (figure 2B). Then signal of the decreasing intensity is sent to the program as feedback and the rough scan process for this incident angle is terminated. All the information about incident angles and vertical positions is recorded. During the round of fine-tune, the program controls the linear vertical stage to move around the "roughly-calibrated" positions again but with a smaller step size to obtain more precise vertical positions. Only when the center of the laser spot overlaps perfectly with the center of the objective lens, the fluorescence intensity is at the highest level (figure 2D). Multiple rounds of fine-tune can be carried out if desired. Then the program updates the information of the angles and positions with the more precise values obtained from fines-tune. The angles and vertical positions are recorded and can be reloaded when starting new experiments.

The speed of the new TIRFM was tested by scanning the incident angle from 82.6°to 67.2° to record fluorescence intensity decay curve of those nanospheres lying on the top surface of the prism. The total number of angles scanned was 64, the exposure time for each angle was 50ms, and it took around 15s to complete the whole scan process. During the scan process, it took a fraction of a second up to a few seconds for the linear vertical stage to travel to the right position for the next incident angle. That accounts for the extra 12 seconds besides the sum of exposure time for the whole scan process. It was noticed that non-essential photo-bleaching could happen if the laser shined the sample during the period required to adjust the vertical position. This problem is avoided by using the homemade program to selectively open the shutter at desired time when the EMCCD camera is required to collect fluorescence signals. In the future, by using higher motion speed linear vertical stage, the time required to perform the whole angle range scan process can be further reduced.

## Sample preparation

**Coverslips coated with metal films.** Thoroughly cleaned coverslips (22mm×22mm, Zinc Titania glass, refractive index 1.523 at sodium D line, Corning, NY) were deposited with 5 nm of chromium followed by 30 nm of gold in an Airco Temscal BJD1800 E-beam evaporator (Berkeley, CA). Then the coverslips were coated with poly-L-lysine (PLL) to generate positively charged surfaces. Negatively charged 28 nm diameter fluorescent nanospheres (Duke Scientific, Palo Alto, CA) were diluted to proper concentration in 18.2MΩ water containing an oxygen scavenging system, composed of 0.5 mg/ml glucose oxidase (Sigma), 40 μg/ml catalase (Sigma), 10% (w/v) glucose (Sigma) and 1% (v/v) β-mercaptoethanol (Fluka). The nanosphere solution was then loaded on a PLL-modified gold-coated coverslip and covered with a clean coverslip. The sample slide was placed on the prism surface. When imaging, a set of one 532 nm longpass filter and one 620/60 nm bandpass filter (Chroma, Rockingham, VT) was put between the EMCCD camera and the microscope to filter away the excitation background from the emission fluorescence.

**Coverslips with cells**. A549 Human lung cancer cells (CCL-185, ATCC, **Manassas, VA)** were cultured in T-25 flasks with minimum essential medium containing 10% fetal bovine serum. When sub-culturing, the cells were seeded on poly-l-lysine (PLL) coated coverslip and grew in 37℃ incubator with 5% $CO_2$ atmosphere. After 24 hours, the cells were incubated in cell culture medium containing 100 nm diameter fluorescent nanospheres for desired time in the same 37℃ incubator. After that, the cells on coverslip were fixed with 3% formaldehyde and 0.1% glutaraldehyde in phosphate buffer at 37℃ for 15 min. Then the cells were immersed in phosphate buffer containing oxygen scavenging system composed of 0.5 mg/ml glucose oxidase (Sigma), 40 µg/ml catalase (Sigma), 10% (w/v) glucose (Sigma) and 1% (v/v) β-mercaptoethanol (Fluka). The oxygen scavenging system helped to reduce photo-bleaching. Finally, the coverslip was put on the TIRFM prism surface for imaging. The same set of filters used above was put between the EMCCD camera and the microscop.

## Results and Discussion

### Precision and reproducibility of instrument

To demonstrate the precision and reproducibility of the system, the new microscope was used to find the exact incident Surface Plasmon Resonance (SPR) angle that produced the most intense evanescent field for metal enhanced TIRFM with a p-polarized (in the plane of incidence formed by the incident and reflected beams) incident laser beam as the illumination light. Two independent runs of the same experiment were carried out. The incident angles at the peak position for the 2 curves were 66.5° and 66.7° respectively. The relative difference between the two values is 0.3% which is very small. The intensity difference between the 2 curves resulted from the photo-bleaching during the first run of the experiment.

### Cell imaging

#### Determination of z-positions of fluorescent nanospheres in cell basolateral part with variable-angle TIRFM

The angle of incident light was first set to be greater than the critical angle so that the instrument functioned as a TIRFM. The incident angle was varied to adjust the penetration depth of the evanescent wave, allowing the fluorescent nanospheres to show up layer by layer. Figure 4 shows such nanospheres inside the cell that showed up sequentially as the incident angle decreased toward the critical angle. These fluorescent nanospheres were distributed in the cell basolateral part which was within several hundred nanometers from the interface of cell culture and glass substrate.

The absolute z-positions of these fluorescent particles can be extracted with the method of NLLS fitting as described in our previous work.[7] Briefly, the fluorescence intensity profile of a chosen nanosphere varies as a function of the incident angle:

$$F(\theta) = A\cos^2\theta e^{-z/d(\theta)} \qquad (1)$$

F(θ) is collected fluorescence intensity; θ is the incident angle; A is the instrument constant; Z is the absolute vertical position of the chosen fluorescent nanosphere; d(θ) is the penetration depth which is defined by the following equation:

$$d(\theta) = \frac{\lambda}{4\pi\sqrt{(n_1 \sin\theta)^2 - n_2^2}} \qquad (2)$$

*$\lambda$ is the wavelength* of the incident light; $n_1$ and $n_2$ are the high and low refractive index of the two media in the TIRF interface. By fitting the fluorescence decay curves with equation (1), the absolute z-positions of the two particles are calculated to be $z_1$ =160 nm and $z_2$ = 280 nm, respectively (figure 4D). The fitting result is consistent with the experimental observation: particle 1 appeared earlier than particle 2 when the incident angle was scanned from large value (66.8°) to small value (64.5°) because particle 1 was closer to the substrate (TIRF interface) than particle 2.

### Imaging fluorescent nanospheres distributed deeper inside the cell with variable-illumination-depth pseudo TIRFM

The instrument functions as a pseudo TIRFM when the incident angle is within the subcritical angle range, that is, a few degrees smaller than the critical angle. The refracted light instead of the evanescent wave penetrates into the cell body and the illumination field depth (the slanted illumination path above the cell culture and glass substrate interface) changes from several hundred nanometers to several micrometers. The narrow subcritical angle range maintains the illumination field close to the substrate, thus providing reasonable signal to noise ratios by keeping the background noise at a low level.

Unlike TIRFM, pseudo TIRFM does not require the center of the laser spot at the cell/glass interface to overlap with the center of the objective lens. When the laser spot is moved away from the center of the objective lens, the refracted laser beam can effectively illuminate much deeper into the cell body.

The micrographs in Figure 5 were taken at the incident angle of 63.5°, less than 1° smaller than the critical angle of 64.4°. The objective's focal plane was scanned from bottom to top through the whole cell body of about 5 μm thick. When the focal plane was set to the cell/glass interface, the fluorescent nanospheres located within the evanescent field of TIRFM could still be detected in pseudo TIRFM with good signal to noise ratios. Then the objective's focal plane was moved away from the interface while the excitation conditions remained constant. More fluorescent nanospheres located deeper inside the cell became detectable layer by layer. Through this scanning process, fluorescent nanospheres at different depths inside the whole cell body were imaged.

To selectively image fluorescent nanospheres within a certain depth inside the cell body, the depth of the illumination field just below the objective lens can be adjusted by changing either the incident angle in the subcritical angle range or the horizontal position of the excitation laser spot at the interface of cell culture and glass substrate. These procedures are demonstrated in Figure 6. Changing incident angle is the only way for objective type pseudo TIRFM to adjust the illumination depth. However, our instrument provides one more option.

## Conclusions

An instrument that can function both as variable-angle TIRFM and variable-illumination-depth pseudo TIRFM was built. When the instrument functioned as variable-angle TIRFM, those fluorescent nanospheres which were close to cell basolateral membrane were imaged and their absolute *z*-positions could be extracted. When the instrument was used as pseudo TIRFM, not only the cell basolateral membrane part, the whole cell could be illuminated. Further, by changing the incident angle or adjusting the horizontal position of the laser spot in the cell culture and glass substrate interface, those fluorescent nanospheres with different vertical positions inside whole cell body could be selectively imaged. It demonstrates that the new instrument can be used to probe the whole cell.

## References

(1) Holz, R. W.; Axelrod, D. *Acta Physiologica* **2008**, *192*, 303-307.

(2) Axelrod, D. In *Biophysical Tools for Biologists, Volume Two: In Vivo Techniques*, 1 ed.; Correia, J. J., Detrich, H. W., Eds.; Academic Press, 2008; Vol. 89, pp 169-221.

(3) Axelrod, D.; Omann, G. M. *Nature Reviews Molecular Cell Biology* **2006**, *7*, 944-952.

(4) Chen, I.; Ting, A. Y. *Current Opinion in Biotechnology* **2005**, *16*, 35-40.

(5) Lang, E.; Baier, J.; Kohler, J. *Journal of Microscopy-Oxford* **2006**, *222*, 118-123.

(6) Wazawa, T.; Ueda, M. In *Microscopy Techniques*; Springer-Verlag Berlin: Berlin, 2005; Vol. 95, pp 77-106.

(7) Sun, W.; Marchuk, K.; Wang, G. F.; Fang, N. *Analytical Chemistry*, *82*, 2441-2447.

(8) Konopka, C. A.; Bednarek, S. Y. *Plant Journal* **2008**, *53*, 186-196.

## Figure Captions

Figure 9.1. The user interface of the home-made auto-calibration auto-scanning software.

Figure 9.2. Schematic experimental setup and the angle scan process for TIRFM. (A) Schematic experimental setup for two color automatic angle scanning prism type TIRFM (only one light path shown). The two light paths are symmetrical at the two sides of the prism. (B) The flow chart explaining how homemade program carries out the angle scan process. (C) The rough angle scan process at a given incident angle. The red dots stand for the fluorescent nanospheres distributed on the prism surface. (D) Experimental images of fine tune process. Top micrograph: the illumination laser spot was to the left of the field of view; middle micrograph: the illumination laser spot overlapped with the center of field of view; bottom micrograph: the illumination laser spot is to the right of the field of view. The right chart is the intensities of 3 chosen fluorescent nanospheres for the 3 left micrographs. X axis stands for 3 nanospheres; Y axis stands for the fluorescence intensity.

Figure 9.3. SPR angle for gold film enhanced TIRFM. (A) Sample preparation and imaging setup illustrating cartoon. (B) 2 Fluorescence intensity curves of the same nanosphere. The 2 curves were generated from two independent runs of the same experiment; the incident angle at the peak position for the 2 curves was 66.5° and 66.7° respectively. The top curve is the 1st run.

Figure 9.4. Fluorescent nanospheres distributed close to the cell basolateral membrane were imaged in variable-angle TIRFM. (A) Schematic graph showing the cell imaged within the EF of TIRFM. The interface of cell culture and glass substrate was pointed out by the black arrow. (B) An A549 cell imaged in bright-field microscopy and TIRFM at an incident angle of 64.5°. The image areas are identical. (C) The TIRFM micrographs of the area defined by the red square in (B). The incident angles are shown at the top-left corner of these micrographs. It is obvious that the relative vertical positions of the two particles labeled as 1 and 2 have a relationship of $z_1 < z_2$. (D) Fluorescence decay curves of the two labeled nanospheres. The NLLS fitting curves are shown in red.

Figure 9.5. Whole cell scanned in pseudo TIRF. (A) Schematic diagram of pseudo TIRFM. The objective's focal plane was adjusted by the objective scanner. (B) Images of cell areas at different vertical depth. The cell was scanned from the basolateral membrane to the apical membrane with 1 μm interval. The whole cell thickness was around 5 μm.

Figure 9.6. Illumination field depth controlled by changing the incident angle or the horizontal laser spot at the interface of cell culture and glass substrate. (A) Schematic diagram showing the illumination field at two incident angles. (B, C) The fluorescence images at two incident angles of 63.5° and 64.0°. The objective's focal plane was fixed at 2 μm away from the cell basolateral membrane. A group of fluorescent nanospheres were imaged at 63.5°, but disappeared at 64.0° due to the shallower illumination field depth at a larger incident angle. (D) Schematic diagram showing the illumination field at the same incident angle but different horizontal positions of the laser spot. (E, F) The fluorescence images at the same incident angle of 62.6° but two different horizontal positions of the laser spot. The objective's focal plane was fixed at the top coverslip. The fluorescent nanospheres absorbed to the top coverslip were not imaged when the laser spot was close to the objective's field of view. They were imaged when the laser spot was moved further away from the objective's field of view.

## Figures

Figure 9.1.

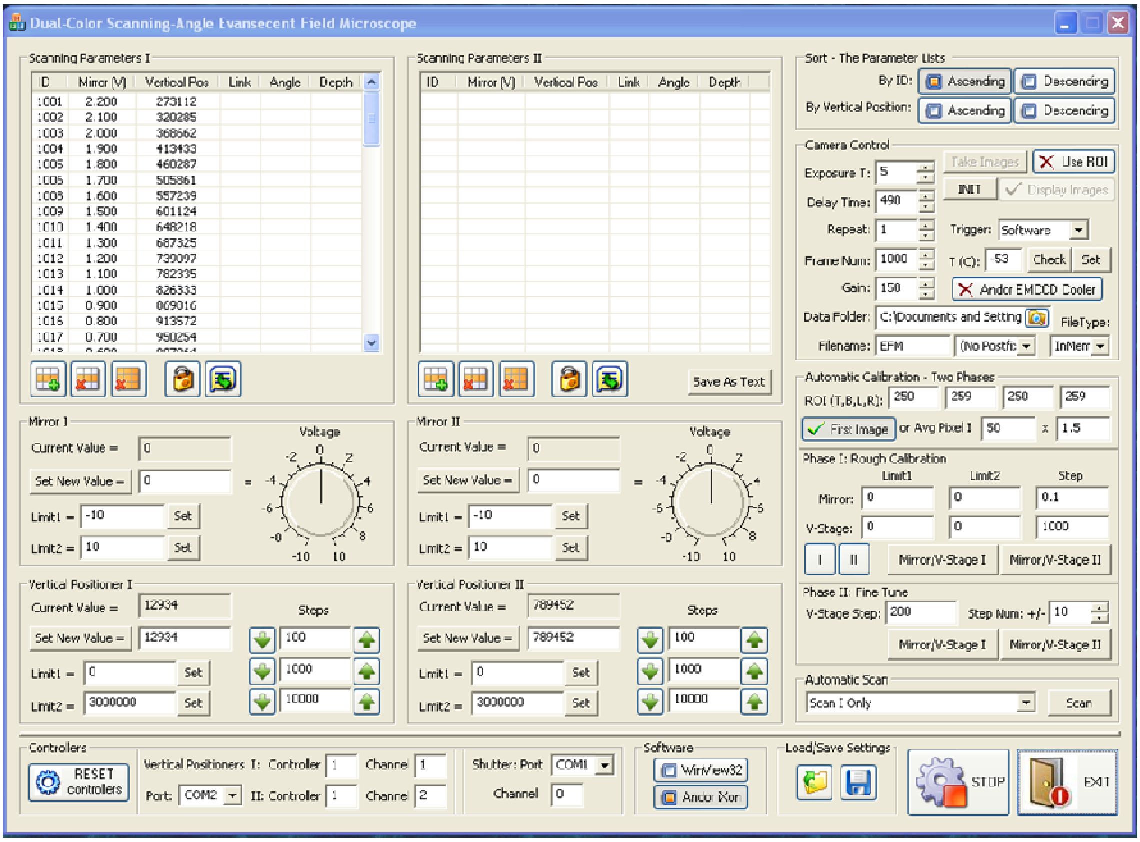

Scanning Parameters I

| ID | Mirror (V) | Vertical Pos | Link | Angle | Depth |
|---|---|---|---|---|---|
| 1001 | 2.200 | 273112 | | | |
| 1002 | 2.100 | 320285 | | | |
| 1003 | 2.000 | 368662 | | | |
| 1004 | 1.900 | 413433 | | | |
| 1005 | 1.800 | 460287 | | | |
| 1006 | 1.700 | 505861 | | | |
| 1008 | 1.600 | 557239 | | | |
| 1009 | 1.500 | 601124 | | | |
| 1010 | 1.400 | 648218 | | | |
| 1011 | 1.300 | 687325 | | | |
| 1012 | 1.200 | 739097 | | | |
| 1013 | 1.100 | 782335 | | | |
| 1014 | 1.000 | 826333 | | | |
| 1015 | 0.900 | 869016 | | | |
| 1016 | 0.800 | 913572 | | | |
| 1017 | 0.700 | 950254 | | | |

Scanning Parameters II

| ID | Mirror (V) | Vertical Pos | Link | Angle | Depth |
|---|---|---|---|---|---|

Mirror I
Current Value = 0
Set New Value = 0
Limit1 = -10
Limit2 = 10

Mirror II
Current Value = 0
Set New Value = 0
Limit1 = -10
Limit2 = 10

Vertical Positioner I
Current Value = 12934
Set New Value = 12934
Limit1 = 0
Limit2 = 3000000
Steps: 100, 1000, 10000

Vertical Positioner II
Current Value = 789452
Set New Value = 789452
Limit1 = 0
Limit2 = 3000000
Steps: 100, 1000, 10000

Camera Control
Exposure T: 5
Delay Time: 490
Repeat: 1
Trigger: Softwars
Frame Num: 1000
T (C): -53
Gain: 150
Data Folder: C:\Documents and Setting
Filename: EFM
(No Postfic
FileType: InMem

Automatic Calibration - Two Phases
ROI (T,B,L,R): 250 259 250 259
or Avg Pixel I 50 x 1.5

Phase I: Rough Calibration

| | Limit1 | Limit2 | Step |
|---|---|---|---|
| Mirror: | 0 | 0 | 0.1 |
| V-Stage: | 0 | 0 | 1000 |

Phase II: Fine Tune
V-Stage Step: 200
Step Num: +/- 10

Automatic Scan: Scan I Only

Controlers
Vertical Positioners I: Controller 1 Channel 1
Port: COM2 II: Controller 1 Channel 2
Shutter: Port COM1
Channel 0

Figure 9.2.

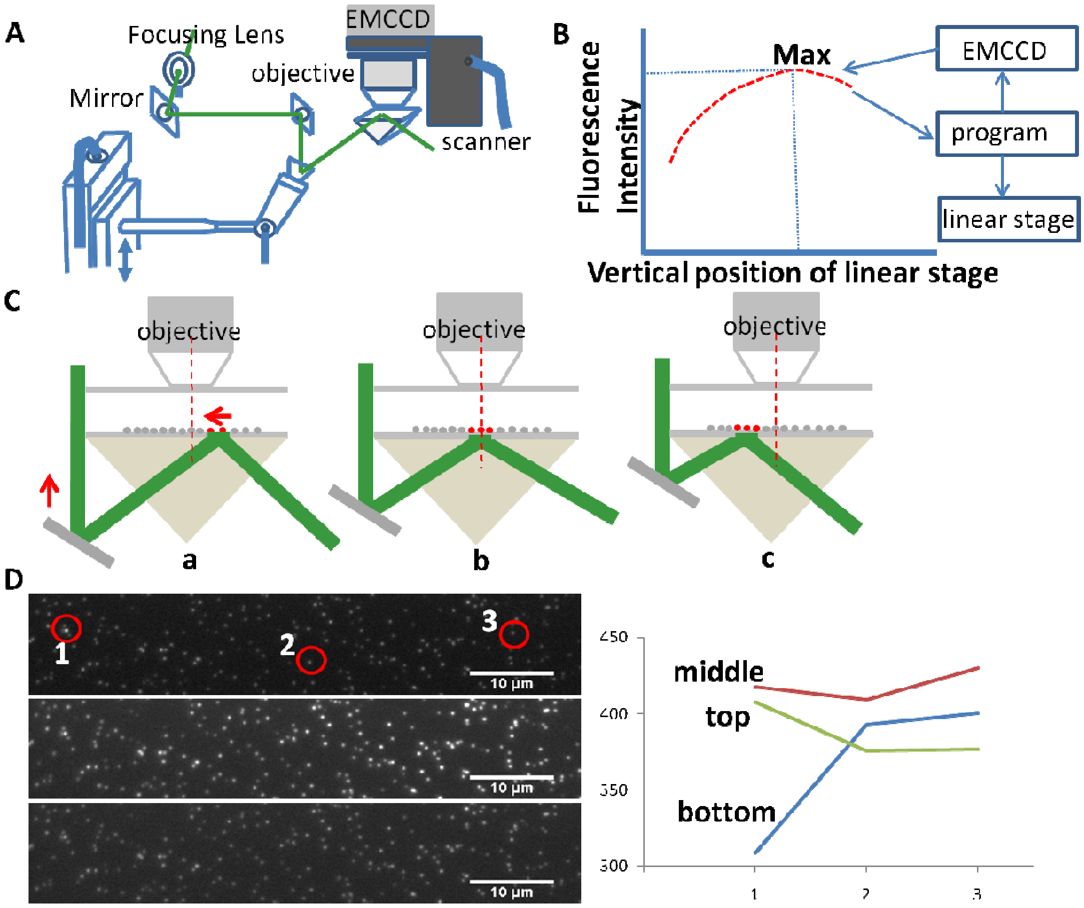
A
Focusing Lens
EMCCD
objective
Mirror
scanner
B
Fluorescence Intensity
Max
EMCCD
program
linear stage
Vertical position of linear stage
C
objective
objective
objective
a
b
c
D
1
2
3
10 µm
10 µm
10 µm
450
400
350
300
middle
top
bottom
1
2
3

Figure 9.3.

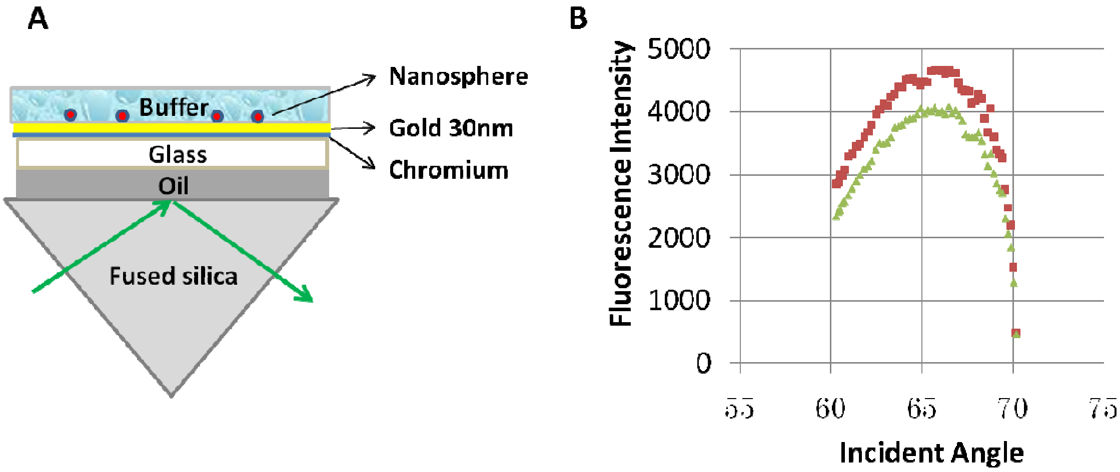
A
Buffer
Nanosphere
Gold 30nm
Chromium
Glass
Oil
Fused silica
B
Fluorescence Intensity
5000
4000
3000
2000
1000
0
55
60
65
70
75
Incident Angle

Figure 9.4.

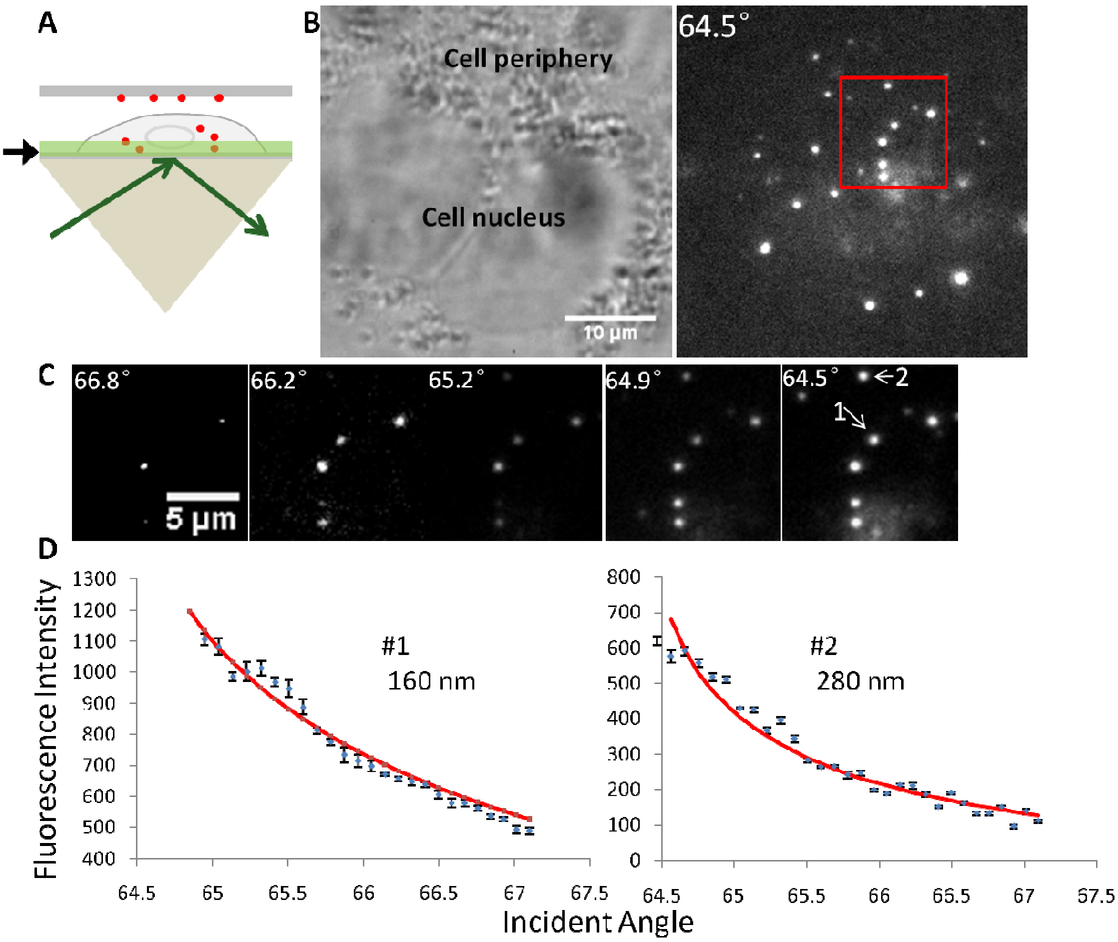
A
B
Cell periphery
Cell nucleus
10 µm
64.5°
C
66.8°
5 µm
66.2°
65.2°
64.9°
64.5°
2
1
D
Fluorescence Intensity
1300
1200
1100
1000
900
800
700
600
500
400
#1
160 nm
64.5
65
65.5
66
66.5
67
67.5
800
700
600
500
400
300
200
100
0
#2
280 nm
64.5
65
65.5
66
66.5
67
67.5
Incident Angle

Figure 9.5.

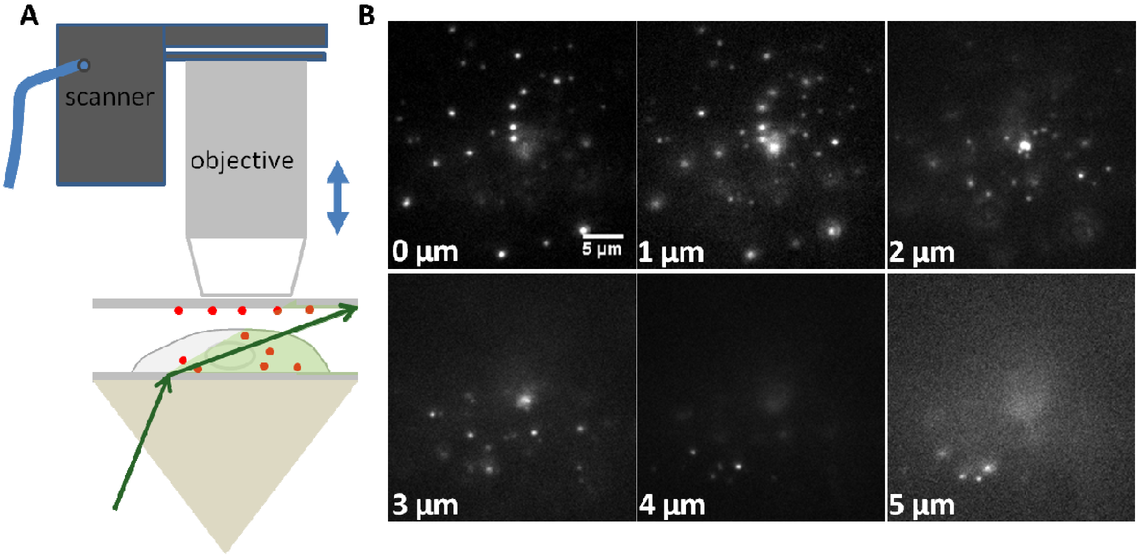

Figure 9.6.

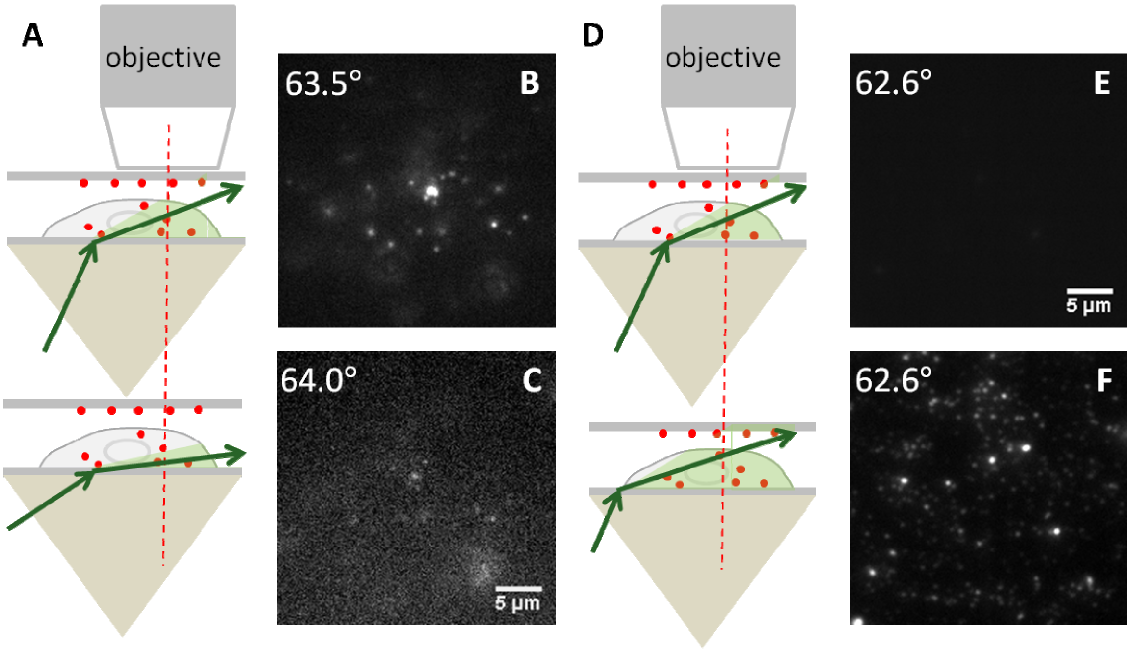

# CHAPTER 10. GENERAL CONCLUSIONS

The work mainly shows the application of modified DIC microscopy and TIRF microscopy in bioanalytical field. Since both of them use far-field detection and wide-field illumination, thus they are non-invasive and can provide high temporal resolution when tracking biological events happening inside live cells.

First, DIC microscopy was successfully used in 3 dimensional tracking of a nanoparticle during the whole endocytosis process in live cells. To overcome the difficulty in distinguishing foreigner nano-probes from native cellular nano-objects which have similar sizes and shapes inside live cells, DIC microscopy was modified to illuminate the sample with two wavelengths that can be selectively changed. In addition, the optical birefringent property of gold nanorods was tested in DIC microscopy. The gold nanorods were further developed as rotational nano-probes based on which a platform of single particle orientation and rotation tracking (SPORT) in live cells was built. Unlike fluorescent probes, gold nanorods don’t introduce photo-bleaching concerns and thus allow researchers to observe infinitely long time in theory. In this work, DIC microscopy was coupled with a highly sensitive and fast detector--EMCCD, dynamic biological processes including endocytosis and intracellular transport were captured, and new rotational information in these two processes was disclosed.

As discussed in chapter 1, no single imaging technique is able to provide researchers all the pursued information, especially in live cell study. A good imaging platform should be compatible with other techniques. For example, a single gold nanoparticle can be detected by DIC and its moving trajectory in live cells can be tracked in DIC. However, the underlying microtubule tracks can’t be directly seen because the microtubules inside cell body produce too weak DIC signals. Then fluorescence labeling and the corresponding fluorescence microscopy technique have to be combined. As shown in chapter 6, the SPORT platform was successfully modified to function as DIC, epi-fluorescence or both modes simultaneously. After modification, the chemical selectivity property of fluorescence microscopy and the high contrast property of DIC microscopy were combined.

Second, an auto-calibrated variable angle TIRFM was built. The axial resolution achieved by using the new instrument can be better than 10 nm. Since TIRFM only illuminates the basolateral cellular part close to the cell culture and substrate interface, the upper part of the cell is beyond the detection scope of TIRFM. To solve this problem, the instrument was modified to function as pseudo TIRFM through adjusting the incident angle of the excitation laser or the horizontal position of the illumination spot on the interface. The illumination depth can be controlled from several tens of nanometers to several micrometers to selectively scan the whole cell body. The new instrument may be a potential tool to study the whole endocytosis, exocytosis or other biological processes happening not only near the cell membrane but also deeper inside the cell body.

The new developed TIRFM instrument can be further combined with other techniques especially STORM. The 20-50 nm lateral resolution provided by STORM and the 10 nm axial resolution obtained in the new TIRFM will make the imaging platform as a super resolution imaging technique in 3D.

## Future Work

In the past several decades, different types of non-fluorescent nanoparticles have been synthesized and studied extensively. These nanoparticles can be made of materials other than pure gold or silver. For instance, it has been reported that nanoparticles can be made of copper or made of mixture materials, such as gold layer coated silica nanoparticles. Besides the materials of the nanoparticles, more and more efforts are being devoted in controlling the morphology of nanoparticles. For example, gold and silver nanoparticles in different shapes, such as nanocubes, nanopyramids and nanostars, have been successfully synthesized. One main reason driving the synthesis is that under different circumstances, different types of nanoparticles may be utilized. It could be based on the accessibility of surface modification, biological toxicity, plasmon resonance peak positions or others. Since most of these nanoparticles share a common feature: they have LSPR effect and they show varying apparent refractive indices at different wavelengths. Our new imaging technique, wavelength-dependent DIC microscopy, can be applied as a general method to track and identify those nanoparticles in complex environments such as live cells.

In this work, the smallest gold nanoparticles that can be detected by DIC on a clean substrate were 10 nm; while the smallest gold nanoparticles used inside live cells were 40 nm. That is because of the increased background noise level in DIC microscopy which resulted from cellular structures. Since all those cellular proteins are only several nanometers or even smaller, it may still alter the proteins' native behaviors if the labeling agent is on the order of several tens of nanometers. Nowadays, people are more interested in single molecule study since every individual molecule behaves heterogeneously. Due to the relatively large size of 40 nm labeling nanoparticles, several copies of proteins may attach on the particles' surface simultaneously. Then the experimental result can't be attributed to single molecule's property. In order to benefit the single molecule study eventually, new types of nanoparticles that have stronger and shallower plasmon resonance peaks are desired because they will be readily detectable in DIC microscopy.

When studying the orientation of targets with SPORT imaging technique, anisotropic gold nanorods were used as the rotational probe. SPORT can also support as a general imaging platform to study the orientation of other materials that have optically anisotropic property in fields other than bioanalytical area. For example, in material science, Janus particles which have at least two physically or chemically distinctive surfaces have become an area of great interest for a variety of applications such as drug delivery, sensors, and stabilization of water-oil emulsions. Thanks to the highly dynamic tracking capability of SPORT, the orientation information of the Janus particles in the liquid-liquid or gas-liquid interfaces can be captured. In addition, in stereochemistry, there is one type of chemical compounds possessing a property called specific rotation which results from the chiral centers in the chemical structure. Solid crystals or liquid solutions made of such compounds may cause levorotatory or dextrorotatory rotation of incident polarized light. The imaging pattern or intensity of the crystals of those compounds in DIC microscopy may change depending on their orientations and sizes. Also, the optical isotropic materials immersed in levorotatory or dextrorotatory rotational solutions could also show variable DIC image patterns when the concentration of the solution changes. Thus, SPORT platform may help to separate different type of crystals or solutions.

# ACKNOWLEDGEMENTS

First of all, I would like to thank my major advisor Dr.Fang for his generous support during my graduate studies. To me, Dr.Fang is a mentor as well as an older brother. He had given me the chance to work with him and taught me whatever he thought necessary. I am very glad that he and I shared the same office during the past several years before the Hach hall was complete. It was routine for us to discuss experimental details and design new approaches to solve new questions since we almost met each other every day. Fortunately, those discussions were very fruitful and helped me expand my view in science and sharpen my skills in solving questions. They are extremely wonderful and meaningful days in my life. More importantly, I find an example that I believe I can follow in my future career. I really enjoyed the days of pursuing knowledge under his guidance. It is so fortunate to have such a wonderful supervisor.

I also want to thank Dr.Yeung, my former major advisor. It is quite a pity for me that I only worked 3 years for him before Dr.Yeung retired. However, Dr.Yeung taught me much and I benefited a lot: it is Dr.Yeung who opened the door of science for me; it is Dr.Yeung who introduced the optical imaging world in which my research interest lies to me. I always take Dr.Yeung's expertise as the touchstone of my research work. The time with Dr.Yeung is great experience in my life.

I am also very thankful to Dr.Gufeng Wang who is a hard working scientist and an easy-going colleague. He taught me how to approach questions in a more systematic and scientific way, and how to write research manuscripts. Besides scientific knowledge, I also learned lots of philosophy of real life from him. The time I spent cooperating with him will be pleasant and valuable memory that accompanies me in the future. I feel so lucky to have him as one of my most important friends in my life.

I also thank Dr.Mary Jo Schmerr who always treated me like her own child. From her, I can fell the warmth and friendship of common American people. It soothed my homesickness especially when I was in the valley of my research. I would also like to thank other members of my POS committee. They are opened for discussion and gave me great advices.

I also want to express my appreciation to my other colleagues and friends in Dr.Fang's and

Dr.Yeung’s groups. They are: Dr.Hui Zhang, Dr.Jiangwei Li, Dr.Jiyong Lee, Dr.Dragan Isailovic, Dr.Aoshuang Xu, Dr.Yun Zhang, Guoxin Lu, Wenjun Xie, Dr. Makoto Tsunoda, Dr.Changbei Ma, Dr.Yong Luo, Dr.Shengda Qi, Yan Gu, Anthony Stender, Kyle Marchuk, Dr.Xiaowei Di, Rui Han and Lin Wei. I learned from all of them and it is my great honor to work with them.

In the end, I want to thank my family for their selfless support in my whole life. They always make me feel beloved no matter I success or not.